

NASA/CR-2011-217157



Compression After Impact Experiments and Analysis on Honeycomb Core Sandwich Panels with Thin Facesheets

*Thomas D. McQuigg
National Institute of Aerospace, Hampton, Virginia*

June 2011

NASA STI Program . . . in Profile

Since its founding, NASA has been dedicated to the advancement of aeronautics and space science. The NASA scientific and technical information (STI) program plays a key part in helping NASA maintain this important role.

The NASA STI program operates under the auspices of the Agency Chief Information Officer. It collects, organizes, provides for archiving, and disseminates NASA's STI. The NASA STI program provides access to the NASA Aeronautics and Space Database and its public interface, the NASA Technical Report Server, thus providing one of the largest collections of aeronautical and space science STI in the world. Results are published in both non-NASA channels and by NASA in the NASA STI Report Series, which includes the following report types:

- **TECHNICAL PUBLICATION.** Reports of completed research or a major significant phase of research that present the results of NASA programs and include extensive data or theoretical analysis. Includes compilations of significant scientific and technical data and information deemed to be of continuing reference value. NASA counterpart of peer-reviewed formal professional papers, but having less stringent limitations on manuscript length and extent of graphic presentations.
- **TECHNICAL MEMORANDUM.** Scientific and technical findings that are preliminary or of specialized interest, e.g., quick release reports, working papers, and bibliographies that contain minimal annotation. Does not contain extensive analysis.
- **CONTRACTOR REPORT.** Scientific and technical findings by NASA-sponsored contractors and grantees.
- **CONFERENCE PUBLICATION.** Collected papers from scientific and technical conferences, symposia, seminars, or other meetings sponsored or co-sponsored by NASA.
- **SPECIAL PUBLICATION.** Scientific, technical, or historical information from NASA programs, projects, and missions, often concerned with subjects having substantial public interest.
- **TECHNICAL TRANSLATION.** English-language translations of foreign scientific and technical material pertinent to NASA's mission.

Specialized services also include creating custom thesauri, building customized databases, and organizing and publishing research results.

For more information about the NASA STI program, see the following:

- Access the NASA STI program home page at <http://www.sti.nasa.gov>
- E-mail your question via the Internet to help@sti.nasa.gov
- Fax your question to the NASA STI Help Desk at 443-757-5803
- Phone the NASA STI Help Desk at 443-757-5802
- Write to:
NASA STI Help Desk
NASA Center for AeroSpace Information
7115 Standard Drive
Hanover, MD 21076-1320

NASA/CR–2011-217157



Compression After Impact Experiments and Analysis on Honeycomb Core Sandwich Panels with Thin Facesheets

*Thomas D. McQuigg
National Institute of Aerospace, Hampton, Virginia*

National Aeronautics and
Space Administration

Langley Research Center
Hampton, Virginia 23681-2199

Prepared for Langley Research Center
under Cooperative Agreement NNL09AA00A

June 2011

Acknowledgments

I would like to make the following acknowledgements of the valuable support I received for this research. First, thank you to my graduate advisor, Dr. Rakesh Kapania, for many years of support and mentorship. Thanks to my Ph.D. Committee: Dr. Mayuresh Patil, Dr. Gary Seidel, Dr. Stephen Scotti, and Dr. Sandra Walker, for their encouragement and advice. Additional thanks to Dr. Scotti and Dr. Walker, for serving as my NASA mentors during my time there. Thanks to Dr. Wade Jackson and Dr. James Ratcliffe for lending their expertise in experiments and analysis, as well as the use of their excellent model. Also, thanks to Dr. Tom Haynie and Dr. Mark Hilburger for the use of, and instruction on, some of the auxiliary instrumentation used in the experiments. Finally, I would like to extend my sincere gratitude to NASA Langley Research Center and the National Institute of Aerospace, both of Hampton, Virginia, for their financial support of my research, and the use of their world-class resources.

This report was submitted as a Dissertation to the Faculty of the Virginia Polytechnic Institute and State University in partial fulfillment of the requirements for the degree of Doctor of Philosophy in Aerospace Engineering.

Trade names and trademarks are used in this report for identification only. Their usage does not constitute an official endorsement, either expressed or implied, by the National Aeronautics and Space Administration.

Available from:

NASA Center for AeroSpace Information
7115 Standard Drive
Hanover, MD 21076-1320
443-757-5802

Compression After Impact Experiments and Analysis on Honeycomb Core Sandwich Panels with Thin Facesheets

Thomas Dale McQuigg

(ABSTRACT)

A better understanding of the effect of impact damage on composite structures is necessary to give the engineer an ability to design safe, efficient structures. Current composite structures suffer severe strength reduction under compressive loading conditions, due to even light damage, such as from low velocity impact. A review is undertaken to assess the current state-of-development in the areas of experimental testing, and analysis methods. A set of experiments on Nomex honeycomb core sandwich panels, with thin woven fiberglass cloth facesheets, is described, which includes detailed instrumentation and unique observation techniques. These techniques include high speed video photography of compression after impact (CAI) failure, as well as, digital image correlation (DIC) for full-field deformation measurements. The effect of nominal core density on the observed failure mode is described. A finite element model (FEM) is developed to simulate the experiments performed in the current study. The purpose of this simulation is to predict the experimental test results, and to confirm the experimental test conclusions. A newly-developed, commercial implementation of the Multicontinuum Failure Theory (MCT) for progressive failure analysis (PFA) in composite laminates, Heliuss:MCT, is included in this model. The inclusion of PFA in the present model gives it the new, unique ability to account for multiple failure modes. In addition, significant impact damage detail is included in the model as a result of a large amount of easily available experimental test data. A sensitivity study is used to assess the effect of each damage detail on overall analysis results. Mesh convergence of the new FEM is also discussed. Analysis results are compared to the experimental results for each of the 32 CAI sandwich panel specimens tested to failure. The failure of each specimen is accurately predicted in a high-fidelity, physics-based simulation and the results highlight key improvements in the understanding of honeycomb core sandwich panel CAI failure. Finally, a parametric study highlights the strength benefits compared to mass penalty for various core densities.

Contents

1	Introduction	1
1.1	Overview of Impact Damage in Composites	1
1.2	Impact Damage	4
1.2.1	Impact Damage in Composite Laminates	5
1.2.2	Impact Damage in Sandwich Composites	7
1.2.3	Considerations for the Experimental Study of Impact Damage	9
1.3	Compression After Impact Experiments	13
1.3.1	CAI Testing of Composite Laminates	14
1.3.2	CAI Testing of Composite Sandwich Constructions	17
1.4	CAI Modeling and Strength Prediction for Sandwich Constructions	19
1.4.1	Experimentally Based CAI Strength Prediction	19
1.4.2	Analytic Solutions of CAI Response	20
1.4.3	Finite Element Models for CAI Response	23
1.4.4	Modeling of Honeycomb Core	27
1.5	Progressive Failure Analysis	30
1.6	Overview of the Present Work	34
2	Impact Damage and CAI Tests of PXX Series Materials	36
2.1	Materials and Test Coupons	37

2.2	Impact Damage Evaluation	39
2.2.1	Static Indentation Tests	39
2.2.2	Drop Tower Impact Survey	45
2.3	Compression After Impact Experiments	52
2.3.1	Apparatus and Instrumentation	53
2.3.2	CAI Failure of PXX Series Coupons	58
2.3.3	Full-field Displacement Measurements Using DIC	64
2.4	Conclusions from Impact Damage and CAI Tests of PXX Series Materials	68
3	Impact Damage and CAI Tests of 3PCF-XX and 6PCF-XX Series	
	Materials	70
3.1	Materials and Test Coupons	71
3.2	Impact Damage Evaluation	74
3.2.1	Static Indentation Tests	74
3.2.2	Drop Tower Impact Survey	78
3.3	Compression After Impact Experiments	87
3.3.1	Apparatus and Instrumentation	87
3.3.2	CAI Failure of 3PCF-XX and 6PCF-XX Series Coupons	90
3.3.3	Full Field Displacement Measurements using DIC	97
3.4	Conclusions from Impact Damage and CAI Tests of 3PCF-XX and 6PCF-XX Series Materials	103
4	CAI Analysis Using Existing Models	105
4.1	General Theory for CAI Prediction	106
4.1.1	Classical Laminate Theory	106
4.1.2	Composite Laminates in Finite Element Analysis	112
4.1.3	Honeycomb Core as an Orthotropic Continuum	116
4.1.4	Honeycomb Core Non-Linear Out-of-Plane Response	121
4.2	FEM with Spring Element Core	122

4.2.1	Explanation of Model Components and Inputs	123
4.2.2	CAI Analysis Results for Spring Element Core Model	126
4.3	FEM with Solid Orthotropic Element Core	129
4.3.1	Explanation of Model Components and Inputs	129
4.3.2	CAI Analysis Results for Solid Element Core Model	134
4.4	Conclusions from CAI Analysis Using Existing Models	137
5	Development of a New Model for CAI Analysis	139
5.1	Progressive Failure Analysis Theory	140
5.1.1	Multicontinuum Theory	141
5.1.2	MCT Failure Theory	145
5.1.3	Material States for Woven Composite Laminates During PFA	148
5.2	Introduction to Proposed FEM for CAI Analysis	149
5.2.1	Geometry, Boundary Conditions and Finite Elements	151
5.2.2	Honeycomb Core Implementation using UMAT	154
5.2.3	Impact Damage Modeling	156
5.3	Mesh Pattern and Convergence	167
5.3.1	Mesh Convergence: Coupon Width Direction (eX)	167
5.3.2	Mesh Convergence: Coupon Load Direction (eY)	170
5.3.3	Mesh Convergence: Coupon Thickness Direction (eZc)	172
5.3.4	Additional Notes from the Mesh Convergence Study	174
5.4	FEM Sensitivity Studies	175
5.4.1	Sensitivity to Impact Damage Definition	176
5.4.2	Sensitivity to Core Damage Depth Definition	180
5.4.3	Sensitivity to Element Stiffness Degradation	182
5.4.4	Final Notes on the FEM's Sensitivities	184
5.5	Conclusions from the Development of the New FEM for CAI Analysis	186

6	Analysis of Test Coupons and Other CAI Analysis Results	188
6.1	Analysis of CAI Response of PXX Series	
	Panels	189
6.1.1	PXX Analysis Inputs	190
6.1.2	PXX Analysis Results	193
6.2	Analysis of CAI Response of 3PCF-XX Series	
	Panels	199
6.2.1	3PCF-XX Analysis Inputs	199
6.2.2	3PCF-XX Analysis Results	202
6.3	Analysis of CAI Response of 6PCF-XX Series	
	Panels	206
6.3.1	6PCF-XX Analysis Inputs	207
6.3.2	6PCF-XX Analysis Results	209
6.4	Parametric Study of CAI Response with Various Core Densities	215
6.4.1	Discussion of Core Crush Property Variance with Core Density	216
6.4.2	Results of the Parametric Study	218
6.5	Conclusions from the Results of Using the New FEM for CAI Analysis	220
7	Conclusions and Future Work	222
7.1	Conclusions	224
7.1.1	Experimental Testing Conclusions	225
7.1.2	Analysis Conclusions	228
7.2	Future Work	231
	Bibliography	234
A	Additional Results of CAI Experiments	246

List of Figures

2.1	PXX series honeycomb core sandwich panel material.	37
2.2	PXX series sandwich panel coupons for testing.	39
2.3	Apparatus used for static indentation of PXX series material coupons.	40
2.4	Semi-hemispherical tip used for static indentation, 0.5 in. diameter.	40
2.5	PXX series material coupon with resulting damage from static indentation.	41
2.6	Results of static indentation testing on PXX series materials: resultant force vs. applied displacement measured at Location 2.	42
2.7	Results of static indentation testing on PXX series materials: resultant force vs. applied displacement measured at Locations 4 and 5.	44
2.8	Drop tower apparatus used for impacting PXX series material coupons.	45
2.9	Results of drop tower impact testing on PXX series materials: dent depth vs. impact energy.	47
2.10	Results of drop tower impact testing on PXX series materials: dent diameter vs. impact energy.	47
2.11	Results of drop tower impact testing on PXX series materials: maximum impact force vs. impact energy.	47
2.12	Results of drop tower impact testing on PXX series materials: impact length vs. impact energy.	48
2.13	Results of drop tower impact testing on PXX series materials: impact force vs. time for Panel 1, Location 3.	48

2.14 Results of drop tower impact testing on PXX series materials: impact force vs. time for Panel 1, Location 4.	49
2.15 PXX series material coupon with resulting damage from drop tower impact, Panel 1.	50
2.16 PXX series material coupon with resulting damage from drop tower impact, Panel 2.	51
2.17 PXX series material coupon with resulting damage from drop tower impact, front of Panel 3.	52
2.18 PXX series material coupon with resulting damage from drop tower impact, rear of Panel 3.	53
2.19 Load frame and coupon mounting apparatus used for CAI testing.	54
2.20 Location of strain gages for CAI testing of PXX series material coupons (all dimensions in inches).	55
2.21 Planform drawing of test frame loading platen which shows of DCDT locations used for CAI testing (all dimensions in inches).	56
2.22 Auxiliary apparatus for CAI testing of PXX series coupons with video instrumentation (above) and Vic-3D digital cameras (below).	57
2.23 Speckled PXX series material coupon for Vic-3D instrumentation of CAI testing.	58
2.24 Results of CAI testing of PXX series materials: typical measured resultant force vs. applied.	59
2.25 PXX series material coupon during CAI testing, post-failure, showing results of indentation propagation failure mode.	59
2.26 Results of CAI testing of PXX series materials: time lapse images taken throughout test.	60
2.27 Results of CAI testing of PXX series materials: time lapse images taken from high speed camera during failure.	61
2.28 Results of CAI testing of PXX series materials: CAI failure stress and strain vs. impact energy.	62

2.29	Results of CAI testing of PXX series materials: typical reaction force vs. strain measured by various methods.	63
2.30	Results of CAI testing of PXX series materials: typical reaction force vs. strain measured by individual gages.	63
2.31	Results of CAI testing of PXX series materials: typical reaction force vs. displacement measured by individual DCDT.	64
2.32	Results of CAI testing of PXX series materials: three dimensional DIC imaging of PXX test coupon at 75% of failure load, out-of-plane deformation shown.	65
2.33	Results of CAI testing of PXX series materials: three dimensional DIC imaging of PXX test coupon after indentation propagation failure, out-of-plane deformation shown.	66
2.34	Results for DIC measurements: dent growth in coupon width direction for PXX test coupons.	67
2.35	Results for DIC measurements: dent growth in coupon load direction for PXX test coupons.	67
2.36	Results for DIC measurements: dent depth increase in coupon load direction for PXX test coupons.	68
3.1	3PCF-XX (top) and 6PCF-XX (bottom) series honeycomb core sandwich panel material.	71
3.2	3PCF-XX (top right) and 6PCF-XX (top left) series material coupons for testing, with top load bearing end (middle) and side views (bottom.	73
3.3	Static indentation of 3PCF-XX (right) and 6PCF-XX (left) series sandwich coupons.	75
3.4	Results of static indentation of 3PCF-XX series material coupons: residual dents.	76
3.5	Results of static indentation of 3PCF-XX series material coupons: resultant force vs. applied displacement.	76

3.6	Results of static indentation of 6PCF-XX series material coupons: residual dents.	77
3.7	Results of static indentation of 6PCF-XX series material coupons: resultant force vs. applied displacement.	78
3.8	Drop tower apparatus used for impact survey of 3PCF-XX and 6PCF-XX series material coupons.	79
3.9	Results of drop tower impact testing on 3PCF-XX and 6PCF-XX series materials: variation of the dent depth vs. the impact energy.	80
3.10	Results of drop tower impact testing on 3PCF-XX and 6PCF-XX series materials: variation of the dent diameter vs. the impact energy.	81
3.11	Results of drop tower impact testing on 3PCF-XX and 6PCF-XX series materials: variation of the maximum impact force vs. the impact energy.	81
3.12	Results of drop tower impact testing on 3PCF-XX and 6PCF-XX series materials: variation of the impact length vs. the impact energy.	82
3.13	Results of drop tower impact testing on 3PCF-XX and 6PCF-XX series materials: variation of the core damage width vs. the impact energy.	82
3.14	Results of drop tower impact testing on 3PCF-XX and 6PCF-XX series materials: variation of the core damage depth vs. the impact energy.	83
3.15	Results of drop tower impact testing on 3PCF-XX and 6PCF-XX series materials: variation of the total dent depth for 3PCF-XX materials vs. the impact energy.	83
3.16	Results of drop tower impact testing on 3PCF-XX and 6PCF-XX series materials: variation of the total dent depth for 6PCF-XX materials vs. the impact energy.	84
3.17	Results of drop tower impact testing on 3PCF-XX series materials: residual dents.	85
3.18	Results of drop tower impact testing on 6PCF-XX series materials: residual dents.	86

3.19	Results of drop tower impact testing on 6PCF-XX series materials: core damage shown through destructive evaluation.	87
3.20	Load frame and coupon mounting apparatus used for CAI testing with 3PCF-XX (left) and 6PCF-XX (right) coupons installed.	88
3.21	Location of strain gages for CAI testing of 3PCF-XX and 6PCF-XX series material coupons (all dimensions in inches).	89
3.22	Auxiliary apparatus for CAI testing of 3PCF-XX and 6PCF-XX series coupons with high speed Phantom cameras and necessary lighting systems.	90
3.23	Results of CAI testing of 3PCF-XX and 6PCF-XX series materials: failure modes of indentation propagation for 3PCF-XX series coupons (left) and crack propagation in 6PCF-XX coupons (right).	92
3.24	Results of CAI testing of 6PCF-XX series materials: time lapse images taken throughout test.	93
3.25	Results of CAI testing of 3PCF-XX and 6PCF-XX series materials: time lapse images taken from high speed camera during failure for 3PCF-XX (right) and 6PCF-XX (left) materials.	94
3.26	Results of CAI testing of 3PCF-XX and 6PCF-XX series materials: failure stress vs. impact energy.	96
3.27	Results of CAI testing of 3PCF-XX and 6PCF-XX series materials: failure strain vs. impact energy.	96
3.28	Example 3D representation of the indentation propagation failure mode for a 3PCF-XX series CAI test coupon.	98
3.29	Example 2D representation of the indentation propagation failure mode for a 3PCF-XX series CAI test coupon.	98
3.30	Example 3D representation of the crack propagation failure mode for a 6PCF-XX series CAI test coupon.	99
3.31	Example 2D representation of the crack propagation failure mode for a 6PCF-XX series CAI test coupon.	99

3.32	Results from DIC Measurements: dent growth in coupon width direction for 3PCF-XX test coupons.	100
3.33	Results from DIC Measurements: dent growth in coupon load direction for 3PCF-XX test coupons.	101
3.34	Results from DIC measurements: dent depth increase for 3PCF-XX test coupons.	101
3.35	Results from DIC measurements: dent growth in coupon width direction for 6PCF-XX test coupons.	102
3.36	Results for DIC measurements: dent growth in coupon load direction for 6PCF-XX test coupons.	102
3.37	Results from DIC measurements: dent depth increase for 6PCF-XX test coupons.	103
4.1	Cellular in-plane geometry of hexagonal cell honeycomb core.	118
4.2	Solid element core crush constitutive model.	122
4.3	Spring element core sandwich panel CAI FEM with boundary conditions. . .	123
4.4	Spring element core crush constitutive model.	125
4.5	Spring element core FEM results: Typical reaction force vs. applied displacement with and without effect of including initial core damage.	126
4.6	Sample spring element core FEM results: indentation propagation failure mode with out-of-plane displacement indicated by colored contours (blue indicates maximum negative displacement).	127
4.7	Sample spring element core FEM results: reaction force vs applied displacement for sample analyses on PXX series panels.	128
4.8	Solid element core sandwich panel CAI FEM with boundary conditions. . . .	130
4.9	Sample solid element core FEM results: typical reaction force vs. applied displacement.	133
4.10	Damaged core elements (left) and damaged facesheet elements (right) in the solid element core model example.	133

4.11	Sample solid element core FEM results: reaction force vs applied displacement, model did not include simulated impact damage in the facesheets.	135
4.12	Sample solid element core FEM results: failure stress vs. impact energy with (WFD) and without simulated facesheet impact damage (NFD).	136
5.1	New CAI model: FEM Geometry.	152
5.2	New CAI model: FEM node points (highlighted in red) for boundary conditions of symmetry (left), simulated potting (center), and applied displacement (right).	152
5.3	Idealized core crush response use to define non-linear constitutive core behavior of 3PCF Nomex core.	156
5.4	New CAI analysis model: close-up view of indented region of FEM.	158
5.5	Examples of core damage from destructive microscopy of 3PCF-XX (left) and 6PCF-XX (right) series materials.	159
5.6	New CAI analysis model: damaged core region example.	160
5.7	Examples of facesheet damage from microscopy of PXX (left) and 3PCF-XX (right) series materials.	161
5.8	Example of matrix cracking as a result of impact damage observed by optical microscopy.	161
5.9	New CAI analysis model:facesheet element regions representing areas of observed IFF (left) and fiber fracture (right), prior to any compressive load analysis steps.	162
5.10	Mesh convergence study results: CAI failure load vs. number of elements (eX).	169
5.11	Mesh convergence results: % change in CAI failure load vs. number of elements (eX).	170
5.12	Mesh convergence results: CAI failure load vs. number of elements (eY).	171
5.13	Mesh convergence results: % change in CAI failure load vs. number of elements (eY).	172
5.14	Mesh convergence results: CAI failure load vs. number of elements (eZc).	173

5.15	Mesh convergence results: % change in CAI failure load vs. number of elements (eZc).	174
6.1	PXX analysis results: reaction force vs. applied displacement for analysis of PXX series test coupons.	194
6.2	Demonstration of correct failure mode prediction for example analysis of PXX series material coupons using the new FEM for CAI analysis.	195
6.3	PXX analysis results: comparison of PXX test coupon analysis failure strength to experimental test results.	196
6.4	PXX analysis results: dent growth in the coupon width direction (x-direction) predicted from FEA of PXX test coupons.	197
6.5	PXX analysis results: dent growth in the coupon load direction (y-direction) predicted from FEA of PXX test coupons.	198
6.6	PXX analysis results: maximum dent depth growth predicted from FEA of PXX test coupons.	198
6.7	3PCF-XX analysis results: reaction force vs. applied displacement for analysis of 3PCF-XX series test coupons.	202
6.8	3PCF-XX analysis results: comparison of 3PCF-XX test coupon analysis failure strength to experimental test results.	204
6.9	3PCF-XX analysis results: dent growth in the coupon width direction (x-direction) predicted from FEA of 3PCF-XX test coupons.	205
6.10	3PCF-XX analysis results: dent growth in the coupon load direction (y-direction) predicted from FEA of 3PCF-XX test coupons.	205
6.11	3PCF-XX analysis results: maximum dent depth growth predicted from FEA of 3PCF-XX test coupons.	206
6.12	6PCF-XX analysis results: reaction force vs. applied displacement for analysis of 6PCF-XX series test coupons.	209
6.13	Demonstration of crack propagation failure mode for example analysis of 6PCF-XX series material coupons using the new FEM for CAI analysis. . . .	211

6.14 6PCF-XX analysis results: comparison of 6PCF-XX test coupon analysis failure strength to experimental test results. 213

6.15 6PCF-XX analysis results: dent growth in the coupon width direction (x-direction) predicted from FEA of 6PCF-XX test coupons. 214

6.16 6PCF-XX analysis results: dent growth in the coupon load direction (y-direction) predicted from FEA of 6PCF-XX test coupons. 214

6.17 6PCF-XX analysis results: maximum dent depth growth predicted from FEA of 6PCF-XX test coupons. 215

6.18 Core crush strength of Nomex honeycomb shown varying with nominal core density, and the data fit calculated for use with the parametric study analyses. 217

6.19 Core crush modulus of Nomex honeycomb shown varying with nominal core density, and the data fit calculated for use with the parametric study analyses. 218

6.20 Parametric study results: failure strength vs. nominal core density associated with continuum core properties. 219

6.21 Parametric study results: percentage strength increase vs. normalized mass increase. 219

A.1 Additional results of CAI testing of PXX series materials: residual dent depth vs. impact energy. 247

A.2 Additional results of CAI testing of PXX series materials: residual dent diameter vs. impact energy. 247

A.3 Additional results of CAI testing of 3PCF-XX and 6PCF-XX series materials: residual dent depth for impacts on coupons used for CAI testing of 3PCF-XX and 6PCF-XX series materials. 249

A.4 Additional results of CAI testing of 3PCF-XX and 6PCF-XX series materials: residual dent diameter for impacts on coupons used for CAI testing of 3PCF-XX and 6PCF-XX series materials. 251

List of Tables

2.1	Results of static indentation testing on PXX series materials: damage measurements	43
4.1	Spring core element FEM analysis: engineering constants used for layers of PXX series sandwich panel facesheets.	124
4.2	Spring core element FEM results: failure metrics.	128
4.3	Sample solid core element FEM analysis: engineering constants used for orthotropic continuum representation of Nomex honeycomb core.	132
4.4	Sample solid core element FEM analyses: inputs used for demonstration. . .	134
4.5	Sample solid element core FEM results: failure metrics.	135
5.1	Nominal input values for MATLAB function for Abaqus input file creation used during the sensitivity studies.	177
5.2	Detailed sensitivity results of 3PCF-02 test coupon model to residual dent maximum depth definition.	179
5.3	Sensitivity study results for various MATLAB function inputs.	179
5.4	Sensitivity study results, core damage region depth input.	181
5.5	Sensitivity study results for element stiffness degradation inputs.	184
6.1	E-glass/Epoxy woven fabric lamina material properties used in the CAI analysis of PXX series test coupons.	191
6.2	E-glass/Epoxy woven fabric lamina strengths used in the CAI analysis of PXX series test coupons.	191

6.3	3PCF Nomex honeycomb core orthotropic engineering constants used in the CAI analysis of PXX and 3PCF-XX series test coupons.	191
6.4	MATLAB program inputs for creation of ABAQUS input files to run analyses of PXX series test coupons.	192
6.5	PXX analysis results: failure load, strength and strain for analysis of PXX series test coupons.	196
6.6	S2-glass/Epoxy woven fabric lamina material properties used in the CAI analysis of 3PCF-XX and 6PCF-XX series test coupons.	200
6.7	S2-glass/Epoxy woven fabric laminate strengths used in the CAI analysis of 3PCF-XX and 6PCF-XX series test coupons.	201
6.8	MATLAB program inputs for creation of ABAQUS input files to run analyses of 3PCF-XX series test coupons.	201
6.9	3PCF-XX analysis results: failure load, strength and strain for analysis of 3PCF-XX series test coupons.	203
6.10	6PCF Nomex honeycomb core orthotropic engineering constants used in the CAI analysis of 6PCF-XX series test coupons.	207
6.11	MATLAB program inputs for creation of Abaqus input files to run analyses of 6PCF-XX series test coupons.	208
6.12	6PCF-XX analysis results: failure load, strength and strain for analysis of 6PCF-XX series test coupons.	212
A.1	Additional results of impact survey of PXX series materials: panel 1 damage metrics.	246
A.2	Additional results of impact survey of PXX series materials: panel 2 damage metrics.	246
A.3	Additional results of impact survey of PXX series materials: panel 3 damage metrics.	248
A.4	Additional results of CAI testing of PXX series materials: impact damage metrics.	249

A.5	Additional results of CAI testing of PXX series materials: CAI failure metrics.	250
A.6	Additional results of CAI testing of 3PCF-XX and 6PCF-XX series materials: 3PCF-XX static indentation results.	251
A.7	Additional results of CAI testing of 3PCF-XX and 6PCF-XX series materials: 6PCF-XX static indentation results.	251
A.8	Additional results of CAI testing of 3PCF-XX and 6PCF-XX series materials: impact survey results describing the residual damage for 3PCF-XX materials.	252
A.9	Additional results of CAI testing of 3PCF-XX and 6PCF-XX series materials: impact survey results describing the force and length of impact for 3PCF-XX materials.	253
A.10	Additional results of CAI testing of 3PCF-XX and 6PCF-XX series materials: impact survey results describing the residual damage for 6PCF-XX materials.	254
A.11	Additional results of CAI testing of 3PCF-XX and 6PCF-XX series materials: impact survey results describing the force and length of impact for 6PCF-XX materials.	255
A.12	Additional results of CAI testing of 3PCF-XX and 6PCF-XX series materials: results for impacts on 3PCF-XX coupons used for CAI testing.	255
A.13	Additional results of CAI testing of 3PCF-XX and 6PCF-XX series materials: results for impacts on 6PCF-XX coupons used for CAI testing.	256
A.14	Additional results of CAI testing of 3PCF-XX and 6PCF-XX series materials: results for failure of 3PCF-XX series panels during CAI testing.	257
A.15	Additional results of CAI testing of 3PCF-XX and 6PCF-XX series materials: results for failure of 6PCF-XX series panels during CAI testing.	258

List of Symbols

(e)	Superscript meaning element
$*$	Superscript indicated effective property
1	Local coordinate or axis, fiber direction
2	Local coordinate or axis, transverse direction
3	Local coordinate or axis, out-of-plane direction
A	Matrix component
B	Matrix component
C	Component of the lamina stiffness matrix
D	Matrix component
E	Extensional Young's modulus
F	Forces
F_S	Shear flexibility
G	Shear modulus
H	Total laminate thickness
I	Stress invariant, used with subscript to identify

K_h	Hourglass stiffness
M	Composite laminate moment resultant
N	Composite laminate normal stress resultant
R	Principle radii of curvature
S	Component of the lamina compliance matrix
U	Displacements
V	Composite laminate transverse stress resultant
Vol	Volume of region
W	‘Waviness’ coefficient
Γ	Hourglass mode
Φ	Rotations
Π	Total potential energy
Θ, Λ, Γ	Finite element deformation modes
Ξ	Deformed coordinates along the laminate midsurface
α	Equation coefficient
\bar{C}	Component of the transformed (global coordinates) lamina stiffness matrix
\bar{S}	Component of the transformed (global coordinates) lamina compliance matrix
δ	Delta operator, variation
γ	Shear components of the shear tensor
γ^o	Shear strain component at the composite laminate midsurface

κ^o	Curvature component at the composite laminate midsurface
λ	Eigenvalue
$[C]$	Constitutive matrix
$[N]$	Finite element shape functions
∂	Indicates partial derivative
ϕ_f	Fiber volume fraction
ϕ_m	Matrix volume fraction
$\phi_{fill/mat}$	Superconstituent volume fraction (fill tow fiber/matrix and ply matrix pockets)
ϕ_{fill}	Fill tow volume fraction (fill tow fiber/matrix)
ϕ_{mat}	Laminate matrix pockets tow volume fraction
ϕ_{warp}	Warp tow volume fraction (warp tow fiber/matrix)
σ	Extensional components of the stress tensor
σ_C^f	Compressive fiber strength
σ_C^m	Compressive matrix strength
σ_{S12}^f	In-plane fiber shear strength
σ_{S12}^m	In-plane matrix shear strength
σ_{S23}^m	Transverse matrix shear strength
σ_T^f	Tensile fiber strength
σ_T^m	Tensile matrix strength

τ	Shear components of the stress tensor
θ	Ply orientation angle with respect to the global coordinate system
ν	Poisson's ratio
ε	Extensional components of the strain tensor
ε^o	Extensional strain component at the composite laminate midsurface
ξ	Coordinates along the laminate reference surface
$\{\varepsilon\}$	Strain tensor
$\{\sigma\}$	Stress tensor
a	Equation coefficient
c	Subscript or superscript meaning composite property
d	Maximum dent diameter
eX	Number of elements in the global model x-direction
eY	Number of elements in the global model y-direction
eZc	Number of elements in the global model z-direction, core region only
f	Subscript or superscript meaning fiber constituent property
h_{max}	Maximum dent depth
i	Subscript indicating tensor placement, or superscript indicating mode
ij	Subscripted indices indicating tensor placement
m	Subscript or superscript meaning matrix constituent property
n	Maximum integer value in summation

o, p, q	Element local Cartesian coordinates
x	Global coordinate or axis
y	Global coordinate or axis
z	Global coordinate or axis, distance from the laminate midsurface

Chapter 1

Introduction

1.1 Overview of Impact Damage in Composites

An aerospace vehicle will probably sustain some type of impact loading during its lifetime, whether during fabrication, maintenance or in some phase of in-service operation. The resulting damage from impact may result in residual strength loss in airframe structures which can be potentially life threatening. A well known example of the potential tragic consequences of impact damage to an airframe can be seen in the 2003 events of the Space Shuttle Columbia disaster. Camarda [1] noted that new design and analysis methods were proposed as a result of this tragedy, and the emphasis on understanding impact damage in aerospace structures was renewed. This emphasis on impact damage has led to experiments and analysis like the work that will be presented in the current research on low velocity impact damage. Although the mechanics are different from the preceding example, understanding low speed impact damage is also of critical importance. Vehicles today are increasingly built from composite structures, such as honeycomb core sandwich panels, which often feature thin, laminated facesheets. In the literature review which follows in the present chapter, structures such as these will be shown to be susceptible to large residual strength reductions due to damage which may not be readily apparent. Research on impact damage in composite structures has largely focused on experiments. Analysis of this problem has not been as thoroughly

performed, which means that design efficiency often suffers because of the complexity and lack of understanding associated with this damage.

A comprehensive review of the work prior to 1999 on the subject of damage tolerance in composite materials was written by Tomblin *et al.* [2] for the U.S. Department of Transportation (DOT) Federal Aviation Administration (FAA) Office of Aviation Research. The researchers noted that the problem of impact damage in composites had already received a wide array of treatment, but the effect of this damage on the mechanical response and residual strength on sandwich composite components has not been as thoroughly developed. This FAA report summarized impact damage on composite laminates and sandwich panels and noted the differences in damage modes between the two classes of materials. Some of these differences will be discussed later in the literature review. They noted, sources of localized damage resulting from low to medium velocity impacts, are similar to both types of materials and include damage during manufacturing, assembly, and handling (e.g. tool drops) and in-service operation (e.g. hail or bird strikes). Other sources of damage include materials, fabrication, and processing defects, but the results of this type of damage is not the focus of the current research and will not be covered in the literature review.

The incentive for the FAA to establish a document on damage tolerance in composites was to ascertain an approach for future designs to meet government safety requirements for airframe certification. In this pursuit, the report by Tomblin *et al.* [2] describes two critical standards which were considered in the present research. First, the authors established relationships between representative damage sizes to design load requirements. Second, a five step methodology for describing composite airframe damage tolerance is explained. (This approach was later formally adopted as guidance for development and certification of composite structures by the FAA [3].) The relationships between damage sizes and design load requirements are as follows. The smallest level damage is defined as that which is below the Allowable Damage Limit (ADL) threshold. This sometimes undetectable damage is also known as Barely Visible Impact Damage (BVID), a common term in the study of composite impact damage. An airframe is required to withstand this type of damage over the op-

erational lifetime of the vehicles without repair at no decrease in ultimate load capability. Tomblin *et al.* [2] next define a damage level, the Critical Damage Threshold (CDT), up to which the damage is viewable, but may not be found except by periodic inspection. Aircraft are required to be able to withstand damage up to CDT while undergoing multiple loadings between specified inspection intervals and at least one lifetime limit load. Damage beyond the CDT is defined as readily apparent to the operator of the vehicle (such as bird strike or engine burst) and a vehicle must be able to safely finish its present flight after such an impact event.

Tomblin *et al.* [2] went on to propose the following five step methodology for describing the damage tolerance of a structure. First, damage formation in a specific sandwich structure subject to low-velocity impact must be investigated experimentally. During this process, the impact energy and velocity, and the impactor shape and diameter are chosen based on previous studied work. The damage induced should then be studied and quantified. The report suggests that this data can be used for semi-empirical model development. In the second step, sandwich panel coupons are tested for residual strength. The report notes that residual strength can be compared to damage size or impact energy level. In the third task, damaged sandwich panels are subjected to fatigue loading, which is important in characterizing types of damage up to the CDT. Next, in step four, a model for predicting impact damage development and residual strength degradation should be developed. During this process, they recommend that a number of analytical, numerical, and semi-empirical models should be considered. It is expected that no one model can account for all types and amounts of damages, or all materials and sandwich configurations. The fifth and final state of the recommended methodology for determining damage tolerance is component, and then full-scale testing and verification of the model results.

The following review of the literature relevant to the current research will cover subjects related to damage resistance or damage tolerance. Damage resistance is a measure of a material or structure's ability to withstand impact damage without sustaining damage. Experiments including quasi-static indentation and impact testing are used to study a com-

ponent's ability to withstand damage. With the data these experiments generate, damage modes can be measured and described and new materials can be designed based on the information learned. Analysis models can also be used to examine a component's damage resistance. Damage tolerance, on the other hand, is the study of a component's ability to carry design loads while damaged. Experimental testing of damaged components as well as analytic models can be used to characterize their residual strength and failure modes. Compression after impact (CAI) loading is the most used method of measuring damage tolerance in a composite material or structure. The largest reductions in residual strength, due to impact damage, occur under compression loading, due to instabilities introduced by this damage.

Through a better understanding of both damage resistance and damage tolerance, safer and more efficient airframes and other structures can be designed and built. The literature review begins in the following section with some highlights in the area of damage resistance. These topics are related to the current research as they serve to establish the damage expected and the evaluation techniques used. The remainder of the literature review will focus on topics of damage tolerance. First, samples of the work done by experimental testing are discussed to define the types of damage relevant to CAI and the failure modes unique to this loading condition. Next, the current state of the analysis efforts which have focused on the CAI problem is given. Some of the techniques and assumptions discussed are used extensively in the present research, while others are not used. Finally, an area of research new to analysis techniques used for considering CAI will be discussed. This area of research is progressive failure analysis of laminated composites and will be a major component of the model proposed in the current work.

1.2 Impact Damage

Tomblin *et al.* [2] suggested that the major purpose of the study of impact damage is to identify airframe load path critical structures and materials, damage modes, detectable

damage sizes, and strength limiting sizes. It is especially important to determine the damage levels that are detectable and at what load levels that damage results in strength reduction to the material or structure. The study of impact damage allows for the design of critical load bearing components in which damage can be detected before failure can occur. It can be rightly pointed out that impact damage in composite laminates and sandwiches have unique damage modes and should be studied separately. The following section first briefly outlines impact damage in laminates and impact damage in sandwich constructions. Then, various damage evaluation techniques are described, some of which were later used in the current research.

1.2.1 Impact Damage in Composite Laminates

Cantwell and Morton [4] identified several failure mechanisms due to impact in fiber reinforced polymer (FRP) composite laminates, including fiber-matrix debonding, fiber pull-out, intralaminar matrix cracking, matrix deformation, delamination, and fiber fracture. Fiber-matrix debonding occurs when the stress in the interphase region of a fiber reinforced polymer material exceeds the local strength allowing a crack to form. This type of debond depends on fiber surface treatment prior to manufacture and can actually reduce the stress raising effect of impact damage because fiber sliding becomes a principal energy absorbing mechanism. Intralaminar matrix cracking is partly responsible for the large areas of damage found following an impact of a fiber reinforced matrix material. This type of cracking can involve large cracks parallel to the fibers in either the matrix or interphase regions of a composite. Plastic matrix deformation occurs in fiber reinforced matrix materials when the matrix yield strength is reached. The ability of the matrix to plastically deform can actually be quite beneficial to reducing stress raising effects and blunting cracks that form at damage. However, due to the high strain rates involved with impact, the dynamic yield strength is usually much higher than measured at near static conditions and the material's toughness is reduced. Interlaminar delaminations occur at ply interfaces and during impact the most severe cases of this type of damage have been shown to occur at locations of large differences

in the orientations of the adjacent plies to the interlaminar region. In cases of impact these regions of delamination are usually linked by a series of intralaminar matrix cracks which incline between delaminations at 45 degrees. Impacts can also create localized fiber fracture in a composite laminate material. Fiber cracks are most likely to be detrimental to a material's tensile loading capability and in general are less detrimental than matrix damage to a composite material's compressive strength. It has also been shown that this type of damage dominates in thin laminates, whereas matrix damage is more common in thicker laminates.

The failure mechanisms described are applicable to both unidirectional and woven fabric FRP laminates. In the current research, only plain woven fabric plies are considered. An example of an experimental investigation on the response of a woven fiberglass reinforced matrix (GFRP) laminate to low velocity impact loading was presented by Hosur, Karim, and Jeelani [5]. The authors reported the effects of single and repeated impacts on GFRP with and without Kevlar stitching as reinforcements. They noted that delaminations are the major cause of failure in impact damaged laminates and that stitching can be used to arrest their development. However, the authors found that penetration was a more likely damage mode in stitched panels, as most of the resulting damage was contained to the impact location. In the study, stitched panels were able to sustain more repeated impacts than unstitched ones. Hosur *et al.* [6] also considered the hybridization of laminates with glass and carbon fibers reinforcing the laminate matrix. The authors noted that improved load carrying capability during impact could be achieved with only minor reductions in stiffness.

Since S2-glass woven fabric material is considered in the current research, an example of impact damage on this type of material is considered in the work by Baucom *et al.* [7]. The authors examined and compared traditional 2D weaves, as well as 3D weaves. 3D weaves involve laminate organization where tows are woven through the thickness direction. This effectively eliminates traditional plies. Scanning electron microscopy was used to obtain high resolution images of the resulting damage. The authors reported traditional impact damage in woven laminates for the 2D weaves (e.g. matrix and fiber cracks, delamination, etc.) which was reduced in the 3D weaves. The 3D woven materials also absorbed more energy before

penetration of the laminate.

In addition to stitching, other factors which play an important role in the damage from low velocity impacts on composite laminates include geometric effects, such as thickness and curvature. An example of these effects can be found in an experimental and analytical study of the effects of panel curvature on the impact response of composite laminates was presented by Ambur *et al.* [8]. The authors presented an analytic solution for the response of flat and curved panels to impact loading using small deflection and first order shear theory which appeared to accurately predict the experimental response. Experimental and analytic data suggested that curvature has a significant impact on the impact response of composite laminates and damage development. Contact force, in general, was found to decrease with increasing curvature radius, while a limit point instability exists for tests of a certain panel curvature radius and impact load force that results in a reduction in contact force due to panel buckling.

1.2.2 Impact Damage in Sandwich Composites

In composite sandwich constructions with FRP facesheets, each of the impact failure mechanisms mentioned by Cantwell *et al.* [4] for composite laminates can be found in the facesheets. Tomblin *et al.* [2] also mentioned several types of impact damage unique to sandwich composites, facesheet-core delamination, core crush, and puncture. Other examples of data from impact damage studies on sandwich composites can be found in various FAA reports and will be summarized in the present section. Tomblin *et al.* [9] also studied scaling of impact damage and residual strength from coupon level tests to component or full scale structures. The results noted that the residual strengths obtained from coupon level component testing can be validly compared to the large level tests. They do, however, note that larger specimens distribute the impact energy and thus sustain less impact damage for a given impact energy.

An example of a thorough impact damage study on sandwich composites can be found in a recent work by Raju *et al.* [10]. In this study, the authors conducted impact testing on

coupons with dimensions of roughly 8.5 in. by 10.5 in. using hemispherically shaped indentors with 1 and 3 in. diameter tips. The smaller tip was found to produce facesheet penetration, as well as regions of highly crushed core material that extended through the thickness of the panels. On the other hand, the larger indenter tip produced small deflections of the facesheet and only a small layer of core damage below the facesheet, but the damage extended over a large area of the panel.

Raju *et al.* [10] also identified a series of damage progression that can be applied to other impact damage studies of composite materials, including those later described in this work. The first type of damage they identified for the lowest levels of impact energy is the initiation of facesheet and core damage. This includes the onset of core crush and plastic deformation of the facesheet which may be accompanied by local constituent damage and failure. Second, the damage propagates through the facesheet (by subsequent constituent or bonding failure) and the core (by crushing). In the third stage, the facesheet may fracture for some sandwich constructions, especially with thick core, while the core may just consolidate for thinner cores. Extreme damage becomes apparent in the fourth stage as complete facesheet penetration occurs and the core completely consolidates. Finally, in the fifth and most extreme stage of impact damage for a material, damage is initiated in the backside facesheet.

Raju *et al.* [10] noted other parameters associated with carrying out the impacts that may be of importance. They showed that the peak force recorded by the impactor for a given impact load will vary with size of the indenter, amount of core crush, and the boundary conditions associated with the panel being impacted. Damage trends, including size and amount, were also shown to vary with these variables. Tomblin *et al.* [11] observed the effects of panel curvature on the properties of impact damage in composite sandwich structures. It was found that when the radius of curvature of a panel was decreased, resulting in increased global bending stiffness, the local contact stiffness near an impact was decreased. This resulted in increased amounts of impact damage when impacted with a sharp tip and decreased amounts of damage when impacted with a blunt impact tip. The effects of panel

curvature were also discussed by Shyprykevich *et al.* [12] and Moody *et al.* [13].

An analytical approach to studying the impact damage in composite sandwich structures was presented by Ambur and Cruz [14]. A local-global approach was used to analyze the effect of several sandwich construction variables on the contact force, displacement, and surface strains on the contacted facesheet, as well as resulting damage. Facesheet thickness was found to be the primary factor influencing the resulting damage of those studied. Another analytic approach to modeling the results of low-velocity impact loading was undertaken by Foo *et al.* [15]. This group modeled the onset of facesheet delamination and fiber fracture, core yield at the impact location, and the propagation of the damage under additional loading. The results of the analytical study were compared to energy based methods and the authors concluded that the impact response of the sandwich panel could be successfully modeled by considering its energy absorption during impact loading.

The use of static indentation as an alternative to low velocity impact when evaluating the damage mechanisms of sandwich panel constructions was considered by Singh *et al.* [16]. The researchers evaluated damage in the BVID range and below in aluminum honeycomb core sandwich panels with 8-ply quasi-isotropic GFRP facesheets. The types of damage found using quasi-static indentation was similar to low-velocity impact damage. The researchers considered three different aluminum honeycomb core materials, four quasi-isotropic facesheet lay-ups, and one and three inch diameter semi-hemispheric indentation tips. Delamination was observed more often in the interply interfaces closest to the core despite the specific layup of the specimen. The data presented showed that core density had the largest effect on the size of the resulting damage. Stiffer cores resulted in more facesheet delaminations, smaller crushed core regions, and smaller residual dents.

1.2.3 Considerations for the Experimental Study of Impact Damage

Several experiments will be described later in Chapters 2 and 3. The design of these experiments takes into account the work and advice of several researchers. Important components

of impact testing include the selected impact mass and velocity, the boundary conditions of the impact specimen, the geometry of the impact specimen as well as the impacting tip of the impact mass, and finally, the methods for detecting and characterizing the resulting damage. As the focus of this work was on the compression after impact experiment and modeling results, this section is intended to be an overview and by no means is meant to encapsulate the range of variables an experimentalist must consider when undertaking the study of damage characteristics and damage resistance in composites.

An excellent example of the experimental techniques associated with the study of impact damage in composites can be seen in the work by Tomblin *et al.* [17]. A well developed drop tower impact apparatus which allows for the variation of impactor mass and end geometry is shown in their work. Other critical components include a rebound catch mechanism and a high speed data acquisition system. In addition, it is important to consider the boundary conditions associated with the panel being impacted. The key measurements during impact testing are impact load, and impactor displacement and velocity. The resulting data that can be considered includes impact force vs. time, impact force vs. displacement, peak impact force vs. impact energy, peak impactor displacement vs. impact energy, and impact duration vs. impact energy.

The influence of the mass of the projectile on the resulting impact damage in composites was considered by Cantwell and Morton [18] in both high and low speed impacts for a single diameter of impacting tip. The authors showed that for a given impact energy, the mass of the impactor has a significant effect on the damage in a composite structure. They concluded that greater mass meant more concentrated damage in a specimen, while lower masses actually produced larger areas of damage. Specimen sizing was also studied by Cantwell [19] in an attempt to understand its effect on the resulting damage for a given impact velocity. He found that the thickness of a specimen had a large effect on the resulting damage, while the length and/or width of the panel did not have an appreciable effect. In a subsequent work, Cantwell and Morton [20] studied the geometry of impact specimens and found that impact resulted in damage initiation at the point of contact for short beams,

while damage initiation began at the lower surface due to beam flexure for longer specimens. The authors also showed that circular specimens tend to absorb more energy and result in a lower damage level for similar impact energy levels.

Some other measurements of interest include planar damage area vs. impact energy and maximum residual indentation vs. impact energy. Several methods for detecting, measuring and describing damage that may be present in a given composite material or structure are available. In their study of high velocity impacts on CFRP materials, Cantwell and Morton [21] described several methods, including X-radiography, ultrasonic C-scanning, optical microscopy and thermal depleting. X-radiography and ultrasonic C-scanning have the advantage of being non-destructive. Therefore, the experimentalist can use these techniques to examine specimens which may then be used in additional experimentation, such as compression after impact. C-scans are useful for giving the user an idea of the in-plane damaged area of the coupon and X-ray images are useful for identifying matrix cracking and delamination; however, neither can clearly show the location and mode of fiber fracture. Optical microscopy and thermal depleting have the disadvantage of destroying the subject being viewed, though they yield greater information about the damaged area of interest. Individual locations and modes of fiber fracture and delaminations can be identified using the destructive techniques.

In a later work, Cantwell and Morton [4] discussed other benefits and penalties which exist for each of the methods discussed previously. For instance, some ultrasonic C-scan methods involve the immersion of the subject in a bath of water. This immersion can be detrimental to the composite if voids exist in the laminate or sandwich composite which may retain the fluid once the scan is complete. In addition, for large components or full-scale tests an immersion of the subject may not be practical due to the large volume of water required. Also, C-scans are most suited to the detection of delamination type fracture and cannot detect fiber fracture, matrix cracking or micro-mechanical damage. X-ray imagery improves upon this by not placing the subject in an environment detrimental to its mechanical properties. In addition, considerably smaller defects can be observed if a fine enough X-ray film is used. This type of inspection is too tedious for routine production and service damage detection,

but can be used for high-resolution damage characterization if the point of inspection is known. Thermal deplying involves the heat treatment of the specimen until the matrix degrades and a razor can be used to separate the plies. This technique is especially useful for examining ply by ply fiber crack location in impact damage composites, but is less effective for examining matrix dependent failure. Optical microscopy can yield detection of all types of damage, but is tedious and labor intensive. It can also be difficult to detect matrix defects without the aid of an imposed dye.

There are still more techniques for damage detection that should be considered. Perhaps the simplest non-destructive technique is visual inspection. This is especially the case for detection of damage due to impact because of the localized dent. Simple inspection of the dent can yield quantitative information that can reveal valuable information about an impact site. Thermography, acoustic emission, eddy currants, fiber optics, holography, Moiré interferometry and various other methods also exist for non-destructive evaluation of impact damage in composites. Also, scanning electron microscopy is a third destructive technique. More information on each of these techniques can found in Ref. [4].

Additional non-destructive techniques were used by Tomblin *et al.* [11] including tap testing and mechanical impedance analysis. Mechanical tap testing involves the collection of force magnitude and impact duration data at locations across the undamaged and damaged regions of the specimen. The duration of the response is subject to the local mechanical properties of the specimen so that the response will be different at damaged and undamaged locations. This type of damage evaluation can also be done acoustically by measuring the acoustic response of the panel at each location tapped. Mechanical impedance analysis is effective as well due to the reduction in impedance of a sandwich structure due to flaws or impact damage that may be present in the material. A newer non-destructive damage detection technique has been developed by Yang *et al.* [22] using thermal wave techniques for debonding damage. This type of imaging was shown to be useful in two typical adhesive structures for general defect location and sizing, although some noise reduction techniques are necessary to make the techniques feasible.

It should be noted that no one technique is perfect for visualizing or assessing all types of damage at an impact location and during any study of impact damage several methods should be employed to obtain the requisite information. Although non-destructive techniques of assessing damage characteristics, locations, and sizes are essential if evaluating before further testing, such as in the case of CAI, a previously mentioned work by Raju *et al.* [10] showed that the results of these techniques can be misleading. For example for some combinations of material property, sandwich constructions, and applied indentation, the size of the residual dent was found to be less than that recorded by the result of ultrasonic C-scan. Both non-destructive and destructive impact damage evaluation techniques were used in the current research. The techniques used are discussed in Chapters 2 and 3 of the present work.

1.3 Compression After Impact Experiments

Residual strength of impact damaged specimens can be measured in response to tensile, compressive and shear loading conditions. In addition, fatigue loading is often of interest and examples of results are available in research by Tomblin *et al.* [11] and Shyprykevich *et al.* [12]. However, the out of plane displacement of sandwich panel components associated with impact damage as shown in various impact tests, result in significant stress raising and instabilities during compressive loading making compression after impact (CAI) the primary tool of residual strength determination. This is especially true in the presence of shear strength driven interply delaminations for composite laminates. In the case of composite sandwich structures, out-of-plane deformation from impact damage can cause additional core crushing during compressive loading and ultimately, unique sandwich panel CAI failure modes. For this reason, CAI strength cannot, in general, be approximated by open hole compressive strength tests, where the open hole is of similar size to CAI strength.

Tomblin *et al.* [23] showed that CAI residual strength is higher for a similar size damage location in sandwich panels since impact damage does not extend through the entire core and does not affect the un-impacted facesheet for low velocity impacts. However, the

CAI strength of a composite laminate found in material property data sheets (e.g. Ref. [24]) is usually worse than the open hole compressive specimen with the hole of an equal size. This is due to the fact that the listed CAI strength is a limit value that corresponds to large amounts of damage, which is usually repaired or the component is replaced upon inspection. Damage amounts equal to or less than BVID are still significant, but cannot be estimated from the listed values for CAI strength or open hole strength. The creation of CAI strength values through statistical analysis will be further explained in references to the work by Nettles and Jackson [25], later in this chapter.

A good general overview of the CAI test procedure can be found in the work of Tomblin *et al* [17]. In general, CAI testing involves the placement of a material coupon under an end loaded uniaxial compressive load. Clamped conditions are simulated at the load application ends of the specimen, and some fixtures may stabilize the panel from buckling by simulating simply supported conditions along the non-load application coupon sides. Typically, the impact damage is located in the center of the test coupon, and strain gages are placed to each side of the damaged location as well as on the undamaged facesheet in the case of sandwich constructions. Multiple strain gages may be used if a strain distribution is desired. Also, force resultant is usually recorded, as well as applied displacement information. CAI residual strength results are usually presented as a function of impact energy, but can also be presented versus other damage measures such as planar damage or maximum indentation. Failure in material coupons in the following section will be shown to vary based on the materials, and types and amount of impact, among other variables. These results of previous work will again be segregated between composite laminate and sandwich constructions because of the unique features of the two types of materials. Test procedures and corresponding testing standards will be further discussed in Chapters 2 and 3.

1.3.1 CAI Testing of Composite Laminates

The characteristics of CAI failure was shown by Rhodes *et al.* [26] for thick rectangular flat laminates. Initially, panels were surveyed for impact damage characteristics at various

impact load levels. Non-destructive and destructive techniques were used to characterize the damage, including C-scans, visually, and by sectioning. Impact levels of interest were then chosen for CAI tests. Three compressive failure modes were observed including delamination propagation, local short-wave buckling, and local shear crippling failure. Material systems involving unidirectional tape and woven fabric were studied and no appreciable difference in the resulting residual strength for a similar impact damage level was found. The residual strengths are significantly lower for damaged laminates than for un-impacted panels even for coupons with impact damage that is not readily apparent to visual inspection.

Starnes *et al.* [27] studied and compared the effect of impact damage to the effects of an open hole in GFRP composite laminated plates under compression loading. The authors did their own study on the impact characteristics of the plates they considered using a survey of impact velocities, followed by non-destructive and destructive evaluation methods of the impact locations. The authors also studied the effect of impacts on compressive strength when the impacts were done on panels already under compressive loads. The authors found that many of the panels failed for a given impact velocity at compressive loads much lower than the loads a panel would achieve if the panel were impacted prior to compression.

Stiffeners of various geometries have been studied as a means of increasing the damage tolerance of composite plates by arresting the propagation of impact damage during compressive loading. Typical cross sections of stiffeners include open sections, such as blade stiffeners, and close sections, including hat stiffeners. Williams *et al.* [28] conducted a series of experiments on composite laminate plate with stiffeners of blade and hat configuration with impact damage in a variety of locations on and around the stiffeners to characterize how each damage location uniquely affects the panel's strength. Demuts *et al.* [29] also considered stiffeners in CAI testing of composite laminates in the form of multi-rib and multi-spar designs. The authors found that impacts in a variety of damage locations can cause significant reductions in residual strength whether or not damage was visibly apparent, even in stiffened panels. Also, it was determined that in multi stiffener designs multiple impacts of one impact level in adjacent bays of a panel separated by stiffeners can cause a more drastic

strength reduction than a single impact of much higher energy level.

During various studies of the CAI response of un-stiffened and stiffened composite laminate plates, some of which were mentioned, it was found that the damage tolerance of the composite system depended, in part, on the epoxy resin used. Williams *et al.* [30] suggested that this was due to its effect on delamination buckling. A significant CAI failure model in laminates were delaminations, initially present as impact damage, which propagate transversely to the applied loading direction until global panel failure. Resin ductility and ultimate strength are identified as two key mechanical properties that can indicate the ability of a resin system to raise the damage tolerance of a laminate. A sufficiently high shear modulus has also been identified as another important design criterion of damage tolerant systems due to these CAI tests.

Although the previously mentioned material examined the CAI response of composite laminates made from unidirectional material plies, recently woven fabric material systems have become of interest. An example of a CAI study on the response of woven fiber reinforced composite laminates was done by Yan *et al.* [31]. The authors noted the following damage of their GFRP panels due to impact damage: a matrix crack along the fill direction, a matrix crack along the warp direction, delamination at the impact area, and additional matrix and fiber cracks within the impact area. Delaminations appeared particularly in the ply interface regions farthest from the side of impact. CAI tests of the specimens found that failure occurred by propagation of the delamination regions and the fill direction matrix crack. The authors also presented a detailed finite element model (FEM) and numerical analysis to predict CAI strength of these laminates by explicitly modeling the woven material geometry within a representative volume element. The authors concluded that delaminations due to impact resulted in a critical reduction in the buckling strength of the panels under compressive load. Analytic results like this one help researchers understand and implement the failure mechanisms in earlier experimental work in structural analysis.

1.3.2 CAI Testing of Composite Sandwich Constructions

Rhodes [32] [33] studied impact and CAI failure in composite sandwich panels at NASA Langley Research Center several decades ago. He utilized the same technique that he, as well as other researchers, had been successful with, in the CAI testing of composite laminates. First, specimens were surveyed to determine the impact velocities and corresponding energies of interest. Rhodes found that the areas of delamination in sandwich panels were much smaller than laminate plates impacted similarly. However, areas of crippled honeycomb core were present beneath the impact areas. Rhodes observed only a sharp well defined facesheet crack as the resulting failure mode of compression testing these specimens. The facesheets of Rhodes' panels were thicker than those that would later be characterized by other authors discussed here.

McGowan and Ambur [34] studied and compared the response of impact damaged sandwich panels under compressive loading where the impact was performed prior to, and during compressive loading. Some impact loadings of composite structures can occur during in-service operation while the composite airframe is loaded, which makes understanding this type of impact damaged compressive response invaluable. The authors point out that while the compressive failure response of panels impacted under the two conditions (loaded and unloaded) does not differ; the initialization of damage is sensitive to this difference. Panels which were impacted while loading were observed to have much higher levels of damage and above an applied compressive threshold would fail instantly.

Recently, an example of an experimental study by Raju *et al.* [10] studied the CAI strength in honeycomb core sandwich panels with both GFRP and CFRP facesheets with damage at various impact energy levels from two different size indentors. The authors made several conclusions about the relationship of CAI strength to sandwich construction, including a dependence on dent diameter and core thickness. It was determined that a thicker core produced a higher CAI strength for a given impact energy. Also, three failure mechanisms were observed, which are common to several other CAI studies. First, some panels failed by strength failure across the width initiating at the damage location. Second, some panels

failed by indentation propagation mechanism, and finally in a third class of failure the indentation propagation is started but then is arrested and facesheet strength failure follows for the remaining width of the specimen. The authors also noted that in CAI strength, often a small residual dent with core crushing can result in a more catastrophic reduction in residual strength of the panel than if the panel contained a through-the-thickness hole of the same diameter.

Tsang and Lagace [35] conducted an interesting experimental study on composite sandwiches to separate the influences of core damage and facesheet damage and thus determine each factor's effect on the compressive failure mode of the sandwich. They showed that core damage had to be present to instigate the dimple propagation failure mode seen in this and other experimental studies, but the presence of facesheet damage accelerated this failure mode. They also showed that facesheet layup determined the final shape of the resulting facesheet crack propagation. Finally, the researchers concluded that both facesheet and core failure modes would need to be included in any CAI failure modeling techniques to accurately represent the sandwich panel's response.

Sandwich panel coupon geometry has also been studied with respect to CAI strength. Moody *et al.* [36] studied the effect on specimen width with respect to CAI strength with BVID. The researchers determined that a larger specimen width resulted in an increased CAI strength of the panel and also found that the resulting failure mode varied. Tomblin *et al.* [9] concluded that wide specimens could exhibit arresting mechanisms to core controlled failure leading to a facesheet strength failure. This result was also mentioned in Ref. [10]. Moody *et al.* [13] also investigated the effect of sandwich panel curvature on CAI strength and concluded CAI strength was independent of panel curvature for panels with radius of curvature on the order of 1 meter (39.3 in.).

Tomblin *et al.* [11] studied thin-facesheet sandwich panels with both honeycomb core and foam core. They reported two types of failure modes, both related to dimple propagation. In one mode the dimple propagated to failure and in the other the dimple was arrested and crack growth resulted in ultimate specimen failure. They found that the crack growth mode

appeared in the thinner two ply per facesheet specimens, while the dimple propagation mode occurred in thicker 4-ply facesheet specimens. This resulted in the conclusion that facesheet stiffness controlled the failure mode. This was somewhat different from previous results which show dimple propagation as the primary failure mode of thin-facesheet sandwich panels and other studies which have shown that the dimple propagation does not occur in thick facesheets. For instance, kink-band failure, a special type of crack growth mode, was found to be the dominant failure mode in thick facesheet composite sandwich panels in research by Edgren *et al.* [37] which involved sandwich constructions using facesheets consisting of 8- and 16-ply lay-ups.

1.4 CAI Modeling and Strength Prediction for Sandwich Constructions

A wide variety of methods have been used for the analysis of impact damaged sandwich panels and the prediction of CAI strength. Moody and Vizzini [38] provided a summary of the state-of-the-art in the field until 2000. They summarized the work of various researchers in the field of CAI response of thin facesheet sandwich panels, some of which will be mentioned in the following section. Also, various techniques, including idealization of core crushing response, and inclusion of damage by reduced stiffness were discussed. The relevance and similarity to the state-of-the-art-today, over 10 years later, indicates the complexity that modeling of CAI response undertakes and the value an accurate and robust model would present.

1.4.1 Experimentally Based CAI Strength Prediction

In the absence of reliable CAI strength prediction models, the design of safe to use composite materials in impact damage susceptible structural component has relied upon high safety margins or strength “knock downs” to account for the drastic reductions of strength due to damage observed in experimental data. One approach to obtaining CAI strength predictions is to rely exclusively on CAI failure experiments to create a statistical material strength value.

An example of the development of this type of tool was presented by Nettles and Jackson [25]. The authors presented experimental results on the damage resistance and tolerance of an aluminum honeycomb core sandwich material. With the data presented, they defined an A-basis and B-basis residual compressive strength curve to fit to the data. These types of curve can then be used to define an acceptable and reliable margin of safety.

Since experimentally determining the damage tolerance of every component designed is neither resourceful nor cost effective, modeling and analysis to predict failure have become an increasingly important focus of CAI studies. Experimentally based design criterion such as the method presented in this section attempt to reduce the safety margins required in load critical structural components. Unfortunately, they do not reduce the reliance on expensive and time consuming experimental testing. Although all models and analysis require experimental validation, numerical, analytical, and finite element models can limit this cost to the design process.

1.4.2 Analytic Solutions of CAI Response

Analytic solutions have been used by various authors to predict the CAI failure of thin facesheet sandwich panels. Some of these solutions are very detailed and numerical results are complex and time consuming. Others have developed simple expressions for CAI strength prediction based on simple inputs. An earlier analytic solution using a single parameter model with experimental validation was put forth by Kassapoglou and Abbot [39]. The authors assume that delamination is the predominant damage produced by the impact and driver of a compression load related failure. However, their methodology ignores the effect of a residual dent which can have a significant effect on damage progression and ultimate failure in thin face-sheet sandwich panels. Around the same time, Lie [40] presented a simple methodology for determining the impact response and CAI response of thin-facesheet honeycomb core sandwich panels using analytic models implemented using FORTRAN code. He presented a buckling solution for predicting CAI strength which was cost efficient to implement, but significantly underestimated the strength of the panels. A comparison of these two models

reveals significant differences in the failure mode modeled for similar sandwich constructions panels. Subsequent models have continued to focus on a single damage propagation model and little effort has been expended to analytically study the competition between failure modes in sandwich panels, or the panel construction variables from which they result. Rather, attention is paid to experimental methods for picking the failure mode to model, and then analytically studying limited specific cases. The methods proposed in the current work will seek to expand upon this by including multiple failure modes within a single model to truly understand their nature by analytic means.

An analytic solution was used by Minguet [41] to predict dimple propagation failure mode in thin-facesheet sandwich construction, by considering the effect of the residual dent and associated core damage on CAI strength. A continuum core model was implemented by assuming its response as a series of springs whose response could be presented as a series of harmonic functions. Through this approach, the mechanical properties of the core could be represented as a 6 by 6 stiffness matrix. Only the out of plane movement of the damaged facesheet, modeled by Classical Laminate Theory, was considered, while the undamaged facesheet's response was fixed in the out-of-plane direction. Core damage and propagation was represented as an assumed idealized version of a flatwise compression test response of a honeycomb core; this technique would be carried over into succeeding models. The resulting model, implemented in FORTRAN, over-predicted the CAI strength of the limited experimental data point presented in the paper. The CAI strength prediction could be calibrated to the experimental results by adjusting the stress carried by the core after crush failure. Minguet's model has proved to be complex in implementation and computationally intensive. The fidelity of subsequent analytic models has been reduced for computational efficiency, while still retaining many of Minguet's core ideas.

Tsang [42] offered a revision to the Minguet continuum core model that included an elastic foundation core. The Tsang model was described by two parameters used as a fit for the displacement and stress distribution in the through-the-thickness direction. This reduced reliance on the assumption that the behavior of a hexagonal honeycomb comb cellular

structure could be simulated as an orthotropic solid. A detailed experimental impact damage and CAI study of thin facesheet composite sandwich panel was presented. The resulting dimple propagation failure mode was simulated using the sandwich model with the two parameter core. It was found that the lack of accounting for facesheet damage and failure propagation contributed to an under-prediction of growth of the initial indentation and over-prediction of the final CAI strength. Currently, the representation of a cellular honeycomb structure as a continuum solid has received more attention, which will be discussed later in the present chapter. However, other authors continued to simplify the Minguet model.

Xie and Vizzini [43] [44] offered a further revised version of the Minguet model with a simple one-parameter representation of the non-linear core crushing response. The out of plane stress acting on the core is simply monitored until the core crush strength is exceeded. Once this occurs, the reaction force of the core is set to zero. It was shown that his model successfully captures the correct propagation of core damage. The authors concluded that the level of safety of a composite structure could be expressed mathematically with respect to a critical far field stress based on an experimental calibration at a known sensor location. The authors also assumed that the significance of facesheet damage was negligible to the dimple propagation failure mechanism in thin facesheet sandwich panels and did not include initial or progressive facesheet failure. Noteworthy assumptions in this model include the negligible effect of the undamaged facesheet as well as the core shear stiffness on sandwich panel response.

An example of an alternate approach to the indentation propagation problem was used by Staal *et al.* [45]. The authors presented an elastic stability solution based on the buckling characteristics of a thin, indented plate on an elastic foundation. For this approach, the plate was represented as a beam of infinite width. During the development of the expression for this beam, an Euler buckling term presents itself and a critical Euler buckling stress can be defined to represent the local buckling failure that occurs during CAI of thin facesheet sandwich panels. They compared the results of this expression to finite element eigenvalue buckling analysis, using both solid 3D and plane stress 2D elements, and made the following

conclusions. A critical damage length exists for a given loading direction panel length (or beam length in a 2D case) and a given damage depth. At damage lengths above critical, failure was based on facesheet instability, whereas for damage below critical, core crushing response dominates the response. The conclusions are validated by experimental results, which show that the CAI failure strength approaches a minimum with increasing damage size.

1.4.3 Finite Element Models for CAI Response

Other researchers have turned to finite element modeling (FEM) as a means of including more realistic damage (e.g. core crushing) while still limiting implementation complexity and computational time. Ratcliffe and Jackson [46] have expanded on the work and input of Minguet, Tsang, and Xie through a simple FEM which includes a shell element represented face-sheet and a non-linear spring element model for the elastic support provided by the core. Impact damage in this model was modeled as a geometric dent included in the facesheet and a region of damaged core elements based on the idealized core crush response of damaged honeycomb core. However, during their work they found that the included "damaged" spring element core region resulted in a gradual global failure which was dissimilar to the case study experimental results they presented as well.

The spring core model is a simple finite element implementation of the assumptions used by Xie and Vizzini [43] [44] and previous similar analytic models. It is computationally efficient and successfully simulates the dimple propagation failure mode in thin facesheet composite sandwich panels. Other authors have considered the spring core model as well. One example is the implementation of this type of FEM by Castanié *et al.* [47], which includes limited experimental validation. McQuigg *et al.* [48] presented a thorough CAI investigation of panels similar to the type Jackson and Ratcliffe had attempted to model and were able to use the spring core model to accurately predict the CAI strength of some of these panels. The authors chose not to use the damaged spring core elements because of the detrimental effect to the speed at which failure was predicted to occur based on the results

in Jackson and Ratcliffe’s paper as well as their own analyses. More detail will be provided about the spring core model and CAI strength predictions made using the spring core model in Chapter 4.

Hwang and Lacy [49] also considered the analytic work of Minguet and others and created a FEM approach for predicting the CAI strength of similar honeycomb core panels. Non-destructive techniques were used to estimate material property degradation due to the initial impact damage and honeycomb core crush tests were used to obtain a non-linear transverse core behavior for implementation. Results were correlated with experimental CAI tests of panels with minimal facesheet damage. The expected CAI strengths were consistently under-predicted by the model for these panels. The authors also briefly considered facesheet failure during CAI strength prediction with their FEM model using a maximum stress criterion for individual elements. This was effective for predicting the onset of facesheet failure, but was not able to model progressive facesheet failure. The authors [50] continued studying the incorporation of facesheet damage in their model by comparing CAI strength prediction results with experimental results.

Another group of researchers made use of the implementation efficiency of modern commercially available finite element analysis (FEA) software to create a much higher fidelity FEM. Czabaj *et al.* [51] presented a high fidelity FEM approach to CAI strength prediction by using a complex model which included geometrically accurate representations of a honeycomb core. The geometrically accurate region was located in the region of expected failure only, and the rest of the core was modeled with solid orthotropic elements to increase the computational efficiency of the model. In addition to predicting the CAI strength, the researchers also wished to correctly model the sandwich panel’s response to quasi-static indentation and found that the accurate geometric depiction of the core provided an improved response to this loading condition over a smeared property solid isotropic core model. The transverse response of the core was modeled after an idealized flatwise core compression experimental result, a common CAI strength prediction technique. The resulting model provided an excellent match to experimental quasi-static indentation data from tests on the

sandwich constructions they sought to model. It however over-predicted the CAI strength prediction, although the authors acknowledge the need to develop a method of modeling progressive facesheet damage.

Two earlier attempts at an FEM for analysis of sandwich panel CAI response using a solid core model was presented by Shyprykevich *et al.* [12]. Before discussing each model, one based on ANSYS FEA software and the other on ABAQUS FEA software, the authors summarized the degraded properties associated with impact damage as degradation of flexural facesheet stiffness for planar facesheet damage and transverse core properties for observed core crushing. The solid element core FEM using the ABAQUS FEA environment presented by the authors included the following aspects of impact damage: a damaged facesheet region, a damaged core region, and an initial geometry dent. The profiles of each of these regions were based on experimentally determined geometry. The transverse properties of the core were based on an idealization of the stress-strain curve resulting from flatwise compression tests of initial damaged and initially undamaged honeycomb core material. These idealized core properties were assumed to average through-the-thickness response of the core, so only one element was used through the thickness. Failure was assumed to be dominated by transverse core crushing only, and so no facesheet fracture was modeled although the authors did note that some of the results suggest it might be necessary to include such failure mode. To correlate the ABAQUS results with experimental tests, the authors attempted to compare facesheet strains to previous experimental results at specific locations on the damage facesheet in the path of the dimple propagation. The effect of stiffness reduction in the area of initial damage on the strain results at these locations was presented. Failure was predicted in their model using comparisons of the strain distributions in the modeled damaged facesheet with experimental results.

The authors [12] also presented a similar model where the FEA was done in the ANSYS software environment. A similar core crushing mechanism was included in the model to simulate failure. Core damage was included in the model as a void with the assumption that damaged core can carry no load. Delamination of the facesheet was included in the model

in the area of facesheet damage. (Cantwell and Morton [4] mentioned that delamination is not a primary damage mode in impact testing on thin facesheet sandwich panels, so delamination of the facesheets is not included as impact damage in the proposed model described in the current research.) The results of this model were again compared to experimental strain gages measurement taken in the path of the core indentation propagation. Knee points in the experimental stress versus strain curves were considered to be the moment where the indentation propagation reaches that particular strain gage. Several cases of lightly impacted sandwich panels were considered and the core crush strength included in the non-linear core model was varied to calibrate the FEM predicted strain curves at each location to the experimentally found curves. Overall, predictions in both the ABAQUS and ANSYS models for residual strength were found to be poor unless calibrated with correlation to experimental data. In addition, both models had difficulty handling very small initial dents in the facesheet.

Xie and Vizzini [52] also presented a finite element which utilized a solid core to approximate the three dimensional orthotropic response of the honeycomb core of a sandwich panel. The researchers again focused on local strain at locations in the path of the advancing crushed core region, by comparing experimentally determined local strain versus applied far field stress to FEA strain results at the same location in the model. The researchers assumed that the far field stress at a critical location in the path of the core crush region propagation was the determining factor in the residual strength. Therefore, failure was assumed when the stress at the particular location reached the level indicated by experiments at failure, instead of allowing the model to propagate damage to failure to determine CAI strength. The researchers only included the core crush mechanism in the region of the sandwich panel closest to the initial damage location.

Xie and Vizzini [53] also studied the effect of delamination damage in the FEM model. Although they found this type of damage to have a marginal effect on CAI strength, they did note that it tended to slightly delay damage propagation because of the increased deformation allowed delaying indentation propagation. Another example of a solid-core model was

presented by Schubel *et al.* [54], but the authors considered thicker facesheets in both an experimental and FEM evaluation. In the thicker facesheets, damage was largely constrained to delamination, and CAI failure was dominated by delamination driven local buckling, rather than any core crush mechanism.

1.4.4 Modeling of Honeycomb Core

It has been shown in the present literature review that the method used to model the honeycomb core response during CAI loading can be critical to the accuracy and efficiency of the model used. The present section will discuss modeling techniques used for various honeycomb core response characteristics, some of which will be included in the proposed model of the present work. Other examples are provided to validate the assumptions used in their implementation. A well known reference on the subject of cellular solids, such as hexagonal pore honeycomb structures is the book by Gibson and Ashby [55]. The authors provide a method of calculating the effective homogenized material properties of honeycomb core based on the two dimensional bending response of cell walls. This theory will be covered in detail, later in Chapter 4. An alternate approach to calculating honeycomb core effective properties is presented in a series of papers by Hohe *et al.* [56] [57] [58]. For hexagonal cell honeycombs, the results are similar between the two methods. The following section provides some examples where these methods have been considered and the results found have been validated by experiments. First linear elastic in-plane properties are considered, then the non-linear core crush response is explained.

In-plane properties of hexagonal cell honeycomb core structures have been predicted from analyses by various authors. Chen and Ozaki [59] studied the effect of core thickness on the elastic modulus using a numerical approximation by the finite element method. It was found that under plane strain conditions, the in-plane elastic modulus of the honeycomb calculated closely approximated the result without this assumption. This result demonstrated the independence of the in-plane properties on the cell wall height (i.e. core thickness). A set of equations was proposed to predict all the in-plane elastic properties given cell geometry for

a specific honeycomb. The results of this were checked against FEM results and found to be in agreement. Hu and Yu [60] analyzed the dynamic in-plane crushing strength of hexagonal cell honeycomb by considering the explicit geometry associated with such a structure.

The known mechanical properties of Nomex paper have been used in finite element modeling of explicit cellular honeycomb structures to determine the linear orthotropic behavior of the honeycomb structure Foo *et al.* [61]. The authors recognized the extensive computational cost of modeling cellular structures in large models and attempted to predict the orthotropic properties and verify them with appropriate experiments. The in-plane properties were predicted very closely, while the accuracy of the predicted transverse modulus was less. The reduction of the out-of-plane modulus's value as the number of cells included in the specimen was increased was shown experimentally, while this dependence was not mirrored in the analysis.

The transverse non-linear response of hexagonal cell honeycomb core due to an out-of-plane crushing load has been incorporated into various CAI strength prediction models in an idealized form. A good explanation of honeycomb core crushing behavior using experimental and numerical results was presented by Aktay *et al.* [62]. They showed the stages of core crush in Nomex and Aluminum honeycomb cores, including buckling initiation, progressive folding, and finally densification using experimental examples. Two numerical models were implemented, one depicting the detailed core structure, and the other with homogenized material properties. The homogenized model used a semi-adaptive coupling (SAC) technique to eliminate failed elements and replace them with discrete particle elements defined by a plastic compression law. The SAC model agreed closely with experimental results and was significantly more computationally efficient than the micromechanical model.

Gornet *et al.* [63] also showed that the linear behavior of a Nomex honeycomb core structure could be determined from an analysis considering the geometry and Nomex paper mechanical properties available from the manufacturer. Using a finite element method analysis of a representative single cell that can reproduce the entire honeycomb geometry by a series of translations, it was shown that the full 3D results could be found for any

cell size, Nomex density, and thickness. The non-linear transverse crushing response of the honeycomb structure could then also be found by an Euler buckling analysis of the finite element model. The resulting core crush strength from analysis was predicted consistently lower than the experimentally found values, though. Heimbs [64] also considered the out of plane crushing response of honeycomb core structures using a detailed FEM model. The author acknowledged the over-prediction of the strength results of similar models and investigated the inclusion of geometric imperfections in the honeycomb cell wall structure. He found in his investigation that the inclusion of imperfections allowed for better predictions of core crushing strength and non-linear response.

A recent analysis of the out-of-plane crushing response of honeycomb core sandwich panels by buckling was carried out experimentally and numerically by Kaman *et al.* [65]. The authors considered various materials, core densities, and cell sizes. In honeycomb cores with paper materials similar to Nomex, they identified three failure modes due to crushing, experimentally, including local buckling, folding failure, and a cracking of the material. Buckling resulted in the most severe reduction in load carrying ability and was preceded by cracking, if present. The critical buckling load was found to significantly increase with cell wall thickness and corresponding core density.

The homogenization of honeycomb core response has been well covered in the literature and is validated by experimental results. It is important that this was considered because in the proposed model in the current research, the honeycomb core will be modeled as homogenized continuum with an assumed linear elastic orthotropic response defined by engineering constants. Also, a non-linear core crush response is included in the proposed model, which is based on an idealization of the results of a flatwise compression test. The characteristic results of this type of test and associated idealization are discussed in Chapter 4. The assumptions considered when these modeling techniques are used was shown in the literature review (e.g. Aktay *et al.* [62], Gornet *et al.* [63], Heimbs [64], etc.) to be well-founded, and they are considered essential to the computational efficiency of the model. They have also been used in models outside of CAI strength prediction successfully, such

as simulation of dynamic crushing response using LS-DYNA by Feraboli *et al.* [66]. In fact, use of this assumption has been done successfully for decades (one example found in the literature by Abd El-Sayed *et al.* [67] dates to 1979).

1.5 Progressive Failure Analysis

The present research includes an implementation of progressive damage modeling in the facesheets of the sandwich panel finite element model. The facesheets are modeled as a composite laminate. Although the analysis of composite laminate stress and strains is well understood and accomplished through common, accepted methods, the analysis and prediction of fiber reinforced composite failure is less well understood. Many methods exist, but there is no universally accepted criterion. As explained by Dávila *et al.* [68], this is due to the varied nature of discrete damage events in a fiber reinforced laminate and high degree of variability in laminate construction. The type of damage events which are pertinent to the present research were previously discussed in the sections concerning impact damage in composite laminates and sandwich panels.

In addition to the degree of variation in the types of damage and orientation possible, the treatment of the analysis and prediction of the formation and propagation of this damage varies with scale of the idealization. The three scales identified by Dávila *et al.* [68] are the micro scale, the meso scale, and the structural scale. In the micro scale, typically representative volume elements formulations are used to predict localized damage, such as matrix cracking or fiber-matrix interface failures. Meso-scale models are popular for being both more computationally advantageous than micromechanics models, as well as more detailed and accurate than structural scale models. Structural scale models institute through thickness cracks (i.e. hard discontinuities) in the model based on critical energy release rates or other methods. These types of damage events in composites are strongly dependent on laminate construction and structural level analysis methods do not take into account the sub-scale interactions which are critical in accurately predicting the propagation of these

cracks. A meso-scale model is used in the present research.

Two distinct types of meso-scale models are identified by Dávila *et al.* [68] and discussed with respect to their advantages and disadvantages. Currently, the most common method for discrete damage analysis in composites is continuum damage mechanics (CDM) models. CDM generally assume homogenous, orthotropic plies and corresponding damage modes. When analysis predicts a damage event, a soft discontinuity is imposed in the form of a stiffness reduction to the damaged material. The failure criteria and material degradation used are often associated with a particular mode of failure. Other damage phenomenon, such as fiber-matrix disbond and fiber kinking are taken into account through techniques such as co-current analysis of a micromechanics model and *in situ* strengths, respectively. A second meso-scale model is discrete damage mechanics (DDM), where hard discontinuities are placed in the model through the extended finite element method. The authors argue that this newer class of composite damage analysis improves upon the diffused nature of damage inherent to a CDM approach, such as over-propagation of inter-fiber fracture (IFF).

Two important components of any laminate strength analysis are, that they are close to physical reality, and they are simple enough for computationally efficient implementation in engineering design work, espoused Puck and Schürmann [69]. The authors consider the following to be the most significant characteristics of any fracture criteria: (1) two independent, but simultaneously fracture criteria for fiber and matrix failure; (2) the transverse tensile and compressive strengths must act independently of each other; (3) continuous stiffness degradation; and (4) consideration of the specific IFF mode. The authors also succinctly describe the requirements of a progressive failure analysis (PFA) which applies to the method of implementation in the current research. Stress and strains must first be analyzed ply by ply. In the present research this will be done through the use of classical laminate theory (CLT). A fracture criterion is applied to single plies. A degradation model must then be utilized which includes the effects of material fractures which may not lead to ultimate laminate failure. Finally, the previously mentioned requirements of the PFA must be implemented iteratively through the use of a computer program. The latter three requirements will be discussed

presently, and additional details are presented in Chapter 5, as they pertain to the present research.

A highlight of the work by Puck and Schürmann [70] for the World Wide Failure Exercise (WWFE) included heavy investigation of IFF fracture mechanisms, with special focus on the orientation of matrix cracks and the consideration of stress with respect to the fracture plane. An important observation from this investigation was the importance of the consideration of brittle fracture characteristics in failure analysis of composites. The well-known work of Hashin [71] included a brittle failure criterion for fiber reinforced composite laminates. Fracture is predicted by a combination of normal and shear stresses which are included in the quadratic formulated Hashin failure criterion. The Hashin failure criterion is used to predict the onset of damage in an implementation of PFA based on the work of Lapczyk and Hurtado [72]. Damage evolution is evaluated by a criteria based on the fracture energy dissipated by damage to the composite laminate. Complications which traditionally arise during numerical implementation of progressive damage models are addressed. A crack band model as well as a viscous regularization scheme is suggested to alleviate problems with mesh sensitivity and convergence, respectively. An implementation of this work can be found in the commercial finite element code ABAQUS [73]. Although the authors noted that all parameters used to define this model have physical meaning, in practice these parameters are difficult to obtain experimentally and have limited availability in literature.

Attempts to account for the effects of micro-mechanics in CDM models have led to the use of multi-continuum theories (MCT), such as the MCT developed by Garnich and Hansen [74]. Garnich *et al.* recognized that the continuum assumption used by general elasticity was insufficient for constituent level analysis of composite laminates and developed the idea of multicontinuum, since it works better with the micromechanics of such materials. A failure criterion for composite laminates which makes use of MCT was later developed in the work by Mayes and Hansen [75]. Mayes and Hansen point out that most composite failure criterion, such as Hashin's, attempt to predict composite failure using composite average stress and strain states, and homogenous laminate properties. A micromechanical model

instead utilizes individual constituent properties and can use them to determine failure as well as interaction between the constituents and relationships of individual constituent failure with laminate response. It should be pointed out that the implementation of MCT involves the use of average constituent stress and strain states, rather than individual values. Also, the accuracy of a failure model implemented using MCT depends upon the accuracy and validity of the experimentally obtained strength values for the constituent materials. The main benefit of MCT is that it allows robust progressive failure analysis of a composite laminate through the use of soft discontinuities. When constituent level failure occurs within a model, the model structure remains intact and the resulting redistribution of load in the model can easily be evaluated. The MCT failure theory by Mayes *et al.* was implemented by Firehole Composites, Inc. in their commercially available software Helius:MCT. A custom version of this software is used in the present research.

Schumacher and Key [76] expounded on the details and merits of multicontinuum theory (MCT) and associated failure models. MCT provides the analyst with not only the traditional smeared composite average material stress and strain fields but also provides the matrix average stress and strain and fiber average stress and strain. The purpose of this additional information is to add additional accuracy in failure mode modeling in composite materials. As characteristic of CDM formulated composite laminate failure criteria, MCT failure criterion involves the reduction of the material stiffness in the finite element based on a degradation model. Ideally, when implemented numerically, the material will be degraded gradually, especially with respect to IFF. Knops and Bögle [77] presented a significant example of the implementation of gradual composite failure using CLT which was validated by empirical evidence. The authors noted a substantial improvement in laminate failure analysis when using a gradual failure analysis calibrated and verified by experimental results. Composite progressive failure analysis involving MCT failure theory through the use of Firehole Composites' software, Helius:MCT in the present research will be further developed in Chapter 5. A user's manual and several examples and tutorials are available from Firehole Composites to describe the commercial use of Helius:MCT.

1.6 Overview of the Present Work

In the present document, a body of research consisting of experiments and analysis on the CAI response of thin facesheet honeycomb core sandwich panels is presented. Chapter 1 has introduced the topic and outlined literature which is relevant to the research topic. In Chapters 2 and 3 which follow, a set of experiments on three sets of sandwich panel material systems will be described. Static indentation and impact using a drop tower apparatus was used to assess the damage resistance of these materials and the characteristics of this damage was observed using non-destructive and destructive evaluation techniques. The measurements taken and observations recorded were then used to select the impact energy levels of interest. These levels are primarily those which result in damage which may be only barely visible. A set of CAI experiments was then completed on each material system using a variety of instrumentation to capture the response of each test coupon during compressive loading and at failure. Unique insight is provided to describe the failure modes observed using high speed photography and digital image correlation. The influence of the density of the honeycomb core sandwich panels on the resulting failure mode is presented in the results of this experimental study. The experimental results presented in Chapters 2 and 3 will be used to validate the new FEM which is the focus of the remainder of the present research.

Chapter 4 is used to discuss the basics of composite laminate theory and the shell theory which is used in ABAQUS. The early stages of model development are then described. This process begins with demonstration of previous analysis efforts, including a spring element core model and a solid element core model. A brief analysis was completed using models of select experimental test coupons to demonstrate the effectiveness of these models and the techniques they make use of which are carried over to the new model that is developed in the present work. Carrying forward, the major development of the new FEM is the inclusion of a method of progressive failure analysis in the facesheets using an implementation of MCT failure theory. A detailed look at MCT and associated failure theory is provided in Chapter 5. The remainder of Chapter 5 details the development of the new FEM. First, the geometry and boundary conditions of the new model are described. Next, detailed information

concerning the inclusion of impact damage in the FEM is given. The chapter concludes with observations from the mesh convergence study which was completed, as well as analysis of the model to sensitivity of the inputs which were used in the creation of every ABAQUS input file used in the present research with the newly developed FEM.

With the new model for CAI analysis described, results which have been obtained using the new FEM are described in Chapter 6. Results are included from analyses of each of the 32 test coupons which underwent CAI testing from the three sandwich panel material systems described in Chapters 2 and 3. In addition, further analysis results are given for a parametric study of the effect of varying core density on the CAI strength and failure mode. The parametric study results are used as the final validation of both experimental and analysis conclusions on the effect of honeycomb core density on the CAI response of the sandwich panels studied. Finally, the conclusions of the current research are given in Chapter 7. The major contributions of the present research to the state-of-the-art of the understanding of the compression after impact response of composite honeycomb core sandwich panels are as follows. First, a detailed set of experimental tests have been completed which determine both the impact damage response and the CAI characteristics of three sandwich panel material systems. In particular, the core density of the sandwich panel is shown to be the sole contributing factor to the CAI failure mode and resulting CAI strength. Second, a new, detailed, computationally-efficient, physics-based FEM is developed to confirm the experimental test results and validate the conclusions made. New contributions to CAI modeling are made in the areas of damage fidelity included in the CAI model, and the included composite laminate PFA. It is shown that each of the impact damage traits included has a significant effect on the CAI model results. The model matches the experimental test results at least as well as current models in all areas, and in many cases makes improvements. More importantly, increased confidence in CAI modeling is achieved, since the new model is validated with more experimental data than seen previously in CAI analysis work.

Chapter 2

Impact Damage and CAI Tests of PXX Series Materials

In Chapter 1, selections from the literature relevant to the study of impact damage and compression after impact (CAI) response of honeycomb core sandwich panels with thin facesheets were summarized. In Chapter 2, a set of experiments on a similar sandwich panel material system is presented. The tests include studies of the impact response of this material using static indentation and drop tower impact, as well as the CAI tests to coupon failure. Information about the material system and coupons used, the impact damage evaluation test apparatus, instrumentation, and results, and the CAI apparatus, instrumentation, and results is given. Many of the techniques shown in this chapter are used in the tests which will be presented in Chapter 3. Also, the results found were used in comparisons to current models studied in Chapter 4 during the development of the new finite element model for analysis of CAI failure in honeycomb core sandwich panels. Experimental test results from this chapter and Chapter 3 are compared to analysis in Chapter 6.

2.1 Materials and Test Coupons

A series of compression after impact (CAI) experiments was performed on a commercial sandwich panel material system consisting of thin glass fiber reinforced polymer facesheets and Nomex hexagonal honeycomb core that is readily available to the consumer. The set of material coupons used for CAI testing were designated P01 through P12 although only 10 coupons were tested in compression and will be referred in general in this document as PXX series materials. These materials were manufactured by AAR Composites and can be ordered for commercial applications. Each facesheet of the sandwich construction consisted of two plies of style 7781 plain woven E-glass fabric with 40% epoxy resin content. The plies were directionally aligned in the 0° direction and the nominal cured thickness for a single face-sheet was 0.020 in. The honeycomb core had a 1 in. thickness, with a 0.125 in. cell size, and a density of 3.0 lb/ft³. The PXX series material is shown in Fig. 2.1, where the translucent property of the thin GFRP face-sheets allows for viewing of the core underneath. This property also allows for improved visual inspection for damage and manufacturing imperfection that may be present in the material.



Figure 2.1: PXX series honeycomb core sandwich panel material.

AAR Composites lists the following material property data for this material, which is given the company designation ATR-FP-101F2. The GFRP facesheets have the following nominal properties. The warp (0) direction and fill (90) direction strength and modulus are listed as 60.0 ksi and 3.0 Msi, respectively, for compressive loading, and 54.0 ksi and 3.0 Msi, respectively, for tensile loading. The in-plane shear strength and modulus are 13.0 ksi and 0.400 Msi, respectively. The in-plane Poisson's ratio is 0.140 and the interlaminar shear strength is 3.5 ksi. The Nomex honeycomb core properties are listed as tested on a 0.5 inch thick specimen. The out-of-plane strength and moduli are 270 psi and 20 ksi, respectively. The shear strengths are listed as 140 psi for the L direction (ribbon direction), and 74 psi for the W direction. The shear modulus are listed as 4.5 and 2.5 ksi for the L and W directions, respectively [78].

Test coupons were prepared from the PXX series material at the nominal size of 6 in. by 6 in. The test coupons are shown in Fig. 2.2. These coupons were used in all of the tests described in the next sections. To avoid premature coupon failure for the uniaxial compression tests, special considerations for load introduction were made. At the top and bottom (the load bearing ends of each coupon) a section of core material was removed from between the facesheets. This section had dimensions of the width (6 in.) and thickness (1 in.) of the coupon and it extended in the loading direction approximately 0.5 in. A clay "potting" material with a higher stiffness than the honeycomb core it replaced was used to fill this void. The purpose of this was to increase the surface area for load transfer between the compression test frame and the coupon. In addition, the potting limited the out of plane bending and brooming (i.e. severe matrix cracking causing separation of fibers) of the coupon facesheets' load direction edges, due to the applied compression load. The potting on the ends of each coupon was ground to straight and level, to a tolerance of 0.001 in.



Figure 2.2: PXX series sandwich panel coupons for testing.

2.2 Impact Damage Evaluation

Two sets of preliminary experimental tests were used to characterize the damage for a particular impact energy level. The two types of testing used were static indentation and impact testing using a drop tower. The results of these tests were used to select the energy levels for the impacts to coupons for CAI testing. The energy levels of interest for the PXX series materials were representative of low velocity impacts which would cause light damage to the impacted sandwich panel. The range of damage included barely visible impact damage (BVID) and extended to clearly visible damage. The testing procedures, apparatus, instrumentation, and results for static indentation and drop impact on PXX series materials will be described in the following sections.

2.2.1 Static Indentation Tests

A brief damage study was conducted on the PXX series panels using static indentation instead of impact. Static indentation is a controlled, easily repeatable method of causing damage in composite sandwich panels. In this research, it was used to gain an initial understanding of the types of damage which would appear in the panels for various energy levels. Although

the types of damage from static indentation are comparable to impact damage, this method produces more damage for a given energy level than a low velocity impact. Thus, it is considered a conservative method of estimating damage resistance in a given material. The hydraulic testing machine used is shown in Fig. 2.3. The 0.5 in. diameter hemispherical tip used for indentation is shown in Fig. 2.4. A 1.0 in. diameter tip was also used in initial damage evaluations.



Figure 2.3: Apparatus used for static indentation of PXX series material coupons.



Figure 2.4: Semi-hemispherical tip used for static indentation, 0.5 in. diameter.

Several indentations of the PXX series material were conducted. The resulting static indentation PXX series material coupon with close ups of the four dents with which data was recorded is shown in Fig. 2.5. For each indentation, the panel was clamped on all four edges using a frame which allowed the rear facesheet of the sandwich panel to be unsupported. This type of boundary condition was used in all subsequent tests. The frame is shown in Fig. 2.3, next to the hydraulic indenter, without a panel mounted. Loading was displacement controlled and applied at a rate of 0.05 inches per minute. Displacement and force was measured at the time of each indentation and the results are discussed here.

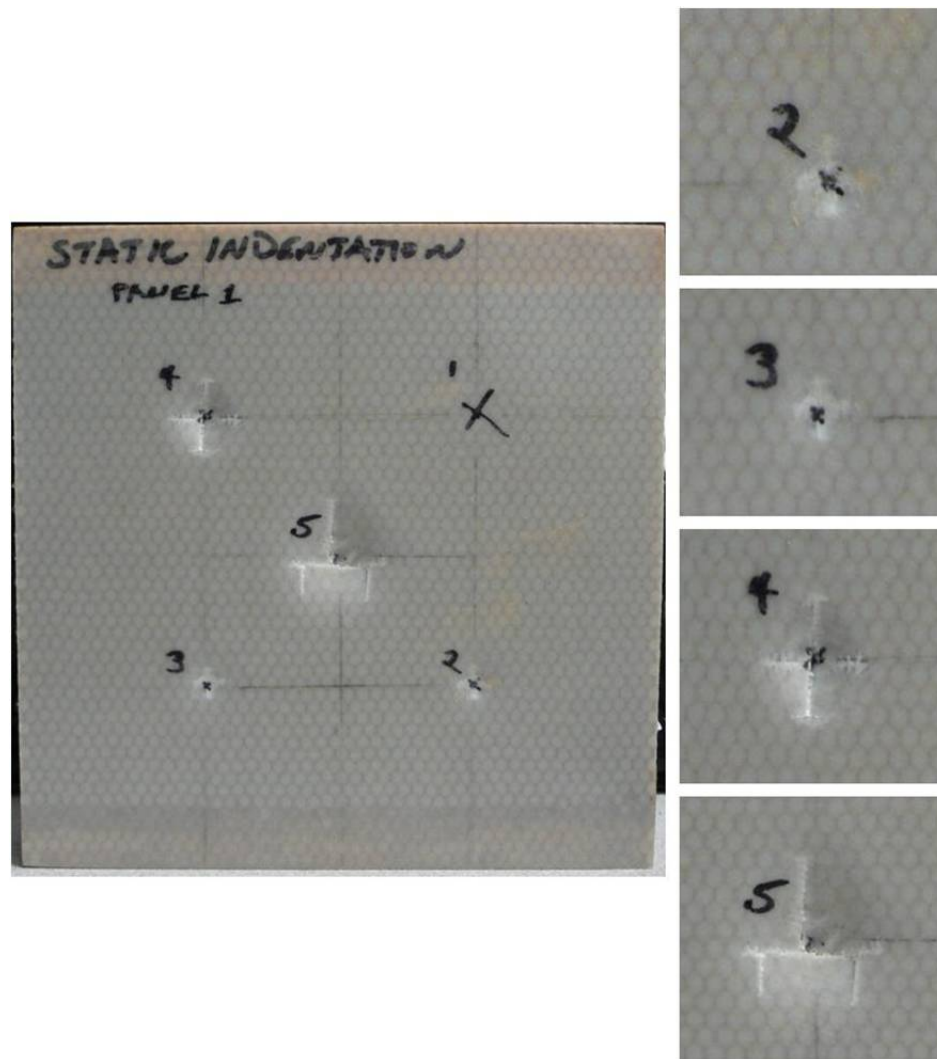


Figure 2.5: PXX series material coupon with resulting damage from static indentation.

Location 1 of the static indentation panel is not discussed because data was not recorded during a brief indentation of that location. Several repeated indentions were conducted at *Location 2*, each with a higher maximum force than the last. First, indentation was done until the resultant force was roughly 50 lbs. and then the indentation tip was completely removed. Subsequently, the same location was loaded to 100 lbs. and then an attempt was made to load to 150 lbs., but the facesheet failed prior to that mark being obtained and the force resultant dropped considerably. As additional displacement was applied the force resultant began to rise again before the static indentation tip was removed from application. During the third load application, just under 0.5 ft-lb. of work was completed, as determined as the area under the force vs. displacement curve calculated using Simpson's Rule. The force vs. displacement results for *Location 2* can be seen in Fig. 2.6.

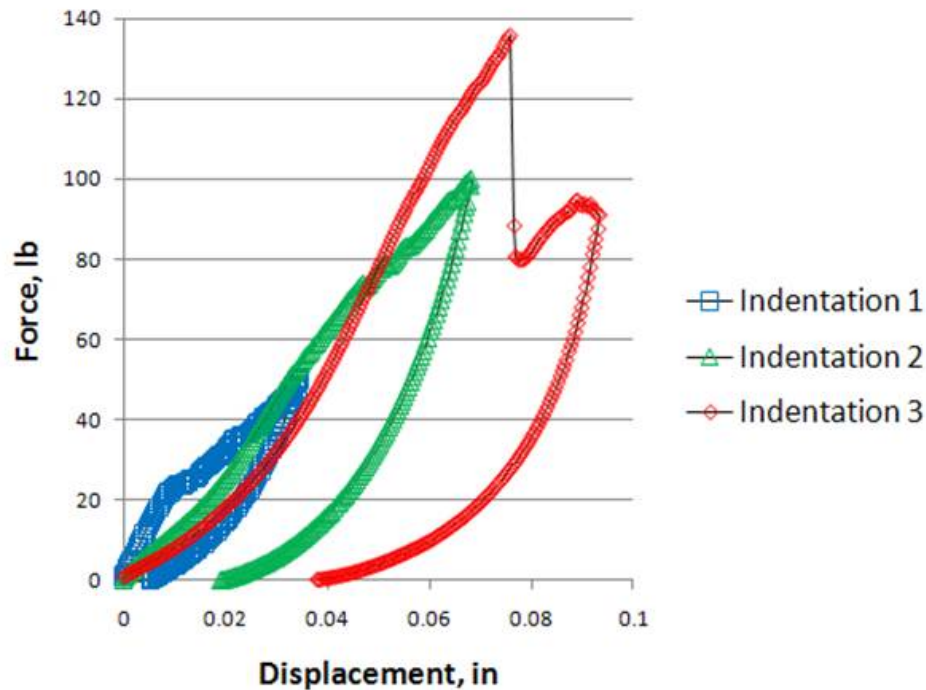


Figure 2.6: Results of static indentation testing on PXX series materials: resultant force vs. applied displacement measured at Location 2.

The effect of the damage present at the location from previous indentation reduces the initial force for a given indentation for subsequent loadings, which can be seen in Fig.

2.6. The appearance of facesheet cracks begin with the sudden drop in force which occurs at about 0.08 inches of displacement during “Indentation 3” in the figure. They are oriented parallel to the warp and fill tows in the woven facesheets and create a cross centered at the indentation center. The presence of crushed core located directly beneath the indentation center is assumed due to the appearance of a residual dent when the load is removed from the sandwich panel. After the final indentation at *Location 2*, the residual dent measured 0.05 inches deep and 0.78 inches in diameter. The complete results of the static indentation test of PXX series materials can be seen in Table 2.1. In the table, “N/A” stands for “not applicable” and refers to the fact that facesheet fracture was not reached for those indentation test. “N/M” stands for “not measured” and refers to the fact that the measurement was not taken.

Table 2.1: Results of static indentation testing on PXX series materials: damage measurements

Location	2	2	2	3	4	5
Indentor Size (in)	0.5	0.5	0.5	0.5	0.5	1
Max. Force (lb)	50.4	100.1	135.6	144.7	135.1	300.9
Max Indentation (in)	0.0346	0.0683	0.0935	0.100	0.200	0.267
Energy, Max Indentation (ft-lb)	0.0809	0.287	0.487	0.632	1.39	3.69
Energy, Facesheet Fracture (ft-lb)	N/A	N/A	0.357	0.604	0.514	1.95
Dent Depth (in)	N/M	0.020	0.050	0.050	0.10	0.15
Dent Diameter (in)	N/M	N/M	0.780	0.800	0.840	1.34

Locations 3 and *4* were indented to 0.1 and 0.2 inches, respectively, with the 0.5 in. indentation tip. The maximum force achieved for each of these indentations was similar to indentation three at *Location 2*. However, the appearance of the force vs. displacement result at *Locations 3* and *4* more closely resemble indentation one at *Location 2* for lower indentation levels. This further illustrates the difference between an indentation on a pristine sandwich panel versus an indentation at a previously damaged location. It also suggests that significant damage exists in the sandwich panel even after indentation at low load levels. The force vs. displacement result for *Location 4* is shown in Fig. 2.7, for illustration. Finally, a 1.0 in. diameter hemispherical tip was used for indentation at *Location 5*. At the time this

test was completed, the 1.0 in. diameter tip was being evaluated for impact of compression after impact panels and this static indentation was necessary for comparison. It should be noted that a much higher maximum force was reached and a higher amount of work was needed to fracture the facesheet at *Location 5* with this indentation tip, suggesting that higher impact energies could be considered for impacts with the 1.0 in. diameter tip. The force vs. displacement result for *Location 5* is also shown in Fig. 2.7. It was concluded that for the PXX material system, very low energy levels (less than 10 ft-lbs.) would be considered for impact testing, including energy levels of less than 2 ft-lbs. for impacts with the smaller tip.

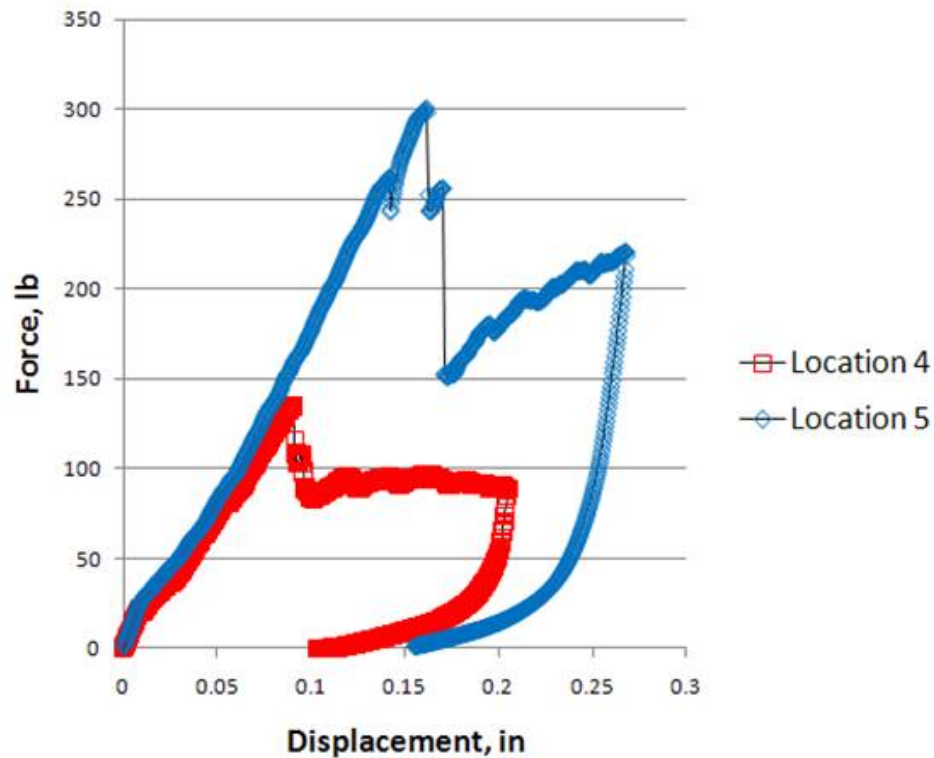


Figure 2.7: Results of static indentation testing on PXX series materials: resultant force vs. applied displacement measured at Locations 4 and 5.

2.2.2 Drop Tower Impact Survey

A survey of impact damage using a mass dropped from a tower was used to gain information about the damage resistance properties of the PXX series sandwich material. The purpose of the impact survey was to determine the characteristic damage at various impact energy levels, and to make a decision about which impact energy levels would be used for compression after impact tests. A PXX series material coupon was clamped on all four edges in the special test fixture, shown in Fig. 2.3 previously, with no support under the opposite facesheet; this boundary condition is considered to be characteristic of a real world structural impact. The test fixture was then clamped to a stout steel table at the point of impact beneath the drop tower, shown in Fig. 2.8.



Figure 2.8: Drop tower apparatus used for impacting PXX series material coupons.

The drop tower consisted of a blue metal tube several yards in length mounted vertically. A pulley system was mounted to the tube to raise and set the drop height of the mass which would impact the sandwich panel coupon. Once in place, the impactor was dropped with a draw string attached to a mechanical release. Upon impact, the mass would rebound from the coupon and a cover could be slid into place over the specimen to keep the mass from striking a second time. Impacts were conducted with both a 0.5 in. and a 1.0 in. diameter hemispherical tip and the weight of the impactor was measured to be 2.7565 lb. and 2.7570 lb. with the 0.5 in. diameter tip and the 1.0 in. diameter tip, respectively. The impactor with the 0.5 in. tip mounted and 1.0 in. tip shown can also be seen in Fig. 2.8. The drop height for a given impact energy level was then calculated by dividing the desired impact energy level by the weight of the impactor. The drop height could be set using the impact tower apparatus to the nearest sixteenth of an inch.

Once an impact on a PXX series material coupon was conducted, the residual dent was measured in terms of its maximum depth and diameter. Each dent was nearly circular although some eccentricities were seen. An attempt was made to consistently determine the largest axis from which to measure the diameter. In addition to this information, the impact force was recorded electronically with respect to time so that impact length could also be determined. The impact length is defined as the time (in seconds) from the moment the impactor strikes the sandwich panel coupon, to when the impactor completely rebounds from the surface. In addition, measured and visual (qualitative) observations were made about the location and characteristics of other types of damage present, including cracking or penetration of the impacted facesheet. Results versus impact energy for residual dent depth, residual dent diameter, maximum impact force, and impact length are shown in Figs. 2.9, 2.10, 2.11, and 2.12, respectively.

A characteristic impact force vs. time plot, for a low velocity impact on a PXX series sandwich panel, has a bell curve shape for low impact energy levels. At a certain threshold energy level, impacts above the threshold will cause significant facesheet damage which results in one or more through-the-thickness cracks that are oriented in the direction

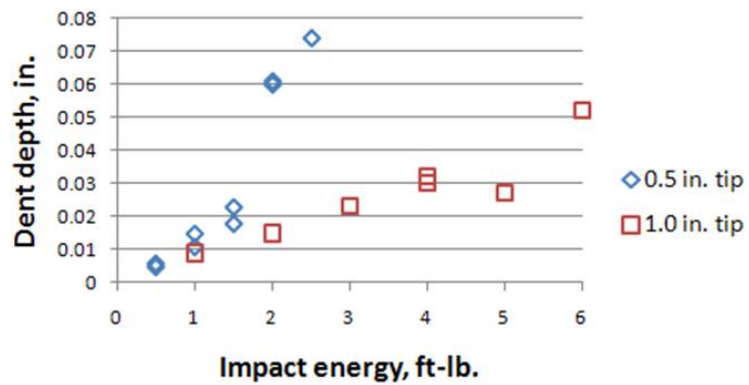


Figure 2.9: Results of drop tower impact testing on PXX series materials: dent depth vs. impact energy.

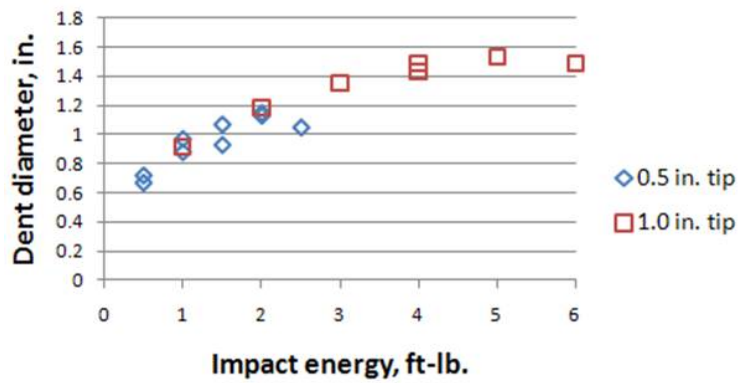


Figure 2.10: Results of drop tower impact testing on PXX series materials: dent diameter vs. impact energy.

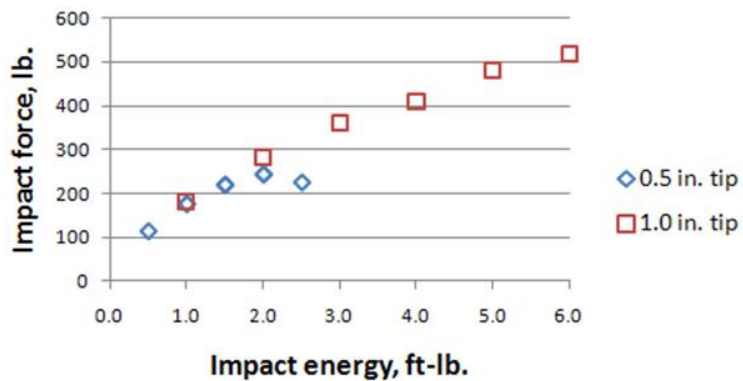


Figure 2.11: Results of drop tower impact testing on PXX series materials: maximum impact force vs. impact energy.

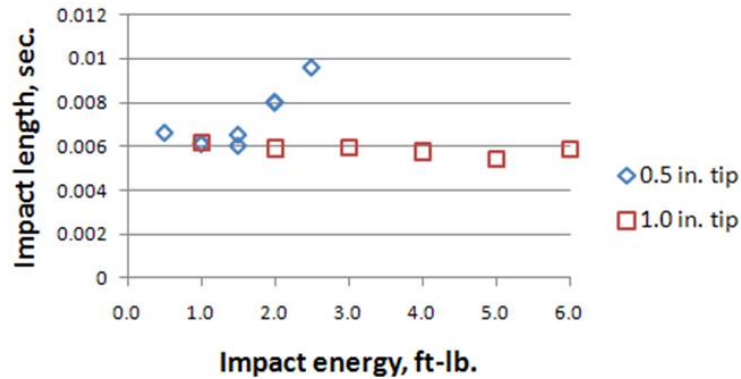


Figure 2.12: Results of drop tower impact testing on PXX series materials: impact length vs. impact energy.

of the warp and fill tows forming either a slit or cross centered at the location of the impact. The force vs. time curve for this type of energy level shows a sudden drastic drop in impact force indicating that the facesheet failure absorbs a large amount of the impact energy. It was also noted that during impacts which resulted in a facesheet fracture, the impactor rebounded considerably less than it would have, had the facesheet not been compromised, like at lower energy levels. An example of the recorded force vs. time with and without the facesheet fracture is shown in Fig. 2.13 and 2.14, respectively.

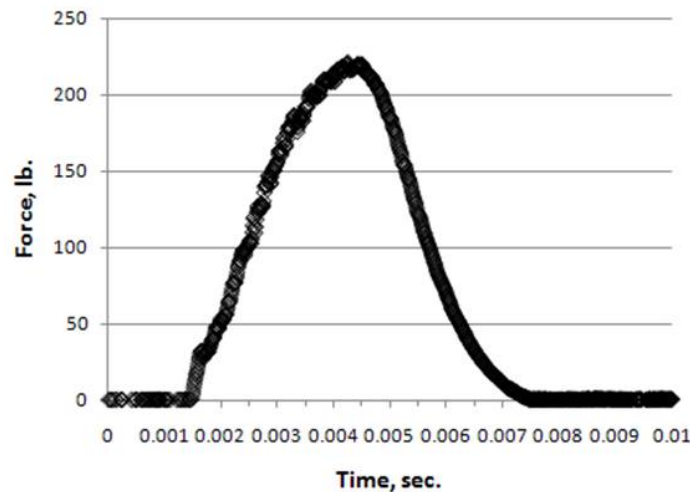


Figure 2.13: Results of drop tower impact testing on PXX series materials: impact force vs. time for Panel 1, Location 3.

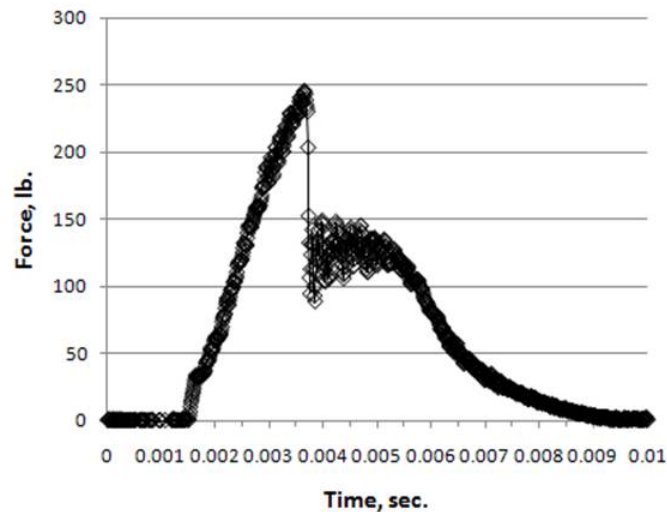


Figure 2.14: Results of drop tower impact testing on PXX series materials: impact force vs. time for Panel 1, Location 4.

Other types of damage noted include facesheet discoloration which suggests matrix cracking, facesheet delamination, or facesheet to core disbond could have occurred. A major difference between static indentation and impact testing is that much more discoloration was seen prior to facesheet fracture during low velocity impact testing; however, facesheet fracture occurred at much higher energy levels for impact testing, as well. This suggests that the high strain rate associated with impact results in higher amounts of localized damage and may explain why static indentation is a more conservative estimate of damage formation for a given energy level. The data collected also shows that the low velocity impacts resulted in larger residual dent diameter, but shallower dent depth. Three coupons were used for the impact survey. They are shown in Figs. 2.15, 2.16, 2.17, and 2.18 with close ups of the resulting damage at each point of impact. It should be noted that due to limited material availability, multiple impact sites are found on a given coupon for the impact survey. The effect of the panel boundary conditions and nearby prior impacts is going to vary slightly from impact location to impact location. For this reason, impact damage was also studied in the impacts done on CAI coupons, prior to CAI testing, for comparison. This data will be presented in the next section.



Figure 2.15: PXX series material coupon with resulting damage from drop tower impact, Panel 1.

Once the information taken during the impact survey of the PXX series sandwich material was reviewed, a decision was made about which damage levels would be the most interesting for CAI testing. During the impact survey, energy levels were considered from 0.5 to 2.5 ft-lbs. at 0.5 ft-lb. increments for the 0.5 in. diameter impact tip and from 1.0 to

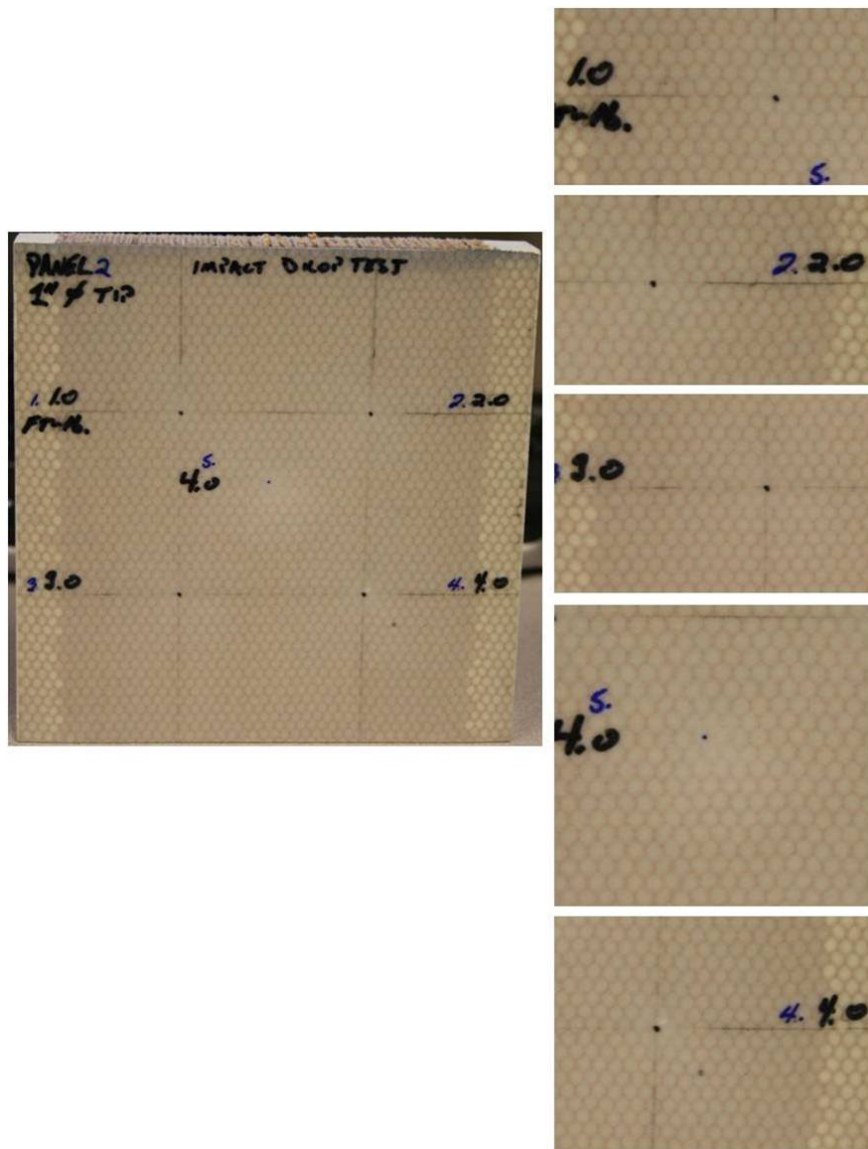


Figure 2.16: PXX series material coupon with resulting damage from drop tower impact, Panel 2.

6.0 ft-lbs. at 1.0 ft-lb. increments for the 1.0 in. diameter impact tip. The impact damage from the 0.5 in. diameter tip was found to be more severe for lower impact energies and is also considered more representative of an impact made by a tool drop during inspection or installation of a sandwich panel airframe, which low velocity impacts simulate. Therefore, impacts using the 1.0 in. diameter impact tip were not considered for CAI coupons, for the most part, although one coupon was tested with damage from this impact tip. Also,



Figure 2.17: PXX series material coupon with resulting damage from drop tower impact, front of Panel 3.

the barely visible impact damage (BVID) range for the PXX series material effectively ends with a facesheet fracture, due to the highly visible nature of the cross like cracks that were noted. Therefore, energy levels above 2.0 ft-lbs. were not considered for CAI testing of these materials. Energy levels of 0.5, 1.0, 1.5, and 2.0 ft-lb. were chosen for impacting CAI coupons of PXX series materials.

2.3 Compression After Impact Experiments

Several test methods were considered when the CAI tests described in this section were designed. ASTM standard test methods (STM) were consulted, but an ASTM STM for compressive residual strength of sandwich constructions has not currently been adopted. The ASTM STM for compressive residual strength of composite plates does describe a procedure and special test fixture for simple plates with centrally located impact damage [79]. This reference was consulted for strain gage placement and allowable failure modes. The ASTM STM for edge-wise compressive strength (undamaged) of sandwich constructions was also considered [80]. This test method was consulted for sizing of the damaged panels, since

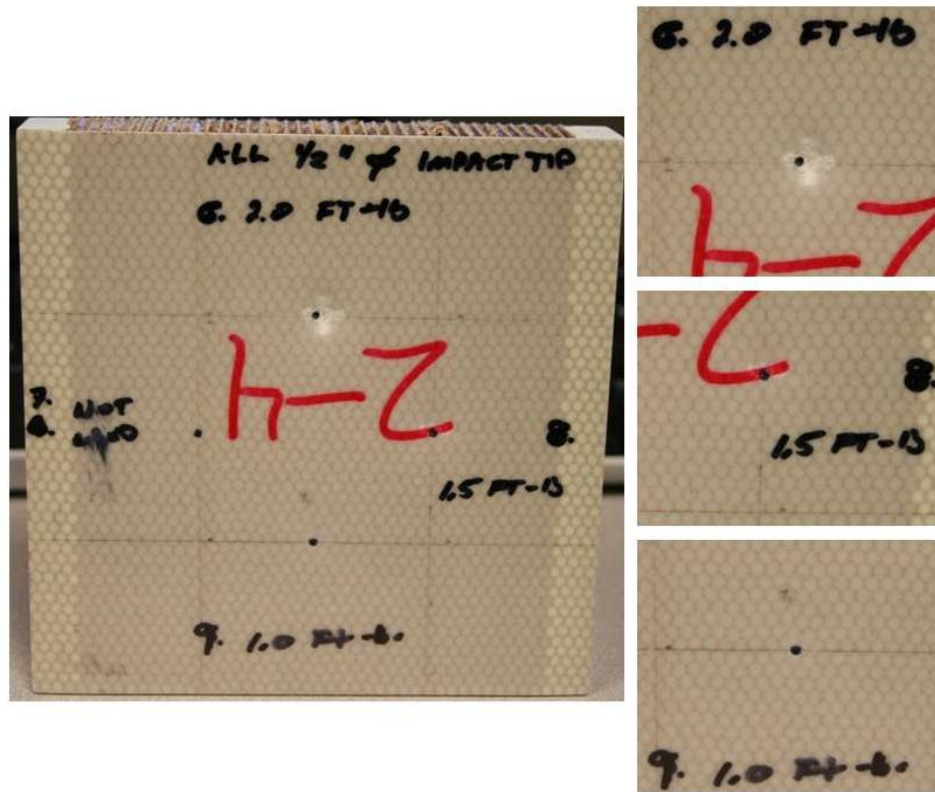


Figure 2.18: PXX series material coupon with resulting damage from drop tower impact, rear of Panel 3.

the increased bending stiffness of sandwich constructions should preclude the use of the test fixture described in Ref. [79]. In the next section, the apparatus and instrumentation used for compression after impact (CAI) testing of PXX series sandwich panel coupons will be completely described. The results of testing will also be presented.

2.3.1 Apparatus and Instrumentation

A servo-hydraulically actuated MTS load frame with a 100-kip maximum load was used for the CAI tests of PXX series sandwich coupons. The sandwich panel coupons were clamped at the top and bottom, placed on top of a small manually adjustable bearing and mounted on the MTS load frame between its two square loading platens. On the load frame, the top platen remained fixed, while the lower platform was also adjustable. The adjustable bearing and lower loading platen could be used to adjust the position of the sandwich panel coupon

with a small load applied to facilitate a uniform compressive loading condition free from significant bending moments. Compressive loading was displacement controlled and applied through hydraulically actuated movement of the lower platen at a rate of 0.02 in. per minute, slow enough to be considered quasi-static for a given measurement point. The load frame and a mounted CAI coupon installed within the apparatus are shown in Fig. 2.19.



Figure 2.19: Load frame and coupon mounting apparatus used for CAI testing.

The following instrumentation was used for each CAI test of the PXX series material coupons. The applied displacement and the measured reaction force were recorded from the load head of the MTS test frame. Far field strain in the direction of loading was recorded on the front and rear facesheets of each CAI coupon throughout testing. In general, five strain gages were placed on the specimen as shown in Fig. 2.20; however, occasionally a strain gage malfunctioned and this was noted when it occurred. At least three of the strain gages numbered 1 through 4 in Fig. 2.20 were necessary to assure coupon alignment within the loading apparatus. Also, three direct current displacement transducers (DCDT) were mounted to monitor the displacement at several locations between the loading platens. The DCDTs can be seen in Fig. 2.19 and their location is described in Fig. 2.21. These three instruments could then be used as auxiliary instrumentation to monitor any applied bending

or to enhance the applied displacement information recorded at the load frame head.

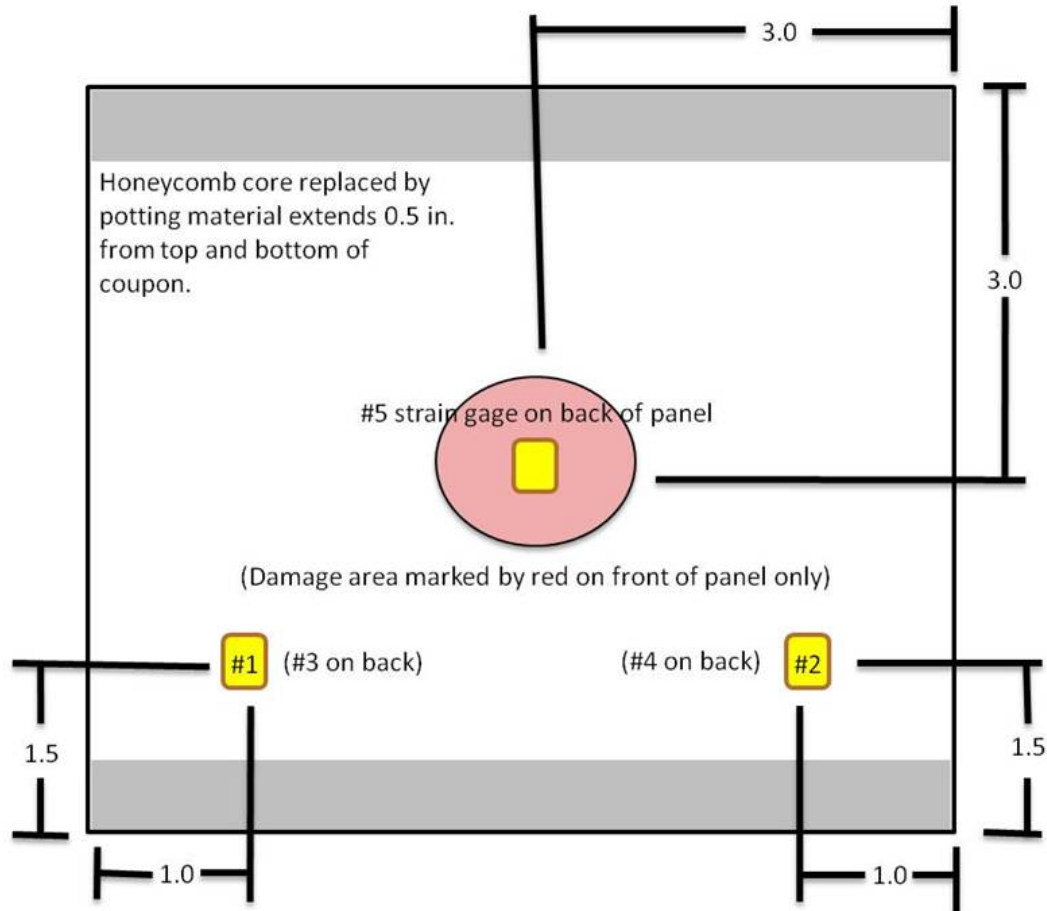


Figure 2.20: Location of strain gages for CAI testing of PXX series material coupons (all dimensions in inches).

Several types of auxiliary instrumentation were used throughout CAI testing. Each test was recorded visually with a high definition video recording system monitoring the front and rear of each specimen. Also, ambient temperature and humidity were noted for each specimen. In addition, high speed footage using a Phantom camera system [81] was taken of a selection of panels which included one panel damaged at each impact energy level considered, as well as an initially undamaged specimen. Another set of panels which also included one damaged panel at each selected impact energy level was prepared for measurement during CAI testing by digital image correlation of digital images using a VIC3D system [82]. The CAI apparatus with various instrumentation configurations is shown in Fig. 2.22.

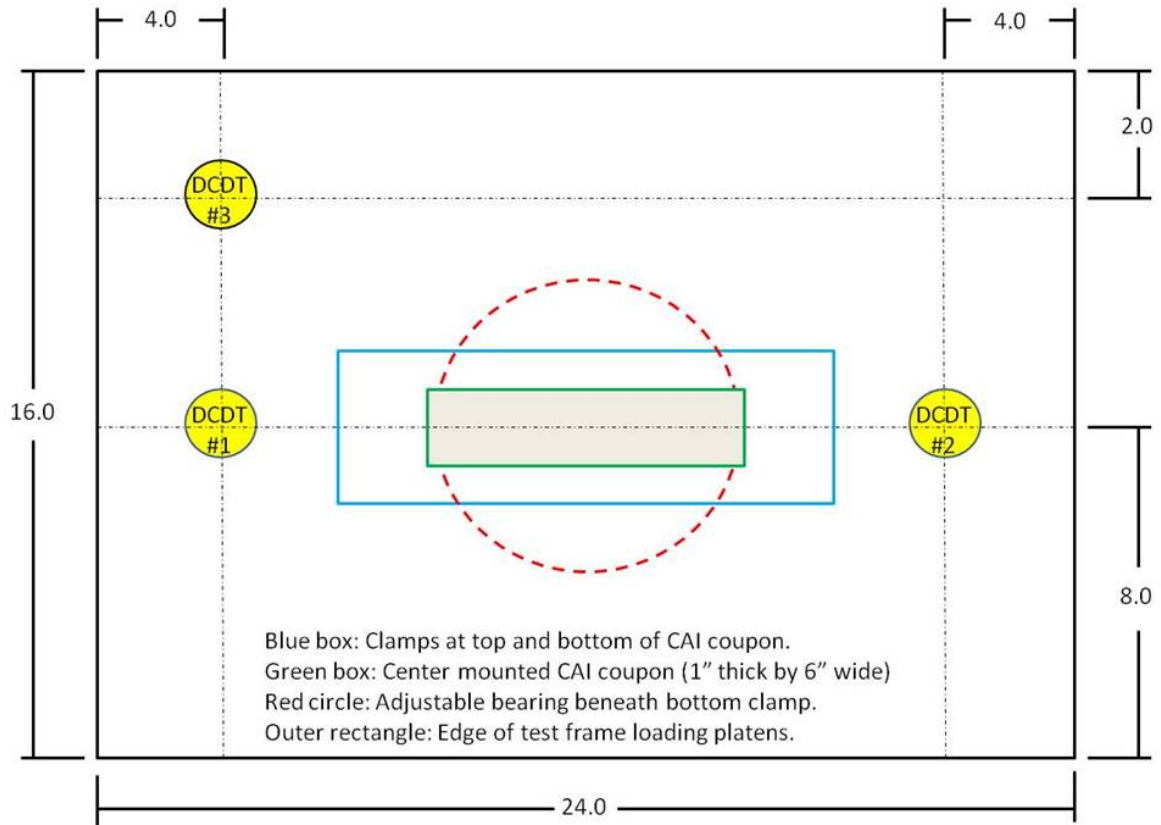


Figure 2.21: Planform drawing of test frame loading platen which shows of DCDT locations used for CAI testing (all dimensions in inches).

The image correlation software allows for collection of full three-dimensional displacements associated with the region of interest during testing. The software can then be used to calculate strains for the region of interest. For the purpose of this testing, the entire front, damaged facesheet, visible between the clamps at the top and bottom of the coupon, was the field of interest. The mounted strain gages must be removed from the field of interest due to optical distortion. In preparation for measurements by digital image correlation (DIC), the entire front facesheet is spray-painted white after the strain gages have been mounted. Afterwards, fields of unique black speckles are added based on the size of the field of view, the displacements expected, and the digital cameras. Two digital cameras are used to capture two synchronous images from which the software can recognize and correlate each unique speckle. Once the system is in place and calibrated, displacement measurements can be made



Figure 2.22: Auxiliary apparatus for CAI testing of PXX series coupons with video instrumentation (above) and Vic-3D digital cameras (below).

using each image pair and information obtained through calibration, such as camera location with respect to target, and various optical image distortion parameters. More information can be obtained on image correlation theory in the resource by Sutton, Orteu, and Schreier [83]. A speckled CAI coupon can be seen in Fig. 2.23.

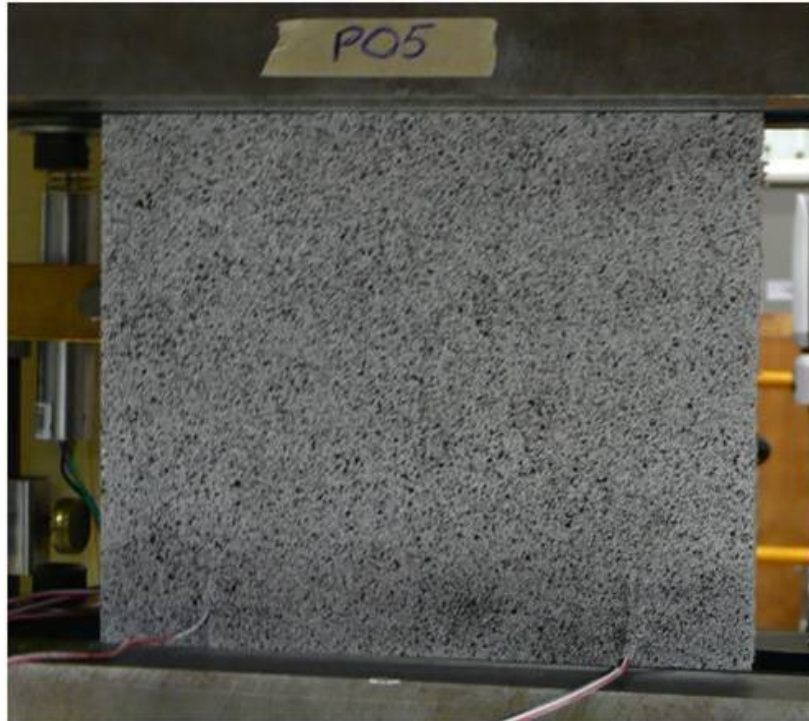


Figure 2.23: Speckled PXX series material coupon for Vic-3D instrumentation of CAI testing.

2.3.2 CAI Failure of PXX Series Coupons

Coupons of PXX series sandwich constructions were centrally impacted on one facesheet using a drop tower impactor, with a 0.5 in. diameter hemispherical shaped tip, at pre-determined energy levels of 0.5, 1.0, 1.5, and 2.0 ft-lb. Two coupons were damaged with impacts at each energy level. One further coupon was damaged with a low velocity impact of 2.0 ft-lb. using a 1.0 in. diameter impact tip. The resulting damage from low velocity impact was similar to the results of the impact damage survey discussed previously. Data on the resulting residual dents in each specimen is available in Appendix A. These coupons and two other, undamaged coupons were tested to failure under displacement controlled compressive loading conditions. The typical force vs. displacement response, as collected from the test frame load head for a CAI test of PXX series materials, is shown in Fig. 2.24.

The force-displacement behavior is linear until panel failure is observed, at which time there is a sudden drop in the reaction force. The global failure is sudden and results in a

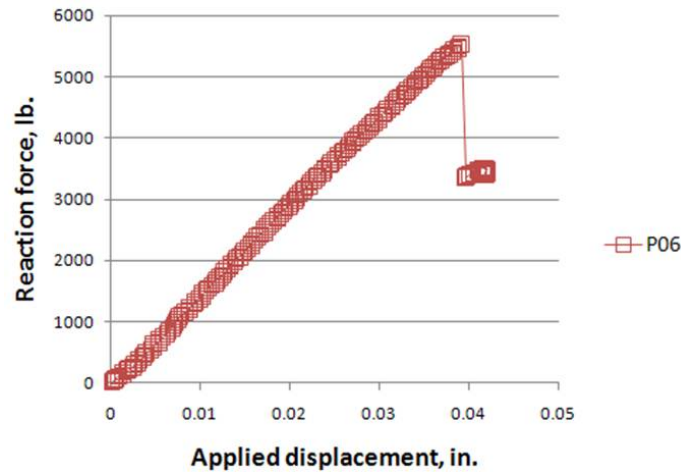


Figure 2.24: Results of CAI testing of PXX series materials: typical measured resultant force vs. applied.

catastrophic reduction in the load carrying capability of the panel, as seen by a drop of nearly 40% in the reaction force. Damage in the failed sandwich panel is noted only in the initially damaged facesheet for CAI specimens. The failed specimen has a region of local buckling, extending transverse to the direction of applied load, from the residual dent initially left by the low velocity impact each coupon was subjected to, shown in Fig. 2.25. Note also, the transverse facesheet crack at the center of the locally buckled facesheet.



Figure 2.25: PXX series material coupon during CAI testing, post-failure, showing results of indentation propagation failure mode.

Video photography allowed the effective capture of the failure mode for these panels. High definition real time cameras monitored each panel so that the following characteristics could be closely documented. For coupon P11, a PXX series coupon initially impacted with a 0.5 in. diameter impact tip with impact energy of 0.5 ft-lb., the small residual dent can be clearly seen in the front facesheet in the recorded video even before loading takes place. Initially, during the linear response of the panel to compressive loading, the residual dent which resulted from low velocity impact can be seen to grow larger, as illustrated by the frames from this video presented in Fig. 2.26.

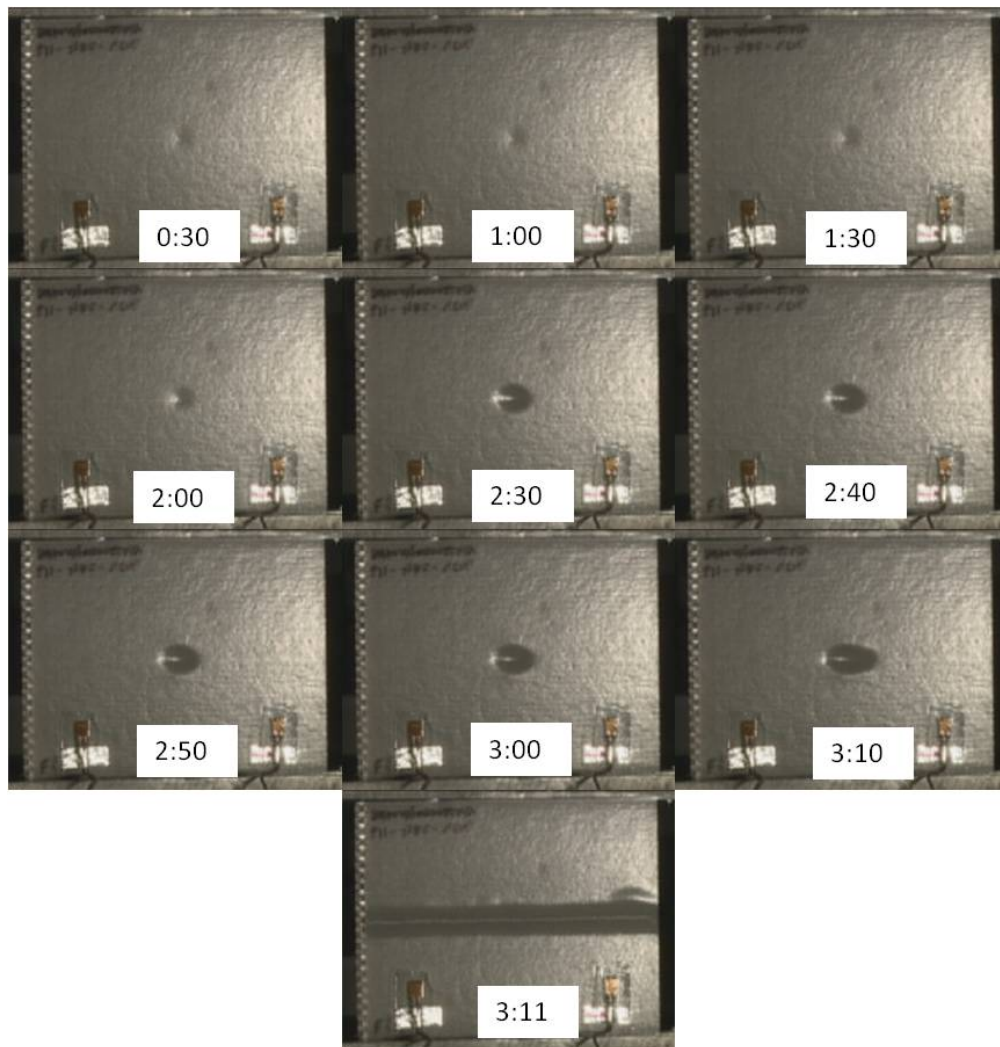


Figure 2.26: Results of CAI testing of PXX series materials: time lapse images taken throughout test.

The video of the P11 panel is about 3 minutes and 30 seconds long and begins just prior to load application. Growth of the residual dent cannot be seen until about 2 minutes into the video. By 2 minutes and 30 seconds, the residual dent is still circular, but its increased depth from the initial dent is readily apparent. Between 2 minutes 30 seconds and 3 minutes and 10 seconds, the dent becomes more elliptical as it begins to expand further along its axis perpendicular to the direction of loading. Failure occurs between 3:10 and 3:11 in the real time video, illustrating the sudden nature of failure.

High speed video photography is necessary to capture the rapid, unstable propagation of dent resulting from local buckling of the facesheet. The Phantom version 7 video system captured and stored images at a rate of 10,000 Hz. Several frames were selected from a high speed video capture of the indentation propagation failure and are shown in Fig. 2.27. With this footage, the unstable propagation of the region of large out-of-plane displacement can easily be seen. Also, the facesheet crack that appears at the mid-point of the locally buckled region of the front facesheet of this coupon can clearly be seen propagating near the front of the advancing indented region.

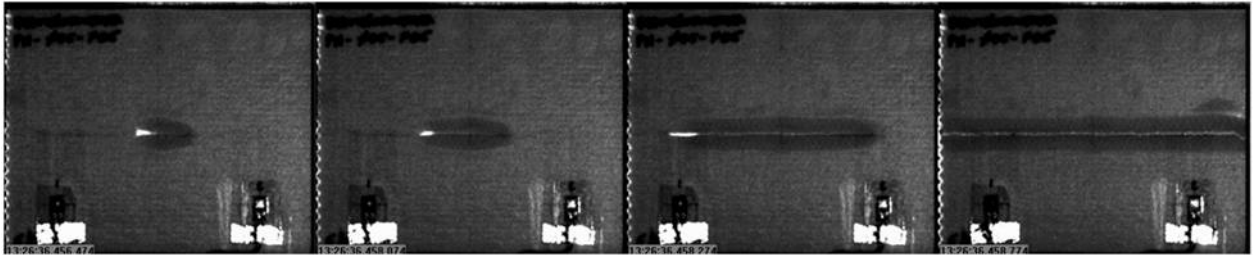


Figure 2.27: Results of CAI testing of PXX series materials: time lapse images taken from high speed camera during failure.

Nominal failure stress, calculated from the measured resultant force divided by the nominal cross sectional facesheet area of each coupon, and average measured far-field failure strain from the five strain gages on each panel were reported for each coupon tested. The results are shown in Fig. 2.28. The complete results of nominal failure stress and failure strain for CAI tests of PXX series materials can be found in Appendix A. The failure strength of PXX sandwich material is shown to drop dramatically even for lightly impact damaged

specimens. This is illustrated by a 5-10 ksi drop in failure strength for coupons which were impact damaged at 1.0 ft-lb. energy levels, from the pristine coupon's strength. The drop of failure strength is shown to decrease in severity with further increasing levels of damage. For specimens damaged at 2.0 ft-lb. energy levels the failure strength is shown to decrease less than a further 5 ksi.

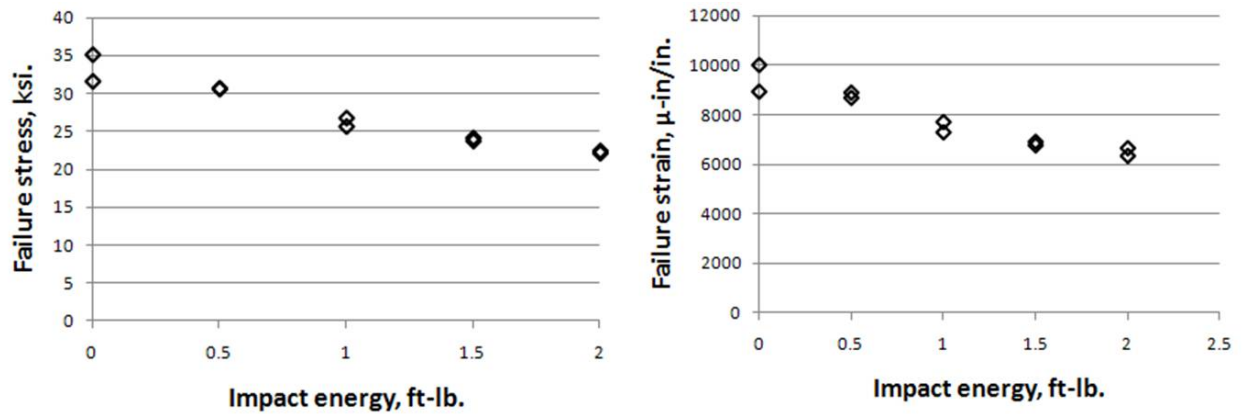


Figure 2.28: Results of CAI testing of PXX series materials: CAI failure stress and strain vs. impact energy.

With various instrumentations available during these CAI tests, multiple measures of failure strain exist for this series of materials. An example of measured resultant force vs. various strain measurements is shown in Fig. 2.29. The measurement types include averages of gages 1-4 and average of all five strain gages, strain calculated from DCDT average divided by nominal coupon length, and applied displacement recorded divided by nominal coupon length. It is interesting to note failure strain measured by averages of strain gages 1-4 and 5 gage averages differ slightly. The fifth gage, being located on the undamaged facesheet but directly adjacent to the damaged region is usually farthest from the average. A typical plot of strain measured by each gage on a coupon is shown in Fig. 2.30 and it illustrates the previous point. It can be noted that the DCDT strain and applied displacement strain continue to increase after failure, while strain gage averaged strain measurements severely drop after failure (along with the resultant force). This is due to the loss of load carrying capability of the failed facesheet. The difference in load carried by the failed and intact

facesheet can also be seen by the difference in the drop in strain measured in gages 1 and 2 vs. gages 3 and 4, which is shown in Fig. 2.30. DCDT displacement measurements are typically uniform, shown in Fig. 2.31, and their average seldom depends on the DCDT used.

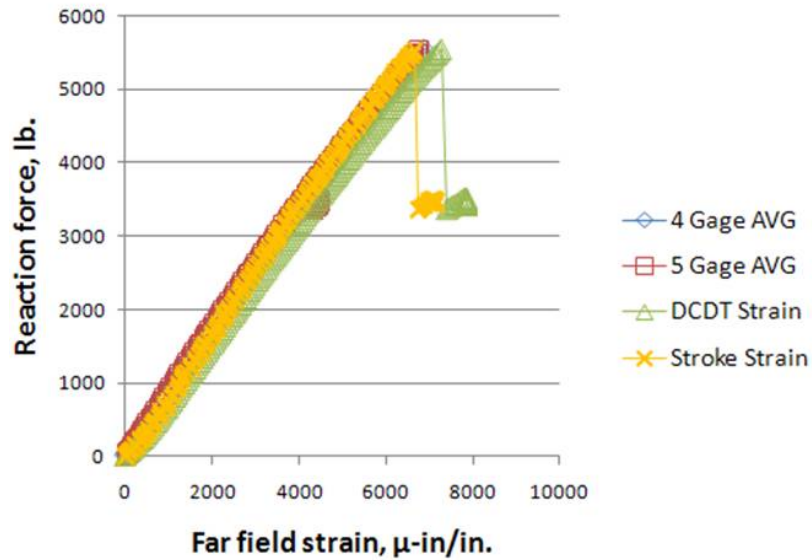


Figure 2.29: Results of CAI testing of PXX series materials: typical reaction force vs. strain measured by various methods.

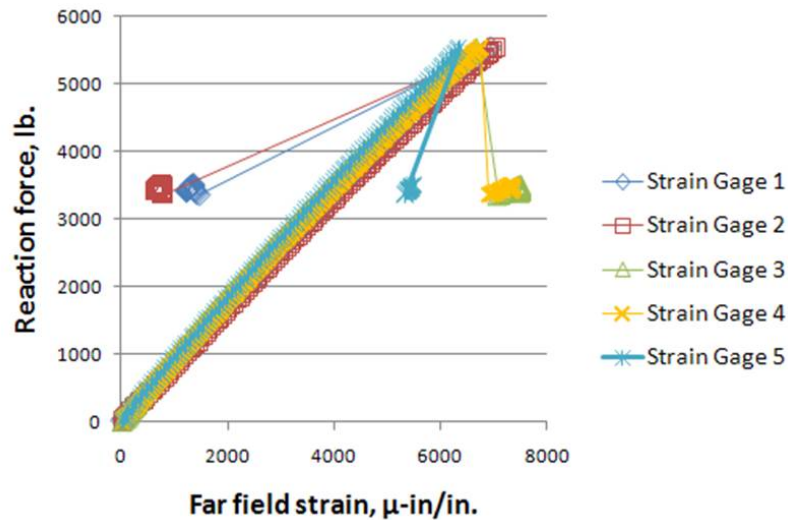


Figure 2.30: Results of CAI testing of PXX series materials: typical reaction force vs. strain measured by individual gages.

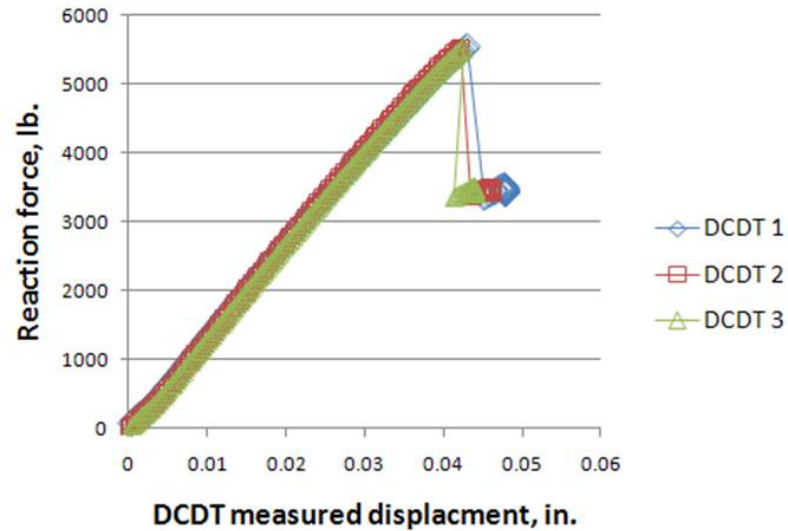


Figure 2.31: Results of CAI testing of PXX series materials: typical reaction force vs. displacement measured by individual DCDT.

2.3.3 Full-field Displacement Measurements Using DIC

A three dimensional (3D) digital image correlation (DIC) system, VIC-3D [82], was used for full-field shape and deformation measurement of a select set of the PXX experimental test coupons during CAI testing. Suttén *et al.* [83] espoused on the history, current state of the art, theory and practical consideration of DIC for full-field shape, deformation, and also, motion measurement. DIC is possible through advanced digital cameras and image matching software. For deformation measurements in three dimensions a stereo-vision camera system consisting of two cameras mounted to a tripod on a rigid cross-member with a between camera pan angle of roughly 30° , measured from a vertex located at the specimen center. Test coupons were spray-painted white and then speckled with a random pattern of black paint dots. The area of interest of the current research was only the front, impact-damaged facesheet of the test coupons. Since the aperture of the digital cameras is reduced to improve the depth of field, auxiliary lighting is used during these tests. The test apparatus used during DIC instrumentation of PXX series experimental tests was shown in Fig. 2.22. The three dimensional imaging capability of the stereo vision DIC system is shown in Fig. 2.32 for a PXX series test coupon loaded to 75% of ultimate. Figure 2.33 shows the same test coupon

after failure where the indentation indicated by the color-marked out-of-plane deformation is propagated to the ends of the coupon in the width direction. The crack in the center of the indentation is the cause of the distortion in Fig. 2.33.

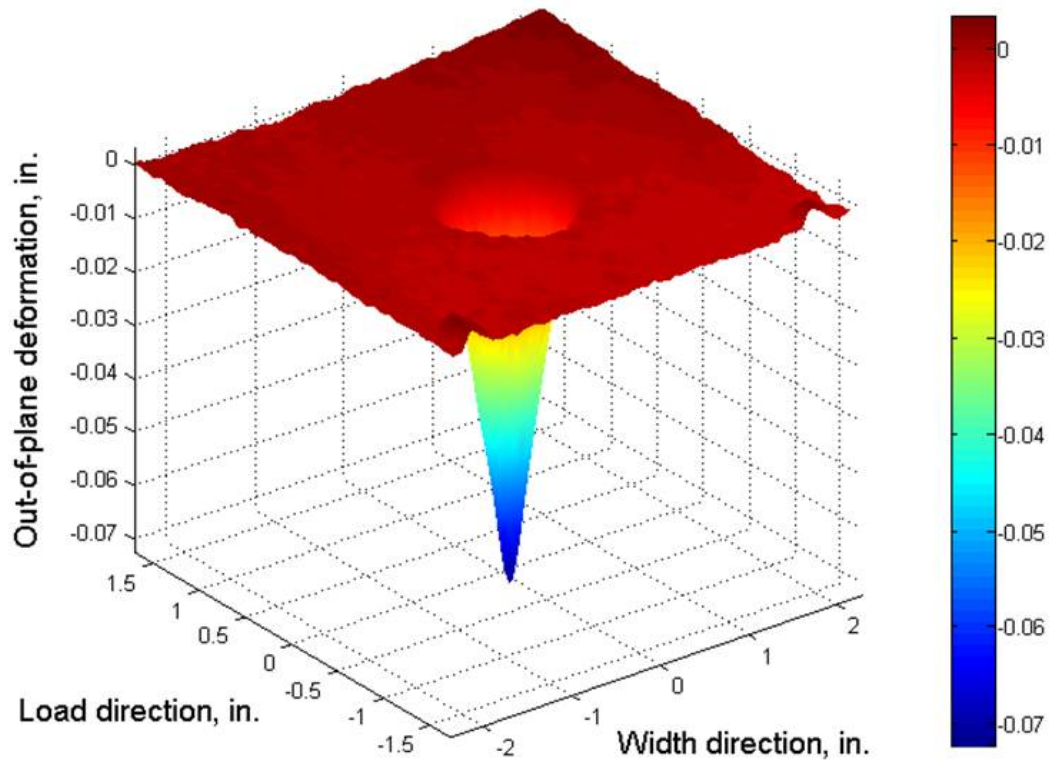


Figure 2.32: Results of CAI testing of PXX series materials: three dimensional DIC imaging of PXX test coupon at 75% of failure load, out-of-plane deformation shown.

A DIC system was used in the present research to monitor the deformation of the initial dent present in each impact damaged test coupon subject to end-loaded uni-axial compression. Previously, time lapse images taken from videography of a sample test were used to show how this dent deforms as a result of the coupon's loading. The images captured using the DIC cameras were analyzed using VIC-3D software [82] and the results were visualized using MATLAB software [84]. This visualization allowed the measurement of the residual dent at various load levels for four PXX series CAI test coupons: P12, P05, P07, and P09. These coupons were damaged with low velocity impacts prior to compression loading at impact energy levels of 0.5, 1.0, 1.5, and 2.0 ft-lbs., respectively. The measurements used in

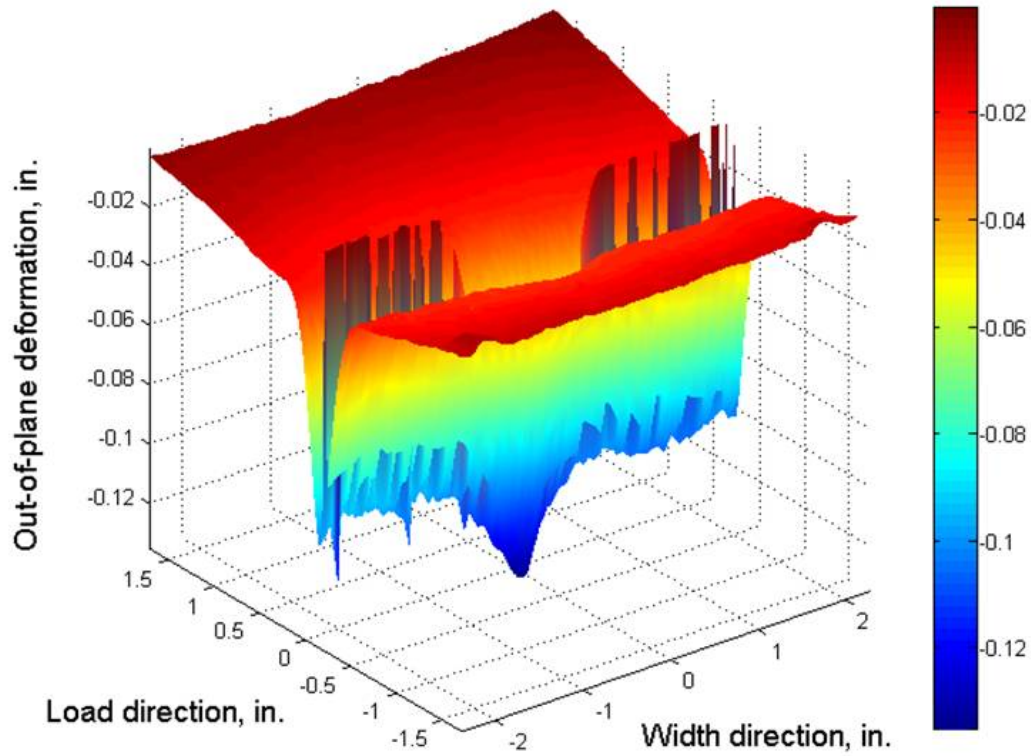


Figure 2.33: Results of CAI testing of PXX series materials: three dimensional DIC imaging of PXX test coupon after indentation propagation failure, out-of-plane deformation shown.

the results presented here were taken at zero load, as well as at 50%, 75%, 90% and 100% (just prior to failure) of the coupon's failure load. It should be noted that the zero load measurements taken using the DIC system vary, marginally, from those taken on the same coupon prior to compression testing by hand measurement.

The results for size of each coupon's indentation, from measurements taken at each of the stated increments, in the coupon width direction, are shown in Fig. 2.34. The corresponding results for the dent growth in the coupon load direction are shown in Fig. 2.35. These results confirm the observations taken from the time lapse images mentioned previously. The indentation grows in size in a stable fashion prior to global coupon failure. This growth is seen predominantly in the X-direction or coupon width direction. The majority of this growth takes place after the test coupon has been loaded to 50% of its eventual failure load. It can be seen in these results that the indentation of each panel grows to maximum

size of 1.5 in. or greater in three out of the four test cases measured with the DIC systems. This represents stable indentation growth to a remarkable 25% of the coupon's width (6.0 in.) or greater.

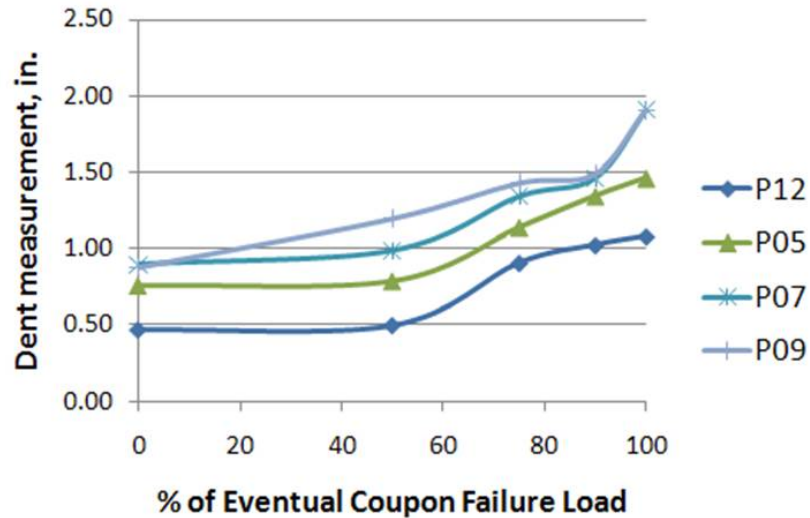


Figure 2.34: Results for DIC measurements: dent growth in coupon width direction for PXX test coupons.

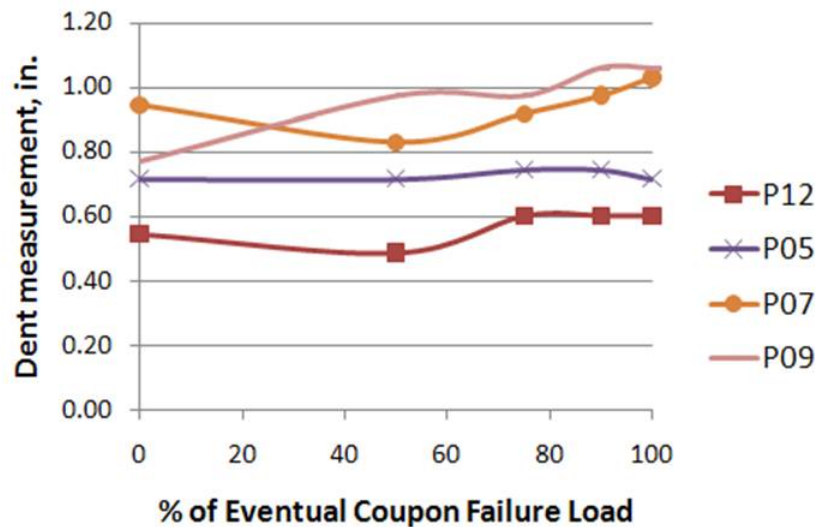


Figure 2.35: Results for DIC measurements: dent growth in coupon load direction for PXX test coupons.

The indentation also grows in depth throughout the coupon's compressive loading.

This result is not seen as well through the time lapse images, so the measurements taken using the DIC system provide further usefulness, in this regard. The results for indentation growth for the coupons observed using the DIC system are shown in Fig. 2.36. The indentations are shown to grow significantly in size from 50% of the eventual failure load until coupon failure. The indentation depth growth must result in further crushing of the honeycomb core beneath the initial indentation. In most of the cases measured, this additional core crush is more than double the initial indentation depth measured.

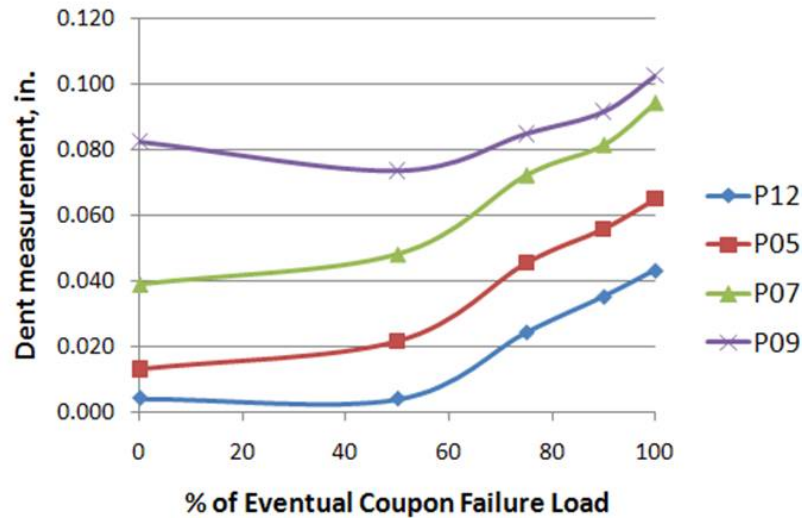


Figure 2.36: Results for DIC measurements: dent depth increase in coupon load direction for PXX test coupons.

2.4 Conclusions from Impact Damage and CAI Tests of PXX Series Materials

In the present chapter, a series of tests to determine the impact and CAI response of PXX series was presented. Typical response of this type of material to static indentation, impact from a drop tower apparatus, and compression loading after impact were given. CAI tests were completed on panels with damage from impacts at energy levels below 2 ft-lbs, as chosen by the damage formation evaluation completed using static indentation and the impact

survey. A large reduction in residual compression strength at the smallest damage levels was seen. Further reduction, but of lower magnitude, was found for increasing damage levels. The indentation propagation failure mode of these panels was clearly indicated by time lapse photography, and was further quantified by measurements from DIC data.

Chapter 3

Impact Damage and CAI Tests of 3PCF-XX and 6PCF-XX Series Materials

Previously, in Chapter 2, a set of experiments on the impact damage and CAI response of a material system consisting of a honeycomb core sandwich panel with thin facesheets was presented. Two further sets of materials will be considered in Chapter 3. In Chapter 2, the apparatus, instrumentation, and procedures used for each these tests was explained in detail. Most of the equipment and techniques described previously have been re-used, although some changes were made as a result of the lessons learned. In the present chapter, the reader will be referred to Chapter 2 for further detail, except where changes made for the current set of experiments are noted in detail. In Chapter 6, the results of the experimental study discussed in Chapters 2 and 3 will be used to validate a new finite element model for analysis of CAI failure in honeycomb core sandwich panel coupons.

3.1 Materials and Test Coupons

A second set of compression after impact (CAI) experiments was performed on two series of materials fabricated specifically for this research initiative by AAR Composites. Each of these new material systems were fabricated with woven, glass fiber reinforced polymer (GFRP) facesheets and Nomex hexagonal honeycomb core. The designation given to each of these new material systems was based on the density of the Nomex honeycomb core included in each of the new material systems. 3PCF-XX series material coupons contain a Nomex core with 3 lb. per cu. ft. density and 6PCF-XX series materials contain a Nomex core with 6 lb. per cu. ft. density. Other material properties are shared by the two material systems. Both cores are 0.75 in. thick and have a 0.125 in. nominal cell size. The 3PCF-XX and 6PCF-XX sandwich materials are shown in Fig. 3.1. The core gives the 3PCF-XX material a yellow hue through the translucent facesheets, while the 6PCF-XX series panels are green for the same reason.

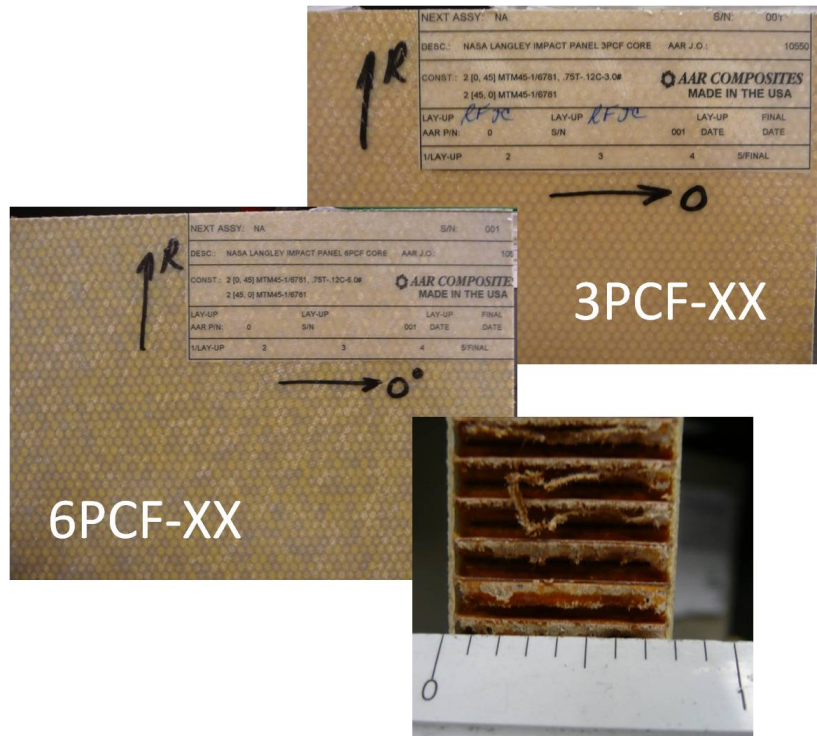


Figure 3.1: 3PCF-XX (top) and 6PCF-XX (bottom) series honeycomb core sandwich panel material.

The facesheets of both the 3PCF-XX and the 6PCF-XX material systems consisted of two plies each of style 6781 woven S2-glass fabric cloth with 35% epoxy resin content. The type of resin present was MTM45-1. The facesheets of these two sandwich panel systems were again thin gage as they consisted of two plies, and the nominal facesheet thickness was again 0.02 in. However, in addition to being fabricated from a higher grade S2 fiberglass, the facesheet plies of these new material systems were oriented with ply directions of 0° and 45° . The overall sandwich panel was a symmetric $[0/45/\text{CORE}/45/0]$ construction for both material systems.

The type of woven S2 glass cloth plies used in the facesheets of these two materials systems has the following material properties according to a National Institute for Aviation Research Qualification Material Property Data Report [85]. The warp (0°) direction strength and moduli are listed as 81.46 ksi and 4.22 Msi, respectively, for tensile loading, and 83.43 ksi and 4.22 Msi, respectively, for compressive loading. The fill (90°) direction strength and moduli are listed as 80.50 ksi and 4.07 Msi, respectively, for compressive loading, and 69.07 ksi and 4.02 Msi, respectively, for tensile loading. The in-plane shear strength and modulus are 5.45 ksi and 0.550 Msi, respectively. The in-plane Poisson's ratio is 0.138.

The Nomex honeycomb core properties for the 3PCF-XX material systems are listed as tested on a 0.5 inch thick specimen. The out-of-plane strength and modulus is 270 psi and 20 ksi, respectively. The shear strengths are listed as 140 psi for the L direction (ribbon direction) and 74 psi for the W direction. The shear moduli are listed as 4.5 and 2.5 ksi for the L and W directions, respectively. For the 6PCF-XX material system, the higher density Nomex honeycomb core properties are as follows from tests on samples of 0.5 in. thickness. The out-of-plane crush strength and modulus are 925 psi and 60 ksi, respectively. The shear strengths are 330 psi and 170 psi for the L and W directions, respectively. The shear moduli are 13.0 and 6.5 for the L and W directions, respectively. The data presented here is available from HexCel Composites, Inc. [86].

Test coupons for impact and CAI testing of 3PCF-XX and 6PCF-XX materials were prepared similarly to the PXX series coupons, though they were fabricated slightly smaller

at the nominal size of 5.5 in. by 5.5 in. based on source material limitations. Examples of the test coupons are shown in Fig. 3.2. A new potting method was also introduced for the new set of coupons. A section of core material was removed from between the facesheets at the load bearing ends of each coupon. This section had dimensions of the width (6 in.) and thickness (0.75 in.) of the coupon and it extended in the loading direction approximately 0.5 in. Instead of traditional clay “potting” material, a piece of wood was cut to tight tolerances and set in place of the removed core material with an epoxy resin. The purpose of this was to decrease the out-of-plane deflection of the facesheets due to contraction during curing of the potting material. This allowed for more desirable load transference to the coupon, and yielded a more successful compressive failure test of undamaged coupons. This is important for comparing CAI failure strength. This new potting method was also successful at prohibiting brooming of the coupon edges. The potting on the ends of each coupon was again ground to straight and level to a tolerance of 0.001 in.



Figure 3.2: 3PCF-XX (top right) and 6PCF-XX (top left) series material coupons for testing, with top load bearing end (middle) and side views (bottom).

3.2 Impact Damage Evaluation

Two sets of preliminary experimental tests were used to characterize damage formation in these two materials for a range of impact energy levels. The two types of testing used were static indentation and impact testing using a drop tower. The results of these tests were used to select the energy levels for the impacts to coupons for CAI testing. The energy levels of interest for the 3PCF-XX and 6PCF-XX series materials were representative of low velocity impacts which would cause low to moderate damage to the impacted sandwich panel. The highest levels of damage included complete facesheet penetration and core crushing through greater than 50% of the coupons thickness. The range of damage included barely visible impact damage (BVID) and extended to clearly visible damage. The testing procedures, apparatus, instrumentation, and results for static indentation and drop impact on 3PCF-XX and 6PCF-XX series materials will be described in the following sections.

3.2.1 Static Indentation Tests

A brief damage study was conducted on the 3PCF-XX and 6PCF-XX series panels using static indentation. Static indentation is a controlled, easily repeatable method of causing damage in composite sandwich panels. In this research, it was used to gain an initial understanding of the types of damage which would appear in the panels for various energy levels. Although the types of damage from static indentation are comparable to damage from an impact, this method produces more damage for a given energy level than a low velocity impact and is considered to be a conservative method of estimating damage resistance in a given material. The hydraulic testing machine used was shown in Fig. 2.3 and the 0.5 in. diameter hemispherical tip used for indentation was shown in 2.4. Static indentation of 3PCF-XX and 6PCF-XX series sandwich coupons is shown in Fig. 3.3.

Indentations of 3PCF-XX and 6PCF-XX series materials were conducted while the coupons were clamped on all four edges using a metallic frame which allowed for the coupon to be suspended with the rear, undamaged facesheet unsupported. This test frame is the

same as discussed previously in use with PXX series coupons, and can be seen in Fig. 3.3. One coupon of each material was used for static indentation and several indentations were made in each coupon. The quasi-static loading was displacement controlled and applied at a rate of 0.05 inch per minute. Both the displacement and the force was measured at the time of each indentation and the results are discussed here.

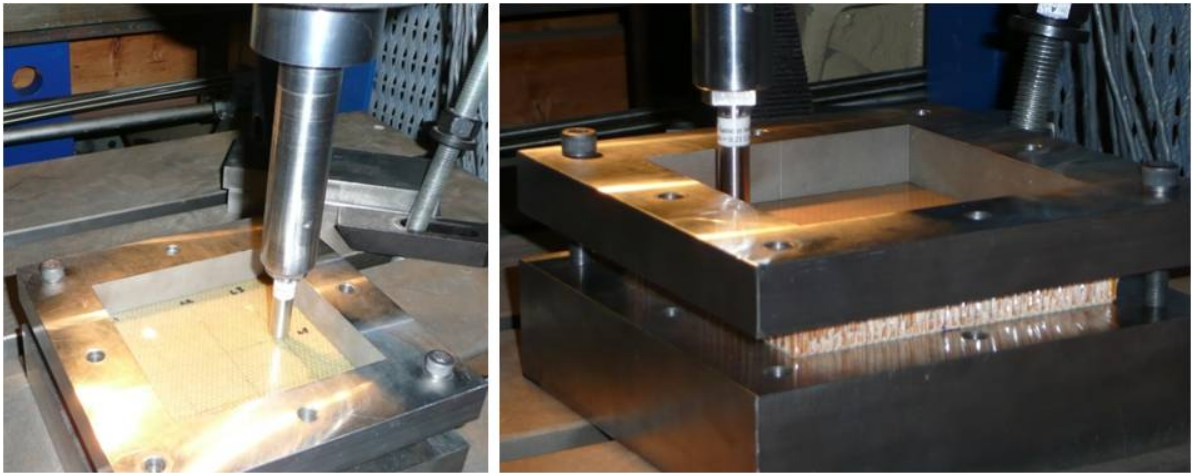


Figure 3.3: Static indentation of 3PCF-XX (right) and 6PCF-XX (left) series sandwich coupons.

Five static indentations were made into a 3PCF-XX material coupon to investigate the coupon's response. The results of static indentation are shown in photographs in Fig. 3.4. The static indentation test at *Location 1* on the coupon was used to find the resultant force measured at facesheet fracture. Facesheet fracture occurred at roughly 170 lbs. It is interesting to note that fracture does not result in a cross pattern of cracks aligned with the woven fiber tows like in PXX series materials shown in Fig 2.5. Instead fiber and matrix fracture saturate the entire point of loading creating a uniform damaged appearance. Damage prior to facesheet failure also results in asterisk shaped discolorations at the location of the residual dent.

The force vs. displacement results for all five static indentation tests can be seen in Fig. 3.5. Facesheet fracture occurred in tests at *Location 1* and *Location 5* and can be seen as a sudden drop in resultant force while the applied displacement is still being increased. Tests were also conducted to 50, 100, and 150 lbs. nominally, for *Locations 2, 3,*



Figure 3.4: Results of static indentation of 3PCF-XX series material coupons: residual dents.

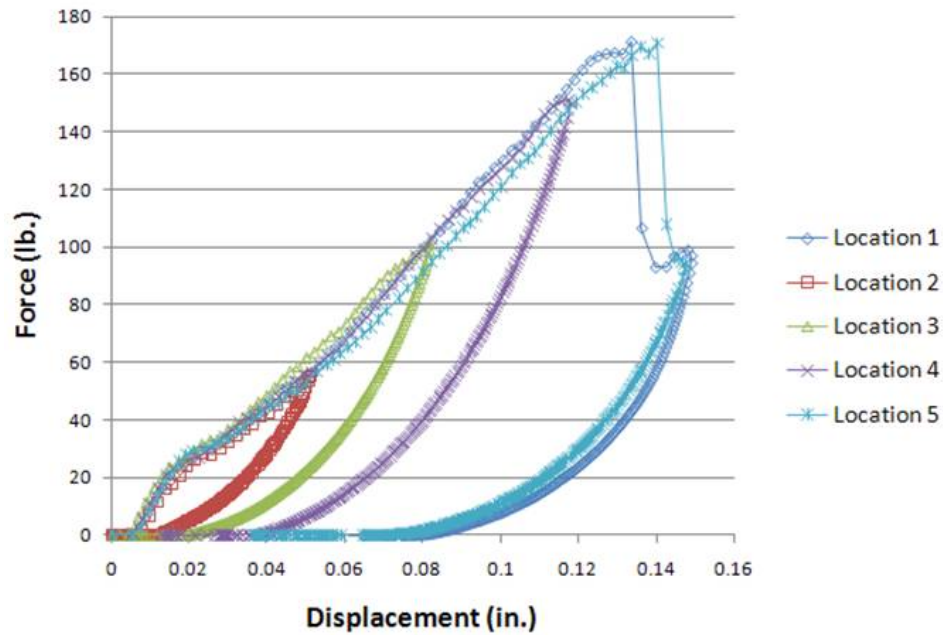


Figure 3.5: Results of static indentation of 3PCF-XX series material coupons: resultant force vs. applied displacement.

and 4, respectively. The detailed results can be found in Appendix A. 3PCF-XX materials which had similar core (except smaller thickness) to PXX materials, but higher strength and modulus facesheet material, were able to withstand greater force before facesheet fracture,

but deflected less for a given applied load. This meant that the panels were stiffer in response to impact loading and impacts of equal energy would result in higher measured resultant force from 3PCF-XX materials than PXX series materials.

Six static indentation tests were completed on a 6PCF-XX series material coupon to make initial evaluations on its response to out-of-plane concentrated loads. The resulting dents and damage can be seen in Fig. 3.6. Force vs. displacement results for these indentation tests are shown in Fig. 3.7. The first indentation was again used to determine the load and energy required for facesheet fracture. Failure occurred at 205.1 lbs. and 0.101 in. of indentation. By integration, the energy absorbed was found to be 0.891 ft-lb. The resulting damage found in this material is similar to damage in 3PCF-XX materials, at similar energy levels. In addition to indentations made to facesheet failure at *Locations 1* and *5*, indentations were made to 50, 100, 150 and 180 lbs. at *Locations 2, 3, 6, and 4*, respectively. A table of the complete results recorded for each of these indentations can be found in Appendix A.



Figure 3.6: Results of static indentation of 6PCF-XX series material coupons: residual dents.

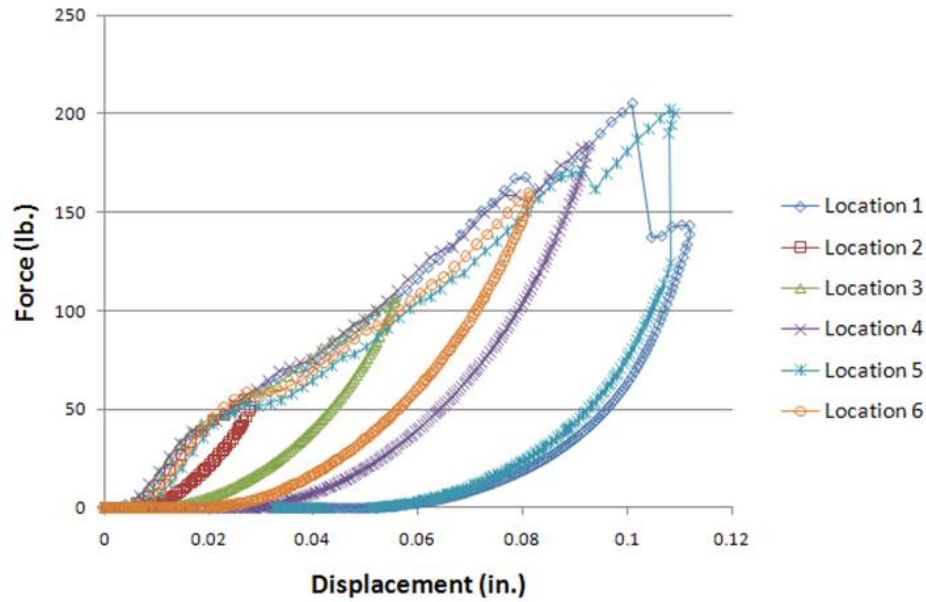


Figure 3.7: Results of static indentation of 6PCF-XX series material coupons: resultant force vs. applied displacement.

3.2.2 Drop Tower Impact Survey

An impact damage survey using a mass dropped from a tower was again used to find the properties of resulting impact damage and to measure the response due to impact of 3PCF-XX and 6PCF-XX series material coupons. The purpose of the impact survey was to determine the characteristic damage at various impact energy levels and to make a decision about which impact energy levels would be used for compression after impact tests. A material coupon was clamped on all four edges in the special test fixture, shown under the drop tower in Fig. 3.8, with no support under the opposite facesheet as done in other tests. The test fixture was then clamped to a stout steel table at the point of impact beneath the drop tower.

The drop tower used for the experiments described in the current chapter consisted of a metal tube several yards in length, mounted vertically. An electronic pulley system was mounted to the tube to raise and set the drop height of the mass which would impact the sandwich panel coupon. Once in place the impactor was dropped with the press of a button which activated a mechanical release. Upon impact the mass would rebound from the coupon and a mechanical catch would spring into place automatically to catch the impactor before it

could strike the coupon a second time. Impacts were conducted with a 0.5 in. hemispherical tip and the weight of the impactor with the tip attached was measured to be 2.4855 lb. The drop height for a given impact energy level was then calculated by dividing the desired impact energy level by the weight of the impactor. The drop height could be set using the impact tower apparatus to the nearest tenth of an inch.

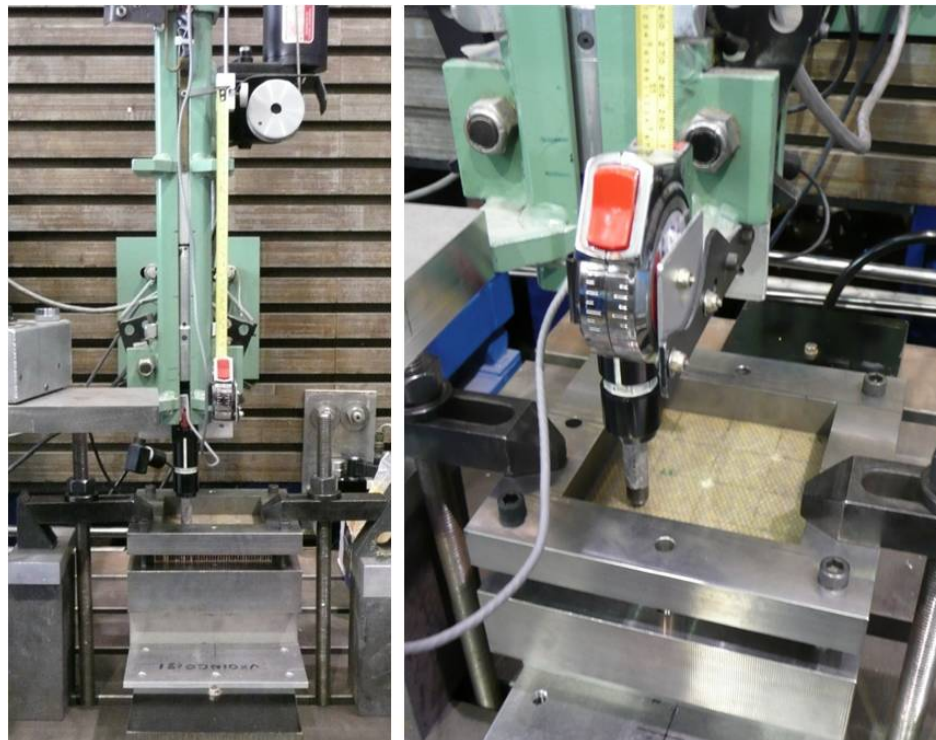


Figure 3.8: Drop tower apparatus used for impact survey of 3PCF-XX and 6PCF-XX series material coupons.

Once an impact on a 3PCF-XX or 6PCF-XX series material coupon was conducted, the residual dent was measured in terms of its maximum depth and diameter just as in the impact survey of PXX materials. After the coupons were visually examined, they were later carefully dissected with through-thickness cuts through the center of each of the indentations in order to assess the condition of the honeycomb core beneath the indentation. Maximum thickness and width of the crushed core region (measured from the bottom of the dented facesheet) was measured using inspection by optical microscope. In addition to this information, the impact force was recorded electronically with respect to time so that impact length

could also be determined. The impact length is the time in seconds from when the impactor comes into contact with the sandwich panel specimen, to when it rebounds completely. In addition, measured and visual qualitative observations were made about the location and characteristics of other types of damage present, including cracking or penetration of the impacted facesheet. Results versus impact energy for residual dent depth, residual dent diameter, maximum impact force, and impact length are shown in Fig. 3.9, 3.10, 3.11, and 3.12, respectively. Results for comparisons of crushed core diameter (width), crushed core depth, and total damage depth comparisons for both 3PCF-XX and 6PCF-XX materials are shown in Fig. 3.13, 3.14, 3.15, and 3.16, respectively. The complete results of the impact survey of 3PCF-XX and 6PCF-XX series materials, including damage descriptions, can be found in Appendix A.

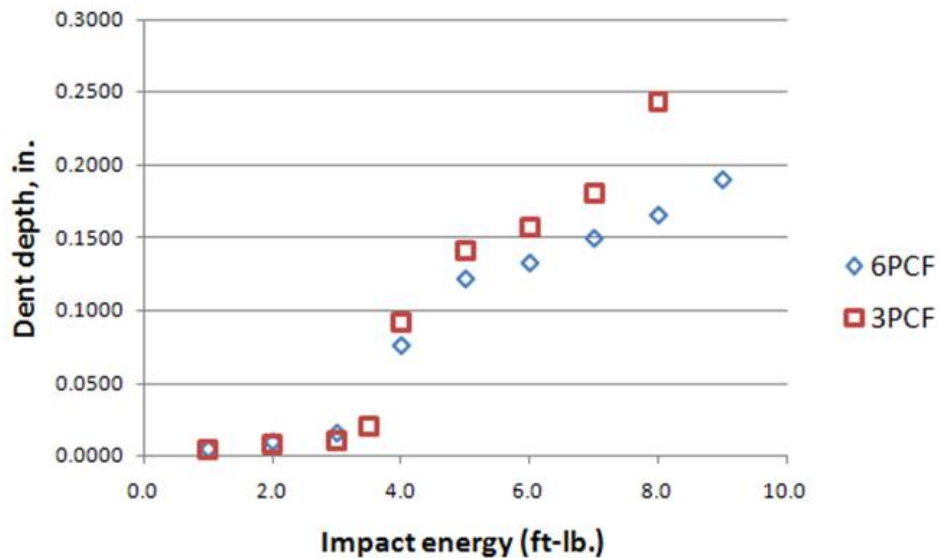


Figure 3.9: Results of drop tower impact testing on 3PCF-XX and 6PCF-XX series materials: variation of the dent depth vs. the impact energy.

Impacts on 3PCF-XX and 6PCF-XX materials with energies ranging from 1 to 9 ft-lbs. were surveyed. The higher energies became of interest during review of background literature because this type of damage had not been considered by other researchers studying CAI strength prediction in thin facesheet sandwich panels. For the 3PCF-XX material, when impacted at 8 ft-lb. the impactor completely impacted the first facesheet and became lodged

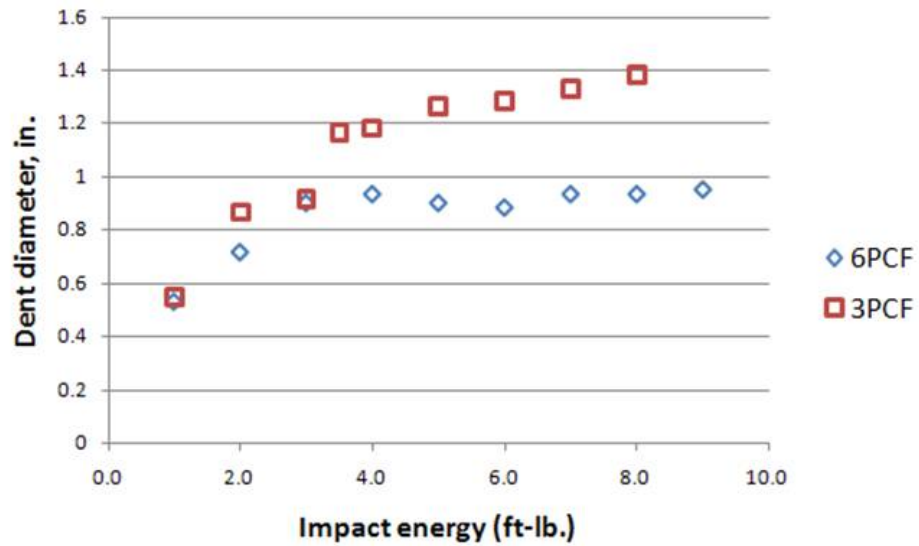


Figure 3.10: Results of drop tower impact testing on 3PCF-XX and 6PCF-XX series materials: variation of the dent diameter vs. the impact energy.

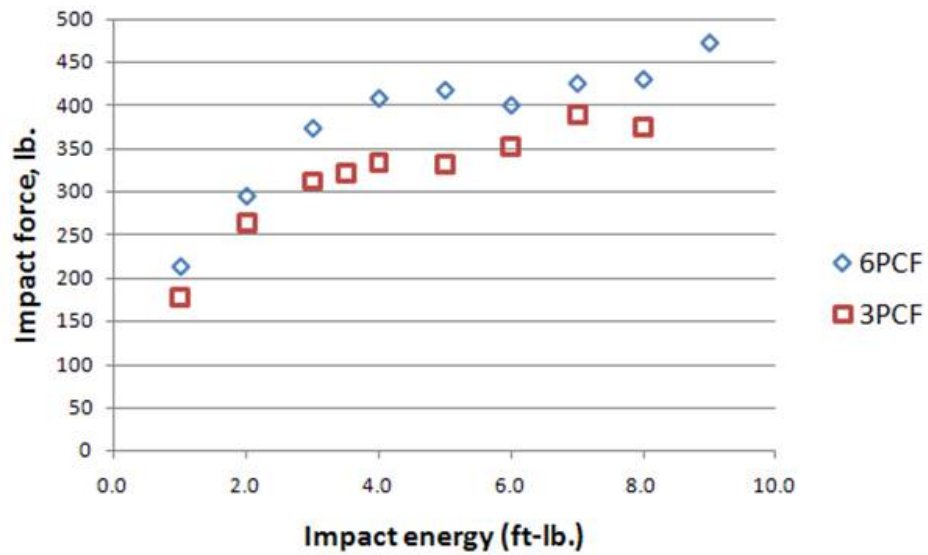


Figure 3.11: Results of drop tower impact testing on 3PCF-XX and 6PCF-XX series materials: variation of the maximum impact force vs. the impact energy.

in the sandwich panel. Since this was well beyond the damage levels of major impact, 9 ft-lb. was not considered. 3.5 ft-lb. was considered instead for the ninth impact location on the specimen. Facesheet fracture occurred at 4 ft-lbs for both types of panels. This can be seen in Fig. 3-9 where the dent depth suddenly becomes much larger with increasing impact

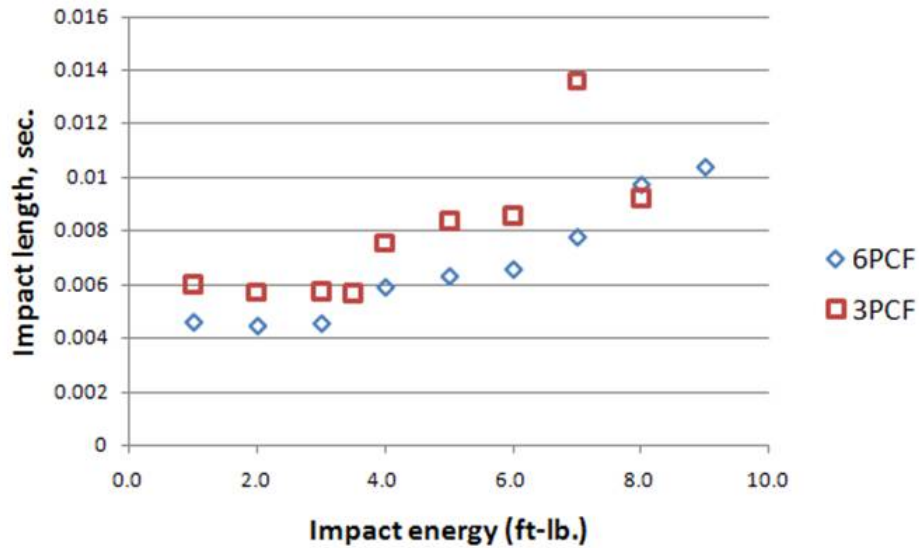


Figure 3.12: Results of drop tower impact testing on 3PCF-XX and 6PCF-XX series materials: variation of the impact length vs. the impact energy.

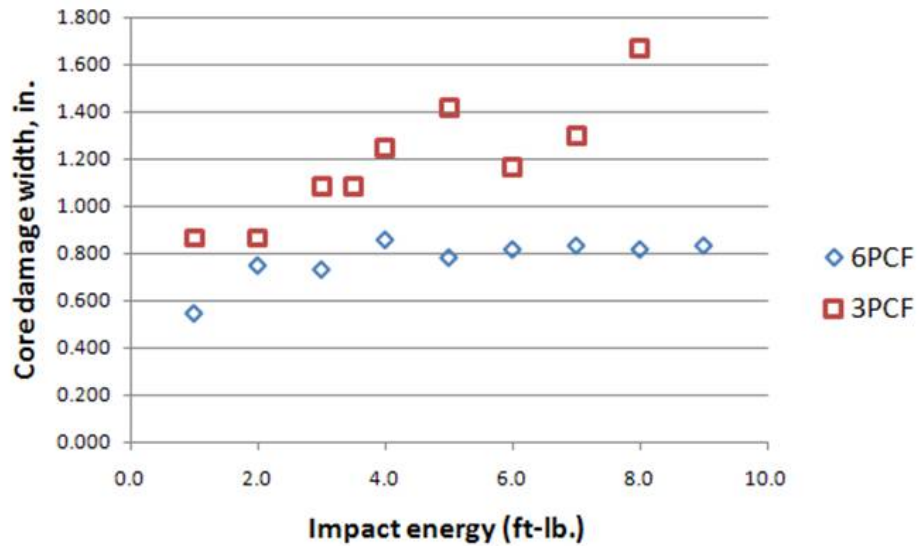


Figure 3.13: Results of drop tower impact testing on 3PCF-XX and 6PCF-XX series materials: variation of the core damage width vs. the impact energy.

energy. The maximum impact force also increases with impact energy until impact levels at which facesheet fracture occurs, and then reaches a maximum. Impact length is longer for impacts where fracture occurred due to the decreased rebound speed as more energy is absorbed by the panel, contributing to damage. Core damage was considered in detail for

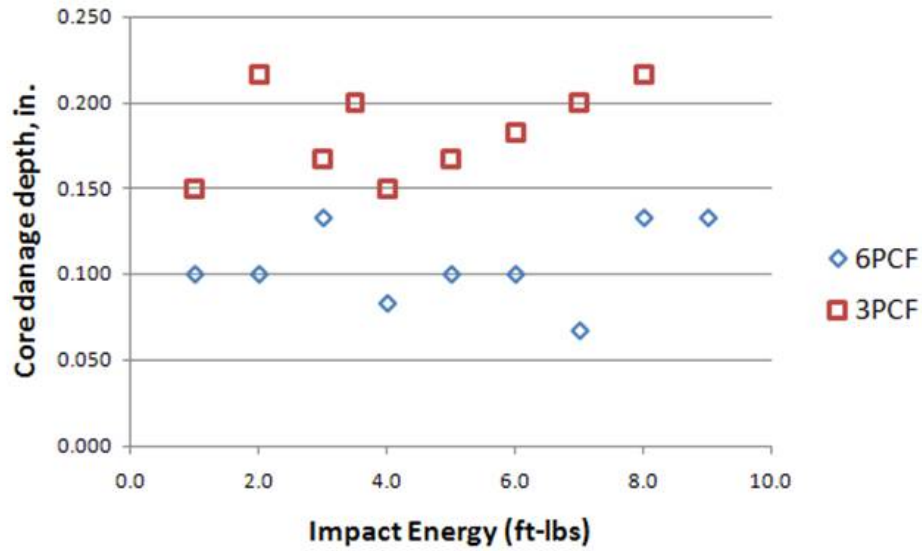


Figure 3.14: Results of drop tower impact testing on 3PCF-XX and 6PCF-XX series materials: variation of the core damage depth vs. the impact energy.

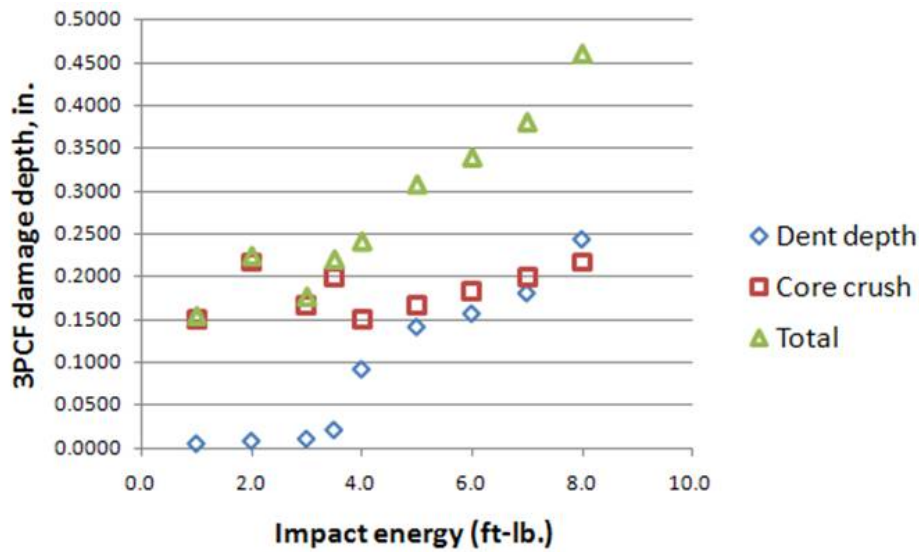


Figure 3.15: Results of drop tower impact testing on 3PCF-XX and 6PCF-XX series materials: variation of the total dent depth for 3PCF-XX materials vs. the impact energy.

3PCF-XX and 6PCF-XX panels. Figure 3.13 and shows that the width of the damaged core region is higher for 3PCF-XX panels then for 6PCF-XX, in general. Also, the maximum thickness of the crushed core region is higher for damage regions in 3PCF-XX materials. The conclusion can be made from these results that the higher strength and stiffness of the

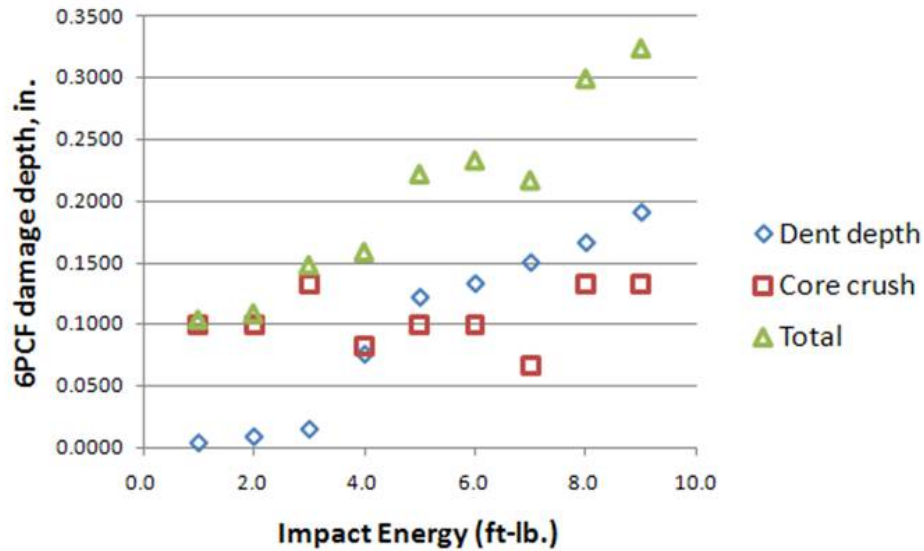


Figure 3.16: Results of drop tower impact testing on 3PCF-XX and 6PCF-XX series materials: variation of the total dent depth for 6PCF-XX materials vs. the impact energy.

6PCF-XX material’s core has a significant effect on the impact resistance of the sandwich panel. It is also interesting to note that the depth of the core crush region beneath the indented facesheet stays about the same for all levels of impact energy.

Several types of damage are present in the impact locations on the 3PCF-XX series materials shown in Fig. 3.17, and the 6PCF-XX materials shown in Fig. 3.18. At very low impact energy levels, 1 to 3 ft-lb. for 3PCF-XX, and 1 to 2 ft-lb. for 6PCF-XX, there is a slight discoloration of the facesheet and almost imperceptible residual dents in the facesheet, which are shown graphically in Figs. 3.9 and 3.10. These levels are considered barely visible impact damage (BVID) as they would be difficult to find even during routine inspection, especially if the facesheets were coated with paint. The maximum impact energy level associated with BVID is about 3 ft-lb. for both sets of materials; although, for the less stiff 3PCF-XX materials it may extend marginally higher. At higher energy levels, the facesheet fracture is very noticeable. At levels of 6 ft-lb. and higher, there is practically an open hole in the facesheet. Photographs of damage cross sections, taken after cuts were made, show that significant core damage is also present for panels with this amount of facesheet damage. An example of this evaluation is shown in Fig. 3.19, but a photograph was not

readily available for damage levels higher than 5 ft-lb. At higher energy levels, the core damage present includes large amounts of tearing and bears little resemblance to the original hexagonal cellular structure.

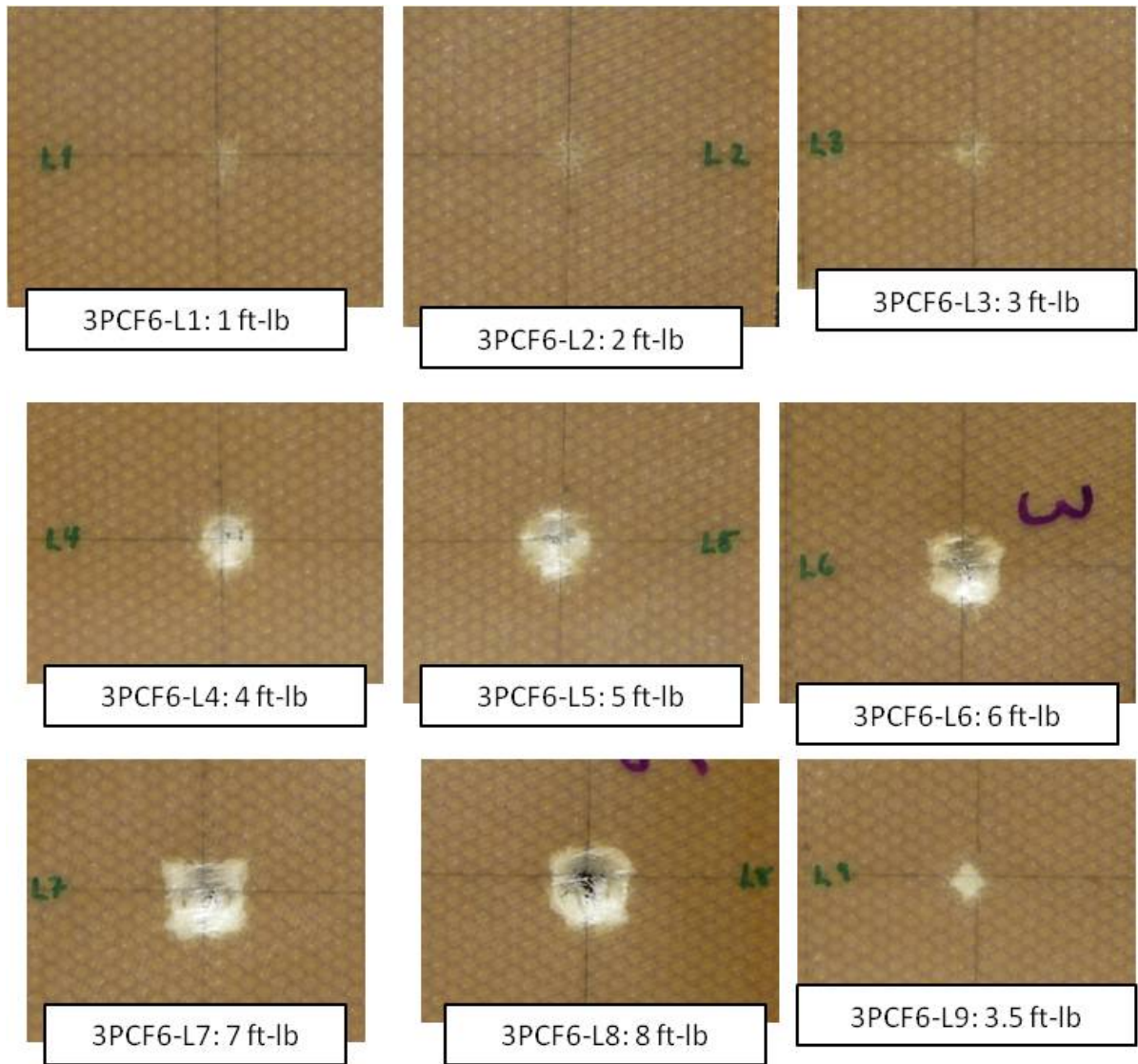


Figure 3.17: Results of drop tower impact testing on 3PCF-XX series materials: residual dents.

The data collected, as a result of the impact survey of 3PCF-XX and 6PCF-XX series sandwich panels, helped establish the energy levels of interest for various CAI test coupons. Higher energy levels for impacts than used in the PXX series tests would naturally be of interest since the BVID range of these panels extended to higher levels. Also, higher levels of

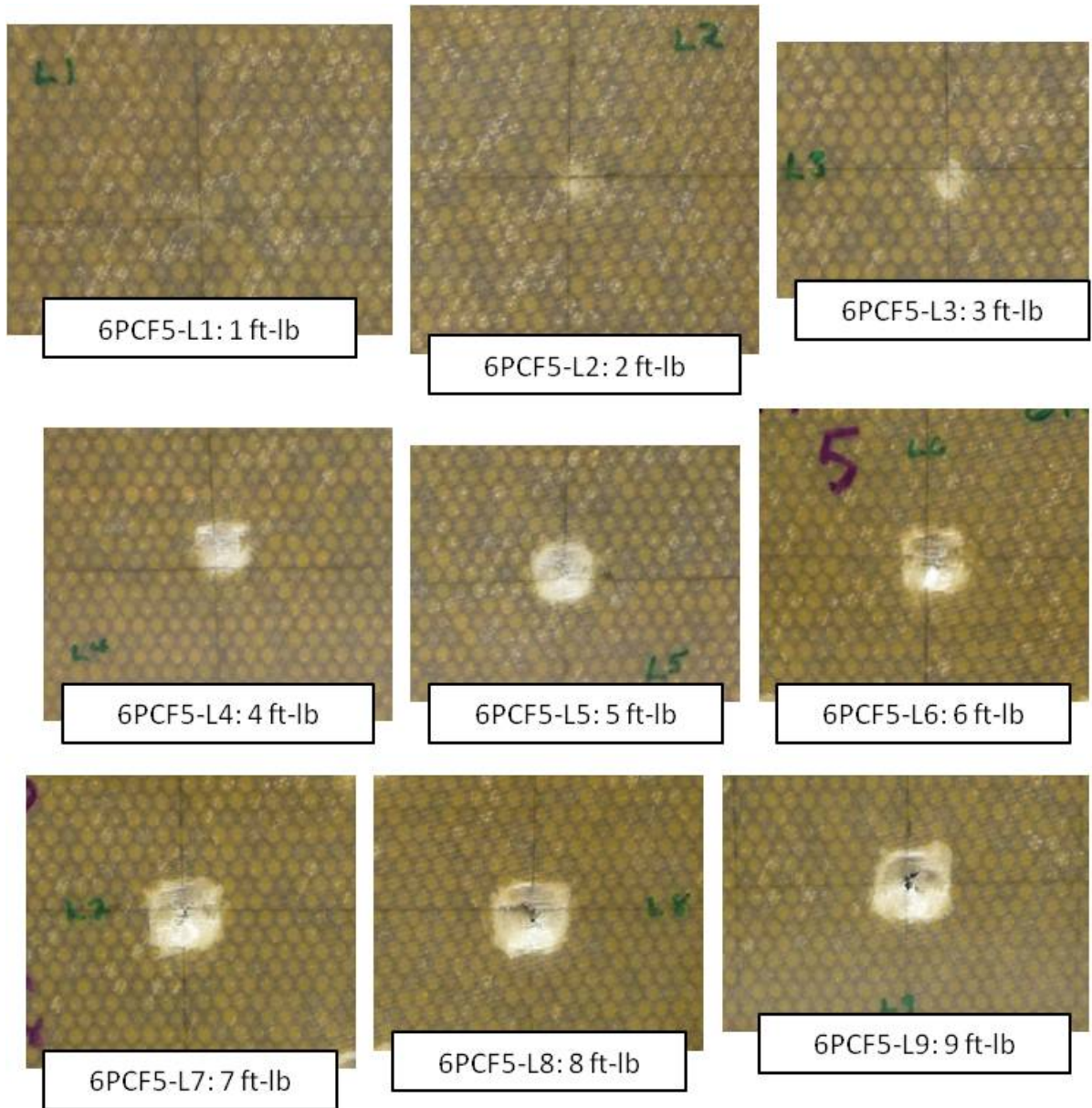


Figure 3.18: Results of drop tower impact testing on 6PCF-XX series materials: residual dents.

damage were of interest, since they have seen less prior attention by researchers studying CAI strength prediction analysis. During the impact survey, impact energy levels of 1 to 9 ft-lbs. were considered for both sets of materials. Energy levels of 1, 3, 5, and 7 ft-lbs. were chosen for impacts on CAI coupons of 3PCF-XX and 6PCF-XX series materials using the 0.5 in. diameter hemispherical impact tip. Three coupons with impacts from each energy level would

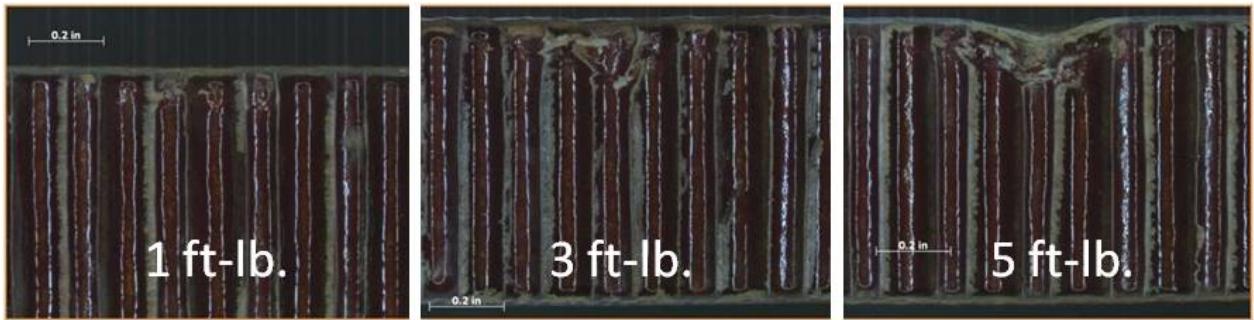


Figure 3.19: Results of drop tower impact testing on 6PCF-XX series materials: core damage shown through destructive evaluation.

be tested for each set of material coupons. In addition, undamaged panels would be tested for comparison of CAI residual strength to initial compression strength. It was expected that 3PCF-XX and 6PCF-XX panels would have nearly identical undamaged compressive strength, since this result depends upon the material strengths of the facesheets, of which the two material systems are identical.

3.3 Compression After Impact Experiments

Several test method standards, mentioned in Chapter 2, were considered when the CAI tests described in this section were designed [79] [80]. In this section, the apparatus, instrumentation, procedure, and results of CAI testing of 3PCF-XX and 6PCF-XX sandwich panel materials will be described. The experimental apparatus and procedure was largely similar to CAI tests of PXX sandwich panels and so less detail will be used in this section, except where needed to establish any differences between the test sets.

3.3.1 Apparatus and Instrumentation

Compression after impact tests of 3PCF-XX and 6PCF-XX series materials were mounted in the same servo-hydraulically actuated MTS load frame used for the CAI tests of PXX series sandwich coupons, using identical apparatus (described in Chapter 2. Compressive loading was displacement controlled and applied through hydraulically actuated movement of the

lower platen at a rate of 0.01 in. per minute. This rate was slower than that used in tests on PXX series materials, to allow for more measurements and observations to be made during a test. The load frame with a 3PCF-XX series coupon installed and a close-up picture of a 6PCF-XX coupon installed within the apparatus are shown in Fig. 3.20.



Figure 3.20: Load frame and coupon mounting apparatus used for CAI testing with 3PCF-XX (left) and 6PCF-XX (right) coupons installed.

The following instrumentation was used for all CAI tests on both 3PCF-XX series and 6PCF-XX series material coupons. The applied displacement and the measured reaction force were recorded from the load head of the MTS test frame. Far field strain in the direction of loading was recorded on the front and rear facesheets of each CAI coupon throughout testing. For the series of tests described in this chapter, in general, four uniaxial strain gages were placed on the specimen as shown in Fig. 3.21; however, occasionally a strain gage malfunctioned and this was noted when it occurred. At least three of the strain gages numbered 1 through 4 in Fig. 3.21 were necessary to assure coupon alignment within the loading apparatus. For select panels, a biaxial strain gage was used in place of uniaxial gage #3 in order to facilitate measurement of Poisson's effects in the coupon. Three direct current displacement transducers (DCDT) were mounted to monitor the displacement at several locations between the loading platens, as described in Fig. 2.21, previously. A fourth

DCDT was used in tests of 3PCF-XX and 6PCF-XX coupons to measure the out-of-plane displacement of the center of the rear (undamaged) facesheet.

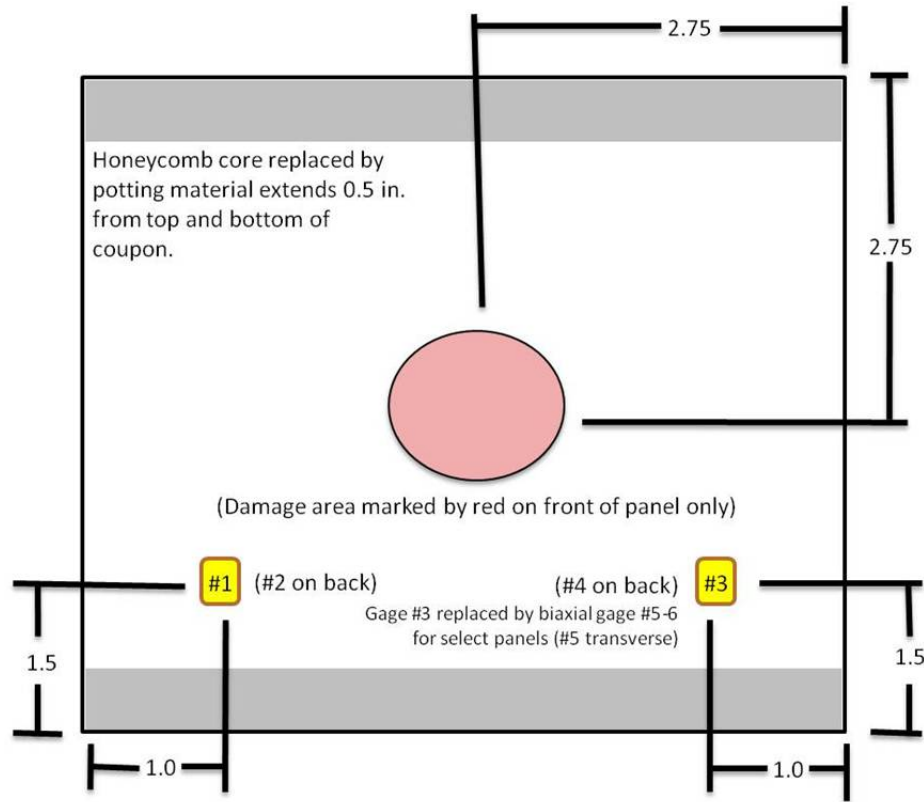


Figure 3.21: Location of strain gages for CAI testing of 3PCF-XX and 6PCF-XX series material coupons (all dimensions in inches).

Several types of auxiliary instrumentation were used throughout CAI testing. The high definition video system was not available at the time of these CAI tests; however, an effort was made to take real time video imagery of selected CAI tests using a handheld digital camera. Ambient temperature and humidity were again noted for each specimen. In addition, high speed footage using a Phantom camera system [81] was again used for select panels, as were digital images using a Vic-3D system [82] for digital image correlation measurements of full-field, three dimensional displacement and strain. At least one panel damaged at each impact energy level, for each material system, was considered by the various auxiliary instrumentations (i.e. coupons damaged at 1 ft-lb. were observed with both high speed photography, real time photography, and DIC, just not at the same time). Two Phantom

cameras were used for high speed video photography of CAI failure. One was placed in front of the test frame as before, while a second camera was placed at an angle to one side in order to capture the out of plane displacement seen during some CAI failures. The CAI apparatus with high speed cameras in place is shown in Fig. 3.22. The CAI apparatus with cameras for digital image correlation measurements was similar to that shown in Fig. 2.22. Digital image correlation was briefly explained in Chapter 2 and further information can be found in a resource by Sutton, Orteu, and Schreier [83].

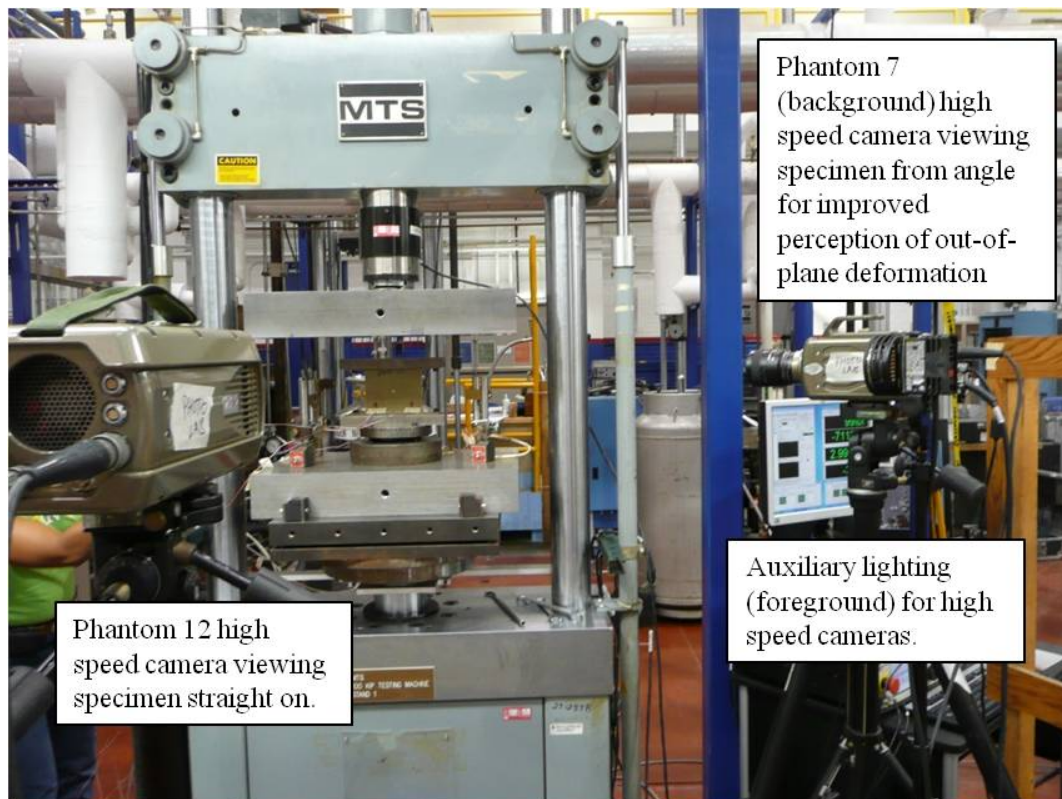


Figure 3.22: Auxiliary apparatus for CAI testing of 3PCF-XX and 6PCF-XX series coupons with high speed Phantom cameras and necessary lighting systems.

3.3.2 CAI Failure of 3PCF-XX and 6PCF-XX Series Coupons

Based on the results of the impact survey, a series of damage levels was chosen to be studied in coupons of 3PCF-XX and 6PCF-XX series materials by compression testing after impact.

Twenty-four coupons were centrally impacted on one facesheet using the drop tower shown in Fig. 3.8. Impacts at energy levels of 1.0, 3.0, 5.0, and 7.0 ft-lbs. were carried out on three coupons each of both material types. Damage was inflicted using the 0.5 in. diameter hemispherical shaped tip. The resulting damage from low velocity impact in the CAI coupons was inspected non-destructively and the metrics describing the residual dent in each panel can be found in Appendix A. A displacement controlled compressive load was applied to each coupon until failure occurred, marked by a sudden drop in the measured reaction force. In addition, two undamaged coupons (one of each construction type) were tested to failure to establish the initial compressive strength of the coupons. The compressive strength result for 3PCF-14 was the higher of the two panels tested and is considered more accurate since failure occurred at the clamped end for 6PCF-8. It is expected that the two types of panels should have nearly identical undamaged compressive strengths since the facesheet constructions are the same.

Failure occurred in the current set of CAI testing similarly to tests of PXX series materials. Global failure of the coupon occurred because of failure in the damaged facesheet only and still carried some load prior to failure. The failure mode of the 3PCF-XX panels was identical to the failure mode seen in PXX series panels, which is termed indentation propagation. However, the 6PCF-XX panels failed by a different failure mode. Instead of a region of local buckling, a crack appears in the initially damaged facesheet, which compromises its load carrying capability. The differences between the two failure modes can clearly be seen in Fig. 3.23.

Stable indentation propagation during CAI testing such as seen in 3PCF-XX tests was shown for a PXX series test in Fig. 2.26 using video photography for PXX series coupons. Video photography was also used for select tests of 3PCF-XX and 6PCF-XX materials. Time lapse photography of a 6PCF-XX series coupons shown in Fig. 3.24 indicates that the initial dent grows very little prior to the specimen failure. It appears to be nearly the same size at 1000 lbs. of load as it does at 5000 lbs. of load for coupon 6PCF-3. This particular coupon was impacted at 5 ft-lbs. of energy, but this was typical of all 6PCF-XX series CAI tests. At

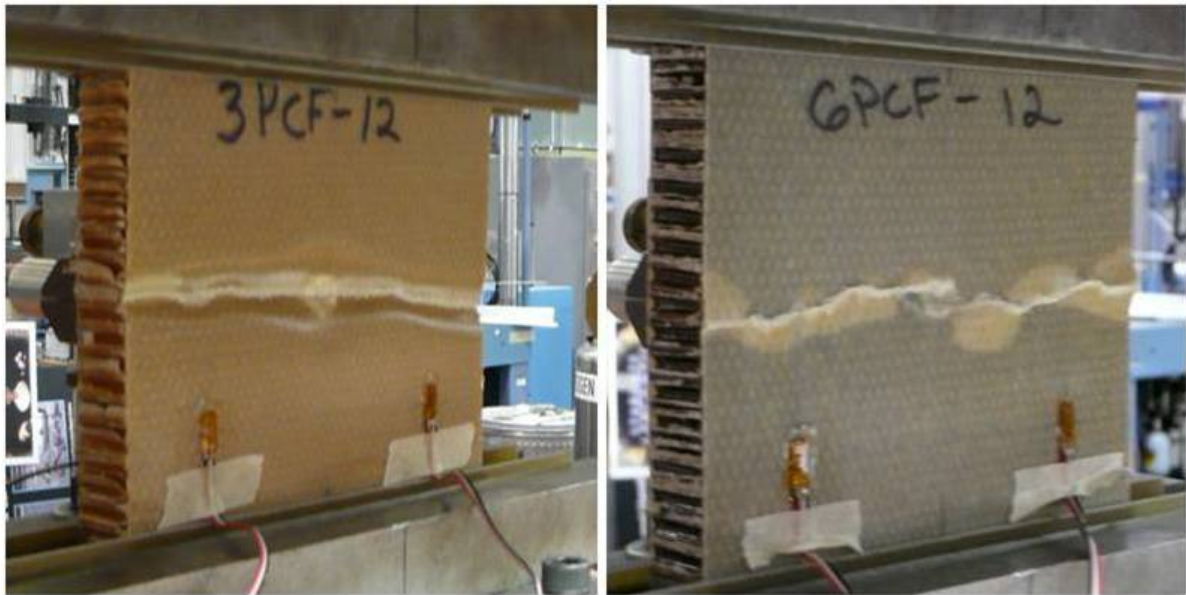


Figure 3.23: Results of CAI testing of 3PCF-XX and 6PCF-XX series materials: failure modes of indentation propagation for 3PCF-XX series coupons (left) and crack propagation in 6PCF-XX coupons (right).

about the 4:00 minute mark, a small crack in the front facesheet appeared, advancing from the initial damage location transverse to the load direction (vertical). By the 4:30 mark, the crack had advanced slightly; however, by the 5:00 minute mark the crack was easily visible and the panel was very near to the residual strength which was found to be 6107 lbs. for the 6PCF-2 coupon. Between the 5:03 and 5:04 marks in the real time video, the crack propagated to the edge of the specimen (accompanied by some interlaminar delamination and facesheet debonding), thus compromising the facesheet. A global failure of the coupon has thus occurred.

Phantom camera systems [81] were again used to capture failure of both 3PCF-XX and 6PCF-XX series materials and were quite essential in fully understanding failure, as it happens extremely quick in real time. A Phantom version 12 video system captured front views of select panels at 15,001 photos per second and a Phantom version 7 video system captured side angles at 12,500 photos per second to illustrate any out-of-plane displacement of the facesheets. Frames taken from footage captured from both view points during CAI testing of coupons 6PCF-12 and 3PCF-15 show, in Fig. 3.25, the contrasting failure modes

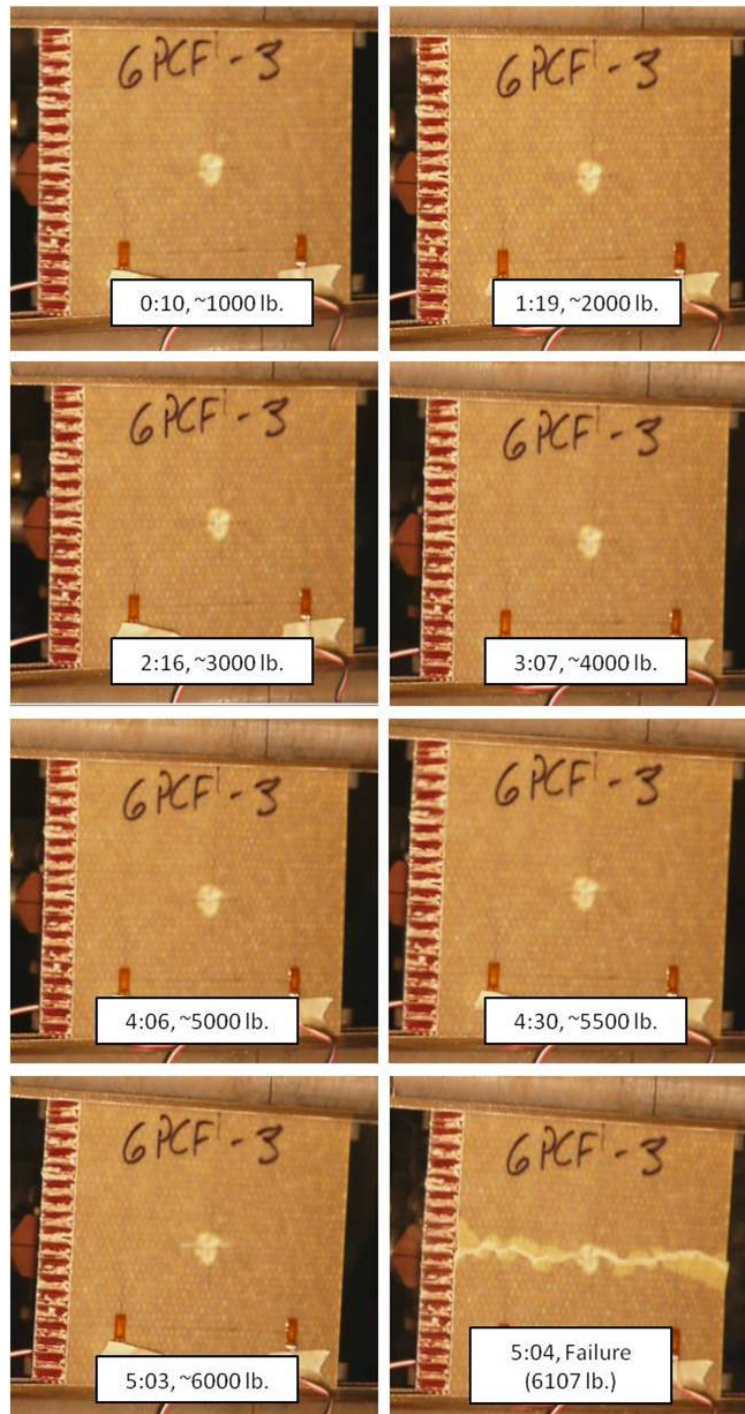


Figure 3.24: Results of CAI testing of 6PCF-XX series materials: time lapse images taken throughout test.

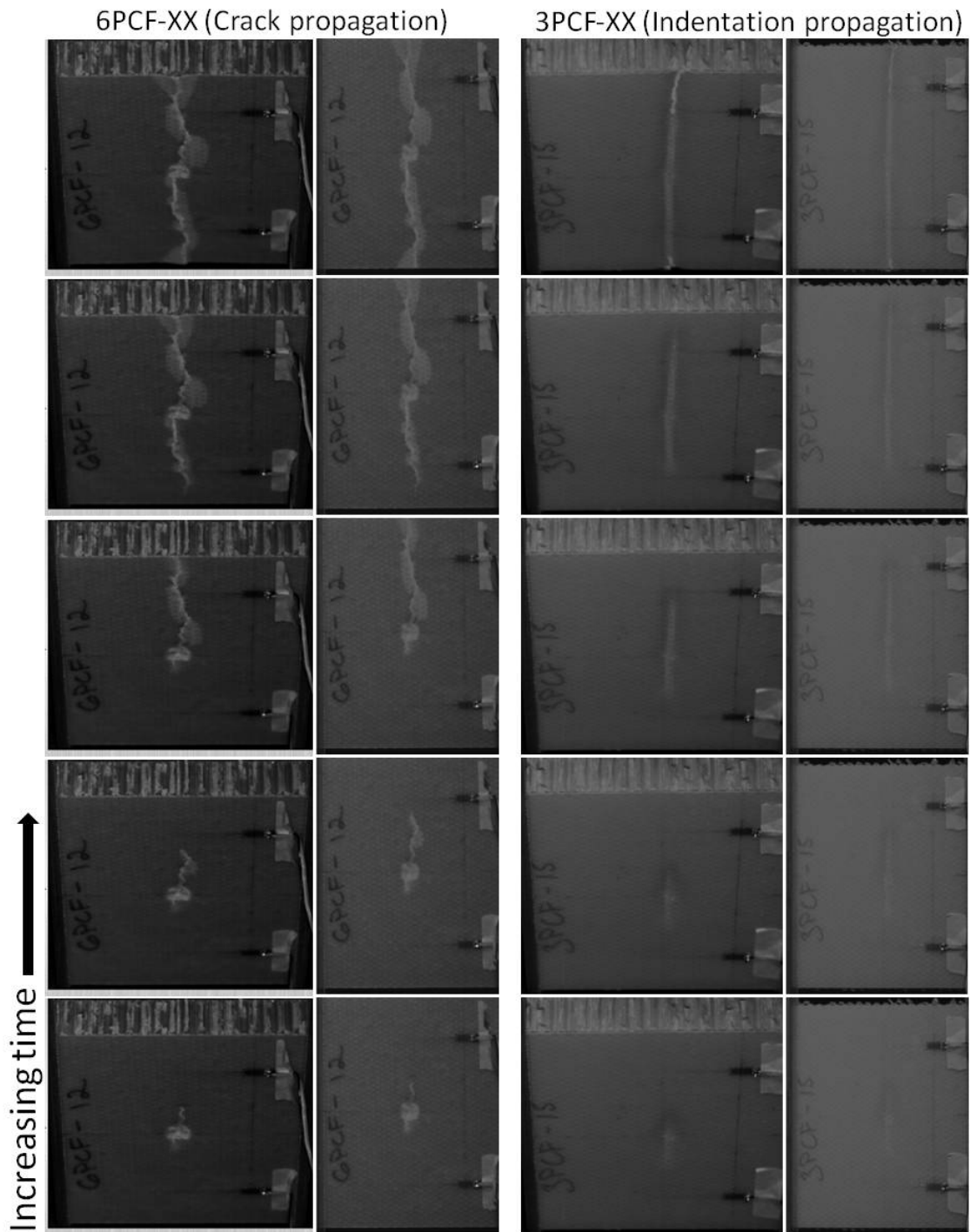


Figure 3.25: Results of CAI testing of 3PCF-XX and 6PCF-XX series materials: time lapse images taken from high speed camera during failure for 3PCF-XX (right) and 6PCF-XX (left) materials.

occurring during the moment of failure. The sequences taken from the two cameras for 6PCF-12 begin with a small crack already visible growing from the initial impact initiated indentation. The crack propagates quickly to each side, although it propagates to the right slightly before the left showing that there may be a difference in stress concentration on either side of the initial damage due to slight coupon misalignment or other factors. In real time, however, this was not noticeable for most test cases. Photos, taken at high speed, of coupon 3PCF-15 show indentation propagation failure that is similar to that shown previously in Fig. 2.27. With the aid of the side mounted camera, the high speed camera footage also shows the out-of-plane deflection in the locally buckled region more clearly than in previous tests on PXX series materials. Also, in both cases the failed facesheet's inability to transfer load causes the entire coupon to buckle globally. Although the global out-of-plane displacement at the middle point of the coupon is small it can be seen in the side images taken from the high speed cameras. In the actual video, this feature is easier to see, as the coupon can be seen to actually move.

Nominal failure stress was calculated from the measured resultant force divided by the nominal cross sectional facesheet area of each coupon and is shown in Fig. 3.26. Average measured far-field strain at coupon failure from the four strain gages on each panel was also reported for each coupon, which is shown in Fig. 3.27. Detailed failure results of nominal failure stress and failure strain for CAI tests of 3PCF-XX and 6PCF-XX series materials can be found in Appendix A.

The failure strength of both 3PCF-XX and 6PCF-XX series coupons is shown to drop dramatically even for lightly impact-damaged specimens. The reduction in coupon strength of roughly 10 ksi from undamaged specimens to damaged specimens impacted at 1.0 ft-lb. energy levels was higher than any subsequent drop, even in the most damaged sandwich panels. The drop of failure strength is shown to decrease in severity with further increasing levels of damage. Tests of 3PCF-XX series panels with a given damage level were more repeatable in terms of their failure level than tests at 6PCF-XX series panels. It is also important to note that failure of 6PCF-XX panels impacted at a given energy level occurred

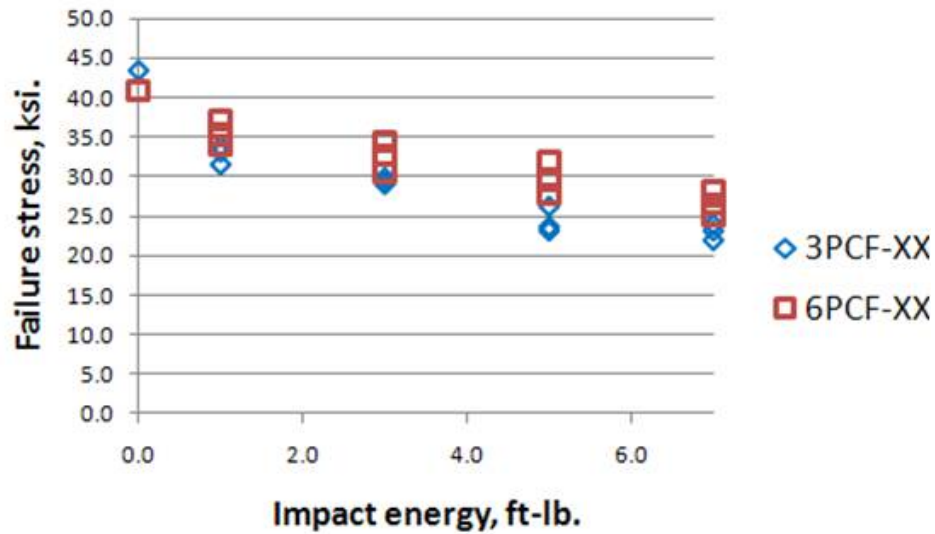


Figure 3.26: Results of CAI testing of 3PCF-XX and 6PCF-XX series materials: failure stress vs. impact energy.

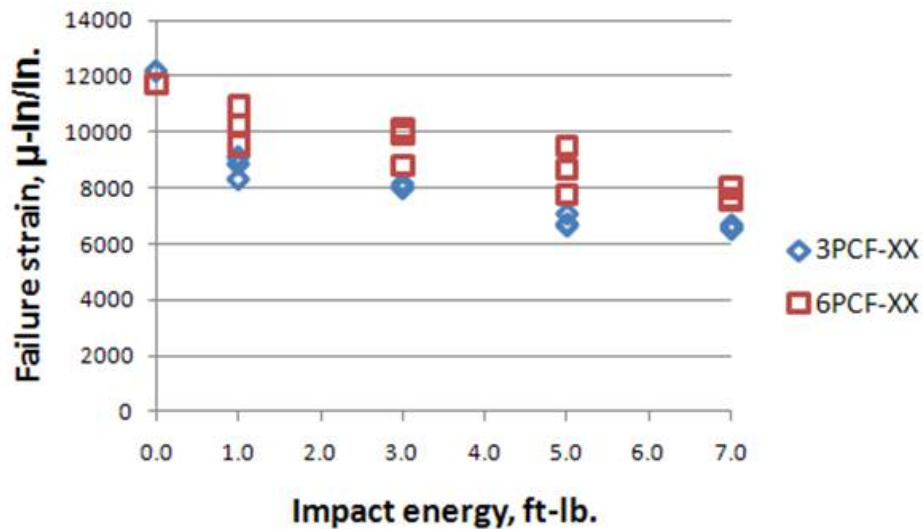


Figure 3.27: Results of CAI testing of 3PCF-XX and 6PCF-XX series materials: failure strain vs. impact energy.

at higher stress and strain levels than 3PCF-XX panels. This suggests that the higher density honeycomb core found in 6PCF-XX panels contributes to the increased CAI strength. It was shown previously that the residual dent increases dramatically in size for panels with 3 lb. per cu. ft. density cores (3PCF-XX and PXX series), while the dent does not increase in

size noticeably for 6PCF-XX series. This is likely due to the higher strength and stiffness of the higher density core in response to out-of-plane compressive loads such as the facesheets pressing inwards at the edges of the initial dent due to the applied compressive load to the panel. The higher out-of-plane stiffness precludes the indentation propagation failure mode; instead, the panels fail due to crack propagation due to in-plane stress concentrations in the facesheet which cause material fiber and matrix failure.

3.3.3 Full Field Displacement Measurements using DIC

A three-dimensional (3D) digital image correlation (DIC) system was again used for full field displacement and surface mapping of a select group of CAI test coupons for the 3PCF-XX and 6PCF-XX series materials. A brief explanation of the DIC system was provided in Section 2.3.3. The DIC system provided important information about the shape and deformation of impact damage in each test coupon surveyed. It also helped to validate observations on the differences between the two observed CAI failure modes, indentation propagation and crack propagation, which were made through time lapse imagery from video footage. The DIC system allows observations about damage growth to be quantified. An example of a 3D DIC representation of the indentation propagation failure mode from a 3PCF-XX CAI test is shown in Fig. 3.28, while the corresponding two-dimensional (2D) image is shown in Fig. 3.29. An example of the crack propagation failure mode for a 6PCF-XX CAI test coupon is shown in Fig. 3.30 with a 3D representation and in Fig. 3.31 for the corresponding 2D representation.

The main benefit of the DIC system to the present research was the ability to quantify the change in size of the out-of-plane impact damage in the damaged facesheet of the sandwich panel test coupon during subsequent compressive loading. Four test coupons from both the 3PCF-XX and the 6PCF-XX series materials were selected for instrumentation using the DIC system. For the 3PCF-XX series tests, coupons 3PCF-05, 3PCF-03, 3PCF-10, and 3PCF-09 were selected to represent the four impact energies used for impacting 3PCF-XX series CAI test coupons, which were 1.0, 3.0, 5.0, and 7.0 ft-lbs., for the four coupons, respectively. For

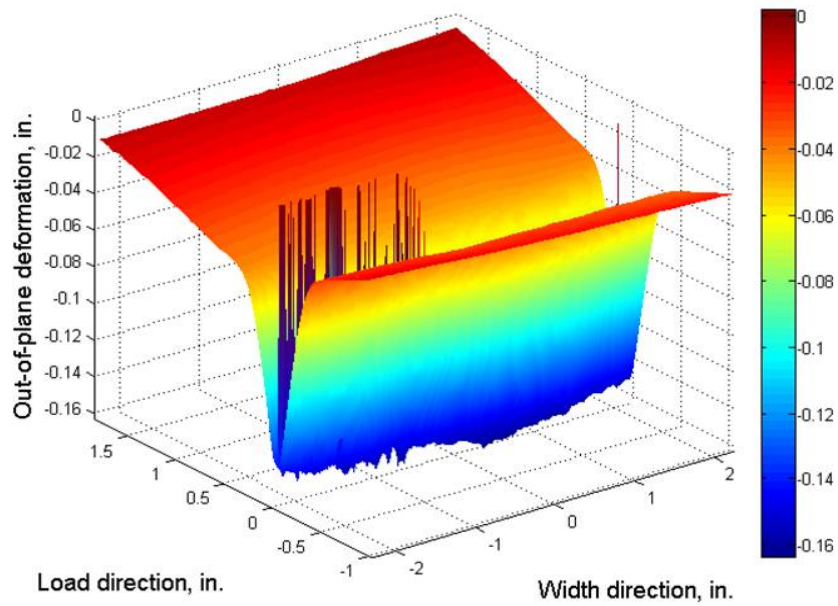


Figure 3.28: Example 3D representation of the indentation propagation failure mode for a 3PCF-XX series CAI test coupon.

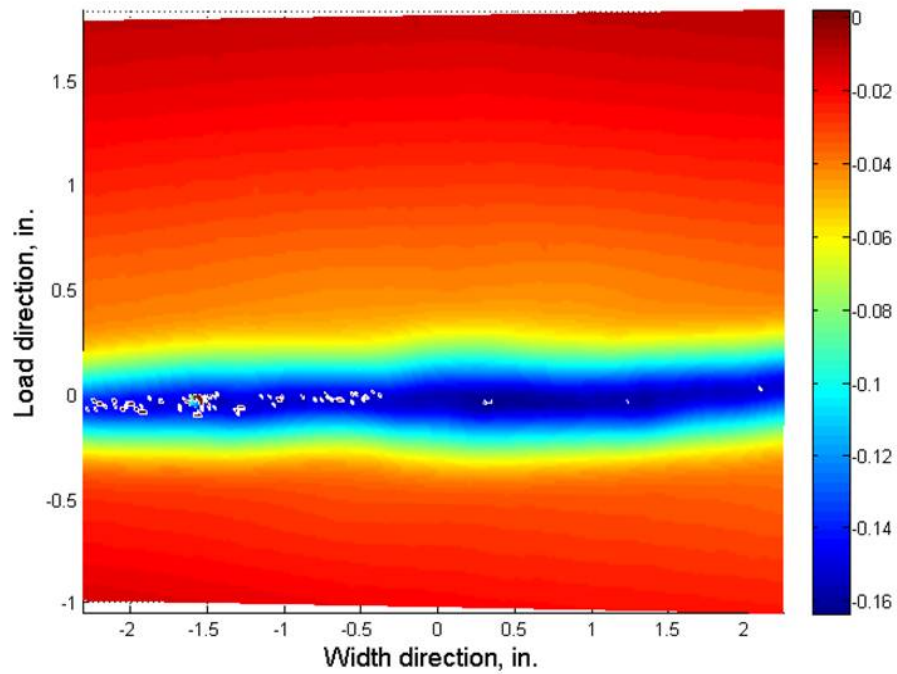


Figure 3.29: Example 2D representation of the indentation propagation failure mode for a 3PCF-XX series CAI test coupon.

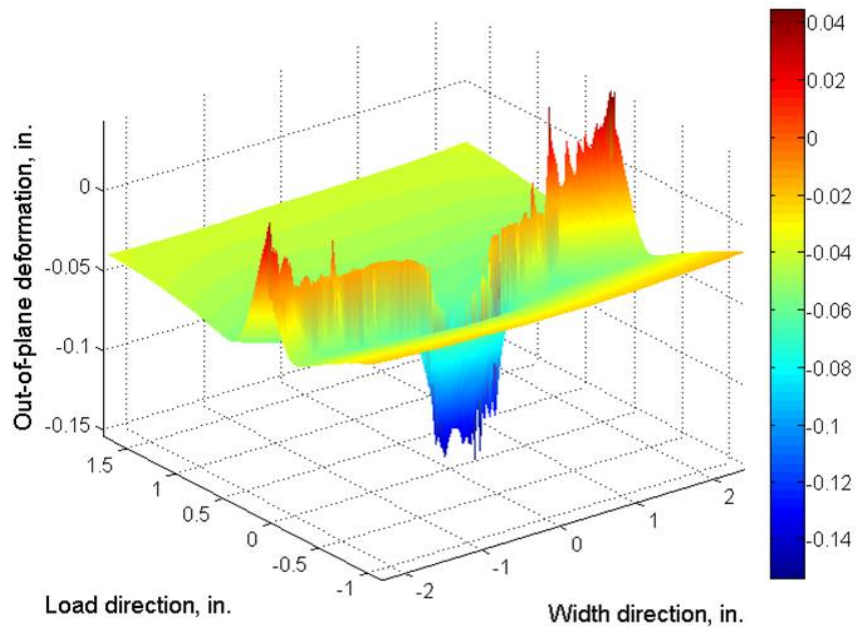


Figure 3.30: Example 3D representation of the crack propagation failure mode for a 6PCF-XX series CAI test coupon.

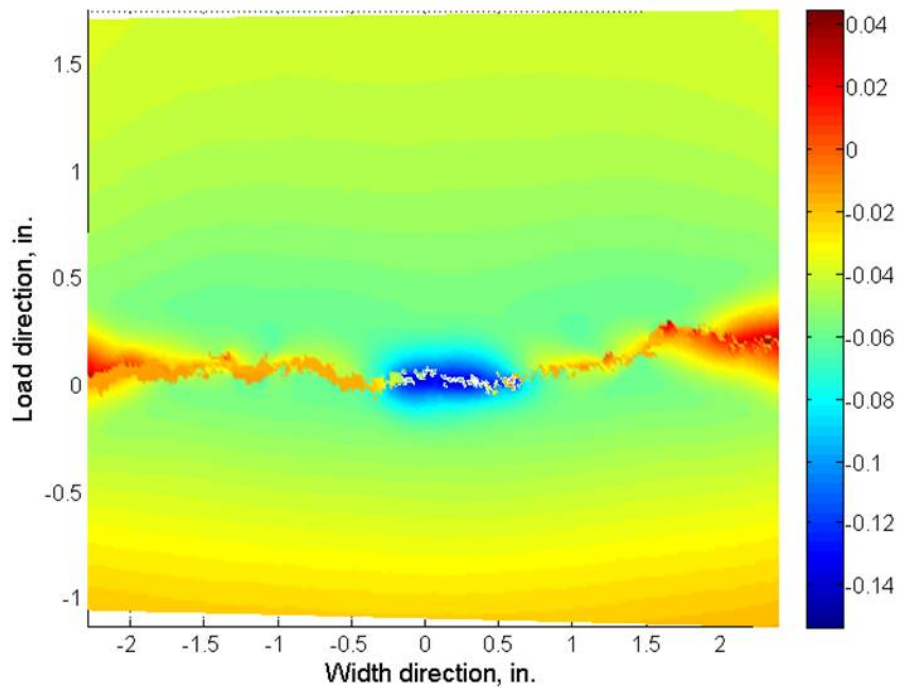


Figure 3.31: Example 2D representation of the crack propagation failure mode for a 6PCF-XX series CAI test coupon.

the selection of results presented, the dent on each test coupon was measured in the direction of the coupon width (X-direction), in the coupon load direction (Y-direction), as well as its depth (out-of-plane or Z-direction). These measurements were made at 0%, 50%, 75%, 90% and 100% (just prior to failure) of the test coupon's failure load, and a spline fit curve was applied to the data points.

The results for the coupon width direction measurements are shown in Fig. 3.32; the load direction measurements are shown in Fig. 3.33; the dent depth measurements are shown in Fig. 3.34 for the 3PCF-XX series test coupons. The results for the 3PCF-XX series test coupons are similar to the results shown previously for PXX series test coupons in Chapter 2. The size of the impact damage in each coupon does not appreciably increase in size prior to 50% of the eventual test coupon failure load. Subsequently, the size in the coupon width direction can increase in a stable fashion to as much as one third of the overall coupon width (5.5 in.). The impact damage size remains constant in the load direction. The depth of the impact damage also increased during testing for each of the coupons studied with the DIC system.

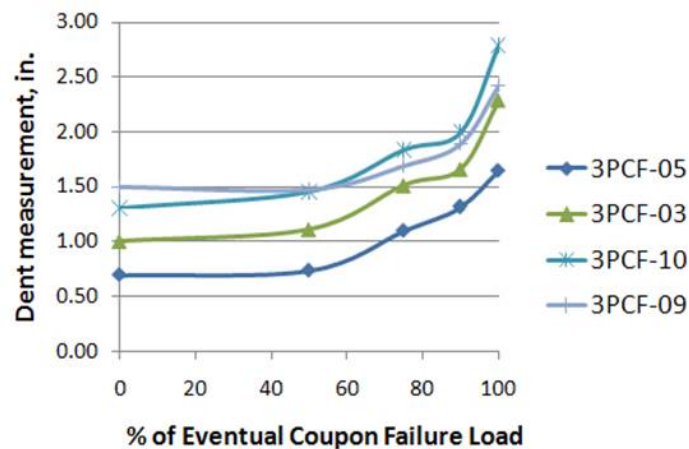


Figure 3.32: Results from DIC Measurements: dent growth in coupon width direction for 3PCF-XX test coupons.

For the 6PCF-XX series material, test coupons 6PCF-10, 6PCF-09, 6PCF-06, and 6PCF-11 were chosen for DIC system observation during compression loading. These panels were impacted at energy levels of 1.0, 3.0, 5.0, and 7.0 ft-lbs., respectively. The impact

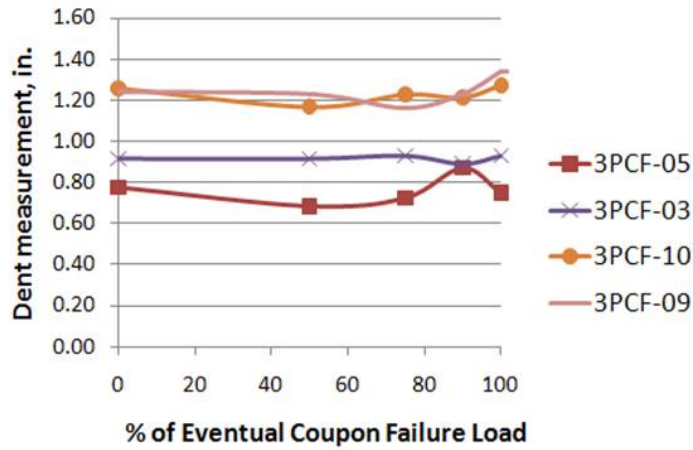


Figure 3.33: Results from DIC Measurements: dent growth in coupon load direction for 3PCF-XX test coupons.

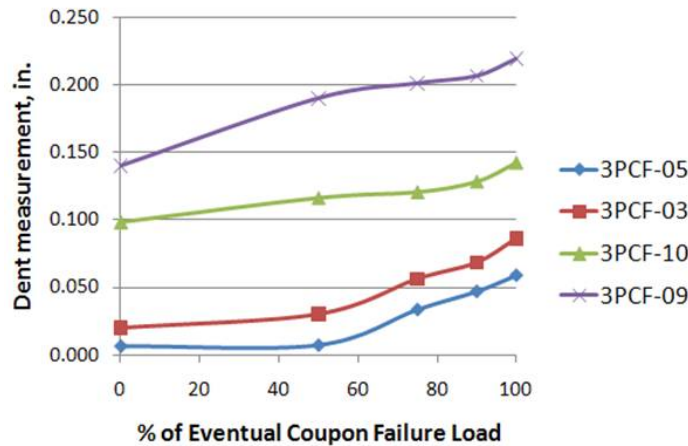


Figure 3.34: Results from DIC measurements: dent depth increase for 3PCF-XX test coupons.

damage growth was again measured for size in the coupon width and load directions, as well as maximum depth. The results for the width direction measurement are shown in Fig. 3.35; the load direction results are shown in Fig. 3.36, and the dent depth measurements are shown in Fig. 3.37. The dent growth measured for the 6PCF-XX test coupons was not nearly as marked as for 3PCF-XX and PXX series coupons. Generally, most of the dent growth for 6PCF-XX test coupons occurred very near to failure, at greater than 90% of the eventual failure load. Additionally, the stable growth amount was much smaller than 3PCF-XX coupons, when compared in terms of total growth, as well as in terms of percentage of test

coupon size. Presumably, the reduced amount of damage growth in 6PCF-XX series coupons is due to the high strength and stiffness of the higher density core materials these sandwich panel test coupons contain. Since, any dent growth must be precipitated by crushing of the honeycomb core underneath the facesheet indentation, a higher stiffness and strength of the core should lead to less growth, in general.

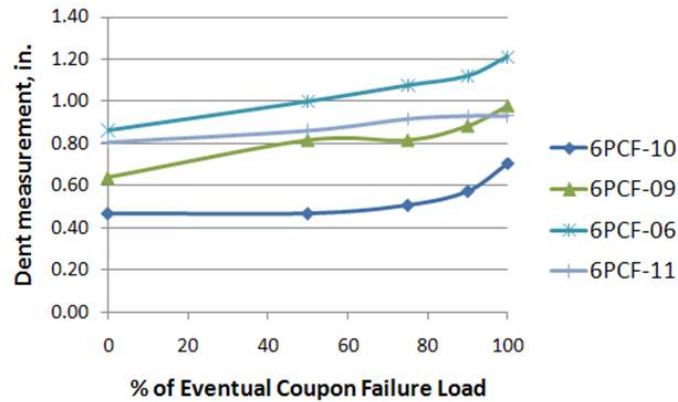


Figure 3.35: Results from DIC measurements: dent growth in coupon width direction for 6PCF-XX test coupons.

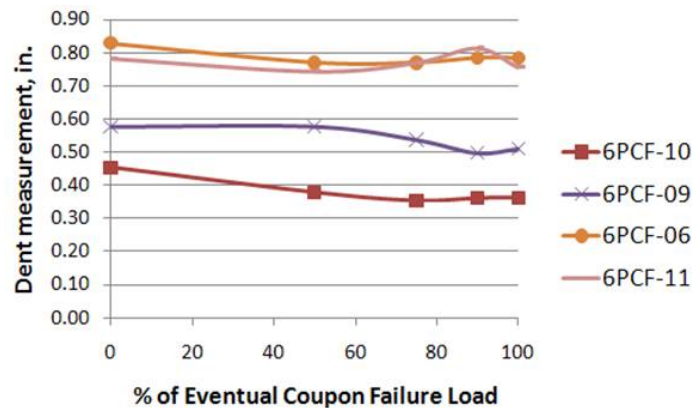


Figure 3.36: Results for DIC measurements: dent growth in coupon load direction for 6PCF-XX test coupons.

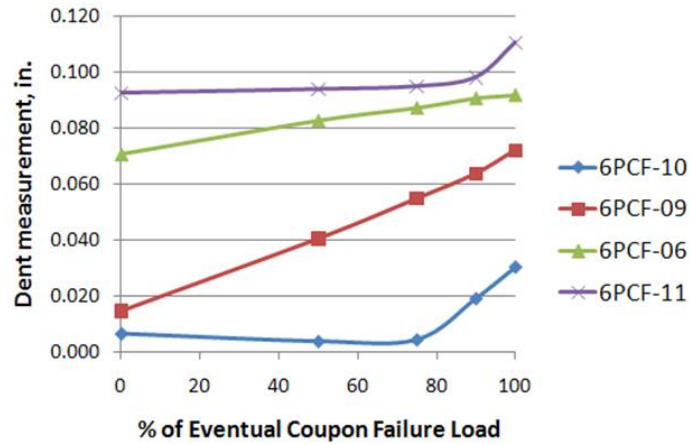


Figure 3.37: Results from DIC measurements: dent depth increase for 6PCF-XX test coupons.

3.4 Conclusions from Impact Damage and CAI Tests of 3PCF-XX and 6PCF-XX Series Materials

A series of tests to determine the impact and CAI response of 3PCF-XX and 6PCF-XX series materials was presented in the present chapter. The techniques used in these experiments were similar to those given in Chapter 2, except where changes were made based on lessons learned, as in the case of material coupon preparation. Based on the damage found during static indentation and the impact survey of the materials in the present chapter, a large range of impact energies were considered for CAI testing, extending up to 7 ft-lbs. The increased damage tolerance, of low velocity impact, of these material systems was attributed to the increased strength of the S2-glass reinforced facesheets. During CAI testing of 3PCF-XX and 6PCF-XX materials, failure was also found to occur at higher strengths than PXX series materials, which were shown in Chapter 2, but similar trends in CAI failure measurements vs. damage energy were shown.

The key difference in the construction of 3PCF-XX series materials and 6PCF-XX series materials was the nominal density in the honeycomb core used. The higher density core contributed to decreased residual dent depth and diameter in those material coupons, which was found from results of the impact survey. Increased CAI strength was also shown for

the coupons with the higher density core (6PCF-XX). Most importantly, it was found that the failure mode for the 6PCF-XX panels was not indentation propagation. Instead, a crack propagation failure mode was demonstrated for these panels. Results obtained using DIC systems for full field displacement measurements highlighted the key differences between the indentation propagation failure and crack propagation failure modes. The differences were also demonstrated using images taken from video footage, and high speed digital photography. The dependence of the failure mode on the nominal density of the honeycomb core of these panels is a result which demonstrates the need for a CAI model to be able to predict multiple failure modes. This need was mentioned in Chapter 1 during the literature review. The current research seeks to develop a model which can predict both failure modes established in Chapters 2 and 3. Next, in Chapter 4, development of this model will begin with examination of the relevant theory and a more detailed review of two models similar to those used in research explained in Chapter 1. Later in Chapter 5, the new CAI model will be more fully developed, and finally, in Chapter 6, the experimental results of the current research will be compared with analysis results using the new model.

Chapter 4

CAI Analysis Using Existing Models

It has been established that even a low, to moderate damage, from low-velocity impacts, can cause critical strength reductions in fiber reinforced matrix composite airframe components. The ability to predict the effect of damage to vehicles and structures made from these materials would represent a valuable design tool. Various attempts have been made to predict compression after impact (CAI) strength in thin facesheet composite sandwich panels, such as the material systems considered in Chapters 2 and 3 of the current work. A new finite element model (FEM), described in the next chapter, for analysis of CAI failure in honeycomb core sandwich panels, builds on current models as described in the literature review given in Chapter 1. Two of the these models will be discussed in the present chapter. Existing models have various limitations, such as handling only one type of failure mode, indentation propagation. However, some of the techniques used are incorporated into the proposed model, so it is pertinent to discuss the theory behind these models, and demonstrate their use, which will be done presently.

In the next section, the theory behind components of existing models, including laminate theory, plate theory as it relates to ABAQUS [73] finite element analysis (FEA), and the relations used to homogenize the honeycomb core response, is presented. In subsequent sections, two existing models are considered: a spring element core finite element model (FEM) and a solid element core FEM. Both of these models are capable of modeling only

indentation propagation failure and a brief selection of results are compared to experimental results from the CAI tests on PXX series materials. The description of the new FEM in Chapter 5 will then continue by building upon this work.

4.1 General Theory for CAI Prediction

Composite sandwich structures consist of two separate composite laminates, called facesheets, adhesively bonded to a low density, high shear strength core structure such as a foam material or some other cellular structure. A common core material is a hexagonal cell honeycomb core structure constructed from aluminum or Nomex, the core material used in the sandwich panel constructions in this research. The high shear strength and offset from the sandwich plate's midplane give the sandwich panel a very desirable high bending stiffness. Both the facesheets and the core of the sandwich panel need to be modeled accurately. This section will describe the theory related to the finite elements representing the facesheet and core components of several recent existing models for predicting the results of CAI testing on sandwich panels.

4.1.1 Classical Laminate Theory

A discussion of the finite element representation of a composite laminate such as the one used in FEM of facesheets for sandwich panels is introduced here. Classical laminate theory is an expansion of classical plate theory based on several assumptions. A layer of a fiber reinforced polymer laminate can be thought of as a thin plate in a plane of a local Cartesian coordinate system (1-2-3). Plate theories are used as a simplified substitution for a three dimensional elasticity solution. A plate theory such as classical plate theory (CPL) or first order shear deformation theory (FSDT) can be applied in the analysis of such a structure if the thickness is significantly smaller than each of the other two dimensions. Each layer is made from a linear, elastic, orthotropic material. The properties of the individual fiber and matrix materials are smeared or lumped together as layer or ply properties. For a single layer

of fiber reinforced matrix composite, the constitutive relations can be expressed in terms of the orthotropic compliance matrix with nine independent elastic constants as shown in Eq. 4.1. Here, ε_i are the extensional strains, γ_{ij} , are the shear strains, E_i , are the extensional moduli, G_i are the shear moduli, ν_{21} are the Poisson's ratio's, σ_i are the extensional stresses, and τ_{ij} are the shear stresses. The subscripted symbols i or ij are indices which are given values 1, 2, or 3 corresponding to the local Cartesian coordinate system.

$$\begin{pmatrix} \varepsilon_1 \\ \varepsilon_1 \\ \varepsilon_3 \\ \gamma_{23} \\ \gamma_{13} \\ \gamma_{12} \end{pmatrix} = \begin{bmatrix} \frac{1}{E_1} & \frac{-\nu_{21}}{E_2} & \frac{-\nu_{31}}{E_3} & 0 & 0 & 0 \\ \frac{-\nu_{12}}{E_1} & \frac{1}{E_2} & \frac{-\nu_{32}}{E_3} & 0 & 0 & 0 \\ \frac{-\nu_{13}}{E_1} & \frac{-\nu_{23}}{E_2} & \frac{1}{E_3} & 0 & 0 & 0 \\ 0 & 0 & 0 & \frac{1}{G_{23}} & 0 & 0 \\ 0 & 0 & 0 & 0 & \frac{1}{G_{13}} & 0 \\ 0 & 0 & 0 & 0 & 0 & \frac{1}{G_{12}} \end{bmatrix} \begin{pmatrix} \sigma_1 \\ \sigma_2 \\ \sigma_3 \\ \tau_{23} \\ \tau_{13} \\ \tau_{12} \end{pmatrix} \quad (4.1)$$

If a Cartesian coordinate system is defined so that the 1-direction axis is parallel to the fibers of the material, a plane of isotropy can be defined for fiber reinforced materials for rotations about this axis. This requires that $E_2 = E_3$, $\nu_{12} = \nu_{13}$, and $G_{12} = G_{13}$. Also,

$$G_{23} = \frac{E_2}{2(1 + \nu_{23})} \quad (4.2)$$

This results in the conclusion that for the lamina, which is assumed homogenous and transversely isotropic, there are five independent elastic constants that are needed to define the lamina. The following classical laminate theory (CLT) also requires that a plane stress condition is assumed, that is $\sigma_3 = \tau_{23} = \tau_{13} = 0$. In practice, the stresses that are assumed to be zero simply must be much smaller than the other three stresses. While these stresses may be small, they can cause failure since transverse and through the thickness strengths in composites are usually small. Also, ε_3 is notably not assumed to be zero. These assumptions allow the reduction in size of the compliance matrix and its inverse, the stiffness matrix. The

reduced compliance (4.3) and stiffness matrix (4.4) are:

$$\begin{Bmatrix} \varepsilon_1 \\ \varepsilon_2 \\ \gamma_{12} \end{Bmatrix} = \begin{bmatrix} \frac{1}{E_1} & \frac{-\nu_{21}}{E_2} & 0 \\ \frac{-\nu_{12}}{E_1} & \frac{1}{E_2} & 0 \\ 0 & 0 & \frac{1}{G_{12}} \end{bmatrix} \begin{Bmatrix} \sigma_1 \\ \sigma_2 \\ \tau_{12} \end{Bmatrix} \quad (4.3)$$

$$\begin{Bmatrix} \sigma_1 \\ \sigma_2 \\ \tau_{12} \end{Bmatrix} = \begin{bmatrix} C_{11} & C_{12} & 0 \\ C_{12} & C_{22} & 0 \\ 0 & 0 & C_{66} \end{bmatrix} \begin{Bmatrix} \varepsilon_1 \\ \varepsilon_2 \\ \gamma_{12} \end{Bmatrix} \quad (4.4)$$

Where,

$$C_{11} = \frac{E_1}{1-\nu_{12}\nu_{21}} \quad C_{12} = \frac{\nu_{12}E_2}{1-\nu_{12}\nu_{21}} = \frac{\nu_{21}E_1}{1-\nu_{12}\nu_{21}}$$

$$C_{22} = \frac{E_2}{1-\nu_{12}\nu_{21}} \quad C_{66} = G_{12}$$

In order to represent the response of a laminate, a global Cartesian coordinate system ($x - y - z$) is defined. A composite laminate consists of one or more layers stacked on top of one or another where their fiber direction (or local 1-direction) can be oriented in any direction within the $X - Y$ plane. A plane stress transformation is defined as follows to transform stresses in each layer from its local coordinate system to the global coordinate system of the laminate

$$\begin{Bmatrix} \sigma_x \\ \sigma_y \\ \tau_{xy} \end{Bmatrix} = \begin{bmatrix} \cos^2\theta & \sin^2\theta & -2\sin\theta\cos\theta \\ \sin^2\theta & \cos^2\theta & 2\sin\theta\cos\theta \\ \sin\theta\cos\theta & -\sin\theta\cos\theta & \cos^2\theta - \sin^2\theta \end{bmatrix} \begin{Bmatrix} \sigma_1 \\ \sigma_2 \\ \tau_{12} \end{Bmatrix} \quad (4.5)$$

Strain can be transformed as:

$$\begin{Bmatrix} \varepsilon_x \\ \varepsilon_y \\ \frac{1}{2}\gamma_{xy} \end{Bmatrix} = \begin{bmatrix} \cos^2\theta & \sin^2\theta & -2\sin\theta\cos\theta \\ \sin^2\theta & \cos^2\theta & 2\sin\theta\cos\theta \\ \sin\theta\cos\theta & -\sin\theta\cos\theta & \cos^2\theta - \sin^2\theta \end{bmatrix} \begin{Bmatrix} \varepsilon_1 \\ \varepsilon_2 \\ \frac{1}{2}\gamma_{12} \end{Bmatrix} \quad (4.6)$$

The transformed reduced compliance matrix is:

$$\begin{Bmatrix} \varepsilon_1 \\ \varepsilon_2 \\ \gamma_{12} \end{Bmatrix} = \begin{bmatrix} \bar{S}_{11} & \bar{S}_{12} & \bar{S}_{16} \\ \bar{S}_{12} & \bar{S}_{22} & \bar{S}_{26} \\ \bar{S}_{16} & \bar{S}_{26} & \bar{S}_{66} \end{bmatrix} \begin{Bmatrix} \sigma_1 \\ \sigma_2 \\ \tau_{12} \end{Bmatrix} \quad (4.7)$$

Where if $n = \cos \theta$ and $m = \sin \theta$, then:

$$\begin{aligned} \bar{S}_{11} &= S_{11}m^4 + (2S_{12} + S_{66})n^2m^2 + S_{22}n^4 \\ \bar{S}_{12} &= (S_{11} + S_{22} - S_{66})n^2m^2 + S_{12}(n^4 + m^4) \\ \bar{S}_{16} &= (2S_{11} - S_{12} - S_{66})nm^3 + (2S_{22} - 2S_{12} - S_{66})n^3m \\ \bar{S}_{22} &= S_{11}n^4 + (2S_{12} + S_{66})n^2m^2 + S_{22}m^4 \\ \bar{S}_{26} &= (2S_{11} - 2S_{12} - S_{66})n^3m - (2S_{22} - 2S_{12} - S_{66})nm^3 \\ \bar{S}_{66} &= 2(2S_{11} + 2S_{22} - 4S_{12} - S_{66})n^2m^2 + S_{66}(n^4 + m^4) \end{aligned}$$

The transformed reduced stiffness matrix is:

$$\begin{Bmatrix} \sigma_1 \\ \sigma_2 \\ \tau_{12} \end{Bmatrix} = \begin{bmatrix} \bar{C}_{11} & \bar{C}_{12} & \bar{C}_{16} \\ \bar{C}_{12} & \bar{C}_{22} & \bar{C}_{26} \\ \bar{C}_{16} & \bar{C}_{26} & \bar{C}_{66} \end{bmatrix} \begin{Bmatrix} \varepsilon_1 \\ \varepsilon_2 \\ \gamma_{12} \end{Bmatrix} \quad (4.8)$$

Where,

$$\begin{aligned} \bar{C}_{11} &= C_{11}m^4 + (2C_{12} + C_{66})n^2m^2 + C_{22}n^4 \\ \bar{C}_{12} &= (C_{11} + C_{22} - C_{66})n^2m^2 + C_{12}(n^4 + m^4) \\ \bar{C}_{16} &= (2C_{11} - C_{12} - C_{66})nm^3 + (2C_{22} - 2C_{12} - C_{66})n^3m \\ \bar{C}_{22} &= C_{11}n^4 + (2C_{12} + C_{66})n^2m^2 + C_{22}m^4 \\ \bar{C}_{26} &= (2C_{11} - 2C_{12} - C_{66})n^3m - (2C_{22} - 2C_{12} - C_{66})nm^3 \\ \bar{C}_{66} &= 2(2C_{11} + 2C_{22} - 4C_{12} - C_{66})n^2m^2 + C_{66}(n^4 + m^4) \end{aligned}$$

In various plate theories, including those used to construct finite elements representing composite laminates, the response of the material is defined in terms of a reference surface.

In classical laminate theory, the composite laminate consisting of the layers of stacked plies defined above is defined about its midsurface. The response of the material to the deformation is a direct result of Kirchhoff's hypothesis, which states that a transverse line drawn through plate straight and perpendicular to the reference surface will remain straight and perpendicular to the reference surface during deformation and is inextensible. As a result if the thickness of the laminate is defined as H and the z is defined as the distance from the midplane, then stress resultants for deformation applied to the laminate can be defined as:

$$\begin{aligned} N_x &\equiv \int_{-H/2}^{H/2} \sigma_x dz \\ N_y &\equiv \int_{-H/2}^{H/2} \sigma_y dz \\ N_{xy} &\equiv \int_{-H/2}^{H/2} \tau_{xy} dz \end{aligned} \quad (4.9)$$

Also, moment resultants for the laminate can be defined as:

$$\begin{aligned} M_x &\equiv \int_{-H/2}^{H/2} \sigma_x z dz \\ M_y &\equiv \int_{-H/2}^{H/2} \sigma_y z dz \\ M_{xy} &\equiv \int_{-H/2}^{H/2} \tau_{xy} z dz \end{aligned} \quad (4.10)$$

The shear strains of material points within the composite laminate plate are defined

by the extensional and shear strains of the midsurface as:

$$\begin{aligned}
 \varepsilon_x(x, y, z) &= \varepsilon_x^o(x, y) + z\kappa_x^o(x, y) \\
 &= \frac{\partial u^o(x, y)}{\partial x} + z \left(-\frac{\partial^2 w^o(x, y)}{\partial x^2} \right) \\
 \varepsilon_y(x, y, z) &= \varepsilon_y^o(x, y) + z\kappa_y^o(x, y) \\
 &= \frac{\partial v^o(x, y)}{\partial y} + z \left(-\frac{\partial^2 w^o(x, y)}{\partial y^2} \right) \\
 \gamma_{xy}(x, y, z) &= \gamma_{xy}^o(x, y) + z\kappa_{xy}^o(x, y) \\
 &= \left(\frac{\partial v^o(x, y)}{\partial x} + \frac{\partial u^o(x, y)}{\partial y} \right) + z \left(-\frac{\partial^2 w^o(x, y)}{\partial x \partial y} \right)
 \end{aligned} \tag{4.11}$$

The stress and moment resultants are related to the deformation of the composite plate by the ABD matrix, given in Eq. 4.12, where the A_{ij} , B_{ij} , and D_{ij} terms are defined in terms of the reduced transformed stiffness matrix components of each layer from Eq. 4.8 and the distance of the top and bottom of each ply to the midsurface of the laminate.

$$\begin{pmatrix} N_x \\ N_y \\ N_{xy} \\ M_x \\ M_y \\ M_{xy} \end{pmatrix} = \begin{bmatrix} A_{11} & A_{12} & A_{16} & B_{11} & B_{12} & B_{16} \\ A_{12} & A_{22} & A_{26} & B_{12} & B_{22} & B_{26} \\ A_{16} & A_{26} & A_{66} & B_{16} & B_{26} & B_{66} \\ B_{11} & B_{12} & B_{16} & D_{11} & D_{12} & D_{16} \\ B_{12} & B_{22} & B_{26} & D_{12} & D_{22} & D_{26} \\ B_{16} & B_{26} & B_{66} & D_{16} & D_{26} & D_{66} \end{bmatrix} \begin{pmatrix} \varepsilon_x^o \\ \varepsilon_y^o \\ \gamma_{xy}^o \\ \kappa_x^o \\ \kappa_y^o \\ \kappa_{xy}^o \end{pmatrix} \tag{4.12}$$

Where

$$\begin{aligned}
 A_{ij} &= \sum_{k=1}^n \bar{C}_{ij}^{(k)} (z_k - z_{k-1}) \\
 B_{ij} &= \frac{1}{2} \sum_{k=1}^n \bar{C}_{ij}^{(k)} (z_k^2 - z_{k-1}^2) \\
 D_{ij} &= \frac{1}{3} \sum_{k=1}^n \bar{C}_{ij}^{(k)} (z_k^3 - z_{k-1}^3)
 \end{aligned}$$

Hyer [87] presented further details concerning classical plate theory including incorporation of the effects of deformation due to moisture or thermal loads, and some classical

composite laminate failure theories. Kapania, Soliman, Vasudeva, *et al.* [88] discussed the important additions of FSDT and higher order shear deformation theory (HSDT) to CPT. Whereas classical plate theory adheres strictly to the tenants of Kirchhoff's theory, in FSDT the normal to the midplanes remain straight during deformation but not necessarily normal leading to additional degrees of freedom considered when evaluating the cross-sectional response in a laminate. In HSDT, the in-plane displacements are assumed to have a cubic distribution and further additional terms are needed to define laminate strain. Also, transverse shear in the laminate can be calculated with greater accuracy.

4.1.2 Composite Laminates in Finite Element Analysis

In ABAQUS [73] a user has two options for defining the behavior of a shell section. First, a general shell section can be used which defines the behavior in terms of the section moments and forces, such as in Eq. 4.12. However, stresses and strains are not available for output when the section properties are given. A second method allows the cross-sectional behavior of the plate to be found by numerical integration through the shell thickness. The ABAQUS User Manual [89] recommends the latter method when non-linear response is expected during analyses.

In each finite element analysis (FEA) performed in the present study, the laminates are defined with composite sections where each layer has individually specified material properties, thickness, and orientation. The cross-sectional behavior which results in the generalized stresses N_{ij} and M_{ij} is defined by integration either by Simpson's rule or Gauss quadrature. Simpson's rule with three points per layer is the default in ABAQUS analyses and is used in the current work except where noted otherwise. In general, Gauss quadrature is more accurate than the Simpson's rule for the same number of integration points and could be used to increase accuracy without a computational time and storage space penalty, if necessary. Numerical integration can be done at the beginning of the analysis or during each analysis step. Additional information can be found in the ABAQUS Theory Manual [90].

Two types of three-dimensional shell elements are available in ABAQUS: conventional and continuum. Conventional shell elements discretize the reference surface of the plate or composite laminate (or sandwich panel facesheets in the current research). The thickness of the element is defined by the section definition, and the nodes have displacement and rotational degrees of freedom. On the other hand, continuum shell elements discretize the entire body and the thickness is determined by nodal geometry. Only the displacement degrees of freedom are considered, as in other solid continuum elements, but the kinematic and constitutive behaviors are defined as in any of the shell theories.

Both conventional and continuum three-dimensional shell elements in ABAQUS use a displacement field which measures bending strains approximately equivalent to those in the Koiter-Sanders thin shell theory [91]. A principal assumption is that the displacement fields normal to the shell reference surface will not produce bending moments and the bending response of the shell neglects the effects of transverse shear and normal strain. The equilibrium relationships of this shell theory are derived from the Principle of Virtual Work. The contribution of the stresses to the virtual work done on the shell in terms of the membrane forces, N_{ij} , and bending moments, M_{ij} , the extensional strain increments along the midplane, $\delta\bar{\varepsilon}_{ij}$, and the membrane curvature increment, $\delta\bar{\kappa}_{ij}$, can be defined with respect to the planar area of the shell as:

$$\delta\Pi = \int_{Area} (N_{ij}\delta\varepsilon_{ij}^o + M_{ij}\delta\kappa_{ij}) dArea \quad (4.13)$$

The equilibrium equations, as originally proposed by Sanders [91] are:

$$\begin{aligned}
 & \frac{\partial \alpha_2 N_{11}}{\partial \xi_1} + \frac{\partial \alpha_1 \bar{N}_{12}}{\partial \xi_2} + \frac{\partial \alpha_1}{\partial \xi_2} \bar{N}_{12} - \frac{\partial \alpha_2}{\partial \xi_1} N_{22} + \frac{\alpha_1 \alpha_2}{R_1} V_1 \dots \\
 & \quad + \frac{\alpha_1}{2} \frac{\partial}{\partial \xi_2} \left[\left(\frac{1}{R_1} - \frac{1}{R_2} \right) \bar{M}_{12} \right] = 0 \\
 & \frac{\partial \alpha_2 \bar{N}_{12}}{\partial \xi_1} + \frac{\partial \alpha_1 N_{22}}{\partial \xi_2} + \frac{\partial \alpha_2}{\partial \xi_1} \bar{N}_{12} - \frac{\partial \alpha_1}{\partial \xi_2} N_{11} + \frac{\alpha_1 \alpha_2}{R_2} V_2 \dots \\
 & \quad + \frac{\alpha_2}{2} \frac{\partial}{\partial \xi_1} \left[\left(\frac{1}{R_2} - \frac{1}{R_1} \right) \bar{M}_{12} \right] = 0 \\
 & \frac{\partial \alpha_2 V_1}{\partial \xi_1} + \frac{\partial \alpha_1 V_2}{\partial \xi_2} - \left(\frac{N_{11}}{R_1} - \frac{N_{22}}{R_2} \right) \alpha_1 \alpha_2 = 0 \\
 & \frac{\partial \alpha_2 M_{11}}{\partial \xi_1} + \frac{\partial \alpha_1 \bar{M}_{12}}{\partial \xi_2} + \frac{\partial \alpha_1}{\partial \xi_2} \bar{M}_{12} - \frac{\partial \alpha_2}{\partial \xi_1} M_{22} - \alpha_1 \alpha_2 V_1 = 0 \\
 & \frac{\partial \alpha_2 \bar{M}_{12}}{\partial \xi_1} + \frac{\partial \alpha_1 M_{22}}{\partial \xi_2} + \frac{\partial \alpha_2}{\partial \xi_1} \bar{M}_{12} - \frac{\partial \alpha_1}{\partial \xi_2} M_{11} - \alpha_1 \alpha_2 V_2 = 0
 \end{aligned} \tag{4.14}$$

Here, α_i are the coefficients of the displacement of the reference surface as defined by Sanders [91], ξ_i are the coordinates along the reference surface, V_i are the transverse stress resultants, R_i are the principal radii of curvature and the strains are defined as:

$$\begin{aligned}
 \epsilon_{11} &= \frac{1}{\alpha_1} \frac{\partial U_1}{\partial \xi_1} + \frac{1}{\alpha_1 \alpha_2} \frac{\partial \alpha_1}{\partial \xi_1} U_2 + \frac{U_3}{R_1} \\
 \epsilon_{22} &= \frac{1}{\alpha_2} \frac{\partial U_2}{\partial \xi_2} + \frac{1}{\alpha_1 \alpha_2} \frac{\partial \alpha_2}{\partial \xi_1} U_1 + \frac{U_3}{R_2} \\
 \epsilon_{12} &= \frac{1}{2\alpha_1 \alpha_2} \left(\alpha_2 \frac{\partial U_2}{\partial \xi_1} + \alpha_1 \frac{\partial U_1}{\partial \xi_2} - \frac{\partial \alpha_1}{\partial \xi_2} U_1 - \frac{\partial \alpha_2}{\partial \xi_1} U_2 \right) \\
 \kappa_{11} &= \frac{1}{\alpha_1} \frac{\partial U \phi_1}{\partial \xi_1} + \frac{1}{\alpha_1 \alpha_2} \frac{\partial \alpha_1}{\partial \xi_1} \phi_2 \\
 \kappa_{22} &= \frac{1}{\alpha_2} \frac{\partial \phi_2}{\partial \xi_2} + \frac{1}{\alpha_1 \alpha_2} \frac{\partial \alpha_2}{\partial \xi_1} \phi_1 \\
 \kappa_{12} &= \frac{1}{2\alpha_1 \alpha_2} \dots \\
 & \quad \left[\alpha_2 \frac{\partial U \phi_2}{\partial \xi_1} + \alpha_1 \frac{\partial \phi_1}{\partial \xi_2} - \frac{\partial \alpha_1}{\partial \xi_2} \phi_1 - \frac{\partial \alpha_2}{\partial \xi_1} \phi_2 + \frac{1}{2} \left(\frac{1}{R_2} - \frac{1}{R_1} \right) \left(\frac{\partial a_2 U_2}{\partial \xi_1} - \frac{\partial a_1 U_1}{\partial \xi_2} \right) \right]
 \end{aligned} \tag{4.15}$$

Here, U_i and Φ_i are the displacements in the i -th direction and rotations about the i -th Cartesian axes, respectively. The i -th direction or axes refers to the x -, y - or z - global Cartesian axes, which may also be represented by a 1, 2 or 3, respectively.

The transverse shear stiffness is also considered in the ABAQUS implementation of shell theory. The transverse shear stress in the i th layer due to a shear force, V_x , where z is the distance from the reference surface and B_{xi} is a component of a matrix operator, is defined as:

$$\tau_{xz}^i = \left[B_{x1}^i (z - z_i) - \left(\frac{1}{2} (z^2 - z_i^2) - z_{x0} (z - z_i) \right) B_{x2}^i + B_{x0}^i \right] V_x \quad (4.16)$$

The subscripted values of z indicate integration points through the shell thickness, or are defined below, where the values for B_{x0}^i are also defined as:

$$B_{x0}^i = \sum_{j=1}^{i-1} t_j \left[B_{x1}^j - \left(\frac{1}{2} (z_{j+1} + z_j) - z_{x0} \right) B_{x2}^j \right] \quad (4.17)$$

$$z_{x0} = \frac{\sum_{i=1}^n t_i \left(\frac{1}{2} (z_{i+1} + z_i) B_{x2}^i - B_{x1}^i \right)}{\sum_{i=1}^n t_i B_{x2}^i}$$

The shear flexibility F_S of the composite section is found by equating the shear strain energy of the section to the result found by integrating the above expression for the shear stress through the section thickness as follows in Eq. 4.18 where F_{S_i} is the shear flexibility defined for the i th layer.

$$\frac{1}{2} \begin{bmatrix} V_x & V_y \end{bmatrix} [F_S] \begin{Bmatrix} V_x \\ V_y \end{Bmatrix} = \frac{1}{2} \sum_{i=1}^n \int_{Z_i}^{z_{i+1}} \begin{bmatrix} \tau_{xz} & \tau_{yz} \end{bmatrix} [F_{S_i}] \begin{Bmatrix} \tau_{xz} \\ \tau_{yz} \end{Bmatrix} dz \quad (4.18)$$

The transverse shear stiffness, τ_{xz}^i , are calculated based on the constitutive properties of the material. ABAQUS can determine these automatically based on the shell section definition. Hourglass stiffness is also required for reduced integration elements whose section

stiffness is not integrated at enough points to keep the element from displacing in in-plane hourglass modes. The in-plane hourglass modes are defined with respect to the undeformed coordinates on the reference surface, ξ , the deformed coordinates, Ξ , the hourglass modes, γ^i , and the nodal coordinates, X_i^i , as:

$$z_i = \frac{\partial \xi}{\partial X_i} \bullet \xi^i \Gamma^i - \frac{\partial \Xi}{\partial X_i} \bullet \Xi^i \Gamma^i \quad (4.19)$$

Here, the hourglass modes are defined as:

$$\begin{aligned} \Gamma^1 &= \frac{1}{\Psi} [X_1^2 (X_2^3 - X_2^4) + X_1^3 (X_2^4 - X_2^2) + X_1^4 (X_2^2 - X_2^3)] \\ \Gamma^2 &= \frac{1}{\Psi} [X_1^3 (X_2^1 - X_2^4) + X_1^4 (X_2^3 - X_2^1) + X_1^1 (X_2^4 - X_2^3)] \\ \Gamma^3 &= \frac{1}{\Psi} [X_1^4 (X_2^1 - X_2^2) + X_1^1 (X_2^2 - X_2^4) + X_1^2 (X_2^4 - X_2^1)] \\ \Gamma^4 &= \frac{1}{\Psi} [X_1^1 (X_2^3 - X_2^2) + X_1^2 (X_2^1 - X_2^3) + X_1^3 (X_2^2 - X_2^1)] \\ \Psi &= \frac{1}{2} [(X_1^3 - X_1^1) (X_2^4 - X_2^2) + (X_1^1 - X_1^4) (X_2^3 - X_2^1)] \end{aligned} \quad (4.20)$$

The hourglass stiffness is then chosen as in Eq. 4.21 where G is the shear modulus and r_F is a small numeric coefficient chosen as 0.005 in ABAQUS/Standard [90].

$$K_h = (r_F G) \frac{\partial N^i}{\partial X_j} \frac{\partial N^i}{\partial X_j} h A \quad (4.21)$$

4.1.3 Honeycomb Core as an Orthotropic Continuum

A second type of modeling must be considered for detailed analysis of composite sandwich panels. Gibson and Ashby [55] define a hexagonal cell honeycomb core as a two dimensional cellular structure with a repeating geometry encapsulating six sided pores. Man-made honeycombs are readily available and easily found in many composite structures made from

isotropic materials, such as aluminum, and transversely isotropic materials such as Nomex. Analysis of this type of structure, analytically, usually involves the characterization of in-plane properties (width and length directions, in the plane of the cellular structure) separately from out-of-plane properties (thickness direction, in the direction of the height of the cell walls). For in-plane loads the cell walls typically bend elastically until a critical load and then they fail by elastic buckling, plastic yielding, creep, or brittle fracture. The nature of cell wall collapse is determined by the material the honeycomb is made from. An out-of-plane loading of the sandwich panel results in elastic extension or compression of the cell walls before failure, and typically the stiffnesses and strength of the structure are much higher in this direction. If loading continues beyond the initial failure either during out-of-plane or in-plane loading, until the cell walls touch, densification of the core begins to occur and the modulus of the response increases drastically with further loading.

The linear elastic deformation of the honeycomb structure can be described by considering the bending response of the cell walls. Consider the cellular geometry described in the $x_1 - x_2$ plane, shown in Fig. 4.1. The following relations were given by Gibson and Ashby [55] for the in-plane response of the Nomex honeycomb. By assuming the wall material is isotropic and has modulus, E_s , and the thickness of each cell wall, t , is constant, the effective modulus, E_1^* , representing the stiffness of the structure in response to a uniaxial load in the x_1 direction is given by Eq. 4.22. The modulus, E_2^* , is given by Eq. 4.23 and the in-plane poisson's ratios, ν_{12} and ν_{21} , are given by Eq. 4.24 and 4.25, respectively. The effective in-plane shear modulus can be determined using Eq. 4.26.

$$\frac{E_1^*}{E_s} = \left(\frac{t}{l}\right)^3 \frac{\cos \theta}{(h/l + \sin \theta) \sin^2 \theta} \quad (4.22)$$

$$\frac{E_2^*}{E_s} = \left(\frac{t}{l}\right)^3 \frac{(h/l + \sin \theta)}{\cos^3 \theta} \quad (4.23)$$

$$\nu_{12}^* = -\frac{\epsilon_2}{\epsilon_1} = \frac{\cos^2 \theta}{(h/l + \sin \theta) \sin \theta} \quad (4.24)$$

$$v_{21}^* = -\frac{\epsilon_1}{\epsilon_2} = \frac{(h/l + \sin\theta) \sin\theta}{\cos^2\theta} \quad (4.25)$$

$$\frac{G_{12}^*}{E_S} = \left(\frac{t}{l}\right)^3 \frac{(h/l + \sin\theta)}{(h/l)^2(1 + 2h/l) \cos\theta} \quad (4.26)$$

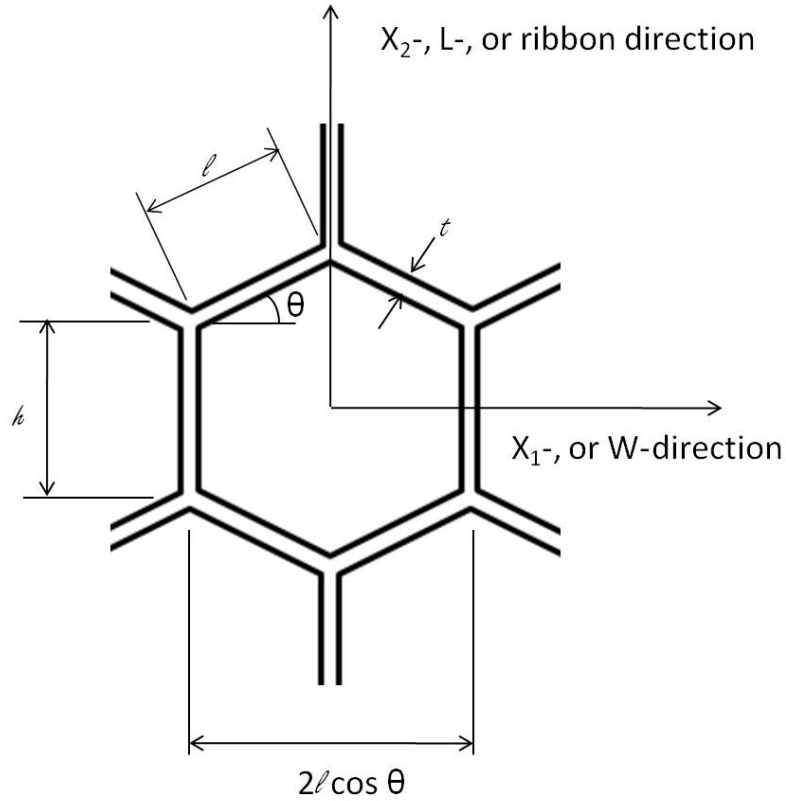


Figure 4.1: Cellular in-plane geometry of hexagonal cell honeycomb core.

A more general method of obtaining effective material properties using energy based methods was described by Hohe *et al.* first for triangular cell structures [56], than for quadrilateral and hexagonal cell structures [57], and finally for general cellular structures [58]. The authors showed that for a volume element of cellular core material and a representative volume element of a homogenized material to behave identically on a mesoscopic level, the internal strain energy due to a given volumetric deformation must be equal for both repre-

sentative elements as:

$$\int_{Vol} (\sigma_{ij} d\varepsilon_{ij}) dVol = \int_{Vol} (\sigma_{ij}^* d\varepsilon_{ij}^*) dVol \quad (4.27)$$

In general, man-made hexagonal cell honeycomb structures often do not have constant wall thickness for each cell wall. This can be due to material and construction flaws, but also is simply typical of the manufacturing process. Also, for honeycombs made of fibrous materials, such as Nomex, the source material is not isotropic, so a single elastic modulus, E_S , cannot be assumed. A more typical honeycomb core cell type was analyzed by Chen and Ozaki [59] where the cell walls oriented parallel to the ribbon direction have double the thickness. They expanded on the results of Eq. 4.23 using this method and validated their model with a detailed FEM prediction.

Detailed FEM is one possible method for modeling the honeycomb core in studies such as the present work. In fact, recently Czabaj et al [51] published a CAI prediction model using ABAQUS shell elements to explicitly model a geometrically correct representation of the cellular structure of the honeycomb core. However, modeling of the explicit cellular honeycomb core geometry is time consuming and the subsequent FEA is computationally expensive. The authors improved the efficiency of their model significantly by only including the detailed FEM in the location of the sandwich panel model where impact loading and failure would be modeled. In the rest of their model, they take advantage of the result of Eq. 4.27 to model the honeycomb core as a homogenous orthotropic solid with constitutive response as in Eq. 4.1. Other authors have recognized the efficiency of this modeling technique and have used homogenized solid core elements in FEM with good results [12] [52].

The finite element representation of the total potential energy of an element for static

analysis of a solid mechanics problem is given by:

$$\begin{aligned} \Pi_p^{(e)} = & \frac{1}{2} \int_{V^{(e)}} \int \int \vec{U}^{(e)T} [B]^T [D] [B] \vec{U}^{(e)} dV - \int_{V^{(e)}} \int \int \vec{U}^{(e)T} [B]^T [D] \vec{\varepsilon}_0 dV \\ & - \int_{S_1^{(e)}} \int \int \vec{U}^{(e)T} [N]^T \vec{F} dS_1 - \int_{V^{(e)}} \int \int \vec{U}^{(e)T} [N]^T \vec{F}_b dV \quad (4.28) \end{aligned}$$

Here, $\vec{U}^{(e)}$ is the displacement vector, $\vec{\varepsilon}_0$, is the initial strain vector, \vec{F} , are the distributed surface forces or tractions, and \vec{F}_b is the body force vector, and $[D]$ is the element stiffness matrix. The matrix $[B]$ is defined as:

$$[B] = \begin{bmatrix} \frac{\partial}{\partial x} & 0 & 0 \\ 0 & \frac{\partial}{\partial y} & 0 \\ 0 & 0 & \frac{\partial}{\partial z} \\ \frac{\partial}{\partial y} & \frac{\partial}{\partial x} & 0 \\ 0 & \frac{\partial}{\partial z} & \frac{\partial}{\partial y} \\ \frac{\partial}{\partial z} & 0 & \frac{\partial}{\partial x} \end{bmatrix} [N] \quad (4.29)$$

The matrix of isoparimetric shape functions $[N]$ for an 8-node solid element like the one used with ABAQUS for the current work, can be written as:

$$\begin{aligned} [N(o, p, q)] = & \frac{1}{8} \Theta + \frac{1}{4} o \Lambda_1 + \frac{1}{4} p \Lambda_2 + \frac{1}{4} q \Lambda_3 \\ & + \frac{1}{2} o q \Gamma_1 + \frac{1}{2} p q \Gamma_1 + \frac{1}{2} o q \Gamma_2 + \frac{1}{2} m p \Gamma_3 + \frac{1}{2} o p q \Gamma_4 \quad (4.30) \end{aligned}$$

Where o , p , and q , are the local Cartesian coordinates defining the node points, and Θ , Λ_i , and Γ_i are vectors representing deformation modes of the element. The last four vectors, Γ_i , represent the hourglass modes which must be accounted for by an hourglass stiffness for

reduced integration elements in the same manner as described for shell elements previously.

4.1.4 Honeycomb Core Non-Linear Out-of-Plane Response

The challenge of accurately representing the honeycomb core response as a homogenous material is including the out-of-plane response, specifically the non-linear compression response. By consideration of the honeycomb cell geometry shown in Fig. 4.1, Gibson and Ashby [55] gave the initial linear elastic out-of-plane response for regular hexagons with equal wall thicknesses defined as the out-of-plane Young's modulus, Poisson's ratios and the shear modulus (with respect to the honeycomb material's shear modulus, G_S) to be:

$$\frac{E_3^*}{E_S} = \left[\frac{h/l + 2}{2(h/l + \sin \theta) \cos \theta} \right] \frac{t}{\bar{l}} \quad (4.31)$$

$$v_{31}^* = v_{13}^* = v_S \quad (4.32)$$

$$\frac{G_{13}^*}{G_S} = \frac{G_{23}^*}{G_S} = \frac{\cos \theta}{h/l + \sin \theta} \left(\frac{t}{\bar{l}} \right) \quad (4.33)$$

Note that in general the shear moduli, G_{ij} , are not equal. During compressive loading at the critical load the response of the honeycomb is no longer linear. Gibson [55] noted that the non-linear response can be due to elastic buckling of the cell walls, plastic collapse of the cell walls or brittle fracture. Analytically, this has been investigated with limited success; however, it was shown in Chapter 1 in review of the relevant literature that several researchers have described the elastic buckling and plastic collapse of cell walls using geometrically correct FEM representations of the honeycomb core structure [62] [63] [64] [65] with good results. In these types of FEA, the response of the honeycomb to a flatwise core crushing load is simulated. The open ends of the cellular structure are fixed as if they were bonded to a facesheet. The major purpose of the simulations is to predict the core crush strength for a given honeycomb configuration, and in some cases the post-failure response.

In the present study, the linear elastic out-of-plane modulus and the core crush strength are defined by experimentally determined constants. The out-of-plane response

of the core is defined as an idealization of a core crush test, as shown in Fig. 4.2. The linear elastic response and initial post-crushing response are modeled. The densification process is ignored as the deformation response of the core during CAI modeling is not expected to be enough to warrant its modeling, as observed from the experimental results. It was explained in review of the pertinent literature in Chapter 1 that this type of homogenized representation of the honeycomb core in CAI modeling of sandwich panels is well accepted and has been employed by various authors [42] - [43] [46] [47] [49] [52].

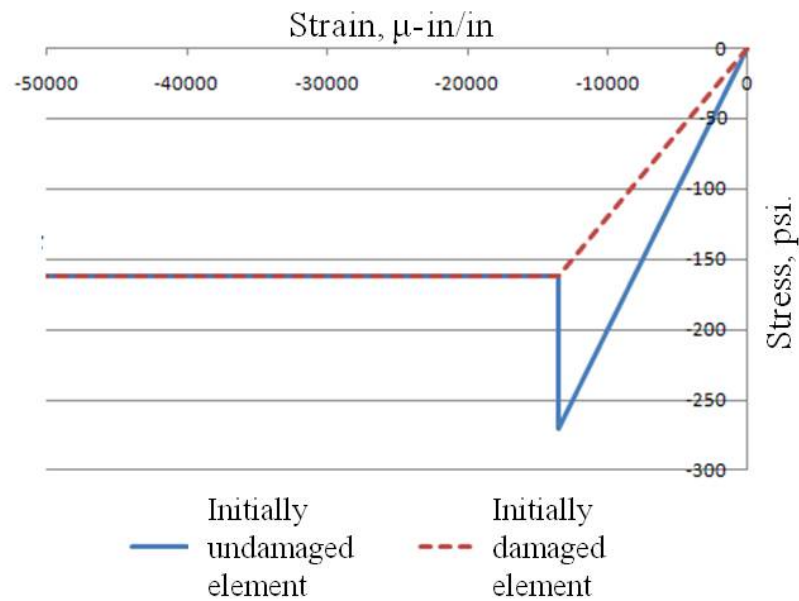


Figure 4.2: Solid element core crush constitutive model.

4.2 FEM with Spring Element Core

Ratcliffe and Jackson [46] as well as Castanié *et al.* [47] considered finite element models using simple spring elements to represent the honeycomb core in impact damage sandwich panels undergoing compressive loading. Ratcliffe and Jackson provided helpful insight into the spring element core model they had developed and encouraged its use in the early stage of the current research. The following section explains their model and analysis that was conducted to predict the response of PXX series coupons during CAI tests, as a demonstration.

4.2.1 Explanation of Model Components and Inputs

The finite element model developed by Ratcliffe and Jackson was for use with the commercial finite element code ABAQUS/Standard [73]. Using symmetry boundary conditions in the sandwich panel width (x -direction) and loading (y -) direction, only one quarter of a CAI coupon was modeled. Furthermore, only the front, damaged facesheet was included in the model. The nodes of the honeycomb core elements which should be attached to a rear facesheet are instead fixed from moving. It was assumed that the CAI failure of the sandwich panel does not depend on the response of the rear facesheet. Load is prescribed to the sandwich panel using a displacement boundary condition. The resulting force at each of the load end facesheet node points is recorded for determining load vs. displacement response as well as the failure load for each analysis. Also, a section of potting is included in the model to simulate an actual CAI coupon closely. In this region, no core elements are included; instead the facesheet node points are fixed in the out-of-plane z -direction. The spring element core model is shown in Fig. 4.3.

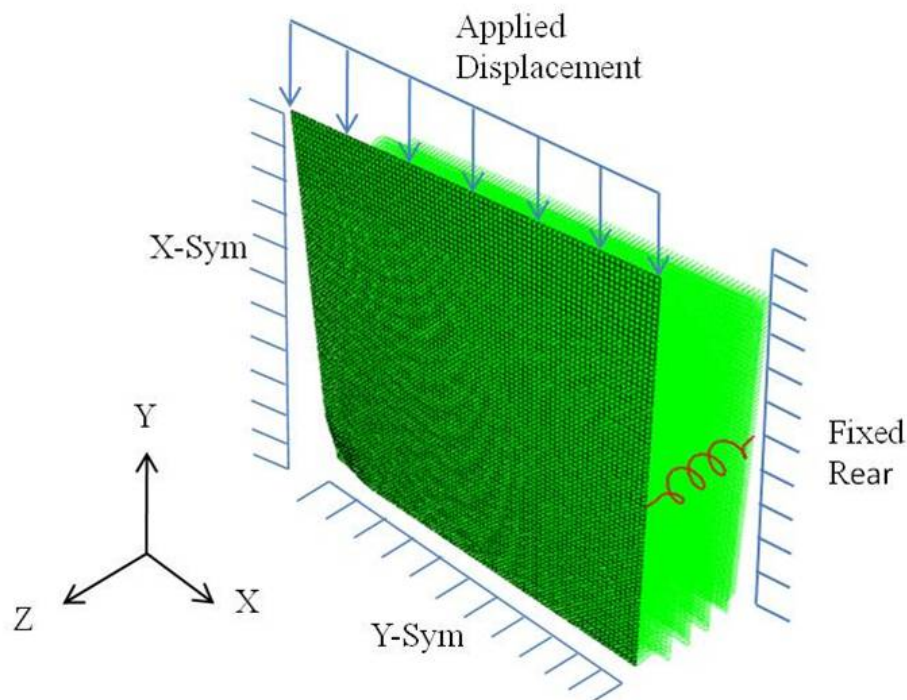


Figure 4.3: Spring element core sandwich panel CAI FEM with boundary conditions.

The facesheet is represented by a mesh of *S4* conventional shell elements with four nodes on each element. The mesh is generated in a rectangular grid fashion in a size of 80×80 elements for the 3 in. by 3 in. region which is one quarter of a PXX series sandwich panel. A mesh convergence study is not presented with the present work since this model was developed by Ratcliffe and Jackson [46]. The shell section is defined as a composite laminate of PXX series type construction, which was presented in Chapter 2 of the current work. The facesheet material's orthotropic engineering constants which define the constitutive response of each layer of the laminate were defined as in Table 4.1.

Table 4.1: Spring core element FEM analysis: engineering constants used for layers of PXX series sandwich panel facesheets.

E_1 (Msi)	E_2 (Msi)	E_3 (Msi)	ν_{12}	ν_{13}	ν_{23}	G_{12} (Msi)	G_{13} (Msi)	G_{23} (Msi)
3.50	3.50	4.00	0.140	0.350	0.350	0.538	0.435	0.435

The core is represented by a computationally efficient mesh of ABAQUS *SPRINGA* spring elements. The springs define the interaction between one node of the facesheet and one node fixed where the rear facesheet would be at a distance equal to the thickness of the honeycomb core, in this case, 1 in. The spring definition used is an idealized representation of the response of a Nomex honeycomb core during a flatwise compression test. *SPRINGA* elements can be defined with a non-linear response using force and displacement data. The force in each spring element per unit planar area (in the x-y plane) is equivalent to the z-direction average stress in the equivalent area of Nomex honeycomb core. For example, for the geometry and mesh described, each spring element represents 0.00141 in.^2 of the honeycomb core. The initial linear elastic modulus of the 3 lb. per cu. ft. density core used in the PXX panels is 20 ksi and the crush strength is 270 psi. The end of the linear elastic region of the spring response (corresponding to core crush failure) would then be stress times area equals 0.380 lbs. at 0.0135 in. of compression inducing displacement. The idealized core crush response used to define the spring elements is shown in Fig. 4.4.

Initial impact damage to the sandwich panel is included in the model only as a dimple

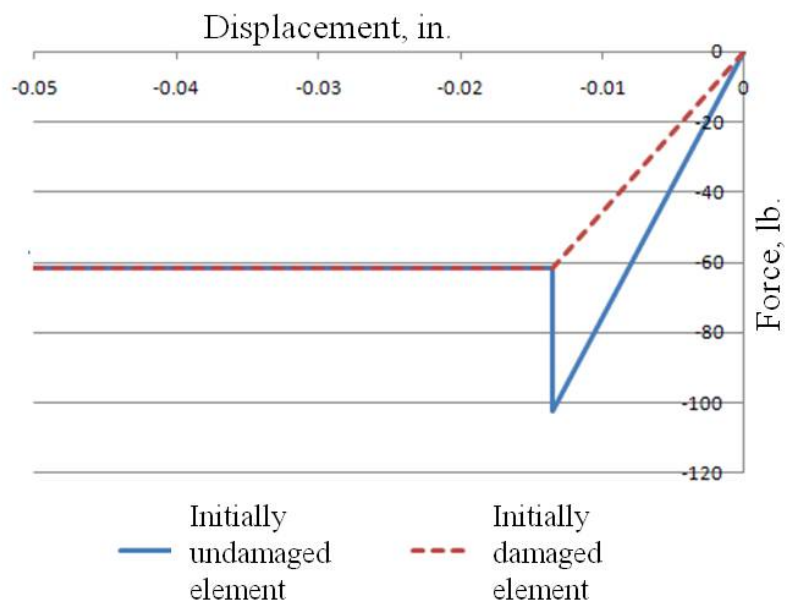


Figure 4.4: Spring element core crush constitutive model.

in the facesheet of the approximate shape of the residual dent corresponding to the PXX series coupon that is being modeled. The indentation is defined by the maximum dent depth and diameter of the appropriate panel, as reported in the experimental results of Chapter 2 of the current work. Panels P11, P04, P06, and P08 were chosen to demonstrate the capabilities of the spring element core model, which covers each of the energy levels that PXX series CAI coupons were impacted at (0.5, 1.0, 1.5, and 2.0 ft-lbs., respectively). Initial core damage from low-velocity impact can be included in the model by modification of the non-linear spring element response in a defined region of the model. The response of damaged core spring elements is shown in Fig. 4.4. In their model analysis, Ratcliffe and Jackson [46] found that inclusion of core damage resulted in a reduction in the predicted failure strength of the model. McQuigg et al [48] later found that inclusion of core damage resulted in a more gradual “rounded” failure which appeared in the force vs. displacement results for a given analysis. Since, the typical force vs. displacement results of the model (shown in Fig. 4.5) were more representative of experimental results, (shown in Chapter 2), core damage was not included in the analysis used to demonstrate the spring element core model. The effect

of including core damage to approximate the region of impact damaged core beneath the residual dent is shown in Fig. 4.5. Additionally, Ratcliffe and Jackson [46] used an tensile core spring element stiffness an order of magnitude greater than the compressive stiffness in order to control unrealistic out-of-plane deformation.

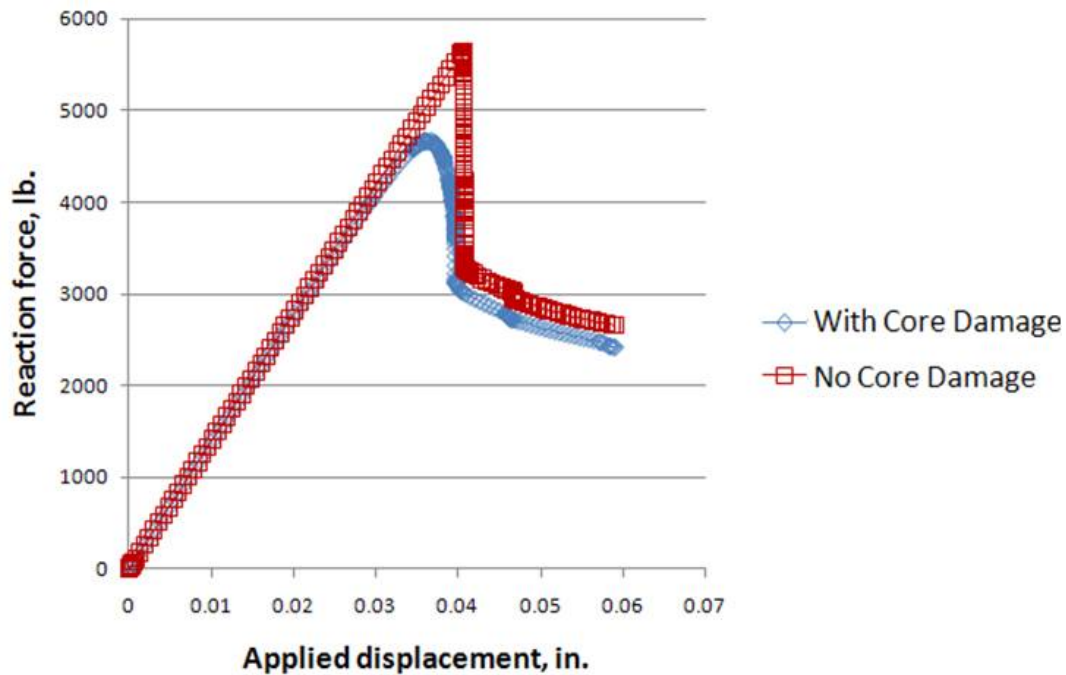


Figure 4.5: Spring element core FEM results: Typical reaction force vs. applied displacement with and without effect of including initial core damage.

4.2.2 CAI Analysis Results for Spring Element Core Model

Four test cases were used to demonstrate the capability of the spring core model. Analysis were performed on the CAI response of sandwich panels with geometry and materials corresponding to PXX series materials with damage corresponding to 0.5, 1.0, 1.5, and 2.0 ft-lb. impact energy as determined in measurements and observations made on the P11, P04, P06, and P08 coupons, respectively. Brief analysis results are presented here. The model correctly predicts indentation propagation failure growth in PXX series sandwich panels. Since no facesheet failure theory is included in the model, this is the only type of failure mode

the model is capable of predicting. The model results typically appear as shown in Fig. 4.6 after failure has occurred. The colored contours in Fig. 4.6 represent out-of-plane displacement. Maximum displacement is slightly more than a tenth of an inch, which is typical of experimental results.

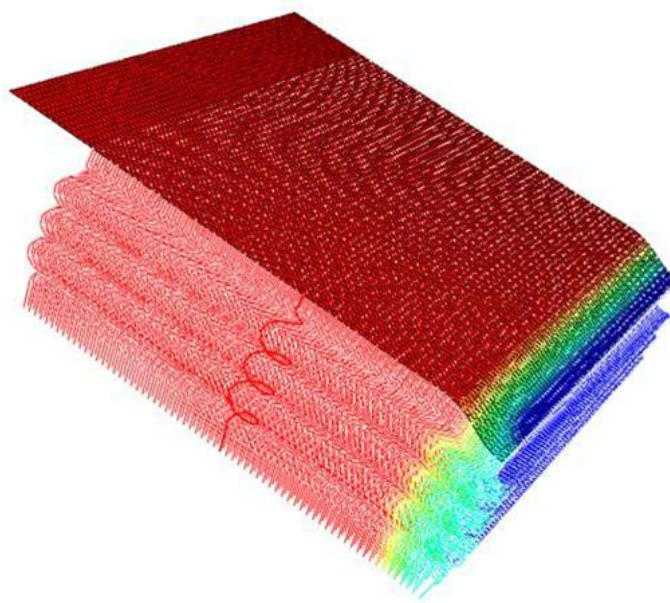


Figure 4.6: Sample spring element core FEM results: indentation propagation failure mode with out-of-plane displacement indicated by colored contours (blue indicates maximum negative displacement).

The force vs. displacement results for each test case are shown in Fig. 4.7. Failure is indicated by a sudden drop in reaction force, the same as in the experimental results. The rounded top of the force vs. displacement results which depicts a more gradual failure than what is expected from experimental results presents itself again for the test cases with the larger initial dents (P06 and P08). This trend suggests the model may provide decreasing accuracy in analysis of CAI coupons with increasing residual dent size.

Analysis results using the spring element core model for failure load, far field failure stress, and far field failure strain are shown in Table 4.2. Select experimental results are repeated from Chapter 2 of the present work for comparison. The analysis results collected using the spring element core model compare favorably to the experimental results. The

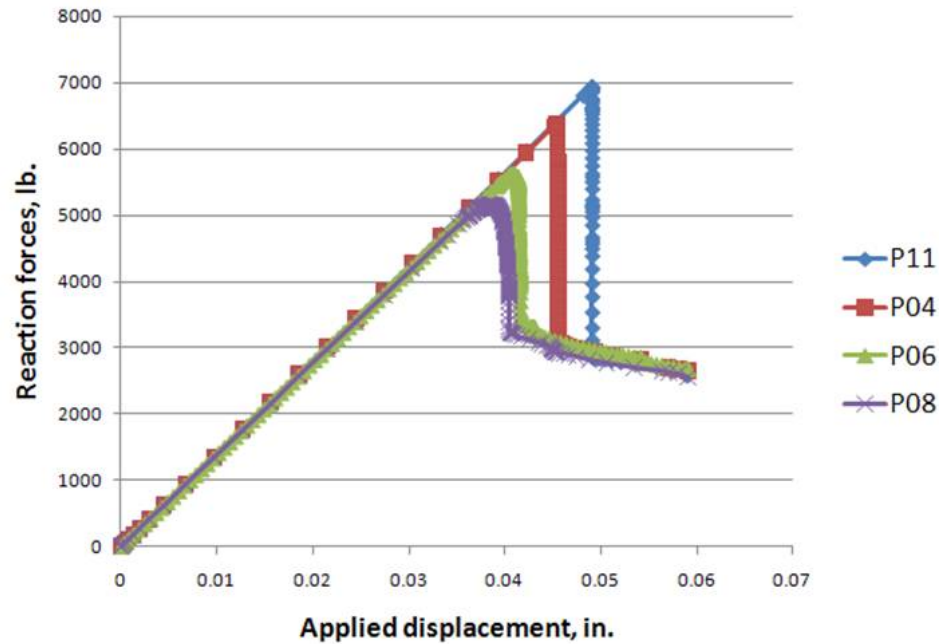


Figure 4.7: Sample spring element core FEM results: reaction force vs applied displacement for sample analyses on PXX series panels.

results compare best for the middle of the damage range considered and the analysis results are less accurate for the least damaged case (P11) and the most damaged case (P08). Damage not included in this model, such as initial core damage, initial facesheet damage, and facesheet failure during CAI response would likely reduce the failure load, stress, and strain predicted by this model. In all cases, this would reduce the accuracy of the predicted results when compared to the experimental findings. Also, for higher impact energy levels the resulting impact damage that is neglected would be more significant. This again suggests that this model would be less accurate for more highly damaged cases.

Table 4.2: Spring core element FEM results: failure metrics.

Panel	Dam. Energy (ft-lbs)	Dent Depth (in.)	Dent Diameter (in.)	FEM Fail Load (lb.)	FEM Fail Stress, (ksi)	Experimental Fail Stress (ksi)	FEM Fail Strain (μ -in/in)	Experimental Fail Strain (μ -in/in)
P11	0.5	0.005	0.4	6922	28.8	30.3	8169	8674
P04	1.0	0.014	0.6	6380	26.6	26.3	7574	7700
P06	1.5	0.042	0.8	5623	23.4	23.4	6819	6760
P08	2.0	0.061	1.0	5162	21.5	22.0	6407	6643

Through the experience of using the spring element core model for analysis of CAI of honeycomb core sandwich panels, the attractiveness of the model as a design tool was highlighted. The main benefits of the model are its simplicity, its ease of implementation and the computational efficiency of the model. A design engineer could very quickly use this type of model to assess a baseline reduced strength for a lightly damaged sandwich panel, with confidence, as long as the expected damage was minimal. The computational efficiency of the model is much better than an FEM with a continuum representation of the core using solid elements since the degrees of freedom in the spring element core model are much less.

4.3 FEM with Solid Orthotropic Element Core

The homogenization of the cellular honeycomb core structures into an equivalent solid continuum greatly simplifies the process of modeling composite sandwich panels while still giving the engineer an ability to model core response with high fidelity. Authors that have used this method for modeling of CAI response of the honeycomb core include Shyprykevich et al [12], Hwang and Lacy [49] [50], Czabaj et al [51], Xie and Vizzini [52] [53], and Schubel [54]. In the present study a FEM was developed using a solid element core. A simple version of this model was used to demonstrate the capability of previous models to capture benefits and challenges of using this type of model. A brief explanation of this model and a limited selection of results are discussed in the present section. A full discussion of this model with the implementation of new techniques for CAI modeling is presented in Chapter 5.

4.3.1 Explanation of Model Components and Inputs

A simple solid element core model was developed here for analysis of CAI sandwich panel coupons. The commercial FEA code ABAQUS/Standard [73] was used in this analysis. Symmetry was employed to reduce the degrees of freedom of the model. From symmetry in both the sandwich panel width (x -direction) and loading (y -direction) directions, only one quarter of a CAI coupon was necessary. Both facesheets were included in the model

and were free to displace as they would with the boundary conditions imposed on them in experimental CAI tests. This is possible because of the shear stiffness given to the sandwich panel by the honeycomb core which is included in the solid element core definition (i.e. it is not necessary to fix the rear facesheet). Although failure is expected in only the failed facesheet, the inclusion of both facesheets in the model allows for the comparison of the loading of both facesheets throughout the analysis. Also, the shear stiffness of the core may play a role in the indentation propagation failure mode. In either case, the fidelity of the model is improved. Load is prescribed to the model through the use of an applied displacement boundary condition and the resulting force is recorded at each node point at the appropriate side of the model. A section of potting is not included in this model, but the end nodes are fixed in the z -direction (out-of-plane direction) to simulate the effect of the applied potting and end clamping. Other effects of potting to the panel response are assumed negligible. The solid element core model is shown for reference in Fig. 4.8.

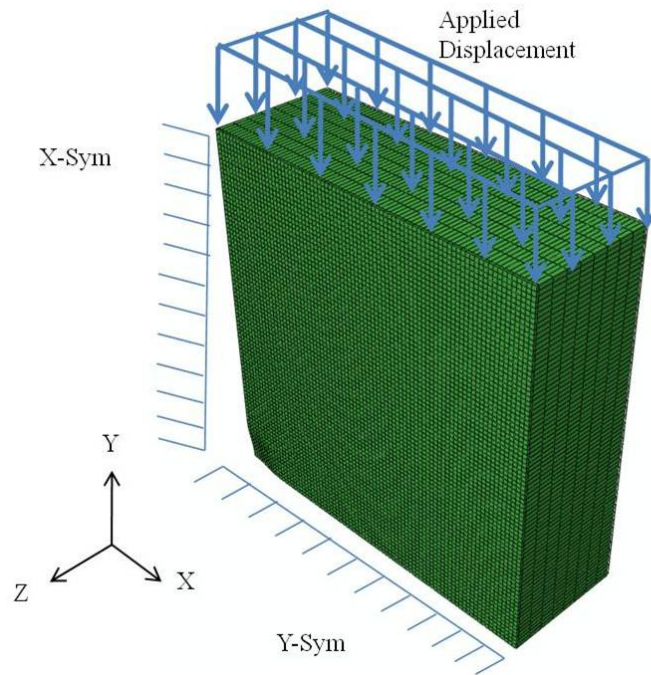


Figure 4.8: Solid element core sandwich panel CAI FEM with boundary conditions.

The continuum shell element, SC8R, was chosen to mesh the facesheets of the sand-

wich panel. This element is an 8-node quadrilateral general-purpose continuum shell, with reduced integration and finite membrane strain formulation. Hourglass control is provided though the appropriate stiffness is required. An $80 \times 80 \times 1$ element grid style mesh was used for each facesheet for the results obtained in the current chapter. The honeycomb core was modeled using the solid three dimensional element, C3D8R. This element is an 8-node linear brick featuring a reduced integration formulation. Hourglass control is used. The core region was modeled using an $80 \times 80 \times 8$ element grid mesh. The model used for the analysis discussed in the present chapter is similar to the new model which will be further developed in Chapter 5. More detail will be provided concerning the mesh pattern and a full mesh convergence study will be presented.

The attributes of the facesheets and core of the sandwich panel model are defined as follows. The facesheets are defined as a composite laminate with two layers of GFRP woven fiber material to simulate the material system used in the PXX series coupons presented in Chapter 2. The engineering constants which define each transversely isotropic layer of the facesheet laminate are in Table 4.2. The orthotropic material response of the continuum represented 3 lb. per cu. ft. Nomex honeycomb core was defined using the material constants in Table 4.3. The non-linear crush response in the z-direction was approximated by the idealized core crush response shown in Fig. 4.2. The linear elastic orthotropic response as well as the crushing failure of the core was implemented using the ABAQUS user subroutine, UMAT as follows. In the z-direction, the compression response of the core elements is linear elastic with a Young's modulus of 20 ksi until the compressive strength which is 270 psi for this material. Failure is determined to have occurred when the corresponding compressive strain, 0.0135 in/in has been reached. At this point the resultant stress from further deformation on the element is reduced to 60% of the stress at failure in all six components of the stress tensor for the material point. This value is chosen to reflect the volume averaged stress resultant from a damaged region of core as determined by experimental core crush response found in literature [46]. Also, the three extensional moduli and the three shear moduli are reduced to zero.

Table 4.3: Sample solid core element FEM analysis: engineering constants used for orthotropic continuum representation of Nomex honeycomb core.

E_1 (ksi)	E_2 (ksi)	E_3 (ksi)	ν_{12}	ν_{13}	ν_{23}	G_{12} (ksi)	G_{13} (ksi)	G_{23} (ksi)
0.001	0.001	20.0	0.500	0.000	0.000	0.05	5.80	2.90

Several types of impact damage can be included in the solid element core model. An initial indentation is included which is defined by the maximum dent depth, h_{max} , and dent diameter, d , found in experimental results on the corresponding coupon to be modeled. The contour of the dent is defined using Eq. (4.34) where x_n and y_n are the Cartesian coordinates of the node location in the damaged area on the surface of the dent. The impact damage dent is assumed perfectly circular in area.

$$z_{dent} = \frac{-h_{max}}{2} \left(1 + \cos \left(\frac{2\pi \sqrt{x_n^2 + y_n^2}}{d} \right) \right) \quad (4.34)$$

Other types of damage which can be included in the solid element core model include degradation of extensional and shear moduli which define the facesheet and core materials included in the model. The purpose of this reduction is to simulate the effects of various types of impact damage, as discussed in Chapter 1, and shown in Chapters 2 and 3. Types of impact damage to the core include buckling and tearing of the honeycomb cell walls. Facesheet damage resulting from low velocity impact can include interlaminar delaminations, intralaminar matrix cracks, and fiber cracks. The reduction of stiffness in the areas of damage is estimated from the severity of damage found by experimental observation. This will be discussed further in Chapter 5. Inclusion of this type of initial impact damage in the model is defined by damaged core area diameter, damaged core area maximum depth, damaged core area stiffness reduction, damaged facesheet area diameter and damaged facesheet area stiffness reduction. The solid core model performs well with inclusion of each of these types of damage. An example of the resulting force vs. applied displacement curve for a typical PXX series coupon where failure is determined by a sudden drop in resulting force is shown in Fig. 4.9.

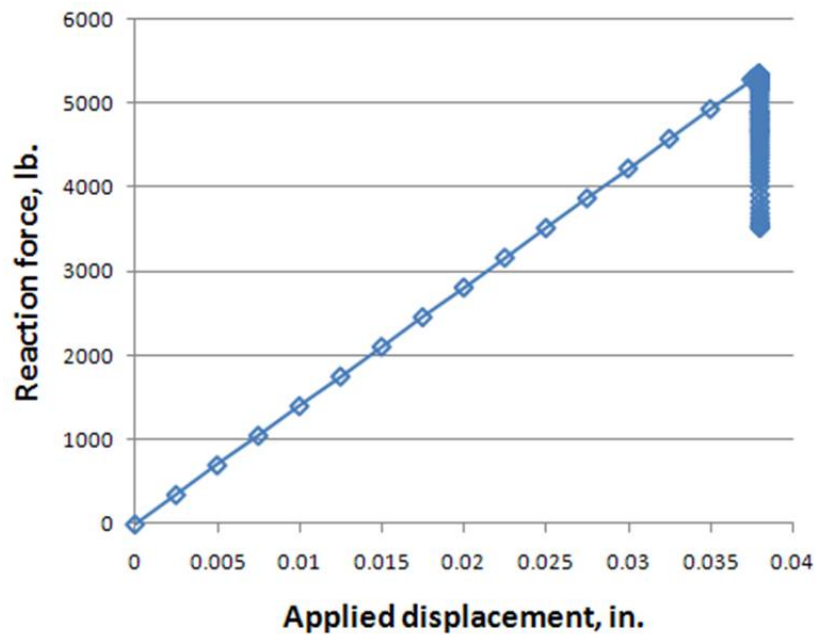


Figure 4.9: Sample solid element core FEM results: typical reaction force vs. applied displacement.

The elements where stiffness reduction of the damaged facesheets and damaged core was included are shown in Fig. 4.10 where the damaged elements are highlighted. For this particular case, the maximum damaged core depth was 0.25 in.; the damaged core area diameter was equal to the dent diameter, the damaged core stiffness reduction was 40%; the damaged facesheet area was 30% of the dent diameter and the stiffness reduction was 40%.

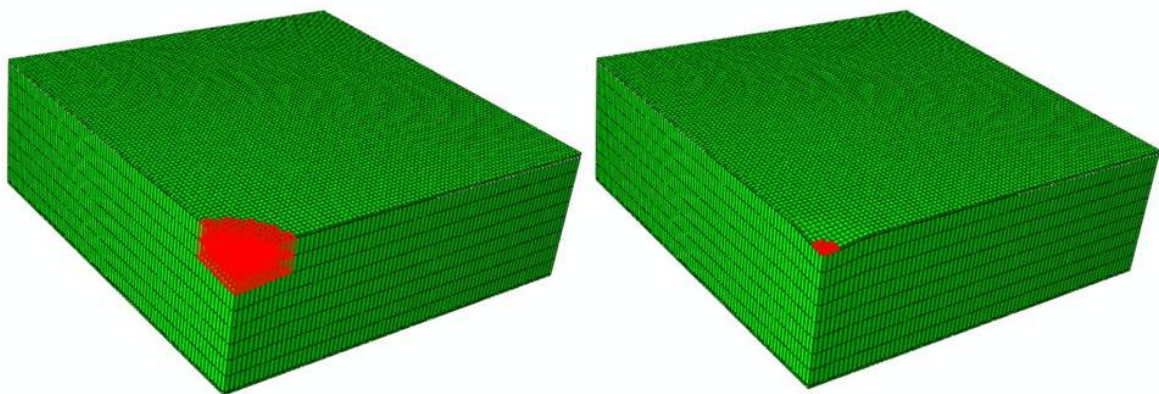


Figure 4.10: Damaged core elements (left) and damaged facesheet elements (right) in the solid element core model example.

4.3.2 CAI Analysis Results for Solid Element Core Model

PXX series coupons P11, P04, P06, and P08 were also used for a brief analysis to demonstrate the results of a solid element core CAI model. These coupons had damage corresponding to impacts at 0.5, 1.0, 1.5, and 1.5 ft-lbs., respectively, and appropriate inputs were made to the model based on the experimental results obtained in observation of these panels which was presented in Chapter 2. The inputs used in this analysis are shown in Table 4.4. Core damage was included in the FEM. The core damage input for damage area diameter is given as a percentage of the geometric dent diameter. The damaged core region depth and stiffness reduction (as a percentage of the pristine properties) was assumed constant for all panels. The analysis was done with and without facesheet damage. The topic of including facesheet damage in the model has not been well covered in the literature, although the technique of reducing constitutive properties of the facesheet materials in the simulated damage region has been used. A selection of facesheet damage was included for each panel to compare to the results found without using facesheet damage. A full study of the inclusion of facesheet damage in the new CAI model presented in the present work is found in Chapter 5, although the fidelity of the new model has been greatly increased from the continuum core model discussed in the present chapter.

Table 4.4: Sample solid core element FEM analyses: inputs used for demonstration.

Panel	Dam. Energy (ft-lbs)	Dent Depth (in.)	Dent Diameter (in.)	Core Damage Area Diameter	Core Damage Area Depth	Core Damage Stiffness Reduction	Facesheet Damage Area Diameter	Facesheet Damage Stiffness Reduction
P11	0.5	0.005	0.4	100%	0.25 in.	40%	0%	0%
P04	1.0	0.014	0.6	100%	0.25 in.	40%	30%	60%
P06	1.5	0.042	0.8	100%	0.25 in.	40%	30%	60%
P08	2.0	0.061	1.0	100%	0.25 in.	40%	60%	90%

The reaction force vs. applied displacement results for the first four analyses done without facesheet damage is shown in Fig. 4.11. The response of each CAI coupon is linear until failure, which is expected from experimental results. The full analysis results

are shown in Table 4.5, including failure load, failure stress, and failure strain as well as the expected experimental values. The results for analyses done without facesheet damage are given the designation, PXX, and the results with facesheet damage are given the designation PXXa. The analysis results presented here are only meant to be preliminary results used as a demonstration of previously used modeling techniques for this type of analyses.

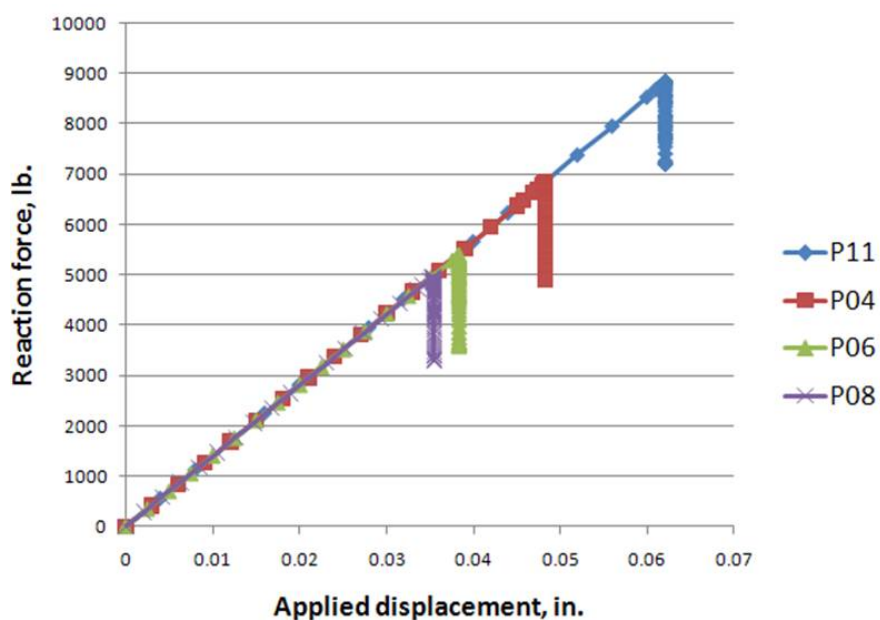


Figure 4.11: Sample solid element core FEM results: reaction force vs applied displacement, model did not include simulated impact damage in the facesheets.

Table 4.5: Sample solid element core FEM results: failure metrics.

Panel	Dam. Energy (ft-lbs)	FEM Fail Load (lb.)	FEM Fail Stress, (ksi)	Experimental Fail Stress (ksi)	FEM Fail Strain (μ -in/in)	Experimental Fail Strain (μ -in/in)
P11	0.5	4420	36.8	30.3	10351	8674
P04	1.0	3416	28.5	26.3	8039	7700
P04a	1.0	3409	28.4	26.3	8023	7700
P06	1.5	2692	22.4	23.4	6374	6760
P06a	1.5	2686	22.4	23.4	6361	6760
P08	2.0	2482	20.7	22.0	5900	6643
P08a	2.0	2730	22.8	22.0	6516	6643

A comparison of the modeling results with and without impact damage modeled in the facesheets is shown in Fig. 4.12. Facesheet damage mostly had only a small effect on the prediction made by the model, except for coupon P08, the panel with the most severe reductions of facesheet properties in the damaged region. The predicted failure stress of the panel actually increased for this case. This suggests that the lack of stiffness in the damaged facesheet area actually delays the onset of indentation propagation, which is an interesting result. It does make physical sense though, as during the initial compressive loading of the panel, the initially indented area would displace compressively in-plane rather out-of-plane into the core because the severe extensional stiffness reduction of the facesheet puts the facesheet stiffness on the same order of magnitude as the core damage stiffness. The predicted failure points for each of the panels is not as accurate when compared to experimental results as the spring element core model presented earlier. However, the fidelity of the model has been increased. It is expected that if the model were studied fully, the results would improve. This work is done for the complete new model introduced in Chapter 5 which takes advantage of new FEM techniques for this type of analysis.

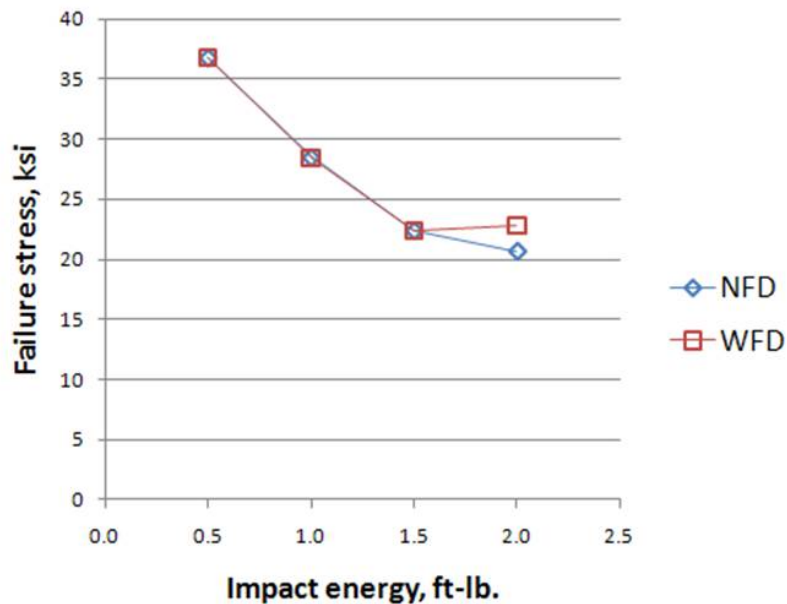


Figure 4.12: Sample solid element core FEM results: failure stress vs. impact energy with (WFD) and without simulated facesheet impact damage (NFD).

4.4 Conclusions from CAI Analysis Using Existing Models

In the present chapter, development of the proposed model began with a more in depth consideration of the existing CAI models than was given in the literature review presented in Chapter 1. First, the theory was presented which is relevant to the finite element modeling techniques used to simulate the facesheets and core of the sandwich panels which are the subject of the current research. This theory included an explanation of classical laminate theory, as well as the development of the specific shell theory, Koiter-Sanders, implemented in ABAQUS shell elements, which are used to simulate the facesheets in the proposed model. The theory presented also included simple techniques for homogenization of the core based on the structural geometry. In the present research, orthotropic material properties will be used to represent a continuum response for the core using solid three-dimensional finite elements. The formulation of these elements by total potential energy was shown. An explanation of the idealization used to represent the core crush response of these elements was also given.

In the latter part of the present chapter, two examples of the existing FEM for analysis of the CAI response of thin facesheet honeycomb core sandwich panels were shown. The examples included a spring element core model, as first presented by Ratcliffe and Jackson [46], and a solid element core model, which is similar to examples given in the literature review in Chapter 1 [12] [52], but is able to effectively capture the full indentation propagation failure. The types of elements used, the initial impact damage modeled, and the analysis cases performed were explained for each of these models. The results of several analyses performed were compared to experimental results from CAI tests of PXX series materials, first reported in Chapter 2. The failure measures, such as stress and strain, compared well for each model. However, it was shown how the spring element model seemed to misrepresent the failure mode for the higher levels of damage and it is presumed that the model would be ineffective for even higher levels of damage, such as those seen in 3PCF-XX and 6PCF-XX series material tests, shown in Chapter 3. A full development of a solid element core model

with a progressive failure analysis for facesheet damage and increased impact damage fidelity will be given treatment in Chapter 5, next.

Chapter 5

Development of a New Model for CAI Analysis

In the previous chapter, development of a new finite element model (FEM) for analysis of CAI failure in honeycomb core sandwich panels began with an overview of the related theory. Later in that chapter, a solid element core FEM was briefly demonstrated as representation of the current models. A new FEM for CAI analysis with a solid element, continuum representation of a honeycomb core using homogenized properties will be fully developed in the present chapter. The new model will contain an implementation of a progressive failure analysis (PFA) for composite laminates in the facesheet region of the sandwich panel model. This inclusion represents an important contribution to the development of analysis of the CAI response of thin facesheet honeycomb core sandwich panels. The need for this type of analysis was recognized by several authors, including Shyprykevich *et al.* [12], Czabaj *et al.* [51], and Schubel *et al.* [54]. This capability allows the model to predict CAI failure by multiple modes and gives the engineer the ability to understand the contribution of nominal core density to failure mode. The need for this capability was shown in the current research in Chapter 3.

In addition to the inclusion of composite laminate PFA for crack or damage propagation in the facesheet of the sandwich panel, a second major contribution to CAI analysis

will be discussed. Impact damage will be defined in the present model as a high fidelity representation based on measurements and observations taken from a detailed first-hand experimental test survey, as described in Chapters 2 and 3 of the current research. The level of detail for the depiction of impact damage in the new CAI model is higher than the current models. It will be demonstrated in the present chapter that this level of damage depiction can be used to develop a much improved level of understanding about what impact damage traits contribute significantly to CAI failure. First, however, development of the pertinent theory will continue with the discussion of Multicontinuum Theory (MCT) and MCT failure theory. Once the discussion of theory is complete and the new model has been fully described, the chapter will conclude with a mesh convergence study, as well as a sensitivity study on key FEM parameters.

5.1 Progressive Failure Analysis Theory

ABAQUS includes an implementation of PFA developed by Lapczyk and Hurtado [72] which includes the Hashin failure criterion [71] for crack initiation and then evaluates damage propagation by considering energy release rates associated with compressive and tensile fiber and matrix fracture. The challenge with using the ABAQUS built-in PFA is establishing the appropriate energy release rates for a given facesheet material. In addition, in the current implementation significant convergence problems exist unless damage stabilization is used to slow damage propagation [89].

An alternative is available for use with ABAQUS in the form of commercially available software, Helius:MCT [92], developed by Firehole Composites, Inc. Helius:MCT is unique in that it makes use of multi-continuum theory, which will be discussed in the present chapter as developed by Mayes and Hansen [75]. The failure theory used considers the three-dimensional state of stress of the element in question and only requires material strength values for the facesheet constituent materials, which makes it considerably easier to implement than ABAQUS' own PFA. Practical use of the commercial version Helius:MCT is easily learned

through documentation consisting of a user's manual, examples, and tutorials.

5.1.1 Multicontinuum Theory

In general, many laminate theories, including the theory implemented in ABAQUS, used to model the linear elastic response of sandwich panel facesheets are considered macromechanical. They homogenize the material properties of the laminate instead of considering the material properties of the constituent materials (i.e. the fibers and the matrix). In the present work, the failure initiation and damage propagation in the composite laminates facesheet will be predicted using a more detailed approach, which will require the fiber and matrix average stress states. In order to facilitate this, a multi-continuum theory (MCT) is used to describe the stress state of the constituent materials in terms of the stress state of the laminate.

The present MCT theory, as summarized by Mayes and Hansen [75], includes the following assumptions. The behavior of the fibers is linear elastic, while the matrix behavior is non-linear elastic. A perfect bonding exists between the fibers and matrix. Stress concentrations which occur at fiber boundaries are only included as a contribution to the volume averaged stress state. Fiber distribution is idealized as uniform and hexagonal and the effect of this distribution on composite strength and stiffness was accounted for by analysis using a finite element model of the microscopic geometry. Finally, a piecewise stress-strain will result from implementation of MCT failure theory because one constituent can fail while leaving the other intact.

A volume average of a representative region of a continuum material is taken to characterize the stress tensor for a given material point as given by:

$$\sigma = \frac{1}{Vol} \int \sigma(x) dVol \quad (5.1)$$

The concept of multicontinuum extends this idea to the constituent level. That is,

within a continuum region there are coexisting materials (i.e. fiber and matrix) whose individual average stress state can also be found by the following volume integrals:

$$\sigma_f = \frac{1}{Vol_f} \int \sigma(x) dVol_f \quad (5.2)$$

$$\sigma_m = \frac{1}{Vol_m} \int \sigma(x) dVol_m \quad (5.3)$$

This leads to the following relationship:

$$\sigma = \phi_f \sigma_f + \phi_m \sigma_m \quad (5.4)$$

Where ϕ_f and ϕ_m are the fiber and matrix volume fractions, respectively. Likewise, the relationship between composite and constituent volume averaged strain state is:

$$\epsilon = \phi_f \epsilon_f + \phi_m \epsilon_m \quad (5.5)$$

For the case of woven fiber composite laminates, the volume averaged stress states are sequentially decomposed into the constituent average stress state of the warp and fill fiber tows and matrix. First, the composite average stress and strain states are mapped into warp tow stress and strain states, and stress and strain states for a super constituent consisting of the fill tow material and the matrix pockets in the woven material as:

$$\sigma = \phi_{fill/mat} \sigma_{fill/mat} + \phi_{warp} \sigma_{warp} \quad (5.6)$$

$$\epsilon = \phi_{fill/mat} \epsilon_{fill/mat} + \phi_{warp} \epsilon_{warp} \quad (5.7)$$

The fill tow / matrix super constituent volume averaged stress and strain state is then

reduced to fill tow and matrix pocket volume averaged stress and strain states as:

$$\sigma_{fill/mat} = \phi_{fill}\sigma_{fill} + \phi_{mat}\sigma_{mat} \quad (5.8)$$

$$\epsilon_{fill/mat} = \phi_{fill}\epsilon_{fill} + \phi_{mat}\epsilon_{mat} \quad (5.9)$$

The fiber and matrix volume average stress and strain states for the warp and fill tows can then be calculated using Eqs. 5.4 and 5.5, respectively.

The constitutive relations between volume average stress and strain states for the composite, and then fiber and matrix constituents are given as:

$$\begin{aligned} \{\sigma\} &= [C]\{\epsilon\} \\ \{\sigma_f\} &= [C_f]\{\epsilon_f\} \\ \{\sigma_m\} &= [C_m]\{\epsilon_m\} \end{aligned} \quad (5.10)$$

Where $[C]$ is the 6x6 constitutive matrix. Since MCT failure theory is piecewise continuous, the constitutive equation used must be assumed to be linearized about the current stress state for when some form of failure has occurred. Substitution of Eqs. 5.10 into Eq. 5.4 results in:

$$[C]\{\epsilon\} = \phi_f [C_f]\{\epsilon_f\} + \phi_m [C_m]\{\epsilon_m\} \quad (5.11)$$

Further substitution results in:

$$[C](\phi_f \{\epsilon_f\} + \phi_m \{\epsilon_m\}) = \phi_f [C_f]\{\epsilon_f\} + \phi_m [C_m]\{\epsilon_m\} \quad (5.12)$$

Which is then solved for $\{\epsilon_f\}$ as:

$$\{\epsilon_f\} = \frac{\phi_m}{\phi_f} ([C] - [C_f])^{-1} ([C_m] - [C])\{\epsilon_m\} \quad (5.13)$$

Substitution of Eq. 5.13 into Eq. 5.5 yields a matrix average strain state in terms of the composite average strain state as:

$$\{\epsilon_m\} = \frac{1}{\phi_m} ([C_m] - [C_f])^{-1} ([C] - [C_f]) \{\epsilon\} \quad (5.14)$$

The fiber average strain state can then be computed as:

$$\{\epsilon_f\} = \frac{1}{\phi_f} (\{\epsilon\} - \phi_m \{\epsilon_m\}) \quad (5.15)$$

The matrix and fiber average stress states can then be found through the appropriate linearized constitutive relations.

For woven materials, the first decomposition of the composite average strain state into the fill tow / matrix pocket super constituent strain state and the warp tow constituent strain state can be written as:

$$\{\epsilon_{warp}\} = \frac{1}{\phi_{warp}} ([C_{warp}] - [C_{fill/mat}])^{-1} ([C] - [C_{fill/mat}]) \{\epsilon\} \quad (5.16)$$

$$\{\epsilon_{fill/mat}\} = \frac{1}{\phi_{fill/mat}} (\{\epsilon\} - \phi_{warp} \{\epsilon_{warp}\}) \quad (5.17)$$

The second decomposition can then be written as:

$$\{\epsilon_{mat}\} = \frac{1}{\phi_{mat}} ([C_{mat}] - [C_{fill}])^{-1} ([C_{fill/mat}] - [C_{fill}]) \{\epsilon_{fill/mat}\} \quad (5.18)$$

$$\{\epsilon_{fill}\} = \frac{1}{\phi_{fill}} (\{\epsilon_{fill/mat}\} - \phi_{mat} \{\epsilon_{mat}\}) \quad (5.19)$$

Here, ϕ_{fill} and ϕ_{mat} are the volume fractions of the fill tow and matrix pockets with respect to the fill tow / matrix pockets super constituent, rather than the composite. The volume average strain state in the warp and fill tows of their respective fiber and matrix

constituents can then be calculated using a third decomposition, as:

$$\{\epsilon_m\}^{fill} = \frac{1}{\phi_m} ([C_m] - [C_f])^{-1} ([C_{fill}] - [C_f]) \{\epsilon_{fill}\} \quad (5.20)$$

$$\{\epsilon_f\}^{fill} = \frac{1}{\phi_f} (\{\epsilon_{fill}\} - \phi_m \{\epsilon_m\}) \quad (5.21)$$

$$\{\epsilon_m\}^{warp} = \frac{1}{\phi_m} ([C_m] - [C_f])^{-1} ([C_{warp}] - [C_f]) \{\epsilon_{warp}\} \quad (5.22)$$

$$\{\epsilon_f\}^{warp} = \frac{1}{\phi_f} (\{\epsilon_{warp}\} - \phi_m \{\epsilon_m\}) \quad (5.23)$$

The corresponding volume averaged stress state can then be calculated using the appropriate linearized constitutive relations.

$$\{\sigma_f\}^{fill} = [C_f]^{fill} \{\epsilon_f\}^{fill} \quad (5.24)$$

$$\{\sigma_m\}^{fill} = [C_m]^{fill} \{\epsilon_m\}^{fill} \quad (5.25)$$

$$\{\sigma_f\}^{warp} = [C_f]^{warp} \{\epsilon_f\}^{warp} \quad (5.26)$$

$$\{\sigma_m\}^{warp} = [C_m]^{warp} \{\epsilon_m\}^{warp} \quad (5.27)$$

5.1.2 MCT Failure Theory

The failure theory used in Helius:MCT is a form of the multicontinuum failure theory first developed by Garnich and Hansen [74] and later revisited by Mayes and Hansen [75]. The MCT failure criterion retains the quadratic form of the Hashin failure criterion [71]. The stress based criterion makes use of four of the five transversely isotropic stress invariants

given as:

$$\begin{aligned}
 I_1 &= \sigma_{11} \\
 I_2 &= \sigma_{22} + \sigma_{33} \\
 I_3 &= \sigma_{22}^2 + \sigma_{33}^2 + 2\sigma_{23}^2 \\
 I_4 &= \sigma_{12}^2 + \sigma_{13}^2 \\
 I_5 &= \sigma_{22}\sigma_{12}^2 + \sigma_{33}\sigma_{13}^2 + 2\sigma_{12}\sigma_{13}\sigma_{23}
 \end{aligned} \tag{5.28}$$

The five transversely isotropic stress invariants are a variant of the usual isotropic invariants of the stress tensor. The usual stress invariants are well-known as the coefficients of the cubic equation found from expansion of Eq. 5.29, which is used when determining the principle stresses and planes for a given stress tensor. It can be noted that the usual stress invariants are valid for all rotations of a given coordinate system. For a transversely isotropic system, only rotations about the 1-axis are considered. It was noted by Hashin [71] that from this premise, it is relatively easy to see that I_1 and I_4 are invariant for rotations about the 1-axis. I_2 , I_3 and I_5 can then be shown to be invariant from comparisons of I_1 and I_4 to the three usual isotropic stress invariants.

$$\begin{vmatrix}
 \sigma_{11} - \lambda & \sigma_{12} & \sigma_{13} \\
 \sigma_{12} & \sigma_{22} - \lambda & \sigma_{23} \\
 \sigma_{13} & \sigma_{23} & \sigma_{33} - \lambda
 \end{vmatrix} = 0 \tag{5.29}$$

The general form of the MCT failure criterion is a simplification of Hashin's criterion based on the following assumptions. Stress interaction terms are not used since experimentally determining their coefficients is very difficult and ignoring them results in only small errors. Linear terms are also not used since they arise due to internal self-equilibrating

stresses. The resulting general form is:

$$a_1 I_1^2 + a_2 I_2^2 + a_3 I_3 + a_4 I_4 = 1 \quad (5.30)$$

The fifth transversely isotropic invariant is simply not used because it is cubic in stress, and the failure criterion is meant to have a quadratic form.

The principal attractiveness of MCT is that it determines fiber and matrix failure by using the fiber and matrix average stress states as opposed to the composite average stress states. Therefore, the general form of the MCT failure criterion is further revised into a matrix failure criterion and a fiber failure criterion for unidirectional composites. For woven composites the fiber failure criteria remains the same, but is used independently for the warp and fill tows, while a revised criterion is used for matrix failure. As set forth by Schumacher and Key [76], the fiber failure criterion is:

$$\pm a_1^f (I_1^f)^2 + a_4^f I_4^f = 1 \quad (5.31)$$

Where the coefficients of the criterion are given with respect to the fiber tensile, compressive, and shear strengths as:

$$\pm a_1^f = \frac{1}{(\pm \sigma_{T/C}^f)^2} \quad (5.32)$$

$$a_4^f = \frac{1}{(\sigma_{S12}^f)^2} \quad (5.33)$$

The matrix criterion for the matrix constituent in both unidirectional and woven composites is given as:

$$\pm a_2^m (I_1^m)^2 + a_3^m I_3^m + a_4^m I_4^m = 1 \quad (5.34)$$

Where the coefficients for the unidirectional composite case are given as:

$$+ a_2^m = \frac{1}{((+\sigma_T^m) + (+\sigma_{T2}^m))^2} \left(1 - \frac{(+\sigma_T^m)^2 + (+\sigma_{T2}^m)^2}{2(\sigma_{S23}^m)^2} \right) \quad (5.35)$$

$$- a_2^m = \frac{1}{((-\sigma_C^m) + (-\sigma_{C2}^m))^2} \left(1 - \frac{(-\sigma_C^m)^2 + (-\sigma_{C2}^m)^2}{2(\sigma_{S23}^m)^2} \right) \quad (5.36)$$

$$a_3^m = \frac{1}{2(\sigma_{S23}^m)^2} \quad (5.37)$$

$$a_4^m = \frac{1}{(\sigma_{S12}^m)^2} \quad (5.38)$$

The coefficients for the woven composite case are given as:

$$\pm a_2^m = \frac{1}{(+\sigma_T^m)} \left(1 - \frac{(\pm\sigma_{T/C}^m)^2}{2(\sigma_{S23}^m)^2} \right) \quad (5.39)$$

$$a_3^m = \frac{1}{2(\sigma_{S23}^m)^2} \quad (5.40)$$

$$a_4^m = \frac{1}{(\sigma_{S11}^m)^2} \quad (5.41)$$

In these equations, the subscripts indicated which material strength is represented by σ : T indicates tensile, C indicates a compressive strength, $S12$ indicates in-plane shear, $S23$ indicates transverse shear, and $T2$ and $C2$ indicate the normal stress corresponding to transverse matrix failure once the matrix has already failed, previously by in-plane failure, for tensile and compressive forces, respectively.

5.1.3 Material States for Woven Composite Laminates During PFA

As a result of MCT failure theory, a composite lamina can be simulated in multiple states of failure since individual lamina constituents are predicted to fail separately. Based on the three level MCT decomposition of the average stress state of a woven fiber lamina into the average stress state of its constituent materials, there are five total constituents to consider. These constituents are the fill tow fibers, the fill tow matrix, the warp tow fibers, the warp

tow matrix, and the matrix pockets in between the woven tows. Each of these constituents can be modeled independently with failed or intact status for a given representative volume element (RVE), although no explicit failure criteria exists for matrix pockets between tows. The matrix pockets are assumed failed if another matrix constituent (in the warp or fill tows) is determined to have failed. The Helius Theory Manual [93] defines nine unique damaged average stress states that take into account combinations of the state of these constituents that are used to describe a (RVE) within a layer for a given sandwich panel facesheet. These states are as follows (matrix pockets between tows are assumed to have failed for states 4-9):

1. All constituents intact
2. Failed fill tow matrix constituent
3. Failed warp tow matrix constituent
4. Failed fill and warp tow matrix constituents
5. Failed fill tow fiber and matrix constituents
6. Failed warp tow fiber and matrix constituents
7. Failed fill tow fiber and matrix constituents, and failed warp tow matrix constituent
8. Failed warp tow fiber and matrix constituents, and failed fill tow matrix constituent
9. Failed warp and fill tow fiber and matrix constituents.

5.2 Introduction to Proposed FEM for CAI Analysis

A new finite element model (FEM) for the prediction of CAI failure in honeycomb core sandwich panel coupons has been developed in the current research. The current model uses some aspects of the solid element core FEM developed by several other authors including Shyprykevich *et al.* [12], Hwang and Lacy [49] [50], Czabaj *et al.* [51], Xie and Vizzini

[52] [53], and Schubel [54]. A simple version of this model which included only previously developed aspects was discussed briefly in Chapter 4. The major contributions of the current research to the state-of-the-art of models for CAI analysis of honeycomb core sandwich panels are covered in the present chapter. This discussion began with an overview of Multicontinuum Theory (MCT) and the associated MCT failure theory for composite laminate failure analysis.

MCT failure theory is used in the current research in an implementation of progressive failure theory (PFA) in the facesheets of the FEM. Firehole Composites implemented MCT failure theory in their commercially available software, Helius:MCT [92]. A custom version of this software was obtained for the present research which would allow for its use in a FEM for CAI analysis. This custom version was compatible with the ABAQUS user subroutine, UMAT, used to implement the core model. The result of the inclusion of Helius:MCT in the current model is the ability to predict the onset of multiple failure modes, including the previously modeled dimple propagation failure mode (also seen in test coupons discussed in Chapters 2 and 3), and also the facesheet crack propagation failure mode (discussed in Chapter 3). The inclusion of a PFA for implementation of multiple competing failure modes in a single model for CAI analysis is the first major contribution for the analysis part of the current research.

A second major development of the current research is the inclusion of increased impact damage detail. In Chapters 2 and 3, a significant level of data was presented from evaluation of damage formation and CAI failure in three honeycomb core sandwich panel material systems. A total of 32 test coupons were compressively loaded to failure with impact damage present. Both destructive and non-destructive evaluation (NDE) techniques were used to describe the impact damage in these test coupons. The availability of this data led to its inclusion in the new model, which is another major unique contribution of the current research. A description of how the impact damage data was included will be discussed in this section. First, the geometry and boundary conditions of the new model will be introduced. Following this introduction, the implementation of the non-linear core model through the ABAQUS user subroutine, UMAT, will also be briefly discussed.

5.2.1 Geometry, Boundary Conditions and Finite Elements

A FEM was developed for analysis of the CAI response of honeycomb core sandwich panel coupons using the commercial FEA code ABAQUS/Standard. The FEM includes representations of both front (damaged) and rear facesheets, as well as a continuum solid representation of the homogenized, honeycomb core. It is only necessary to model one quarter of the sandwich panel coupon during an analysis due to symmetry of the coupon, the impact damage present in the front facesheet, and the expected failure modes. A global coordinate system will be established in the following manner. If the major two dimensions (i.e. length and width) of the sandwich panel plate are located in the $x - y$ plane of a Cartesian coordinate system, where the loading direction is parallel to the y -axis, only the top right quarter of the sandwich panel coupon is modeled. This is the region located in the Cartesian quadrant where points are defined by positive x and positive y coordinates. The length of the model in the y -direction is then $l/2$ where l is the length of the coupon modeled. Likewise, the width in the x -direction modeled is $w/2$, and the thickness is $(t_c + 2t_f)$ where w is the coupon width, t_c is the thickness of the core, and t_f is the facesheet thickness. The area of the model used to simulate impact damage will thus be located on the front facesheet on the z -axis of the global coordinate system, as highlighted in Fig. 5.1.

The following boundary conditions were used in the current model. It is required that the element node points located along the line $x = 0$ be fixed in the x -direction for symmetry in this direction. For y -direction symmetry, nodes along the line $y = 0$ are fixed from displacement in the y -direction. Rotational boundary conditions are not necessary for any node points since the elements used are defined using only displacement degrees of freedom. A third initial boundary condition was applied at the facesheet nodes located at $(x, y = l/2, z)$, to simulate the effects of the coupon clamp and potting used in experimental conditions. At the facesheet nodes only at these locations, the nodes were restricted from displacement in the out-of-plane, z -direction. During the analysis step, loading was applied to the nodes located at the coordinates $(x, y = l/2, z)$ using an applied displacement boundary condition to simulate the displacement controlled loading used in CAI testing described in

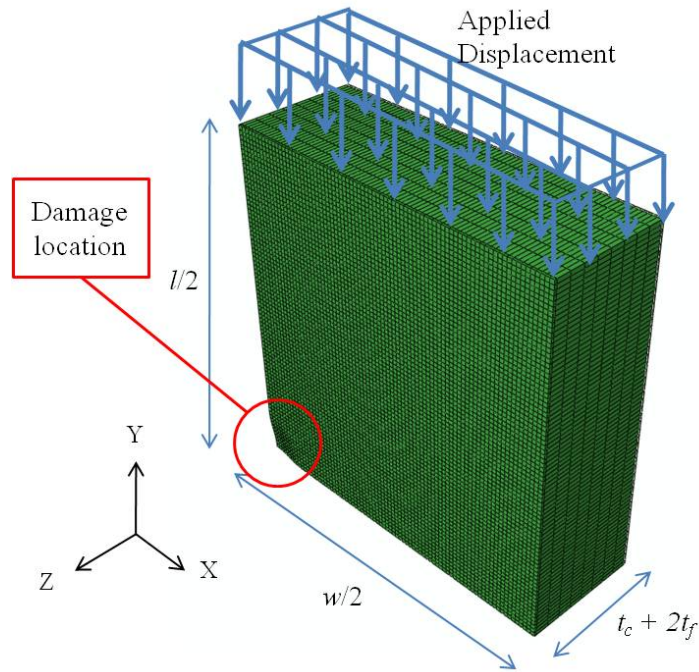


Figure 5.1: New CAI model: FEM Geometry.

Chapters 2 and 3. The boundary conditions of the new CAI model are shown in Fig. 5.2.

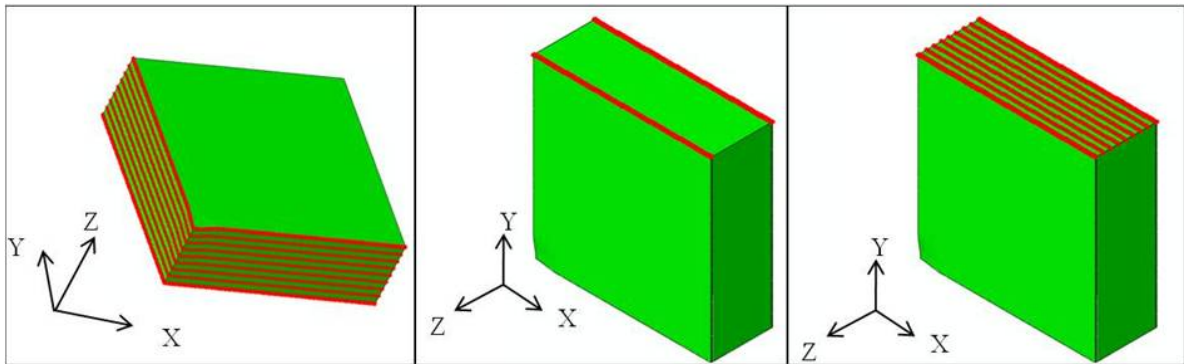


Figure 5.2: New CAI model: FEM node points (highlighted in red) for boundary conditions of symmetry (left), simulated potting (center), and applied displacement (right).

Shell elements and solid brick elements were used to model the facesheets and the core of the sandwich panel, respectively. The ABAQUS continuum shell element, *SC8R*, was used in the finite element representation of the sandwich panel facesheets. The main benefit of continuum shell elements relative to conventional shell elements is the explicit consideration

of the shell thickness. In the continuum shell formulation, only displacement degrees of freedom are considered, as opposed to displacement and rotation degrees of freedom, as used in conventional shell elements. The *SC8R* elements are a reduced element formulation that increases the computational efficiency, while making marginal accuracy sacrifices, if any, due to the location of the Gauss integration points. The constitutive response of the element shell section is defined as in classical laminate theory (CLT), which was discussed in Chapter 4. Each ply layer of the composite shell section was defined using orthotropic engineering constants found from various experimentally derived material data available in the literature. The exact material constants used in each analysis are discussed in Chapter 6.

Special consideration is given to the front, impact damaged facesheet in the form of the progressive failure analysis, accomplished through the Helius:MCT software discussed previously. The use of Helius:MCT does not change the element formulation or the constitutive model. It simply requires the explicit specification of various material and element properties, some of which are normally automatically calculated by the ABAQUS/Standard solver. The use of Helius:MCT requires a special material file written using the Firehole Composites auxiliary software, “Helius Material Manager.” The Material Manager determines the *in situ* properties of the lamina’s fiber and matrix constituents based on the material constants provided, usually from experimentally determined sources for a given material. Through the course of the analysis, Helius:MCT uses these *in situ* constituent material properties to determine the fiber average stress state and matrix average stress state for a given material point based on the average stress state of the lamina determined by the ABAQUS/Standard finite element solver. The constituent material properties will thus also be given in Chapter 6. Normally, in the course of pre-processing for a FEA using Helius:MCT, the auxiliary Firehole Composites software, “x-STIFF”, is used to calculate extraneous stiffness parameters, such as the thickness modulus and the hourglass stiffness necessary for the reduced integration specific element formulation. These properties can also be estimated using various relationships given in the ABAQUS Theory Manual [90].

The 8-node, solid brick, ABAQUS finite element, *C3D8R*, was used to represent the

honeycomb core of each sandwich panel CAI test coupon modeled as a homogenized, continuum region. The elastic response of this element was implemented using nine orthotropic engineering properties to represent the constitutive model. The out-of-plane modulus, the L-direction shear modulus, and W-direction shear modulus for the corresponding honeycomb core were given in the literature [86] as experimentally determined constants found using the appropriate test standards (e.g. ASTM). The in-plane extensional moduli and shear modulus for the continuum representation were determined using the equations given in the theory section of Chapter 4. All of the appropriate constants used to define each analysis will be given in Chapter 6. Since, a non-linear model was necessary for the out-of-plane response of the homogenized core, an ABAQUS subroutine, UMAT, was written in FORTRAN to implement both the linear elastic response and the idealization of the non-linear flatwise core crush curve described previously, in Chapter 4. The implementation of the core response by UMAT will be described in the next section.

5.2.2 Honeycomb Core Implementation using UMAT

The linear elastic orthotropic response as well as the non-linear crushing failure of the core was implemented using the ABAQUS user subroutine, UMAT, which is written in the FORTRAN programming language. As written, the UMAT requires the following inputs to be read from the ABAQUS/Standard input file under a “user material” ABAQUS keyword for the appropriate material. First, the nine orthotropic engineer constants are given which define the linear elastic response of the material as defined by Eq. 4.1. The 10th value is a constant which acts as a marker for the material point which defines it as either a “damaged” or “undamaged” material point. This is only with respect to the initial material model, and has no bearing on the results of any subsequent failure analysis. The flatwise core crush strength of the material, given as the associated failure strain value is the 11th material constant. Finally, the 12th material property sets the stress reduction in the element which results when an element is determined to have failed from out-of-plane compressive loading during an analysis step. This stress reduction is also defined by experimental data (i.e. a

flatwise core crush test result for the stress-strain response). The specific inputs used in individual analyses of experimental test coupons under CAI load are given in Chapter 6.

The damaged region is determined by user inputs which are discussed in the last section of the present chapter. The reduction in stress is an idealization of the resulting stress after failure for a flatwise compression test. Experimental core crush results for Nomex material generally show a brittle wall collapse and folding which results in a succession of rising and falling stress resultant for a displacement controlled test [62] [63] [64]. This behavior is averaged to a single stress value, which was selected based on the idealization of core crush experimental results. Ideally, a flatwise compression test would have been completed on the materials used in this research in order to gain material specific information; however, this was not completed so the estimate was used. Once the initial crush strength has been reached, successive cell wall collapse occurs at a much lower level of applied load since the cell wall stability has been compromised. Cell wall densification, and the corresponding eventual increase in crush stiffness, are not modeled in the present analysis, since this core behavior is not typically found due to indentation propagation failure during CAI testing. For all current analyses, after failure, the stress tensor components are reduced to 60% of their initial values. All extensional and shear moduli are set to zero so the stress remains constant after failure, resulting in perfectly plastic response for any remaining deformation. The non-linear crush response in the z -direction for a 3PCF Nomex honeycomb was approximated by the idealized core crush response shown in Fig. 5.3. The 6PCF core response used is similar, except the appropriate constants are used for linear elastic modulus and core crush strength to define the idealization. The red and blue curves in Fig. 5.3 represent the response of impact damaged and initially undamaged core elements, respectively. The marker, which was mentioned as the 10th subroutine input, previously, determines which curve is used for a given material point.

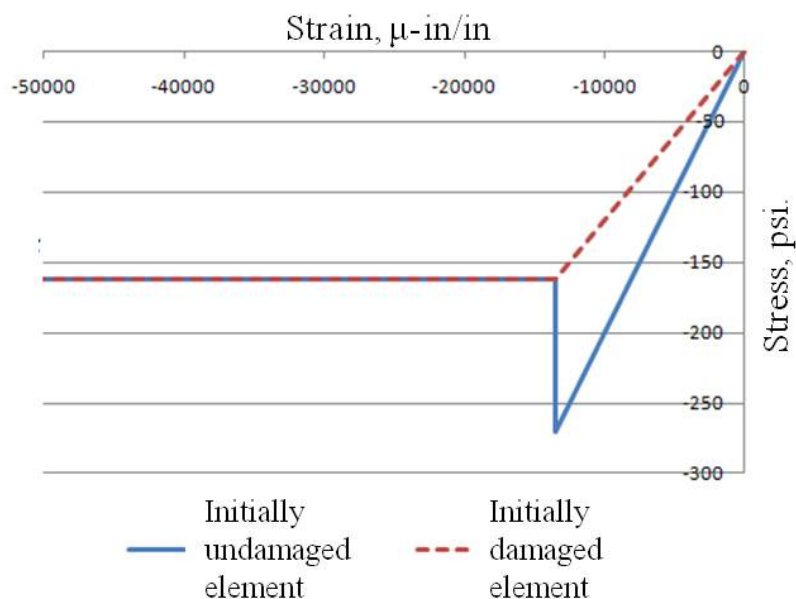


Figure 5.3: Idealized core crush response use to define non-linear constitutive core behavior of 3PCF Nomex core.

5.2.3 Impact Damage Modeling

Impact damage present in a test coupon during CAI testing of honeycomb core sandwich panels plays an important role in determining the failure strength for a given coupon. The subject of damage formation in composites, including honeycomb core sandwich panels, has been studied extensively. The literature review of Chapter 1, detailed selections from this body of work. The inclusion of impact damage in the various analysis methods used currently for CAI failure of sandwich panels, also presented in Chapter 1, has been treated to a much lesser extent. The large amount of data available from the current research, discussed in Chapters 2 and 3, makes possible the incorporation of impact damage to a much fuller extent in the new analysis model. The treatment of initial impact damage in models of CAI sandwich panel test coupons is the subject of the present section. The sensitivity of the FEM to each of the measurements used to define the impact damage model will be discussed in a later section of this chapter. This information represents one of the major contributions of the present work.

The most commonly included type of impact damage in models for analysis of sandwich panel CAI failure is a dimple in the geometry of one facesheet. This is used to represent the residual dent that results from a low velocity impact on such a structure. In the new FEM, a residual dent is included in the coupon geometry using measurements from the corresponding experimental test coupon for the dent's maximum depth and maximum diameter. From symmetry, only one quarter of the residual dent is modeled, and the dent is assumed to be circular. This assumption is used since the test coupons modeled were impacted with a hemispherical shaped blunt impact tip. The indentation modeled affects the facesheet geometry, as well as the core geometry, and their resulting finite element meshes. The contour of the dent at the front facesheet to core interface is defined using Eq. 5.42 where the maximum dent depth, h_{max} , and dent diameter, d , are necessary to inputs into the model, and x_n and y_n are the nodal Cartesian coordinates. The lower surface of the facesheet follows the surface defined by this curve. The upper surface follows the same curve but is offset by the defined thickness of the facesheet which is 0.02 in. in all analyses. This dimension is the nominal facesheet thickness of the sandwich panel test coupons described in Chapters 2 and 3. No thickness change is modeled in the impact damage region of the facesheets. The top surface of the continuum core also follows the curve defined by Eq. 5.42. The through the thickness nodal locations are adjusted so equal spacing is maintained for element node locations between the indented top surface and the lower surface of the continuum core. A close up view of the geometry of the initial indentation included in the facesheet is shown in Fig. 5.4.

$$z_{dent} = \frac{-h_{max}}{2} \left(1 + \cos \left(\frac{2\pi \sqrt{x_n^2 + y_n^2}}{d} \right) \right) \quad (5.42)$$

In addition to the geometric indentation, other types of damage can be incorporated into the FEM, many of which have not been used or adequately discussed in the prior literature reviewed. The impact damage model described here attempts to simulate the presence of the various types of damage seen in the tested materials, discussed in Chapters 2 and 3. This damage was observed and quantified through destructive and non-destructive evaluation

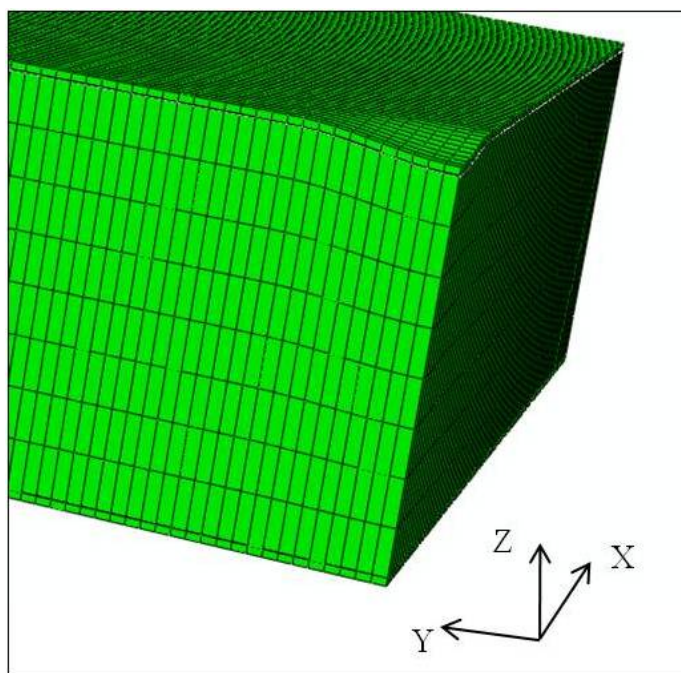


Figure 5.4: New CAI analysis model: close-up view of indented region of FEM.

(NDE) techniques after static indentation, and low velocity impact tests, to specifically study impact damage formation in these materials. In addition, some measurements were collected in observation of damage present on the CAI test coupons, so additional information is available pertaining to particular test coupons which will be used in analysis. Types of damage observed in the facesheets of the PXX, 3PCF-XX, and 6PCF-XX series materials include delaminations, longitudinal matrix cracks, transverse fiber cracks and facesheet penetration. Types of damage observed in the core of the sandwich panels include brittle fracture of the cell walls, buckling of the cell walls, and voids in the cellular material where the cellular structure had been completely crushed. The effect of each of these damage types can be included in the model on a macroscopic level by degradation of the constitutive material properties of the corresponding damaged region (e.g. damaged facesheet region, or damaged core region). These regions must be defined by both their dimensions and the proper material property degradation amount. Both of these will now be described, first with respect to the damaged core region, and second, with respect to the damaged facesheet region.

Typical core damage in a thin facesheet honeycomb core sandwich panel from low

velocity impact damage is shown in Fig. 5.5. The damaged core region is assumed to be circular in shape and concentrically located with respect to the residual dent previously discussed. It can therefore be described geometrically using a maximum radius and depth, measured from the front, damaged facesheet. The measurements used for this definition are taken from the low velocity impact damage survey corresponding to the specific material modeled. The impact damaged core region is assumed to be uniform in depth, to simplify the FEM input file definition. This assumption represents a conservative estimate of the size of the damaged core region.

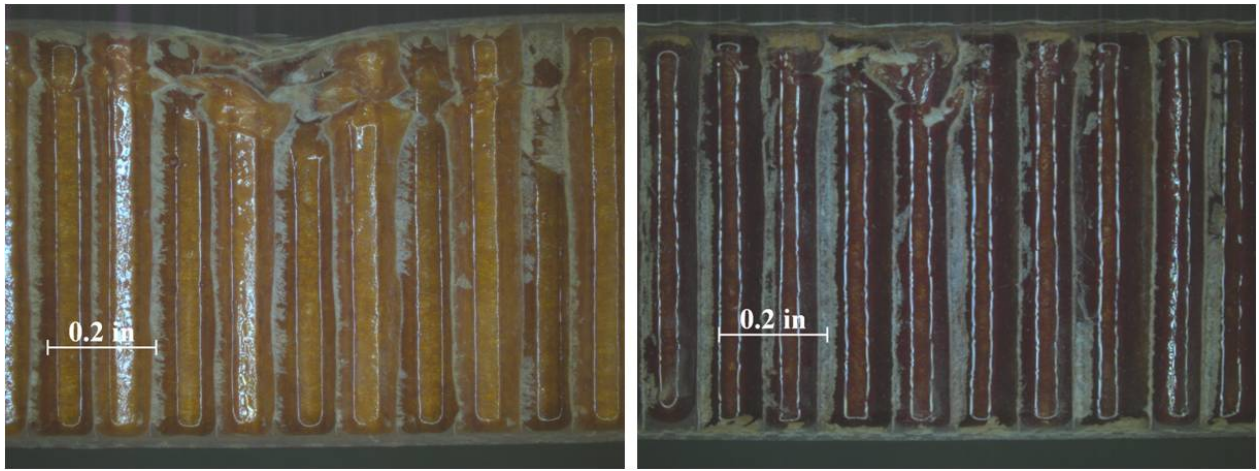


Figure 5.5: Examples of core damage from destructive microscopy of 3PCF-XX (left) and 6PCF-XX (right) series materials.

An example of the damaged core region included in the new FEM model is shown in Fig. 5.6. In addition to the geometric definition of this region, the damage also requires a set value for the material property degradation (i.e. an element stiffness reduction). In the present research, it is assumed that the stiffness of the damaged core region is 60% of the initial properties. This was based on the idealization of stress-strain curves found by flatwise core crush test by similar materials by other researchers [46]. The effect of the uncertainty of this value, as well as the geometric dimensions of the damaged core region will be discussed in a subsequent section of this chapter.

Images from microscopy of impact damaged test coupons in Fig. 5.7 show the variation in facesheet damage between lightly damaged (left) and more heavily damaged test

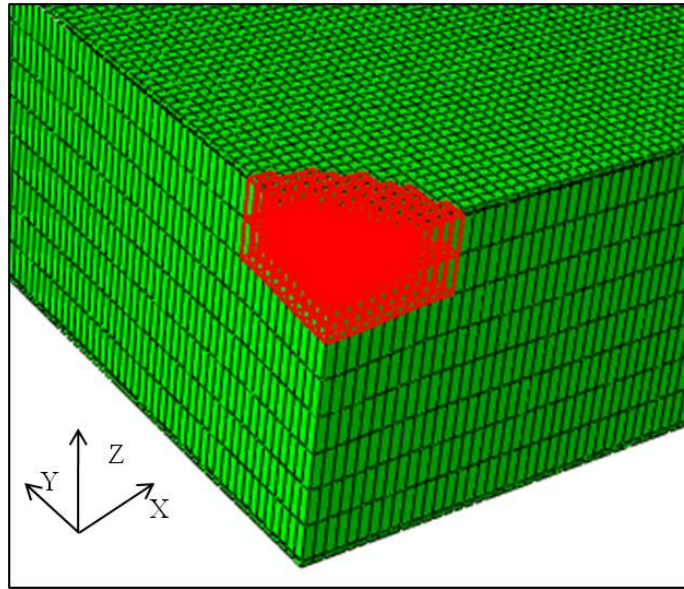


Figure 5.6: New CAI analysis model: damaged core region example.

coupons (right). In the more heavily damaged coupons, a region of facesheet fracture (failed fibers and matrix) is readily apparent. To incorporate these differences, the damaged facesheet region of the new model is actually two separately defined element groups. First, a region of moderate facesheet damage is included in all CAI test coupon models based on the location of inter-fiber fracture (IFF) or matrix cracking found from observations and measurement by optical microscopy. An example of a microscopically observed matrix crack is shown in Fig. 5.8. The area of matrix-damaged facesheet incorporated in the new FEM for CAI analysis is assumed circular and concentrically located with respect to the facesheet dimple. Geometrically, it is only necessary to define this region by an experimentally determined diameter. It is also defined by a reduction in the element stiffness from the stiffness based on pristine material properties, which will be discussed later. The second region of facesheet damage is only modeled for heavily damaged sandwich panels, where facesheet fiber fracture was observed. An example is shown in Fig. 5.7. This region is assumed to be one element wide in the coupon load (y-)direction, and is defined in the coupon width (x-)direction by the corresponding length measured during testing for damage formation. It is also defined by a reduction in stiffness from pristine material properties. The geometric representations of

the two damaged facesheet regions used in the new FEM model to represent impact damage prior to any compressive loading is shown in Fig. 5.9. The stiffness reductions used for the two damaged facesheet regions will now be discussed.

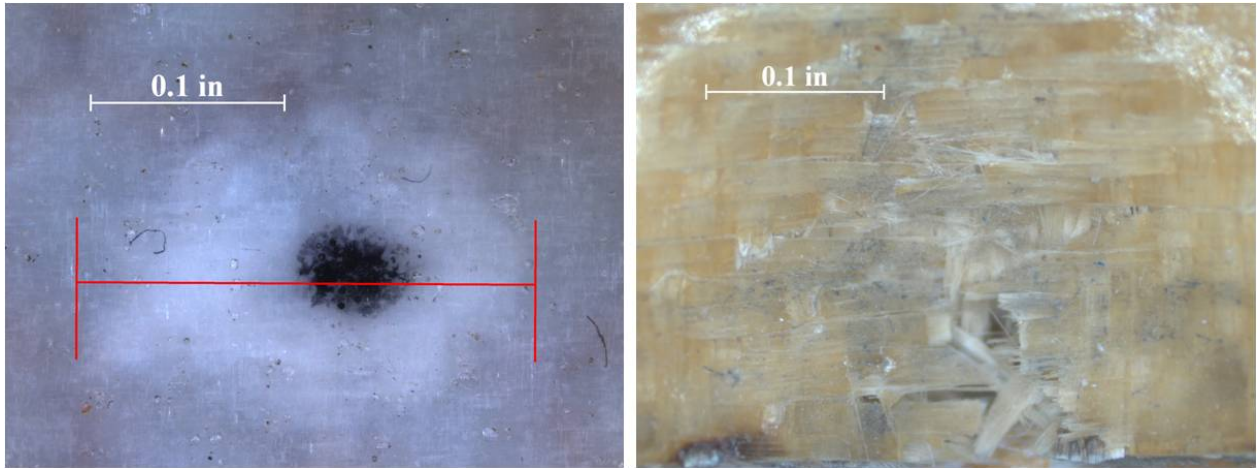


Figure 5.7: Examples of facesheet damage from microscopy of PXX (left) and 3PCF-XX (right) series materials.

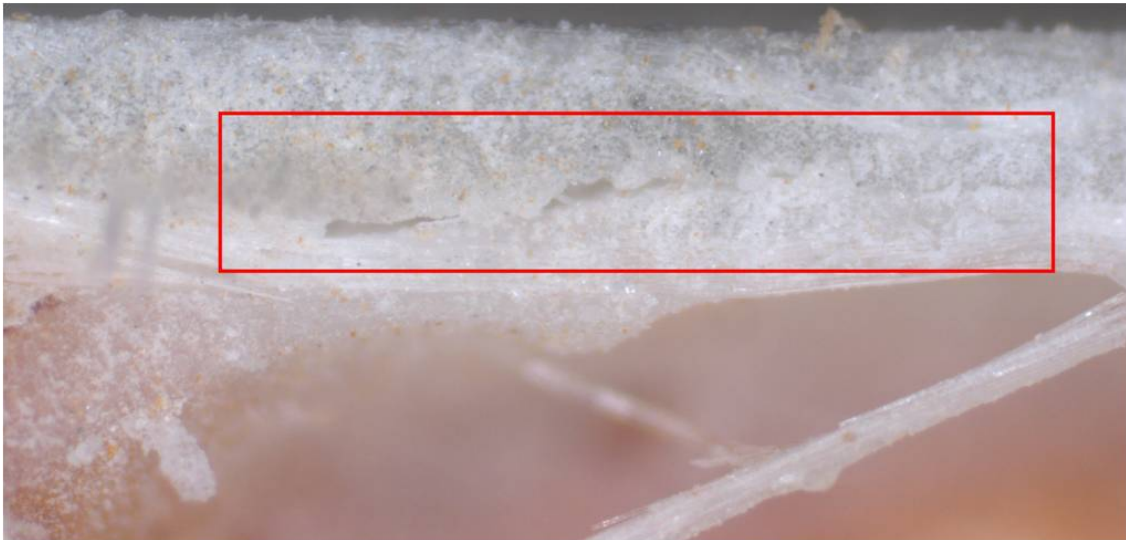


Figure 5.8: Example of matrix cracking as a result of impact damage observed by optical microscopy.

The two regions of facesheet damage require individual reductions in stiffness. The IFF region requires a reduction in stiffness consistent with matrix damage to that area of the woven fiberglass facesheets. The region of fiber fracture requires a reduction in stiffness

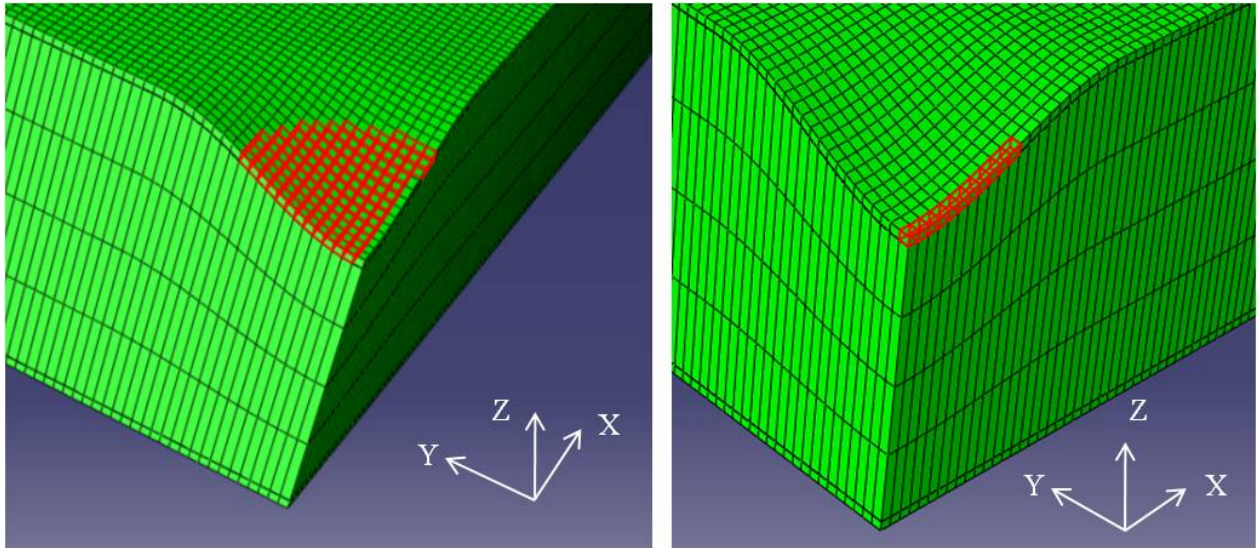


Figure 5.9: New CAI analysis model:facesheet element regions representing areas of observed IFF (left) and fiber fracture (right), prior to any compressive load analysis steps.

consistent with both matrix failure and fiber failure. In keeping with model consistency, the stiffness reductions used by Helius:MCT for the progressive failure analysis will also be used to define the impact damage of the initial model. The stiffness reduction recommended by Firehole Composites for use with their Helius:MCT software for matrix failed elements is 90% for the matrix constituent material properties. This stiffness reduction is used for the region representing impact induced IFF. The reduction for fiber failed elements (matrix failure assumed to have occurred prior to fiber failure) is 90% for matrix constituent material properties and 99% for fiber constituent material properties. These reductions are used for the region representing impact induced fiber failure. The constituent material properties which are used for both fiber and matrix materials are the *in situ* properties determined by the Helius Material Manager based on the ply properties of the material found in the appropriate literature. Once the appropriate stiffness reduction has been applied to the fiber and matrix constituent material properties associated with each region, the laminate level material properties are calculated from the appropriate relationships.

The calculation of damaged lamina level properties from damaged constituent level properties involves the calculation of effective moduli of woven composites. This is an area

of micromechanics analysis which has received some research attention; however, unlike the calculation of unidirectional fiber-reinforced composite laminas, there are no widely accepted micromechanics relationships. The principal focus of establishing the appropriate relationships has centered on strategies to estimate the effects of waviness on woven lamina engineering properties. Whitcomb and Tang [94] reviewed previous attempts and noted they varied from simple models based on modified classical laminate theory, to full three-dimensional finite element models. The authors began the development of their own work with the study of the characteristics of a weave which dominate its response. For instance, they noted that the 8-harness weave exhibits very slight coupling between in-plane extension and shear. They found that weave-specific behavior depends on properties such as tow stacking order, weave type, and of course, waviness. The authors continued with the development of a building block approach to simple formulations for engineering properties based on waviness and other weave properties, before comparison to a detailed FEM model.

The types of weave used in the facesheets of the sandwich panels studied in the present research are style 7781 E-glass weaves for PXX series materials (discussed in Chapter 2) and style 6781 S2-glass weaves for 3PCF-XX and 6PCF-XX series materials (discussed in Chapter 3). Both of these weaves are identical 8-harness satin weaves, with the only difference being the quality of the fibers (S2 glass is considered higher quality with superior stiffness and strength). The micro- and meso-mechanics of these types of weaves were studied by Searles *et al.* [95]. The authors noted that 8-harness (8H) satin weaves reduce the number of exchanges of the fill and warp tows, thereby improving the composite stiffness and strength of the woven ply. In addition, these materials are especially important in aerospace structures since they can be molded into highly complex structures and shapes. The authors chose cubic splines to approximate the two-dimensional cross section of 8H weaves. Using these approximations to incorporate any inherent irregularities in the weave architecture, the authors then used composite cylinder assemblage to approximate effective micromechanics properties of the local weave and classical laminate theory (CLT) to approximate the 8H weave as a two layer laminate.

Another example of work considered in the present research includes a method by Gao *et al.* [96] to consider calculation of damaged weave material properties through analysis of specific damage geometry using Castigliano's second theorem. Also, Angioni *et al.* [97] classified various methods as either micromechanics of materials, finite element analysis, and asymptotic expansion homogenization methods (AEHM). The authors then compared AEHM to other analysis methods in order to draw conclusions on its relative effectiveness at predicting the engineering properties for various weave architectures. AEHM proved equal to the best analytic method and the authors mentioned it has the added benefit of providing the ability to determine local stresses and strains.

Each analysis method discussed in the four examples, seeks to consider the effective moduli of woven composites. The various methods differ in the amount of weave definition considered, as well as the complexity of implementation. Typically, tow waviness is the principal consideration on the resulting material property definition, even though it is not the only consideration in a more detailed approach. In the present research, a very simple method for estimating damaged weave properties will be used, since analysis of weave properties is not the primary concern of the current research. The following describes the method, original to the current research, to approximate the effect of waviness on damaged material properties.

A ply layer of epoxy matrix pre-impregnated woven fiberglass is considered as a four layer composite laminate. Four plies are considered instead of two so that the laminate can be considered balanced and symmetric. This allows for appropriate engineering constants to be easily calculated from CLT. The appropriate relations used in CLT were given as Eqs. 4.3 through 4.12. The stacking sequence of unidirectional layers used to represent a single woven layer is $[0/90]_S$. In order to use this method, the engineering properties associated with the individual layers were calculated using formulas from the mechanics of materials. These formulas were taken from the book by Hyer [87]. The rule of mixtures result is used to calculate the fiber direction Young's modulus, E_1^C , and the in-plane Poisson's ratio, ν_{12}^C . The rule of mixtures uses the fiber and matrix volume fractions, ϕ^f and ϕ^m , and the appropriate

constituent material properties.

$$E_1^c = \phi_f E_1^f + \phi_m E^m \quad (5.43)$$

$$v_{12}^c = \phi_f v_{12}^f + \phi_m v^m \quad (5.44)$$

The modified rule of mixtures [87] is generally used in Mechanics of Materials for unidirectional results for increased level of accuracy in estimation of the transverse extensional modulus. The inverse of the transverse layer modulus is given with respect to the fiber volume fraction, the transverse fiber modulus, and the matrix modulus as in Eq. 5.45.

$$\frac{1}{E_2^c} = \frac{1 - \sqrt{\phi_f}}{E^m} + \frac{\sqrt{\phi_f}}{\sqrt{\phi_f} E_2^f + (1 - \sqrt{\phi_f}) E^m} \quad (5.45)$$

Finally, the expression for in-plane shear modulus of a unidirectional layer used for Mechanics of Materials is taken from the concentric cylinders result [87]. The composite shear modulus, G_{12}^c , is given with respect to the matrix shear modulus, G_m , the fiber volume fraction and the fiber shear modulus, G_{12}^f .

$$G_{12}^c = G_m \left[\frac{(G^m + G_{12}^f) - \phi_f (G^m - G_{12}^f)}{(G^m + G_{12}^f) + \phi_f (G^m - G_{12}^f)} \right] \quad (5.46)$$

The Mechanics of Materials relations are used with the *in situ* pristine fiber and matrix constituent properties found by the Helius Material Manager to calculate unidirectional ply properties. CLT is then used to calculate idealized properties of a single woven layer using the stacking sequence that was mentioned above. These idealized properties are generally much higher than the expected properties of the corresponding woven ply. Since, the actual pristine properties of a woven ply are known, a “waviness factor”, W , for each engineering

property can be calculated as follows (for E_1 in this example) in Eq. 5.47.

$$W_{E_1} = \frac{E_1^{\text{actual}}}{E_1^{\text{CLT}}} \quad (5.47)$$

Here, E_1^{actual} , is the lamina extensional modulus determined by the appropriate ASTM test standard and available in published literature, and E_1^{CLT} , is the idealized lamina extensional modulus calculated using the method outlined. Now, that this “waviness factor” has been determined, idealized versions of the damaged material properties for the matrix damaged element regions of the FEM, as well as the fiber damaged element regions of the FEM are next calculated using the CLT method, but this time using fiber and matrix constituent properties with the appropriate stiffness degradations (e.g. 90% reduction in matrix stiffness and 99% reduction in fiber stiffness for the region associated with fiber cracking in the FEM). The “waviness factor” is then used to calculate more appropriate degraded properties as follows in Eq. 5.48 for the damaged Young’s modulus in the fill tow direction. Here, E_1^{idealdam} is the idealized damaged Young’s modulus calculated from CLT.

$$E_1^{\text{dam}} = W_{E_1} E_1^{\text{idealdam}} \quad (5.48)$$

The damaged warp modulus, E_2^{dam} , and the damaged in-plane shear modulus, G_{12}^{dam} , are calculated in the same fashion. The Poisson’s ratios are not degraded from the values used from literature. The out-of-plane Young’s modulus, E_3^{dam} , is assumed to degrade from the values used from literature by the same amount calculated for the fill modulus. Additionally, the calculated degradation of the in-plane shear modulus is applied to the other two shear moduli required for the fully orthotropic engineering property definition of the damaged facesheet plies. Obviously, there are quite a few assumptions associated with the method outlined in this section for calculating the degraded properties of impact damaged regions of the model. Although, the methods used may not be accurate in the strictest sense necessary for research in the specific area of calculation of woven engineering properties, they

do give approximations which are accurate enough to be useful for the present research. The sensitivity of the new FEM model to uncertainty in the degraded material properties will be further discussed later in the current chapter.

5.3 Mesh Pattern and Convergence

A three-dimensional grid pattern was used to mesh the model geometry for both the core and the facesheets. This allows for efficient model creation without the need for a pre-processor such as ABAQUS/CAE [73]. Instead, the ABAQUS input file, for each completed analysis, was written by a custom MATLAB [84] function. The mesh density, panel geometry, and damage definition could be efficiently adjusted for various analyses while retaining mesh connectivity, and the connectivity between the facesheets and the core of the panel. The ABAQUS continuum shell element, *SC8R*, was used to simulate the facesheets of the sandwich panel, while the ABAQUS linear solid brick element, *C3D8R*, was used to model the continuum-represented, homogenized, honeycomb core. The grid mesh was defined by the number of elements in the coupon width direction (eX), the number of elements in the coupon load direction (eY), and the number of elements in the out-of-plane direction (in the core region only, eZc). Only one continuum shell element was used through the thickness of each facesheet. The total number of elements for a given analysis is then given by the following expression: $eTOTAL = eX * eY * (eXc + 2)$. Mesh convergence was studied individually in the coupon width, load, and through the thickness direction, while keeping the mesh density in the directions not being studied at a nominal value. The mesh pattern and convergence study is presented in the following sections.

5.3.1 Mesh Convergence: Coupon Width Direction (eX)

For the mesh convergence study in the coupon width direction, four test cases were chosen from the 32 coupons tested to CAI failure. Of the four coupons chosen, two were chosen from the 3PCF-XX series materials, and two were chosen from the 6PCF-XX series materials.

Information about both sandwich panel material systems was given in Chapter 3. The reason for this selection was that mesh convergence for the new model in the coupon width direction would be studied for both CAI failure modes found in experimental testing (indentation propagation and crack propagation). The specific coupons, chosen from each material system, included one lightly damaged test case (i.e. damaged by a 1 ft-lb. energy level impact), and one heavily damaged test case (i.e. damaged by a 7 ft-lb. energy level impact). The lightly damaged panels selected were 3PCF-02 and 6PCF-07, and the heavily damaged test cases were 3PCF-16 and 6PCF-14. More information about these specific test coupons can be found in Chapter 3. Specific inputs used to define the ABAQUS input file can be found in Chapter 6 (other than the mesh used, which will be described in this section). The PXX series materials were not used for this portion of the mesh study, since the results would be expected to be similar to the results for the 3PCF-XX series test cases.

Each of the test cases would be considered with the following number of elements in the coupon width direction: 40, 60, 80, 120, and 160. 80 elements was considered to be a moderate mesh density, so the number of elements in the coupon load direction was set to 80. The number of elements in the thickness direction was 10 (2 facesheet elements and 8 core elements) for 3PCF-XX test cases, and 6 (2 facesheet elements and 4 core elements) for 6PCF-XX test cases. The reason for the reduction in elements in the thickness direction for 6PCF-XX test cases was this. Experience gained during model development had shown that the crack propagation failure mode did not depend on the through the thickness number of elements, since that part of the mesh largely effected the out-of-plane deformation of the model (although this was not explicitly studied). The reduction in model degrees of freedom for the 6PCF-XX test cases improved computational efficiency. (Analysis of 6PCF-XX test case took more computation time, since it largely depended on the progressive failure analysis.)

The mesh dependency of the new FEM for CAI analysis was evaluated based on the result of global coupon CAI failure load. Other results for CAI failure strength (stress) or strain could also have been measured, but the results would have been similar. Each test

case was subjected to the boundary conditions described previously in this chapter and a displacement prescribed load, in order to simulate an experimental CAI test. The CAI failure load was determined when a sudden drop in reaction force was observed, just as it was in experimental testing described in Chapters 2 and 3. The results for each test case used in this portion of the mesh convergence study are shown in Fig. 5.10.

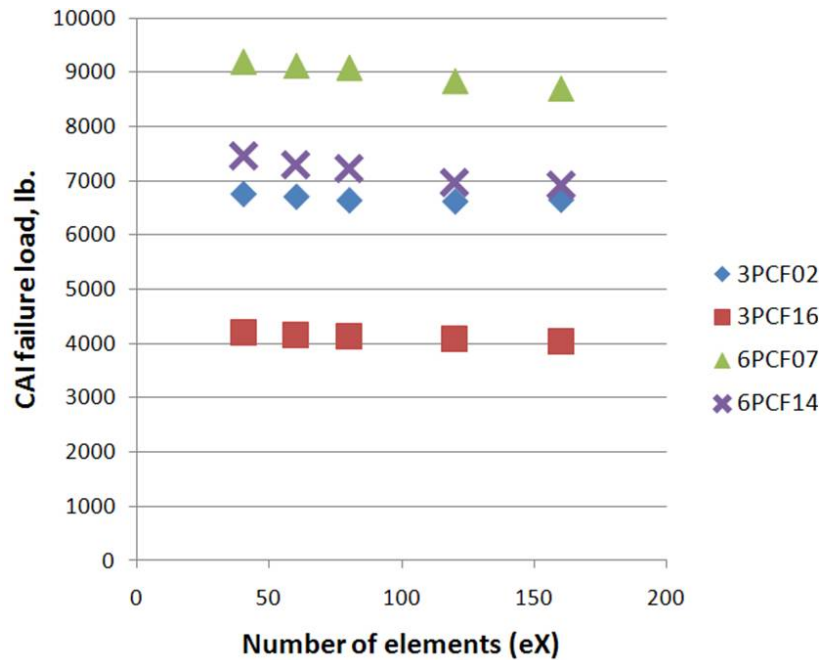


Figure 5.10: Mesh convergence study results: CAI failure load vs. number of elements (eX).

The results of the study of the dependence of the FEM result for CAI failure load of the test coupons on the number of elements in the coupon width direction are as follows. The results for the 3PCF-XX test coupons had little dependency on the eX mesh density, for neither the lightly damaged test case, nor the heavily damaged test case. On the other hand, 6PCF-XX cases do appear to be dependent, though the results are very similar for both the lightly and heavily damaged test cases. Another manner of checking solution convergence is to look at the change with increasing number of elements. The solution change from the next lower density (as a percentage) vs. number of elements is shown in Fig. 5.11. This result shows that the overall change in model result for each additional amount of elements was very small (about 3% or less for every data point).

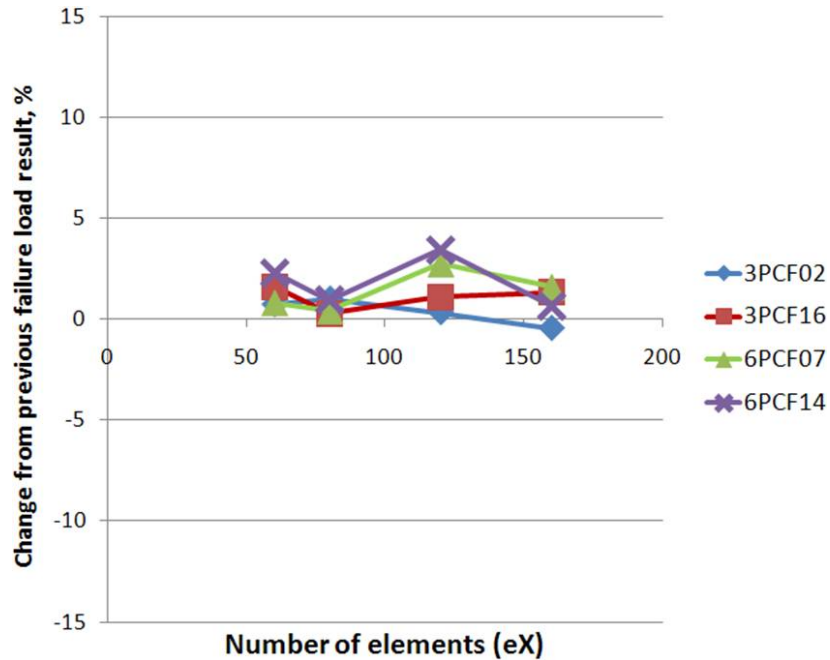


Figure 5.11: Mesh convergence results: % change in CAI failure load vs. number of elements (eX).

5.3.2 Mesh Convergence: Coupon Load Direction (eY)

The same four test cases were chosen for the coupon load direction convergence study, as in the study described in the previous section. Each of these cases was again studied for mesh dependence (though this time in the coupon load direction) with the following number of (eY) elements: 40, 60, 80, 120, and 160. The number of elements in the coupon width direction was set to the nominal value of 80, and the number of elements in the thickness direction was 10 (2 facesheet elements and 8 core elements) for 3PCF-XX test cases, and 6 (2 facesheet elements and 4 core elements) for 6PCF-XX test cases. The mesh dependency of the new FEM for CAI analysis was again evaluated based on the solution for the CAI failure load. Each test case was subjected to the boundary conditions described previously in this chapter, and a displacement prescribed load, in order to simulate an experimental CAI test. The results for each test case used in this portion of the mesh convergence study are shown in Fig. 5.12.

The results for the mesh dependence on element density in the coupon load direction were slightly skewed. The largest dependence was again found for a 6PCF-XX series test

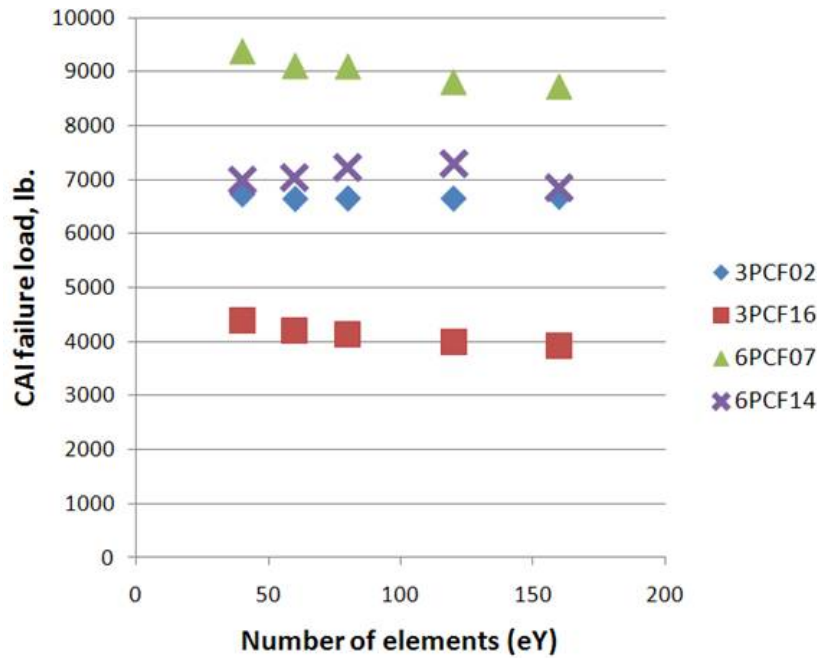


Figure 5.12: Mesh convergence results: CAI failure load vs. number of elements (eY).

case (the lightly damaged 6PCF-07); however, little dependence on the number of elements was shown for the other, highly damaged 6PCF-XX series test case. On the other hand, little mesh dependence was shown for the lightly damaged 3PCF-XX series test case, while some mesh dependence was shown for the highly damaged 3PCF-XX series case. The mesh density in the coupon load direction for the 3PCF-16 test case showed convergence when the number of elements was increased to 80 based on the limited change in CAI failure load achieved when increasing the mesh density further. These trends are also apparent by looking at the % change in CAI failure load versus number of elements, shown in Fig. 5.13.

In Fig. 5.13, the convergence of three of the four test cases can be seen clearly. The highly damaged 6PCF-14 test case does not appear to converge as well with the data displayed in this form; however, it was shown in Fig. 5.12, previously, that the CAI failure load predicted for this test case is roughly the same for both 40 elements and 160 elements. The failure load is slightly increased for the intermediate mesh densities, but the overall mesh dependence is low.

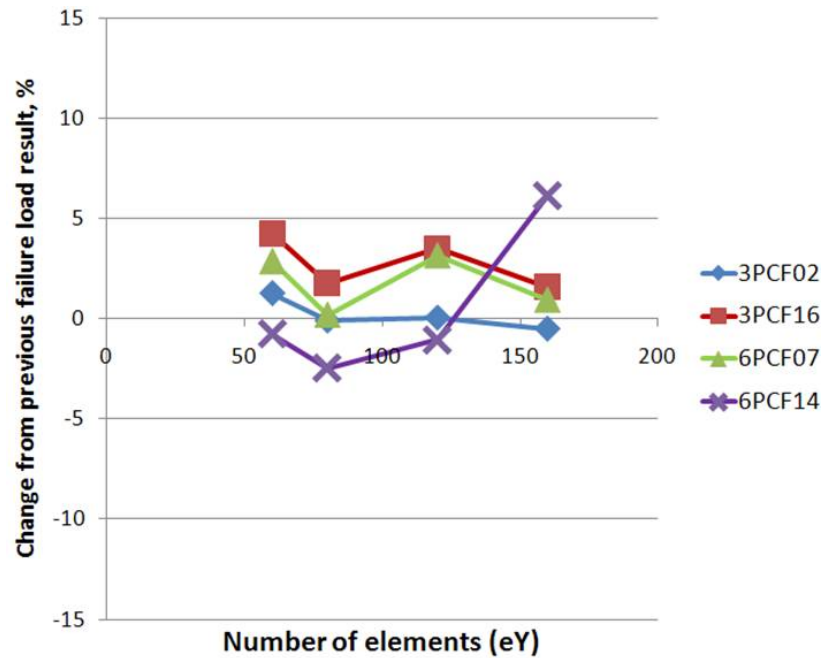


Figure 5.13: Mesh convergence results: % change in CAI failure load vs. number of elements (eY).

5.3.3 Mesh Convergence: Coupon Thickness Direction (eZc)

Four test cases were again used for the third, and last, section of the mesh convergence study. This section covers mesh dependence in the through the thickness direction of the core region. Only coupons expected to fail by the indentation propagation failure mode were considered for this portion of the study. As was discussed earlier, the through the thickness mesh density primarily effects only the out-of-plane deformation of the model. Since, the out-of-plane deformation was shown in experimental tests to contribute very little to the crack propagation failure mode, the same results can be expected from the physics-based FEM. Two test cases were chosen from the PXX series materials, and two were chosen from the 3PCF-XX series materials. Information about both sandwich panel material systems was given in Chapters 2 and 3, respectively.

The specific coupons used included one lightly damaged, and one heavily damaged coupon from each of the material systems. The lightly damaged panels selected were P11 and 3PCF-02, and the heavily damaged test cases were P09 and 3PCF-16. More information

about these specific test coupons can be found in Chapters 2 and 3. Specific inputs used to define the ABAQUS input file can be found in Chapter 6, while the mesh used in each of these analyses will be described in the present section. The through-the-thickness number of elements in the core region of the model was varied from four to eleven elements. Four elements is the lowest number of elements which can be used while reasonable FEM results can be expected. For all test cases, convergence was found by the time the number of elements was increased to eleven. The number of elements in the coupon load and width directions were both set to the nominal values of 80. The mesh dependency of the new FEM for CAI analysis was evaluated based on the result of global coupon CAI failure load, as it was for the two previous parts of the mesh studies. The results for each test case used in this portion of the mesh convergence study are shown in Fig. 5.14.

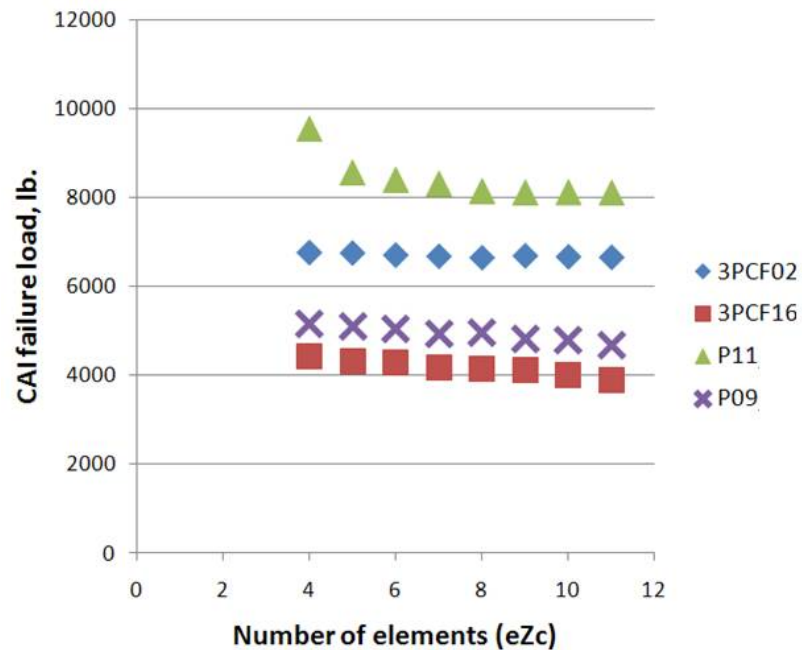


Figure 5.14: Mesh convergence results: CAI failure load vs. number of elements (eZc).

The results for this mesh dependence study are also somewhat varied. For lightly damaged coupons, mesh convergence is shown, although for the 3PCF-02 case, it actually appears that the case is hardly mesh dependent at all on the through the thickness number of elements. Mesh convergence is also less apparent for the highly damaged coupons. The

percent change with increasing number of elements in Fig. 5.15 is more encouraging, however. The change for almost all test cases is 3% or less, with the lone outstanding value being from an analysis with low mesh density. Still, while it does not appear that the mesh of the highly damaged test cases has converged, it can be said that a reasonable mesh density can be selected as eight elements. Only an insignificant change in analysis result would be expected for higher mesh densities.

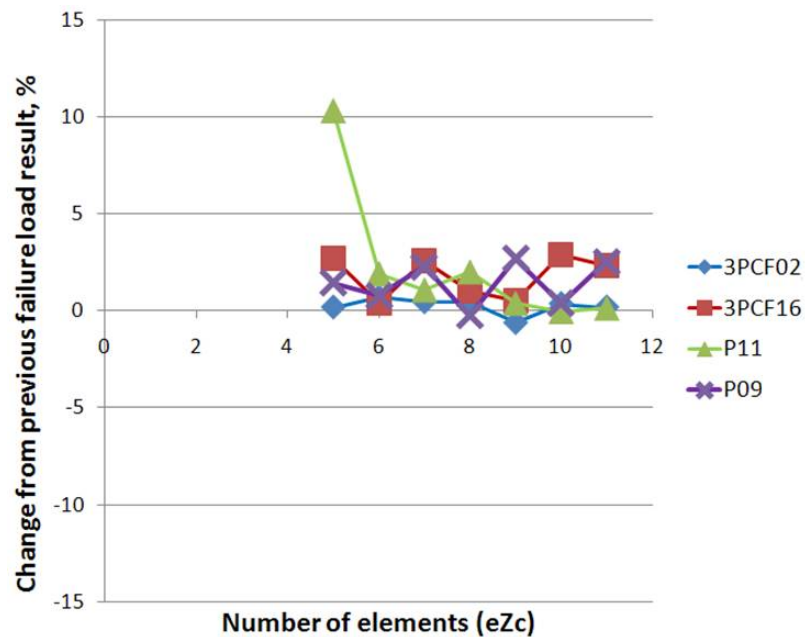


Figure 5.15: Mesh convergence results: % change in CAI failure load vs. number of elements (eZc).

5.3.4 Additional Notes from the Mesh Convergence Study

The new FEM model's dependence on mesh density in the test coupon width, load, and through the thickness directions was studied. The dependence of the CAI failure load was more dependent on mesh density in the coupon width (eX) and load (eY) direction for test cases which failed by crack propagation (6PCF-XX series materials) than for test cases which failed by indentation propagation (3PCF-XX series materials). This was anticipated since the failure theory used by Heliuss:MCT progressive failure analysis software can be expected to be mesh dependent. As element size decreases near an area of stress concentration

in the model, element stress will increase, especially at the material points closest to the stress concentration. This means that as the mesh density increases, failure will begin and propagate more quickly. This requires that the mesh size in the coupon load and width direction be fixed at a value which is known to produce reasonable results. For this reason, a mesh of 80 x 80 (eX x eY) was chosen for subsequent analyses expected to exhibit the indentation propagation failure mode, while a mesh of 120 x 120 was chosen for the analyses expected to exhibit the crack propagation failure mode. Less mesh dependence was shown in results for through the thickness number of core elements (eZc) for PXX and 3PCF-XX series materials. A nominal value of eight eZc elements was chosen based on this convergence. Four elements through the core region thickness will continue to be used for 6PCF-XX series materials. Although no specific tolerance was selected to define mesh convergence, these meshes were found to produce reasonable results for the test cases considered. It was shown that only small changes in results could be expected by increasing the mesh density further for all cases.

5.4 FEM Sensitivity Studies

The FEM representation of low velocity impact damage in CAI test coupons was previously discussed in Section 5.2.3. The large amount of CAI test data generated in the experimental portion of the current research, which was discussed in Chapters 2 and 3, meant that important details could be included in the FEM prior to analysis. The following section will describe how each detail affects the overall model results for CAI analysis. The purpose of this study is to identify the confidence level associated with various aspects of the model. In addition, some aspects of the model are identified as areas of necessary improvement for future CAI model development, or use of the current model in an engineering design problem.

The damage included in the FEM prior to analysis using the ABAQUS/Standard solver is defined using a series of inputs to an original, custom “function” written in the MATLAB programming language. The majority of the function inputs are the result of

explicit measurements taken using destructive evaluation and NDE techniques, and have low levels of uncertainty associated with them. The following section will describe most of these inputs, including the measurements of the residual dent's diameter, the residual dent's maximum depth, the core damage region's diameter, the facesheet's IFF region's diameter, and the facesheet's fiber fracture region's length (only used in models of highly damaged test coupons). Each of these measurements is applied to the corresponding individual model with a high precision, due to mesh density or other factors.

One additional MATLAB function input, taken from explicit measurement of a given test coupon, is the depth of the impact damaged core region of the model. Unfortunately, due to the mesh pattern and density used, the application of this measurement to the FEM is done with reduced precision. The possible effect of this uncertainty on the CAI analysis results is discussed in its own section. Finally, the last three model inputs discussed are the stiffness reductions given to the material properties associated with damage in the model's core and facesheet regions. These three inputs were taken from various sources, and are not experimental test measurements. The unique uncertainty they add to the model will be discussed in the third sensitivity study subsection which follows.

5.4.1 Sensitivity to Impact Damage Definition

This section will describe the sensitivity of the new CAI model to the following MATLAB function inputs: the residual dent's diameter, the residual dent's maximum depth, the core damage region's diameter, the facesheet's IFF region's diameter, and the facesheet's fiber fracture region's length. Four test coupon models were used in these sensitivity studies: 3PCF-02, 3PCF-16, 6PCF-07, and 6PCF-14. These models were specifically chosen for the following reasons. Two panels were chosen from material systems expected to fail at each of the two CAI failure modes discussed in the current research: indentation propagation (3PCF-XX), and crack propagation (6PCF-XX). This will allow the sensitivity of the model for these inputs to be tested for each specific failure mode. For each of these two material systems, a lightly damaged test coupon was studied (3PCF-02 and 6PCF-07), as well as a

highly damaged test coupon (3PCF-16 and 6PCF-14). This will allow the sensitivity of the model to various initial levels of damage to be determined.

Each sensitivity study was conducted for one specific input, while the remaining inputs were kept constant. Both a conservative change and a non-conservative change were studied, so that the total number of sensitivity analyses conducted was twice the number of inputs. The nominal inputs for each of the four test cases used in the sensitivity studies are given in Table 5.1 below. The effect of an uncertainty of +/-15% with respect to each of the model inputs was considered. This level of uncertainty is very large with relation to the actual precision associated with the measurements of the inputs studied; however, some inputs will have larger effect on the model than others. This large level was chosen so that at least some change could be seen in each of the analyses completed. Since the change in each inputs was the same, each of the inputs discussed in the current section could be directly compared and ranked.

Table 5.1: Nominal input values for MATLAB function for Abaqus input file creation used during the sensitivity studies.

MATLAB Function Input	3PCF-02 (in. or %)	3PCF-16 (in. or %)	6PCF-07 (in. or %)	6PCF-14 (in. or %)
Residual Dent Depth	0.0050	0.1820	0.0060	0.1590
Residual Dent Diameter	0.633	1.333	0.583	1.000
Core Damage Region Depth	0.1000	0.1820	0.1088	0.1999
Core Damage Region Diameter	0.8695	1.0922	0.6718	0.8595
Core Damage Stiffness Reduction	40%	40%	40%	40%
Facesheet IFF Region Diameter	0.279	0.591	0.444	0.601
Facesheet Fiber Fracture Region Length	Not Applicable	0.458	Not Applicable	0.498
Facesheet Damaged Matrix Stiffness Reduction	90%	90%	90%	90%
Facesheet Damaged Fiber Stiffness Reduction	99%	99%	99%	99%

A specific example can be used to explain the process used to study model sensitivity to each input. The sensitivity of the FEM to the measurement of the residual dent depth

and subsequent ABAQUS input file definition of the 3PCF-02 test coupon will be used. The measured dent depth of this particular test coupon was 0.005 in. using a dial caliper, which had a measurement tolerance of 0.001 in. As was mentioned previously, an uncertainty of +/-15% was studied. This meant that two analyses were completed. With all other model definition inputs left at their nominal values, an analysis was completed of the 3PCF-02 coupon with a conservative dent depth value of 0.00575 in. and a non-conservative value of 0.00425 in. Each of the two cases was considered for their effect on coupon CAI failure. The global failure of the the test coupon can be discussed with respect to failure load, failure stress, and failure strain. For this example, all three will be discussed, although it will be shown that the results are very similar. Thus, for the results thereafter, only coupon failure load will be used.

The sensitivity study results for the example problem (change in 3PCF-02 model failure load due to potential uncertainty of the residual dent depth input) are shown in Table 5.2. The failure load, failure stress, and failure strain for both the non-conservative and conservative analyses are shown. The average of the two results is also given. Finally, the percent change from this average for either a 15% conservative or non-conservative estimate is given. This information was gathered for each of the inputs considered in the current section. For each test case, the sensitivity of the model to each input could then be ranked from most sensitive to least sensitive. Thus, the importance of each input to the overall CAI analysis result can be shown.

The overall results of the study of the sensitivity of the CAI model to the MATLAB function inputs of the residual dent's diameter, the residual dent's maximum depth, the core damage region's diameter, the facesheet's IFF region's diameter, and the facesheet's fiber fracture region's length are shown in Table 5.3. For the lightly damaged coupons, which do not include the fiber fracture region, the sensitivity is ranked from 1 (most) to 4 (least sensitive). For the highly damaged coupons, which include a fiber fracture region, the ranking is from 1 to 5.

The sensitivity of the model to a relatively large uncertainty (+/-15%) was surpris-

Table 5.2: Detailed sensitivity results of 3PCF-02 test coupon model to residual dent maximum depth definition.

		Conservative Dent Depth	Non-conservative Dent Depth
3PCF-02	Failure Load (lbs)	7666	8142
	Average (lbs.)	7904	
	% +/- Average	3.01	
	Failure Stress (ksi)	34.85	37.01
	Average (ksi.)	35.93	
	% +/- Average	3.01	
	Failure Strain (μ -in/in)	9803	10401
	Average (μ -in/in)	10102	
	% +/- Average	2.96	

Table 5.3: Sensitivity study results for various MATLAB function inputs.

Panel	Input	Percent	Rank
3PCF-02	Dent depth	3.01	1
	Dent diameter	2.26	2
	Damaged facesheet diameter	0.92	3
	Core damage diameter	0.08	4
Panel	Input	Percent	Rank
3PCF-16	Dent diameter	16.40	1
	Core damage diameter	11.00	2
	Dent depth	5.32	3
	Crack length	0.86	4
	Damaged facesheet diameter	0.20	5
Panel	Input	Percent	Rank
6PCF-07	Damaged facesheet diameter	1.08	1
	Dent diameter	0.86	2
	Dent depth	0.64	3
	Core damage diameter	0.45	4
Panel	Input	Percent	Rank
6PCF-14	Dent diameter	2.68	1
	Damaged facesheet diameter	1.98	2
	Dent depth	1.39	3
	Core damage diameter	1.07	4
	Crack length	0.45	5

ingly small for most test cases. Except for two studies, the model sensitivity was 5% or less. For most of the inputs used for each of the four test cases, the sensitivity was less than 2%. The exceptions were the 3PCF-16 model's sensitivity to dent diameter and core damage diameter inputs. Fortunately, for both of these inputs, the actual uncertainty associated with the measurements is much smaller than the uncertainty studied. The experimental measurements for these two inputs, shown in Table 5.1, were about 1 in. Thus, the uncertainty studied (15%) meant that the conservative and non-conservative estimates varied from the nominal value by about 0.15 in. The experimental uncertainty associated with these measurements can be estimated as $1/60^{\text{th}}$ of an inch for the dent diameter, and is less than 0.001 in. for the core damage region diameter. Therefore, since the actual uncertainty associated with these two measurements is much smaller, the change in model results is expected to be much smaller.

A few other interesting trends can be seen in the results. First, the measurement of the dent diameter has a significant effect on all cases considered. Thus, it is important that this input is accurate. Additionally, the test cases which can be expected to fail by crack propagation (6PCF-XX) had very little sensitivity to changes in the core damage region's size. This can be expected since core damage primarily impacted out-of-plane deformation of the test coupons, which is already very small during the crack propagation failure mode. Finally, each input considered in the current section was shown to have some effect on the model results. So, it can be concluded that each of these inputs should not be neglected in the CAI model.

5.4.2 Sensitivity to Core Damage Depth Definition

Special attention was given to the sizing of the core damage region's depth. This measurement, taken using the destructive evaluation of test coupons by optical microscopy, has a low uncertainty level associated with the experimental result. However, due to the low mesh density used, it cannot be implemented with the same precision. The sensitivity of the FEM analysis results was studied using the test cases described previously: 3PCF-02, 3PCF-16,

6PCF-07, and 6PCF-14. The measurements used as input for the depth of the core damage for each of these cases can be found in Table 5.1. The MATLAB function for ABAQUS input file creation was programmed in such a way as to define the core damage region's depth to the nearest element. The mesh was defined with eight elements through the core thickness. The sensitivity was studied with respect to a change in core damage region depth of +/- one element, since this is the possible error. The results of this portion of the sensitivity studies are shown in Table 5.4. The global coupon CAI failure load was again used as the primary indication of sensitivity.

Table 5.4: Sensitivity study results, core damage region depth input.

	% Change in Failure Load
3PCF-03	5.39
3PCF-16	0.2
6PCF-07	0.938
6PCF-14	0.979

Remarkably, the change in CAI failure load associated with the core damage region's depth was small for three of the four test cases. For both crack propagation cases (6PCF-07 and 6PCF-14), the percent change for each case was just less than 1%. Of course, it should be expected that this input will have less effect on the crack propagation failure mode, than for the indentation propagation failure mode. This is due to the fact that the core damage primary impact out-of-plane deformation, as has been mentioned previously. However, for the highly damaged low density core test case (3PCF-16), the percent change was even smaller. For the lightly damaged case, 3PCF-02, the percent change was the largest, but this was mostly due to the lack of core damage in the non-conservative case (minus one element meant no damaged core elements were used). This result suggests that the depth of core damage is less important; however, it is important that at least some finite core damage depth is used.

5.4.3 Sensitivity to Element Stiffness Degradation

The final portion of the sensitivity study was done with respect to the degradation in stiffness from pristine material properties which are incorporated in the elements within the “damaged” regions of the FEM. The three damaged regions in the models have been previously described within the present chapter, and include a damaged core region, and two damaged facesheet regions. The principal damaged facesheet region represents a region of inter-fiber fracture (IFF), while for the highest damage test cases, a secondary damaged facesheet region is modeled which represents failure to both matrix and fiber constituents. The manner in which these regions are defined, and the stiffness degradations are incorporated was previously discussed in Section 5.2.3.

Three separate material property degradation values are required, one for each region. The elements which are incorporated into the core damage region are reduced to 60% of their initial stiffness. From Fig. 4.3, it can be seen that at the point an initially undamaged element reaches compressive failure, the stress is reduced to the stress level at which a damaged element would have obtained. Therefore, the stiffness reduction controls this level, in addition to the damaged element stiffness. The damaged facesheet elements have material properties which were calculated from constituent material properties and a “waviness” factor. The constituent material properties are degraded as follows. For an element representing the IFF region, matrix properties are degraded by 90% from their initial stiffness. For an element representing a fiber failed region, matrix properties are still degraded by 90%, but fiber properties are also degraded by 99% which means that overall a large “soft” discontinuity will exist in the mesh.

The conservative and non-conservative changes to these material property degradation amounts were as follows. An uncertainty of +/-15% was again used for the damaged core element material property degradation. This means that a non-conservative degradation of 25% and a conservative degradation of 55% were studied. This range considers the values which can be considered reasonable from the literature [62] [63] [64]. The values used for matrix and fiber degradation were recommendations from Firehole Composites for use

with their software, Helius:MCT. However, in general, these values are based on fitment to and understanding of experimental results specific to the materials being studied. This is especially true for the matrix degradation value. Fiber degradation is generally less important, as long as it is sufficiently large. Therefore, since a large amount of uncertainty is associated with these values, the values used to study model sensitivity were set as follows. For matrix property degradation, a conservative value of half the damaged stiffness (5%), and a non-conservative value of twice the damaged stiffness (20%) was chosen. (90% degradation for matrix constituent material properties means that these properties are 10% of their initial values.) For the damaged fiber properties, which are 1% of the pristine stiffness, the conservative value of 0.5%, and the non-conservative value of 2% was used. It should be noted that in addition to the degradation of model regions which are modeled as damaged, these stiffness reductions are also used by the Helius:MCT software during the CAI analysis for progressive damage. The sensitivity study takes this into account by adjusting these values as well.

The results of the third and final portion of the sensitivity studies are shown in Table 5.5. The sensitivity is again shown as a percent change in the CAI failure load. First, the core stiffness reduction value is shown to influence the coupons which fail by indentation propagation more than those which fail by crack propagation, as expected. In fact, for the lightly damaged 6PCF-07 test case, the change in core stiffness reduction has almost no effect. For the more highly damaged case, 6PCF-14, there is another interesting effect. There is increased out-of-plane deformation present in this test case due to the dent's geometry. Despite the high density core, the large dent depth causes increased though the thickness load transfer from front facesheet to core, causing higher deformation. Fiber stiffness reduction has a very small effect on the overall model result for most test cases, although it is slightly increased for the 6PCF-14 test case. It is recommended that a conservative estimate of stiffness degradation normally be used if there is some question of the nominal value. In fact, in a newer version of the Helius:MCT software package, not used in this research, Firehole Composites reduced the recommended residual stiffness of the fiber constituent from 1% to

0.0001%.

Table 5.5: Sensitivity study results for element stiffness degradation inputs.

Panel	Input	Percent
3PCF-02	Core stiffness reduction	5.42
	Fiber stiffness reduction	0.00
	Matrix stiffness reduction	2.47
3PCF-16	Core stiffness reduction	5.77
	Fiber stiffness reduction	1.37
	Matrix stiffness reduction	0.89
6PCF-07	Core stiffness reduction	0.04
	Fiber stiffness reduction	0.24
	Matrix stiffness reduction	7.15
6PCF-14	Core stiffness reduction	2.71
	Fiber stiffness reduction	3.92
	Matrix stiffness reduction	2.73

Finally, the change in matrix stiffness degradation has a varied effect on the resulting CAI failure load. In the literature, this value is discussed in regards to the type of progressive failure, the type of matrix cracks present, and their orientation [69] [70]. From observations made during the present research, a specific recommendation would be to implement a gradual degradation approach to matrix failure, as opposed to the single stiffness degradation which is done in the Helius:MCT software for woven composites. This observation is made with regards to the progressive failure analysis, rather than the initial stiffness reduction that is given to the impact damaged regions of the facesheet. In the present research, matrix failure in analysis results is similar to experimental test results. It does not display the large amounts of matrix failure which can be characteristic of a continuum damage model, due to the large stress concentrations considered in CAI analysis.

5.4.4 Final Notes on the FEM's Sensitivities

A study of sensitivity to the inputs associated with the new CAI analysis model has been completed. The results are very positive from this study, since most of the changes in failure

load observed were very small, given the large changes in the nominal input values which were considered. For some results which did show large changes in CAI failure load for a given input, it was stated that model confidence for these inputs was still high if the uncertainty associated with the actual measurement is very low. The following conclusions can be made which separate model confidence in the inputs studied into the three categories: excellent, good, and reduced.

For the model inputs for the residual dent depth, the dent diameter, the damaged core region diameter, and the crack length (i.e. length of the fiber fracture region present in the more highly damaged test coupon cases), the model confidence is evaluated to be “excellent.” This is based on low sensitivity of the model to these inputs, combined with very high precision with which these measurements were taken. The model confidence in the input which defines the diameter of the facesheet IFF region is only slightly less and is the sole input with confidence defined as “good.” The reason for this is slightly reduced precision at which this measurement was taken, but still very low sensitivity of the model to this input. Finally, the confidence associated with the remaining model inputs can be defined as “reduced.”

The “reduced” confidence inputs are considered the most reasonable source of any error that may be found in the analysis results when they are compared to the experiments. While all of the inputs are significant to the analysis results, these inputs are in need of the most future attention if the accuracy in the prediction of CAI failure is to be improved. The confidence in the following inputs is considered to be “reduced”: the depth of the damaged core region, and the stiffness reduction associated with “damaged” elements in the core, the facesheet IFF region, and the facesheet fiber fracture region. The uncertainty in the core damage depth could be easily improved by refining the model’s mesh. However, it was shown that the depth of the core damage has limited impact on the analysis results, as long as some damage is present. The stiffness reduction inputs are the areas of highest uncertainty. The core reduction input should be found in future research through a simple flatwise core crush test. The matrix and fiber degradation values come from cutting edge areas of composite

damage research. With future research, the confidence in these values will increase.

5.5 Conclusions from the Development of the New FEM for CAI Analysis

The development of a new model for CAI analysis of thin facesheet honeycomb core sandwich panels was described in the present chapter. Two significant contributions of this research to the understanding of CAI analysis were given as follows. One is the implementation of PFA for facesheet failure using a commercial implementation of multicontinuum failure theory, Helius:MCT, by Firehole Composites. An explanation of the relevant theory to the current research then continued with the development of multicontinuum theory (MCT), as developed by Garnich and Hansen [74], and MCT failure theory, as developed by Mayes and Hansen [75]. The second significant contribution made in the current chapter is the inclusion of significant low velocity impact damage detail in the the new CAI model. A small amount of micromechanics theory was used in the description of how this impact damage is included in the model.

The chapter continued with an in-depth introduction to the new CAI model. This section included details on model geometry, boundary conditions, and type of elements used. Two final sections of the current chapter discussed the mesh pattern and convergence, as well as the model sensitivity to uncertainties associated with the important inputs to the custom MATLAB function for creation of the ABAQUS input files. The mesh convergence section showed that a relatively simple mesh can be used to obtain good results. Additionally, it was shown that only small changes should be expected to analysis results as a result of increasing mesh density. It was later shown that through the thickness mesh density is important to test cases which fail by indentation propagation, while coupon load and width direction density is more important to test cases which fail by crack propagation. The latter result is expected since mesh has a significant influence on continuum damage models.

The sensitivity study was used to show the importance of each input to the overall

model results. Each input was discussed with relation to overall model confidence. The most uncertainty in the model was found to come from the values which determine the amount that the stiffness associated with “damaged” elements are degraded from pristine material property values. The uncertainty in each input has some finite effect on the CAI model result, but confidence is achieved through careful and accurate measurement of the inputs during experimental testing. This concluded the development of the new CAI model in the present chapter. Chapter 6, which follows, will discuss the finite element analysis of each of the 32 experimental test coupons. The analysis results will be compared to experimental test results found in Chapter 2 and 3, and these results will ultimately be used to validate the use of the new model. In addition, specific attention will be given to the effect of core density (and resulting continuum core properties) on the failure strength and CAI failure mode of the test coupons. This will be done through a parametric study of varying core density.

Chapter 6

Analysis of Test Coupons and Other CAI Analysis Results

A new finite element model (FEM) for the compression after impact (CAI) analysis of thin-facesheet honeycomb core sandwich panels with low velocity impact damage has been developed. In Chapter 4, theory about the basics of classical laminate theory (CLT), ABAQUS finite element formulations, and continuum representation of homogenized honeycomb core material properties was discussed as pertinent to the new FEM. Also, in the chapter, the use of two models which represent the current state of development of finite element analysis (FEA) of CAI failure in honeycomb core test coupons was presented. The use of these models has shown that a limited representation of the indentation propagation failure mode existed prior to the current research.

Subsequently, in Chapter 5, the new developments of the current research for CAI analysis was presented. The two major advantages of the new model include the incorporation of a progressive failure analysis for damage propagation in the facesheets, and a detailed representation of the impact damage included in the model prior to the CAI analysis. The former's importance is two-fold. First, a more accurate representation of the indentation propagation failure mode can be achieved. Second, the new FEM has the ability to represent multiple failure modes, to include the crack propagation failure mode of the high density

honeycomb core materials found during the current research. The detailed impact damage representation has benefits as well. In addition to providing a more accurate representation of the CAI test coupons, each part of the damage was studied for its specific contribution to the CAI result.

The purpose of the present chapter is to validate the new FEM by comparing analysis results with experimental test results. In Chapters 2 and 3, tests were completed on several honeycomb core sandwich panel material systems. A total of 32 test coupons were damaged with a low velocity impact and tested to CAI failure. The impact damage in each of these test coupons was considered using non-destructive evaluation (NDE) techniques. This data, combined with some data taken using dissection of impact survey coupons, was used to define 32 total analyses. In the present chapter, the results of these analyses are compared with experimental test results. Comparisons are done primarily with respect to global coupon failure results (e.g. CAI failure load). In addition, results from alternate observation techniques are used, including time lapse images from high speed video photography, and measurements that were taken by digital image correlation (DIC).

6.1 Analysis of CAI Response of PXX Series Panels

The following section will be used to compare the analysis results obtained using the new FEM with experimental test results for PXX series CAI test coupons, which were discussed in Chapter 2. During these CAI tests, a total of eight coupons were tested to failure under end-loaded compressive conditions. Low velocity impact damage was inflicted on each of these test coupons, prior to compressive loading in the energy level range from 0.5 to 2.0 ft-lbs. Two coupons were impacted at each of the following energy levels: 0.5, 1.0, 1.5 and 2.0 ft-lbs. A unique FEM was created to represent each of the tested coupons, and an analysis was completed to assess the coupons' CAI response. The results of these analyses will be presented and compared to the experimental results, but first, each model will be described.

6.1.1 PXX Analysis Inputs

Each FEM used for analysis of PXX series CAI tests was defined with appropriate geometry. Since, the models take advantage of symmetry, a 3 in. by 3 in. quadrant of the 6 in. by 6 in. PXX test coupons was modeled with appropriate boundary conditions. The materials, discussed in more detail in Chapter 2, consisted of E-glass/Epoxy woven fabric facesheets with two 0.01 in. plies in each facesheet for a total thickness of 0.02 in. and 1 in. thick, 3 lb/ft³. Nomex honeycomb core. These dimensions were used to define the facesheets and core, respectively, in the FEM.

The material properties associated with the plies of the composite laminate facesheets are defined in Table 6.1. The lamina material properties are similar to the properties given by AAR composites [78], while the fiber and matrix constituent properties are the *in situ* properties calculated using the Helius Material Manager. Deviations in the lamina material properties from the AAR Composites provided properties were done when it was found during experimental testing that the Young's modulus was not accurate. The Young's modulus of all PXX series experimental test coupons was about 3.5 Msi. Additional material properties were consulted, and since the exact epoxy material was unknown, the Advanced General Aviation Transport Experiments (AGATE) properties for 3M E-Glass Fabric were chosen since they most closely resembled the experimentally determined stiffnesses. The strengths corresponding to E-glass/epoxy materials are given in Table 6.2 [98]. The strengths include the weave knee strengths, which are used by the commercial software, Helius:MCT, to predict matrix failure. The weave knee strengths were set at 85% of the lamina strengths.

In Table 6.3, the homogenized orthotropic properties for the continuum representation of the Nomex honeycomb core are given. These material properties were either given by the Hexcel Corp. data sheet [86], or were calculated by the appropriate equations found in Gibson and Ashby [55]. The flatwise compressive strength of the Nomex honeycomb was 270 psi. [86]; the corresponding compressive failure strain used in the ABAQUS user subroutine was 0.0135 in/in. Each analysis was displacement controlled. A sufficiently large displacement (usually 0.035 in.) was given in the input file; however, the analysis was usually not carried

Table 6.1: E-glass/Epoxy woven fabric lamina material properties used in the CAI analysis of PXX series test coupons.

E-glass Lamina	E_1 (Msi)	E_2 (Msi)	E_3 (Msi)	ν_{12}	ν_{13}	ν_{23}	G_{12} (Msi)	G_{13} (Msi)	G_{23} (Msi)
	3.482	3.482	1.507	0.138	0.412	0.412	0.541	0.336	0.336
Fiber Constants	E_1 (Msi)	E_2 (Msi)	E_3 (Msi)	ν_{12}	ν_{13}	ν_{23}	G_{12} (Msi)	G_{13} (Msi)	G_{23} (Msi)
	9.924	9.924	9.924	0.185	0.185	0.156	3.978	3.978	4.291
Matrix Constants	E_1 (Msi)	E_2 (Msi)	E_3 (Msi)	ν_{12}	ν_{13}	ν_{23}	G_{12} (Msi)	G_{13} (Msi)	G_{23} (Msi)
	0.396	0.396	0.396	0.407	0.407	0.407	0.141	0.141	0.141

Table 6.2: E-glass/Epoxy woven fabric lamina strengths used in the CAI analysis of PXX series test coupons.

Lamina Strengths	$^{(+)}S_{11}$ (ksi)	$^{(-)}S_{11}$ (ksi)	$^{(+)}S_{22}$ (ksi)	$^{(-)}S_{22}$ (ksi)	$^{(+)}S_{33}$ (ksi)	$^{(-)}S_{33}$ (ksi)	S_{12} (ksi)	S_{13} (ksi)	S_{23} (ksi)
	47.00	-51.00	47.00	-51.00	47.00	-51.00	17.00	0.00	0.00
Knee Strengths	Tensile (ksi)		Compressive (ksi)		In-plane Shear (ksi)				
	39.95		-43.35		14.45				

out until the maximum applied displacement due to convergence problems which appear post-failure in the analysis. This does not affect the CAI response and failure that the analysis predicts, but limit the usefulness of the model for post-failure response analysis. (Post-failure response was not a goal of these analyses.)

Table 6.3: 3PCF Nomex honeycomb core orthotropic engineering constants used in the CAI analysis of PXX and 3PCF-XX series test coupons.

3PCF Core	E_1 (ksi)	E_2 (ksi)	E_3 (ksi)	ν_{12}	ν_{13}	ν_{23}	G_{12} (ksi)	G_{13} (ksi)	G_{23} (ksi)
	0.500	0.500	20.0	0.500	0.000	0.000	0.125	4.50	2.50

Damage incorporated into the model to simulate the low velocity impact damage was detailed in Chapter 5. The components of this damage first included a geometric dent, defined by a maximum diameter and depth. Also, a specific set of core elements was defined as “damaged” based on experimental observations. This region requires a depth and diameter, as well as a stiffness degradation to be specified. Next, a set of facesheet elements was defined

as damaged based on the presence of inter-fiber fracture (IFF). This set was defined by a measured diameter, and a stiffness degradation of the matrix constituent material properties. Finally, for highly damaged test coupons, a second set of elements was included, along the x-axis (width direction) of the FEM, defined using a length, measured from the model’s coordinate system origin, to represent fiber fracture. A fiber constituent material property degradation was also included in this region, in addition to the matrix property degradation.

The dent depth and diameter definition was taken from the actual experimental measurements of individual PXX series CAI test coupon, prior to compressive loading. The inputs of damaged core region depth and diameter, as well as the damaged facesheet region diameter (and length for the fiber damaged region in highly damaged coupons), was taken from results of the drop tower impact survey of damage formation. Thus, models of test coupons impacted at the same impact energy (e.g. P11 and P12, or P04 and P05) have identical inputs for these damage components. The numeric values which concern the geometry of the impact damage dent and the damaged material regions can be found in Table 6.4.

Table 6.4: MATLAB program inputs for creation of ABAQUS input files to run analyses of PXX series test coupons.

FEM Coupon Name	Impact Energy Represented (ft-lb.)	Residual Dent Diameter (in.)	Residual Dent Depth (in.)	Damaged Core Region Diameter (in.)	Damaged Core Region Depth (in.)	Facesheet IFF Region Diameter (in.)	Facesheet Fiber Fracture Region Length (in.)
P04	1.0	0.6	0.014	0.8876	0.1340	0.2326	Not Applicable
P05	1.0	0.6	0.017	0.8876	0.1340	0.2326	Not Applicable
P06	1.5	0.8	0.042	0.9447	0.1247	0.2367	Not Applicable
P07	1.5	0.8	0.048	0.9447	0.1247	0.2367	Not Applicable
P08	2.0	0.9	0.061	1.0606	0.1194	0.4206	0.400
P09	2.0	1.0	0.069	1.0606	0.1194	0.4206	0.400
P11	0.5	0.4	0.005	0.6417	0.1061	0.1250	Not Applicable
P12	0.5	0.3	0.005	0.6417	0.1061	0.1250	Not Applicable

The three values which define the material property degradation in all analysis models are as follows.

1. The stiffness of “damaged” core element was reduced to 60% of the pristine properties.

2. The stiffness of the matrix constituent properties of “damaged” elements in the IFF region of the facesheet model was reduced to 10% of the pristine properties.
3. For the fiber fracture region in some analysis models, fiber properties are reduced to 1% of their pristine value in addition to the 90% reduction in matrix properties.

6.1.2 PXX Analysis Results

A set of analyses on the CAI response and failure of each of the eight PXX series test coupons was performed. First, to demonstrate the appropriate response of the coupon at failure, the reaction force vs. applied displacement is considered. From experimental testing, in Chapter 2, it is expected that at failure, a sudden, instantaneous drop in reaction force will occur. This response is demonstrated in the reaction force vs. the applied displacement results obtained for each of the eight analyses, which are shown in Fig. 6.1. The reaction force is obtained in the analysis by summing the force resultant at each node where displacement is applied, and then multiplying by two (since symmetry is used).

For the PXX series tests, the failure mode expected is indentation propagation. In order to correctly predict this failure mode, the present model needs to be able to predict local buckling of the facesheet as well as the facesheet crack which propagates with the region of local buckling. The present model is highly successful at capturing this failure mode, as shown in Fig. 6.2, through the use of a non-linear core model, as well as simulated facesheet failure using the implementation of progressive failure analysis. In Fig. 6.2, the indentation propagation failure of an example test coupon, as predicted by analysis, is compared to a sequence of photos from high speed photography, which was first shown in Chapter 2. Model results for out-of-plane displacement shows where local buckling as occurred. Model results for element damage show how damage propagates in both the core (by crushing), and the facesheets (simulating crack propagation).

The typical results used to establish the condition of the simulated sandwich panel coupon at CAI failure are failure load, failure stress, and failure strain. The results obtained for the analysis of PXX series coupons are shown in Table 6.5. The results for failure stress

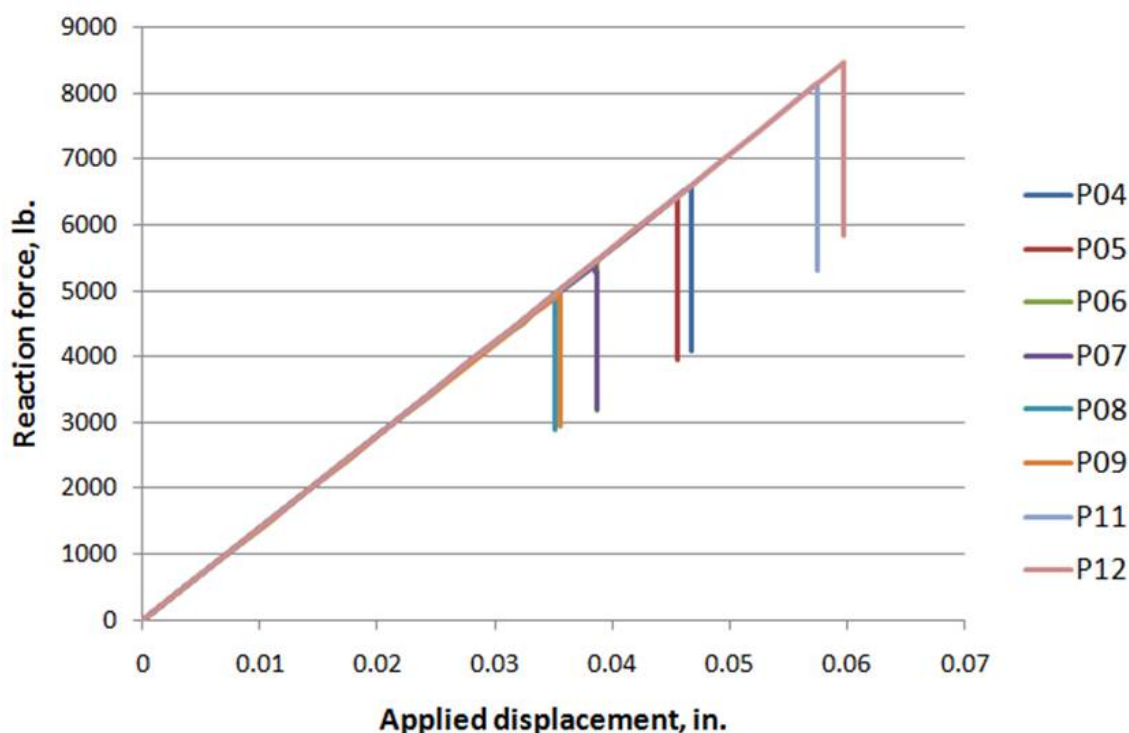


Figure 6.1: PXX analysis results: reaction force vs. applied displacement for analysis of PXX series test coupons.

were used for validation of the model by comparison to experimental test results, although if failure load or strain had been used, the results would have been similar. The results comparison is shown in Fig. 6.3.

The correct failure mode, indentation propagation, was established for all eight of the analyses completed. The analysis results for CAI strength of the eight PXX test coupons show good agreement with experimental test results. The error range was from about 20%, to less than a percent; the largest error pertains to the two lightly damaged test cases, P11 and P12. Although the largest errors are significant, the analysis results are conservative. More importantly, however, the analysis results and experimental test results appear to approach similar minimum levels of coupon strength with increasing impact energy. This phenomenon, where a minimum failure stress is approached, is the basis for the CAI failure strength which typically appears in literature. The ability of the FEM to predict this behavior is a strong indication that a significant level of fidelity has been achieved.

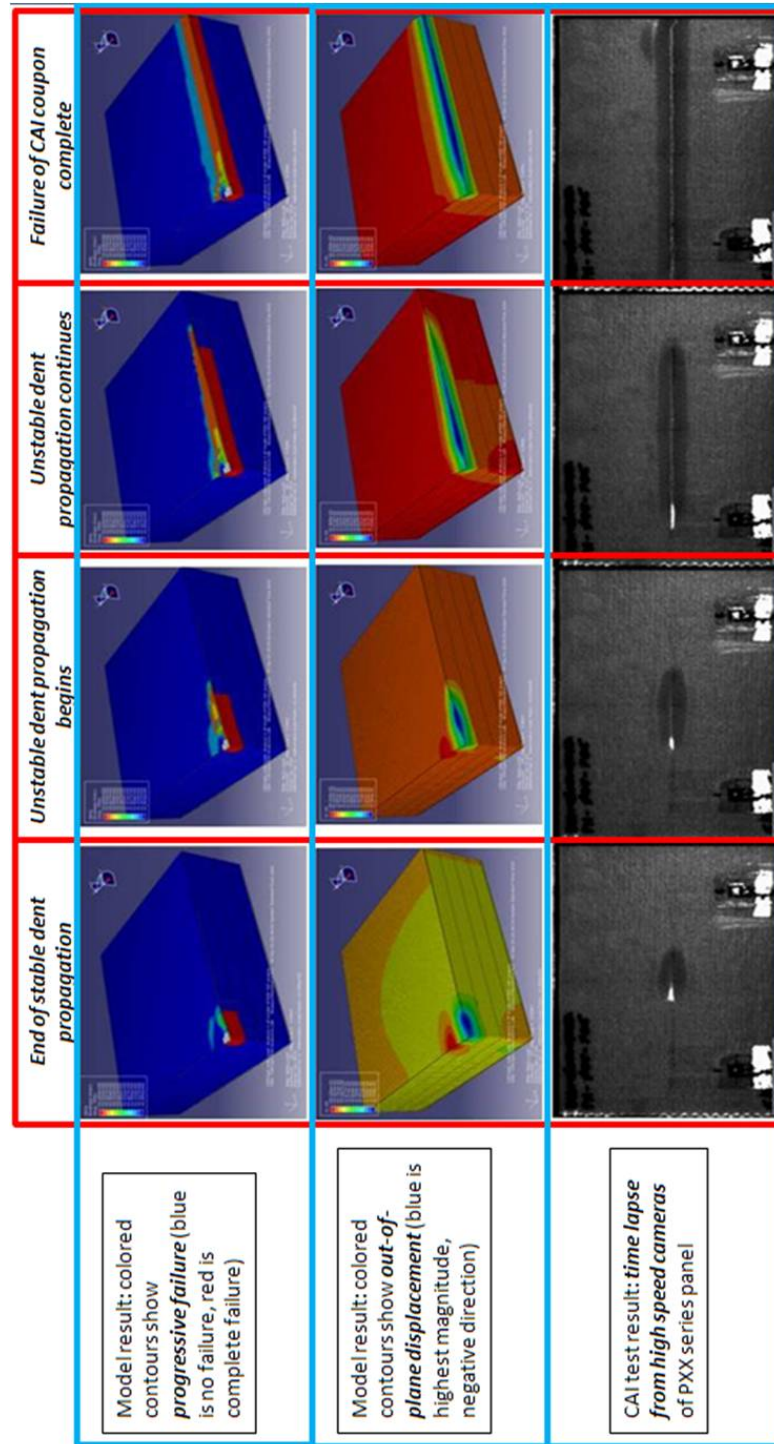


Figure 6.2: Demonstration of correct failure mode prediction for example analysis of PXX series material coupons using the new FEM for CAI analysis.

Table 6.5: PXX analysis results: failure load, strength and strain for analysis of PXX series test coupons.

Panel	Impact Energy (ft-lb)	Analysis Failure Load (lb.)	Tested Failure Load (lb.)	Error (%)	Analysis Failure Strength (ksi)	Tested Failure Strength (ksi)	Error (%)	Analysis Failure Strain (μ -in/in)	Tested Failure Strain (μ -in/in)	Error (%)
P11	0.5	8147	7276	12.0	37.03	30.83	20.1	10445	8674	20.4
P12	0.5	8476	7301	16.1	38.53	30.94	24.5	10859	8885	22.2
P04	1.0	6594	6330	4.2	29.97	26.82	11.7	8489	7700	10.2
P05	1.0	6436	6116	5.2	29.25	25.92	12.8	8290	7283	13.8
P06	1.5	5422	5619	-3.5	24.64	23.81	3.5	7024	6760	3.9
P07	1.5	5417	5769	-6.1	24.62	24.44	0.7	7022	6900	1.8
P08	2.0	4898	5289	-7.4	22.27	22.41	-0.6	6377	6643	-4.0
P09	2.0	4951	5363	-7.7	22.50	22.72	-1.0	6462	6332	2.1

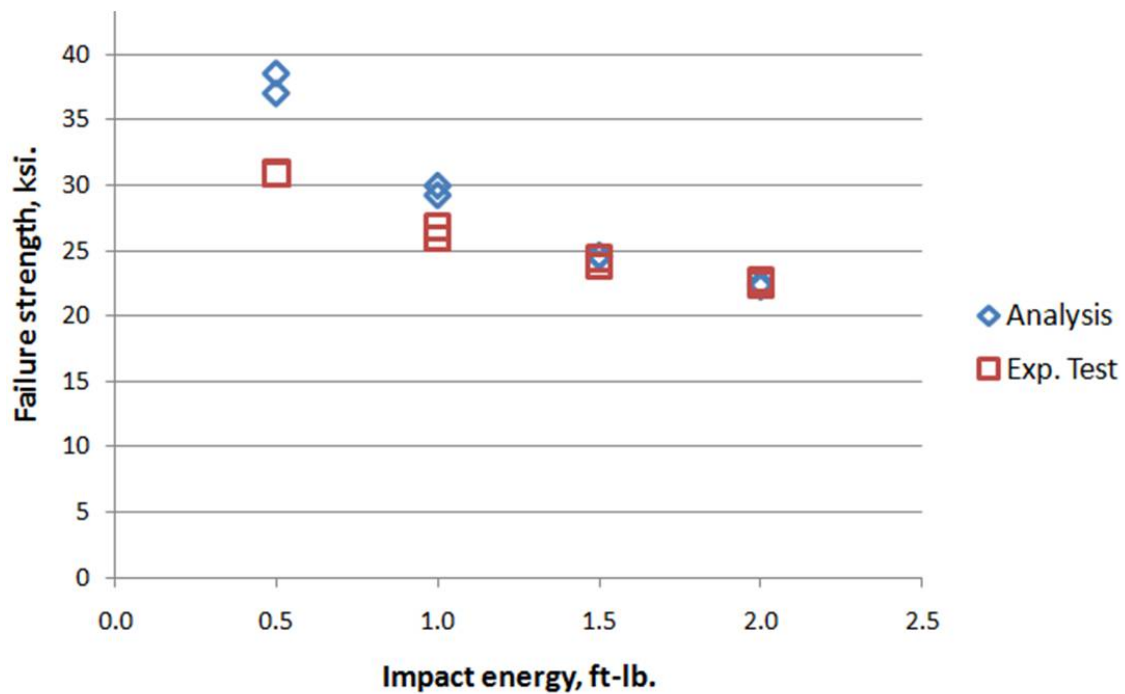


Figure 6.3: PXX analysis results: comparison of PXX test coupon analysis failure strength to experimental test results.

One final comparison which can be made between the PXX series analysis results and experimental test results is of indentation growth predicted during analysis to measure-

ments taken using the digital image correlation (DIC) system during experimental testing. A DIC system is used to take full-field displacement measurements and is capable of full-field, three-dimensional surface mapping. For comparisons, similar data from analysis was collected using the ABAQUS post-processor, ABAQUS/Viewer. In Chapter 2, DIC measurements were shown for the size of the indentation in the front damaged facesheet of select panels throughout the linear elastic portion of the CAI test, to show the magnitude of the stable indentation propagation. The measurements that were taken included the maximum length of the elliptical indentation along its semi-major axis (taken in the coupon width or X-direction), the maximum width of the elliptical indentation along its semi-minor axis (taken in the coupon load or Y-direction), and the maximum depth of the indentation. For comparison purposes, the corresponding length, width, and depth of the CAI analysis predicted indentation propagation (found using ABAQUS/Viewer) is shown in Figs. 6.4, 6.5, and 6.6, respectively.

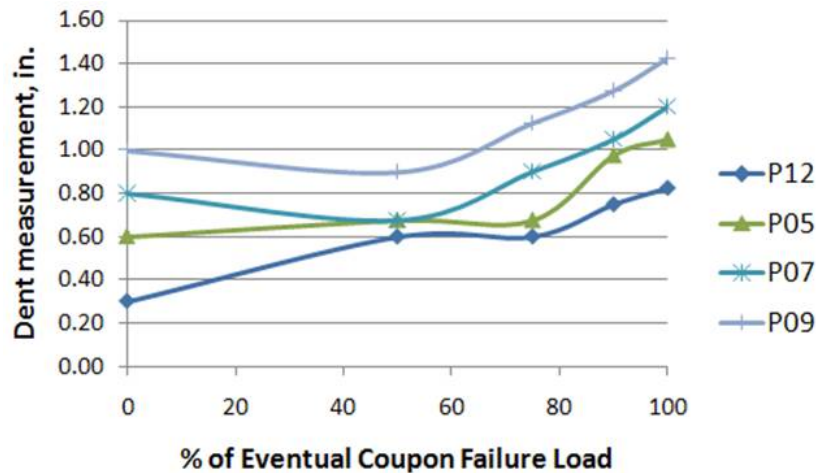


Figure 6.4: PXX analysis results: dent growth in the coupon width direction (x-direction) predicted from FEA of PXX test coupons.

The indentation growth in Figs. 6.4, 6.5, and 6.6 is very similar to the DIC experimental test results shown in Figs. 2.34, 2.35, and 2.36, respectively. It should be noted that the four test cases used in each figure are the same for both analysis and experimental test results. The analysis successfully demonstrates stable dent growth in the coupon width

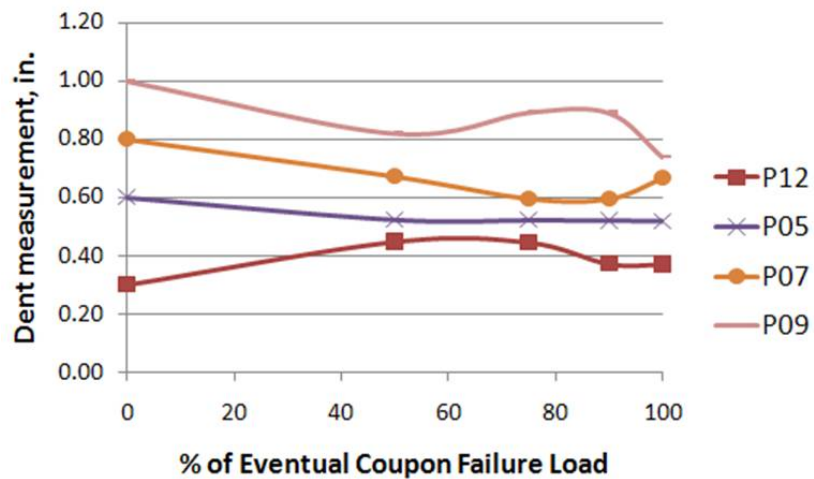


Figure 6.5: PXX analysis results: dent growth in the coupon load direction (y-direction) predicted from FEA of PXX test coupons.

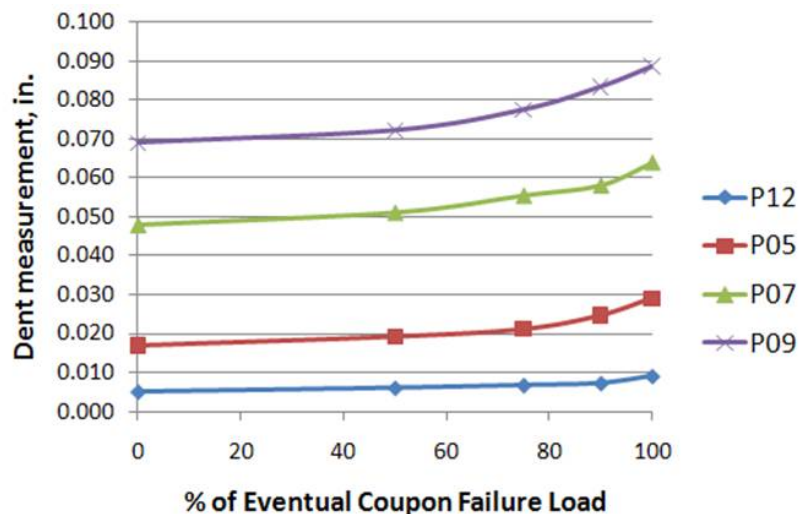


Figure 6.6: PXX analysis results: maximum dent depth growth predicted from FEA of PXX test coupons.

direction (also the analysis x-direction), while the size of the dent remains nearly constant in the load direction. The size of the FEM dent stays approximately unchanged until 50% of the coupon's eventual failure load, which is expected from experimental testing. The magnitude of the dent growth in analysis does not reach the same amount of dent growth as found experimentally. The final dent size just before failure is smaller during FEA. This is readily apparent in the results for the maximum depth. The maximum dent depth at failure, in

each of the four cases considered, is a whole order of magnitude less than the maximum dent depth at failure found from the DIC result. This can be seen by comparing Fig. 6.6 with Fig. 2.36.

6.2 Analysis of CAI Response of 3PCF-XX Series Panels

CAI tests were conducted on two additional, nearly identical, sandwich panels, with the only difference in construction being the density of the honeycomb core. The experimental testing on these materials was described in Chapter 3. The first of these materials, given the designation 3PCF-XX, contained the lower of the two core densities. It was expected, and in fact found, that the CAI failure mode (indentation propagation) of the 3PCF-XX test coupons would be identical to that of the PXX series panels. In the following section, the CAI analysis results for 3PCF-XX series test specimens will be compared with experimental test results for these panels. For the 3PCF-XX series CAI tests, a total of twelve coupons were tested to failure. Low velocity impact damage was inflicted on each of these test coupons, prior to compressive loading. Three coupons were impacted at each of the following four energy levels: 1.0, 3.0, 5.0 and 7.0 ft-lbs. An analysis of each coupon has been completed using a unique FEM using inputs from observations made on experimental test coupon. The following section will describe the inputs used to create the FEM, the analysis results, and the experimental test comparison.

6.2.1 3PCF-XX Analysis Inputs

Each FEM, which takes advantage of symmetry as described in Chapter 5, represents a 2.75 in. by 2.75 in. quadrant of a 3PCF-XX series coupon. The 0.02 in. thick facesheets consisted of woven S2-glass plies, and the core was a 0.75 in. thick 3 lb/ft³. Nomex honeycomb. Additional material details can be found in Chapter 3. The elastic facesheet material properties used in the analyses are summarized in Table 6.6. The lamina material properties

are similar to the those published for the material by the National Institute of Aerospace Research (NIAR) [85], though they differ slightly due to processing by the Helius Material Manager. The matrix and fiber constituent properties are the *in situ* properties calculated by the Material Manager. The material strengths used can be found in Table 6.7 for the S2-glass/epoxy facesheets, which includes the knee strengths for matrix failure prediction, which are set at 85% of the lamina strengths. The material strengths are based on the NIAR data [85], except the in-plane shear strength which was artificially increased to prohibit unrealistic matrix failure during analysis in the 45 degree plies. (It can also be noted that the experimental test results for in-plane shear, which can be obtained by contacting the NIAR test engineers, do not exhibit a true failure point. The engineers stop the test prior to failure once 5% strain was reached.)

The material properties used in the continuum representation of the Nomex honeycomb are shown in Table 6.3, previously. These material properties were either given by in the literature by Hexcel Corp. [86], or were calculated using the equations found in Gibson and Asby [55]. The out-of-plane compressive failure strength was again 270 psi [86] and the corresponding compressive failure strain for the Nomex honeycomb was 0.0135 in/in. Each analysis was displacement controlled, similar to the description given in the previous section for the PXX series analyses.

Table 6.6: S2-glass/Epoxy woven fabric lamina material properties used in the CAI analysis of 3PCF-XX and 6PCF-XX series test coupons.

S2-glass	E_1 (Msi)	E_2 (Msi)	E_3 (Msi)	ν_{12}	ν_{13}	ν_{23}	G_{12} (Msi)	G_{13} (Msi)	G_{23} (Msi)
Lamina	4.622	4.527	1.287	0.109	0.361	0.362	0.613	0.385	0.385
Fiber	E_1 (Msi)	E_2 (Msi)	E_3 (Msi)	ν_{12}	ν_{13}	ν_{23}	G_{12} (Msi)	G_{13} (Msi)	G_{23} (Msi)
Constants	15.70	11.59	11.59	0.254	0.254	0.201	6.656	6.656	4.825
Matrix	E_1 (Msi)	E_2 (Msi)	E_3 (Msi)	ν_{12}	ν_{13}	ν_{23}	G_{12} (Msi)	G_{13} (Msi)	G_{23} (Msi)
Constants	0.466	0.466	0.466	0.331	0.331	0.331	0.175	0.175	0.175

The components of impact damage used to define the geometry of “damaged” regions of the model and the appropriate material properties are as described in the previous section

Table 6.7: S2-glass/Epoxy woven fabric laminate strengths used in the CAI analysis of 3PCF-XX and 6PCF-XX series test coupons.

Lamina Strengths	⁽⁺⁾ S ₁₁ (ksi)	⁽⁻⁾ S ₁₁ (ksi)	⁽⁺⁾ S ₂₂ (ksi)	⁽⁻⁾ S ₂₂ (ksi)	⁽⁺⁾ S ₃₃ (ksi)	⁽⁻⁾ S ₃₃ (ksi)	S ₁₂ (ksi)	S ₁₃ (ksi)	S ₂₃ (ksi)
	79.92	-69.07	79.92	-69.07	79.92	-69.07	15.00	0.00	0.00
Knee Strengths	Tensile (ksi)		Compressive (ksi)		In-plane Shear (ksi)				
	67.93		-58.71		13.00				

for the PXX series coupons. Further detail was described in Chapter 5. The numeric values which govern the geometry of the impact damage dent and the damaged material regions in the 3PCF-XX analysis models can be found in Table 6.8.

Table 6.8: MATLAB program inputs for creation of ABAQUS input files to run analyses of 3PCF-XX series test coupons.

FEM Coupon Name	Impact Energy Represented (ft-lb.)	Residual Dent Diameter (in.)	Residual Dent Depth (in.)	Damaged Core Region Diameter (in.)	Damaged Core Region Depth (in.)	Facesheet IFF Region Diameter (in.)	Facesheet Fiber Fracture Region Length (in.)
3PCF-01	3.0	0.917	0.0050	1.0612	0.1670	0.3360	Not Applicable
3PCF-02	1.0	0.633	0.0050	0.8695	0.1000	0.2790	Not Applicable
3PCF-03	3.0	1.033	0.0195	1.0612	0.1670	0.3360	Not Applicable
3PCF-05	1.0	0.717	0.0060	0.8695	0.1000	0.2790	Not Applicable
3PCF-07	7.0	1.300	0.2170	1.0922	0.2273	0.5910	0.458
3PCF-08	5.0	1.200	0.1500	1.0929	0.1570	0.5220	0.345
3PCF-09	7.0	1.400	0.1755	1.0922	0.2273	0.5910	0.458
3PCF-10	5.0	1.300	0.1195	1.0929	0.1570	0.5220	0.345
3PCF-12	5.0	1.283	0.1400	1.0929	0.1570	0.5220	0.345
3PCF-13	3.0	0.983	0.0190	1.0612	0.1670	0.3360	Not Applicable
3PCF-15	1.0	0.633	0.0045	0.8695	0.1000	0.2790	Not Applicable
3PCF-16	7.0	1.333	0.1820	1.0922	0.2273	0.5910	0.458

The three values which define the material property degradation in all analysis models are as follows, and they are identical to those used for PXX series analyses:

1. The stiffness of “damaged” core element is reduced to 60% of the pristine properties.
2. The stiffness of the matrix constituent properties of “damaged” elements in the IFF region of the facesheet model is reduced to 10% of the pristine properties.

3. For the fiber fracture region in some analysis models, fiber properties are reduced to 1% of their pristine value in addition to the reduction in matrix properties.

6.2.2 3PCF-XX Analysis Results

The indentation propagation failure mode was demonstrated for each of the 3PCF-XX analyses completed, as expected from experimental testing discussed in Chapter 3. The FEM representation of this failure mode was shown previously for a PXX series example in Fig. 6.2. The appropriate reaction force vs. applied displacement was also predicted in each analysis, where a sudden drop in reaction force is found at failure. This response is demonstrated for the 3PCF-XX series analysis in Fig. 6.7.

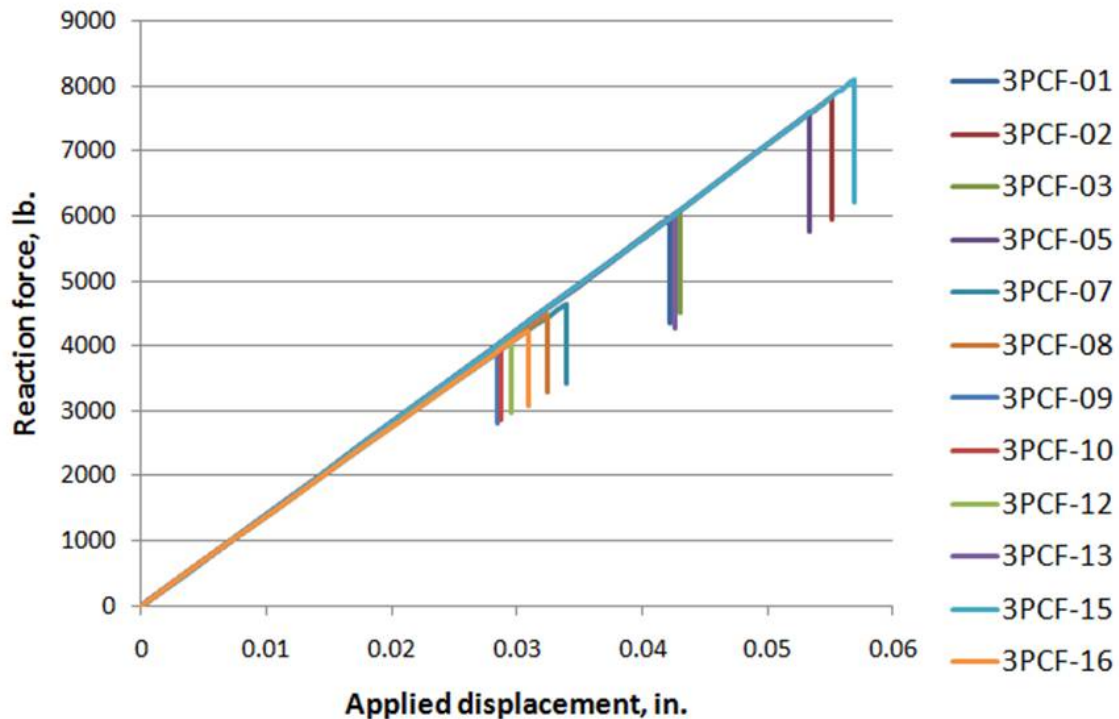


Figure 6.7: 3PCF-XX analysis results: reaction force vs. applied displacement for analysis of 3PCF-XX series test coupons.

The main comparisons between analysis results and experimental test results will again be made using results for coupon failure strength. Results can also be obtained from FEA for failure load and failure strain. The results obtained for the analysis of 3PCF-XX

series coupons are shown in Table 6.9, for each predicted CAI failure analysis result, with comparisons to experimental test results and the associated errors. The results comparison is shown graphically, in Fig. 6.8, for CAI failure strength of the 3PCF-XX series specimens, though this comparison would be similar if shown for failure load or failure strain.

Table 6.9: 3PCF-XX analysis results: failure load, strength and strain for analysis of 3PCF-XX series test coupons.

Panel	Impact Energy (ft-lb)	Analysis Failure Load (lb.)	Tested Failure Load (lb.)	Error (%)	Analysis Failure Strength (ksi)	Tested Failure Strength (ksi)	Error (%)	Analysis Failure Strain (μ -in/in)	Tested Failure Strain (μ -in/in)	Error (%)
3PCF-02	1.0	7838	6953	12.7	35.63	31.61	12.7	10019	8323	20.4
3PCF-05	1.0	7589	7459	1.7	34.5	33.91	1.7	9706	8865	9.5
3PCF-15	1.0	8094	7307	10.8	36.79	33.21	10.8	10341	9117	13.4
3PCF-01	3.0	5949	6450	-7.8	27.04	29.32	-7.8	7662	8005	-4.3
3PCF-03	3.0	6082	6583	-7.6	27.64	29.92	-7.6	7820	8150	-4.0
3PCF-13	3.0	6020	6406	-6.0	27.36	29.12	-6.0	7741	8033	-3.6
3PCF-08	5.0	4481	5786	-22.6	20.37	26.30	-22.5	5891	7094	-17.0
3PCF-10	5.0	3978	5206	-23.6	18.08	23.66	-23.6	5222	6670	-21.7
3PCF-12	5.0	4083	5097	-19.9	18.56	23.17	-19.9	5377	6732	-20.1
3PCF-07	7.0	4650	5283	-12.0	21.14	24.01	-12.0	6173	6701	-7.9
3PCF-09	7.0	3880	5103	-24.0	17.64	23.20	-24.0	5157	6549	-21.3
3PCF-16	7.0	4228	4837	-12.6	19.22	21.99	-12.6	5608	6597	-15.0

Many of the 3PCF-XX analysis results show good agreement with experimental test results. The error ranged in magnitude from about 20% to less than a percent, for failure load, strength, and strain. Although the largest errors are significant, the analysis results are generally conservative, except for the test coupons with the lowest amounts of damage. From this result, it can be concluded that the damage included in the analysis of 3PCF-XX test coupons to represent a low velocity impact at 1.0 ft-lbs. was non-conservative. The analysis results for failure strength approach a minimum, which is shown by comparison of the analysis results for the models with damage representing both 5.0 and 7.0 ft-lbs. energy level impacts. The failure stress result for each of these six analysis data points are similar. The behavior of the CAI models with large amounts of damage suggests that the model

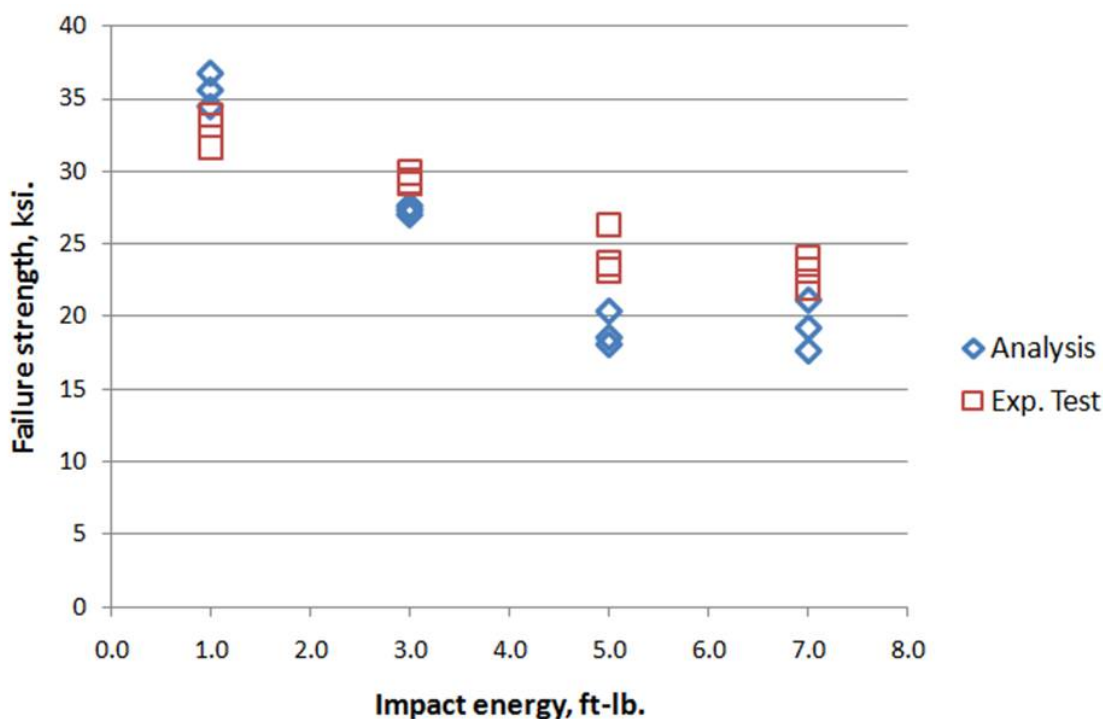


Figure 6.8: 3PCF-XX analysis results: comparison of 3PCF-XX test coupon analysis failure strength to experimental test results.

would be useful in estimating the CAI strength of coupons which fail by the indentation propagation failure mode.

A comparison can again be made between the stable dent growth predicted in the FEA and the stable dent growth measured using the DIC system. The DIC system was used for a select set of four 3PCF-XX series test coupons, and was discussed previously in Chapter 3. Results for the predicted indentation growth found during analysis were also produced using the ABAQUS/Viewer for these four test cases. One test case was considered at each of the four damage levels (1.0, 3.0, 5.0 and 7.0 ft-lbs.) The analysis results for the dent length measurements in the coupon width (x-) direction, coupon load (y-) direction, and the dent depth measurement in the through the thickness (z-) direction are shown in Figs. 6.9, 6.10, and 6.11, respectively. These analysis results can be compared to the DIC experimental results shown in Figs. 3.32, 3.33, and 3.34, respectively.

The results for dent growth during FEA of 3PCF-XX series tests, and the comparison

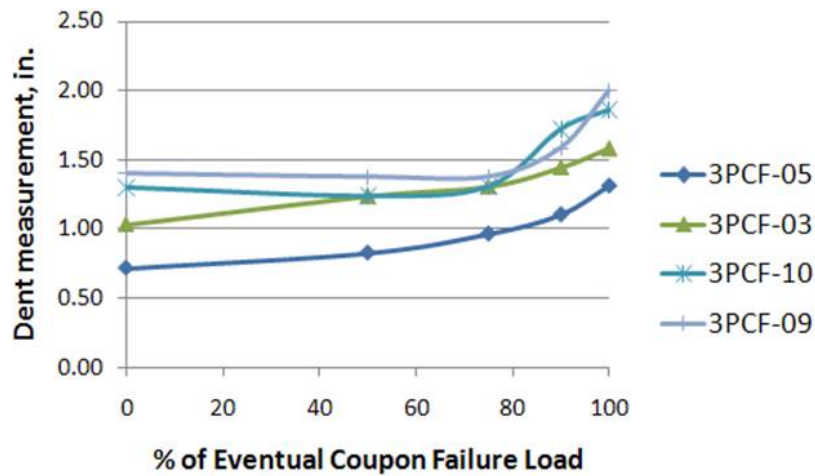


Figure 6.9: 3PCF-XX analysis results: dent growth in the coupon width direction (x-direction) predicted from FEA of 3PCF-XX test coupons.

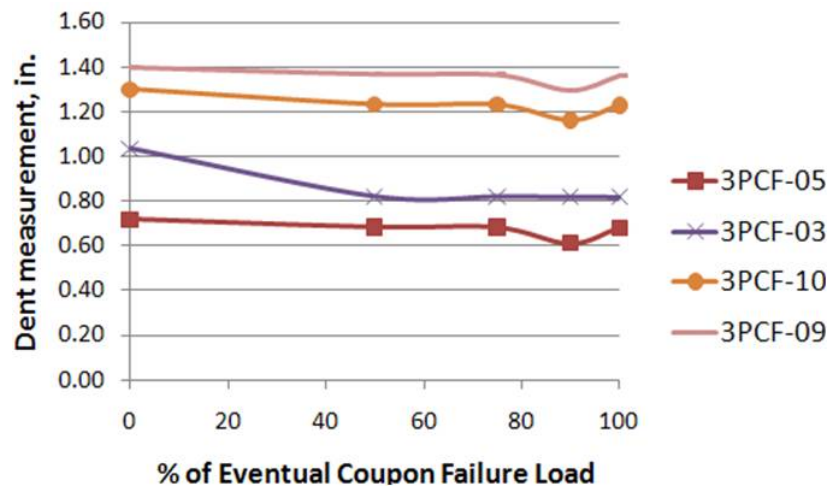


Figure 6.10: 3PCF-XX analysis results: dent growth in the coupon load direction (y-direction) predicted from FEA of 3PCF-XX test coupons.

to experimental test results, was very similar to the results previously shown for PXX series tests. As expected from experimental testing, more growth is seen in the coupon width direction, than in the coupon load direction. The stable dent growth measurement in the width direction is only slightly smaller than the measurements taken with the DIC system. However, as seen in PXX series results, the dent depth does not obtain the same amount of growth seen in DIC measurements of 3PCF-XX series experimental tests. This can be shown by comparison of Fig. 6.11 to Fig. 3.34. The dent depths found in analysis are about

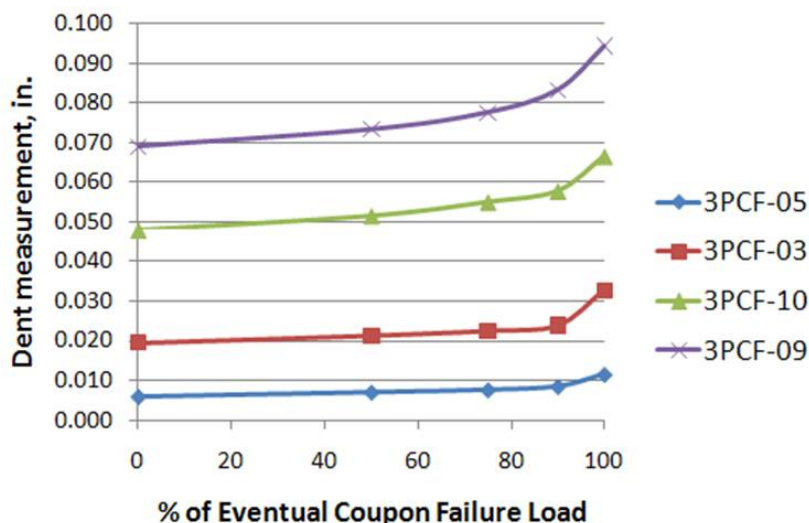


Figure 6.11: 3PCF-XX analysis results: maximum dent depth growth predicted from FEA of 3PCF-XX test coupons.

half the size at failure as the corresponding measurements taken in experimental tests. From this result, it appears that the model is less stable and more prone to local buckling due to out-of-plane deformation than an experimental test panel.

6.3 Analysis of CAI Response of 6PCF-XX Series Panels

Analysis of the second of two nearly identical honeycomb core sandwich panels, described in Chapter 3, will be discussed in the following section. The only difference in the construction of these two materials was the density of the honeycomb core. The subject of the current section, dubbed 6PCF-XX, contained the higher density core. A different failure mode, called crack propagation in the current research, was found to result from the presence of the high density honeycomb core. CAI analysis results obtained for the 6PCF-XX series test coupons will be compared with experimental test results in this section. Like the 3PCF-XX series CAI tests, a total of twelve 6PCF-XX coupons were tested to failure. Low velocity impact damage was inflicted on these test coupons at each of the following four energy levels: 1.0,

3.0, 5.0 and 7.0 ft-lbs. The following section describes each CAI analysis completed, the analysis results, and then the comparison to the experimental test results.

6.3.1 6PCF-XX Analysis Inputs

The geometry of the 6PCX-XX test coupon models was identical to those described previously for the 3PCF-XX set. Complete details on the construction of these materials were given in Chapter 3. The elastic material properties used in the analyses were summarized in Table 6.6 for the S2-fiberglass/Epoxy facesheets, and the corresponding lamina strengths and knee strengths were given in Table 6.7. These values are similar to those available in the literature [85], but some differences were discussed in the previous section. The elastic material properties for the higher density 6 lb/ft³. (6PCF) honeycomb core are given in Table 6.10. These properties are either given in by Hexcel Corp. [86], or were calculated using the relations found in Gibson and Ashby [55]. The out-of-plane compressive failure stress for the higher density, 6PCF, Nomex core was 925 psi [86], and the corresponding compressive strain value used to mark the onset of flatwise compressive failure in the ABAQUS UMAT was 0.0154 in/in. Each analysis was again displacement controlled as described in Section 6.1.1.

Table 6.10: 6PCF Nomex honeycomb core orthotropic engineering constants used in the CAI analysis of 6PCF-XX series test coupons.

6PCF Core	E_1 (ksi)	E_2 (ksi)	E_3 (ksi)	ν_{12}	ν_{13}	ν_{23}	G_{12} (ksi)	G_{13} (ksi)	G_{23} (ksi)
	1.500	1.500	60.0	0.500	0.000	0.000	0.375	13.00	6.50

The components of impact damage used to define the geometry of “damaged” regions of the model and the appropriate material properties are as described previously in the current chapter, and in further detail in Chapter 5. The numeric values which govern the geometry of the impact damage dent and the damaged material regions in the 6PCF-XX analysis models can be found in Table 6.11. As was mentioned in previous sections, the dent depth and diameter were measured using the individual experimental test coupons prior to

compressive loading. Other inputs were taken from coupons used in the damage formation tests when destructive evaluation techniques were necessary. Thus, they are common to a particular impact energy level (e.g. the damaged core region geometry will be the same for all analysis models representing coupons damaged at 3.0 ft-lbs. impact energies). The three values which define the material property degradation in all analysis models are as follows, and are identical to those used in PXX and 3PCF-XX series analyses:

1. The stiffness of “damaged” core element is reduced to 60% of the pristine properties.
2. The stiffness of the matrix constituent properties of “damaged” elements in the IFF region of the facesheet model is reduced to 10% of the pristine properties.
3. For the fiber fracture region in some analysis models, fiber properties are reduced to 1% of their pristine value in addition to the reduction in matrix properties.

Table 6.11: MATLAB program inputs for creation of Abaqus input files to run analyses of 6PCF-XX series test coupons.

FEM Coupon Name	Energy Represented (ft-lb.)	Dent Diameter (in.)	Residual Dent Depth (in.)	Damaged Core Region Diameter (in.)	Damaged Core Region Depth (in.)	Facesheet IFF Region Diameter (in.)	Facesheet Fiber Fracture Region Length (in.)
6PCF-01	7.0	1.000	0.1605	0.8595	0.1999	0.6010	0.498
6PCF-02	3.0	0.783	0.0155	0.7738	0.1791	0.4970	Not Applicable
6PCF-03	5.0	0.833	0.1220	0.8200	0.1415	0.5830	0.493
6PCF-06	5.0	0.917	0.1190	0.8200	0.1415	0.5830	0.493
6PCF-07	1.0	0.583	0.0060	0.6718	0.1088	0.4440	Not Applicable
6PCF-09	3.0	0.633	0.0170	0.7738	0.1791	0.4970	Not Applicable
6PCF-10	1.0	0.517	0.0055	0.6718	0.1088	0.4440	Not Applicable
6PCF-11	7.0	0.900	0.1560	0.8595	0.1999	0.6010	0.498
6PCF-12	5.0	0.867	0.1080	0.8200	0.1415	0.5830	0.493
6PCF-14	7.0	1.000	0.1590	0.8595	0.1999	0.6010	0.498
6PCF-15	3.0	0.800	0.0185	0.7738	0.1791	0.4970	Not Applicable
6PCF-16	1.0	0.583	0.0060	0.6718	0.1088	0.4440	Not Applicable

6.3.2 6PCF-XX Analysis Results

The newly developed FEM for analysis of CAI test coupons was used to study the 6PCF-XX series test coupons. This set of materials was of particular interest during analysis, because one of the principal contributions of the current research is the implementation of progressive failure analysis (PFA) of the FEM facesheets. This inclusion gives the model the ability to predict a new failure mode, crack propagation, not previously shown in sandwich panel CAI analysis. The following results will show that the new model is successful in predicting crack propagation failure in each of the twelve 6PCF-XX CAI test coupons with the higher density 6 lb/ft³. Nomex honeycomb core. First, to demonstrate the appropriate response of the coupon at failure, the reaction force vs. applied displacement is considered. From the results of experimental testing, discussed in Chapter 3, it is expected that at failure an instantaneous drop in reaction force will occur. This is demonstrated in the FEA analysis results for reaction force vs. applied displacement, which are shown in Fig. 6.12.

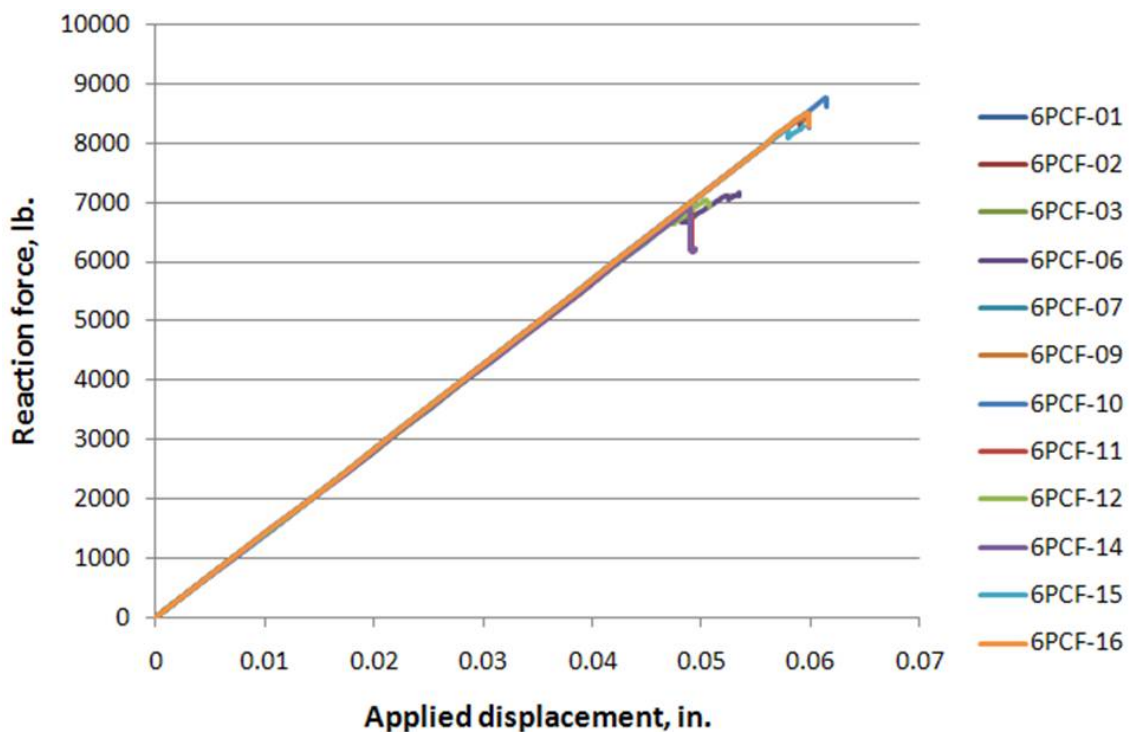


Figure 6.12: 6PCF-XX analysis results: reaction force vs. applied displacement for analysis of 6PCF-XX series test coupons.

For most of the results shown in Fig. 6.12, there was a very clear reduction in reaction force, although it is not as large as seen in previous analysis results for PXX and 3PCF-XX series materials, shown in Figs. 6.1 and 6.7, respectively. Once the drop in reaction force begins in the 6PCF-XX analysis results, the ABAQUS/Standard solver begins to demonstrate poor solution convergence in each subsequent iteration, more so than it did for the indentation propagation failure. The result is that either the ABAQUS/Standard solver exits, or a user input halts the analysis to keep the size of the resulting ABAQUS output database file (.ODB file) reasonable. One analysis, for the 6PCF-06 coupon, continues to increase in reaction force once initial reduction has been reached. Although the soft discontinuity, or “crack” in the FEM has propagated across the front facesheet, the coupon still continues to hold substantial load. This is due to softening of elements after matrix failure, generally when excess matrix failure occurs, prohibiting appropriate fiber failure later. The possibility of this occurring is one drawback of using a continuum damage model for PFA in the current research. It was noted during the course of the research, that for a less dense mesh this was less likely to occur. Adjusting the mesh is thus one solution which can be used to obtain a better result.

For the 6PCF-XX series material coupons, the failure mode expected from the experimental test results is crack propagation. It is expected that, in the linear elastic portion of a 6PCF-XX test coupon’s CAI response, there will be minimal growth of the impact damage dent. There may be some modest, stable growth of a facesheet crack which begins at the location of the impact damage. The new model is successful, using Helius:MCT, at capturing the crack propagation failure mode, as shown in Fig. 6.13. The unstable crack propagation for an example test coupon in the FEA analysis is compared to a sequence of photos from high speed photography of an experimental test, which was first shown in Chapter 3. Model results for out-of-plane displacement shows that no local buckling is predicted, and there is very little dent growth during the analysis. FEA results for element damage predict the facesheet crack which appears in experimental results.

The point of sudden drop in coupon reaction force in the FEA results for force vs. displacement indicates the point of global coupon failure. (For the 6PCF-06 case, the failure

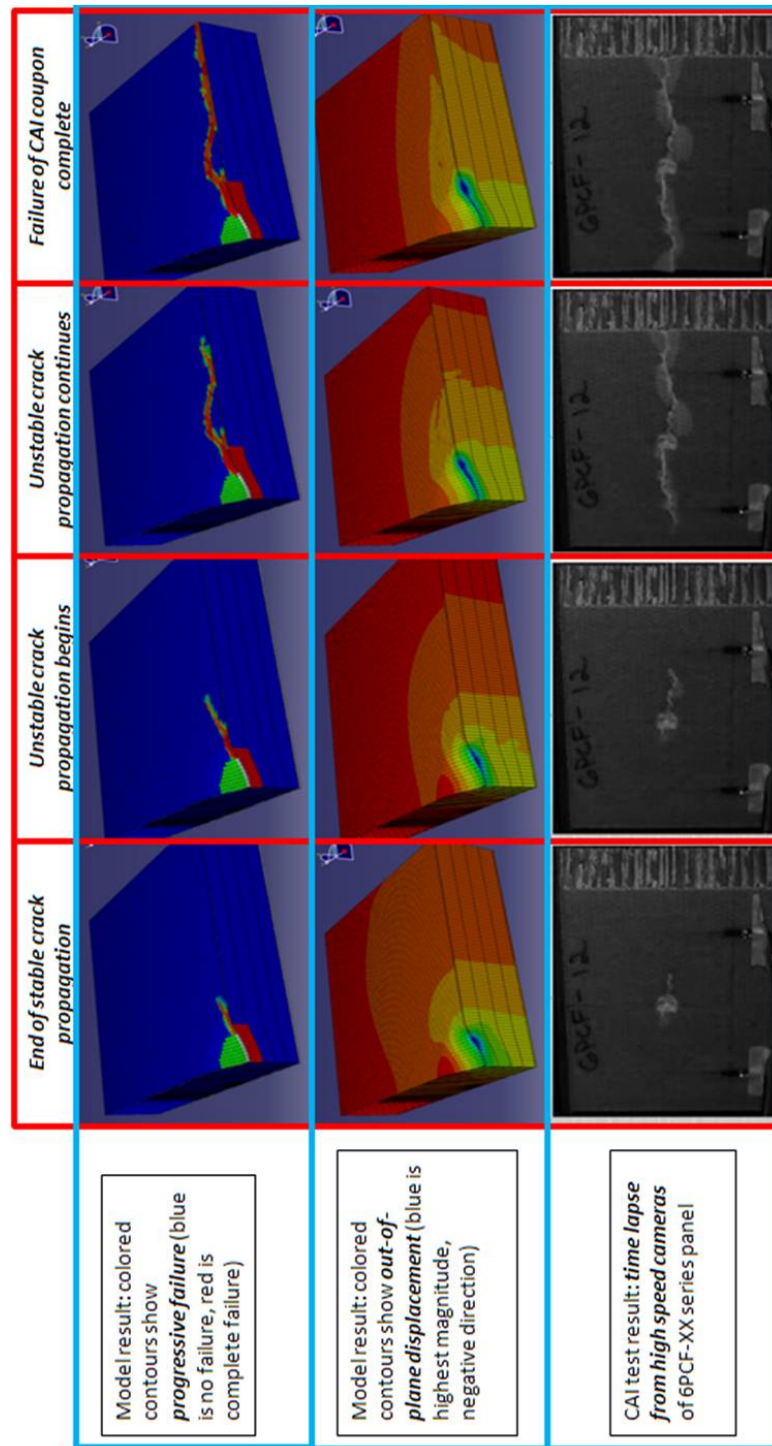


Figure 6.13: Demonstration of crack propagation failure mode for example analysis of 6PCF-XX series material coupons using the new FEM for CAI analysis.

point chosen was the first sudden drop in reaction force. Where the reaction force increased again after failure, this behavior is thought to be a flaw of the composite damage analysis method chosen, due to excess matrix failure predicted in the model.) The main focus of this discussion on the the differences between the analysis results and the experimental test results will again be CAI strength. However, results can also be obtained from FEA for failure load, and failure strain, and these analysis results compare to experimental test results in a similar manner. The results for the analysis of 6PCF-XX series coupons are shown in Table 6.12, for CAI failure load, strength, and strain, with numerical comparison to experimental test results. The results comparison is shown graphically, in Fig. 6.14, for failure stress.

Table 6.12: 6PCF-XX analysis results: failure load, strength and strain for analysis of 6PCF-XX series test coupons.

Panel	Impact Energy (ft-lb)	Analysis Failure Load (lb.)	Tested Failure Load (lb.)	Error (%)	Analysis Failure Strength (ksi)	Tested Failure Strength (ksi)	Error (%)	Analysis Failure Strain (μ -in/in)	Tested Failure Strain (μ -in/in)	Error (%)
6PCF-07	1.0	8514	7462	14.1	38.70	33.92	14.09	10846	9537	13.7
6PCF-10	1.0	8777	8201	7.0	39.89	37.28	7.00	11163	10916	2.3
6PCF-16	1.0	8514	7755	9.8	38.7	35.25	9.79	10846	10256	5.8
6PCF-02	3.0	8431	6702	25.8	38.32	30.46	25.80	10735	8789	22.1
6PCF-09	3.0	8464	7557	12.0	38.47	34.35	11.99	10793	10124	6.6
6PCF-15	3.0	8275	7203	14.9	37.62	32.74	14.91	10530	9926	6.1
6PCF-03	5.0	6796	6107	11.3	30.89	27.76	11.28	8757	7776	12.6
6PCF-06	5.0	6773	6510	4.0	30.79	29.59	4.06	8728	8687	0.5
6PCF-12	5.0	6680	6992	-4.5	30.36	31.78	-4.47	8602	9489	-9.3
6PCF-01	7.0	6909	5826	18.6	31.41	26.48	18.62	8887	7572	17.4
6PCF-11	7.0	6938	5512	25.9	31.54	25.06	25.86	8921	7605	17.3
6PCF-14	7.0	6913	6220	11.1	31.42	28.27	11.14	8891	8012	11.0

The FEA results of the 6PCF-XX series test coupons tended to be non-conservative. This is shown in Fig. 6.14. Numerically, the errors for predicted failure load, stress and strain varied from about 20% to less than a percent, as in the analyses for the two other material systems. Only a few of the results were in error by 20%; however, most were under 15%. There does not appear to be any correlation between the accuracy of the model for a

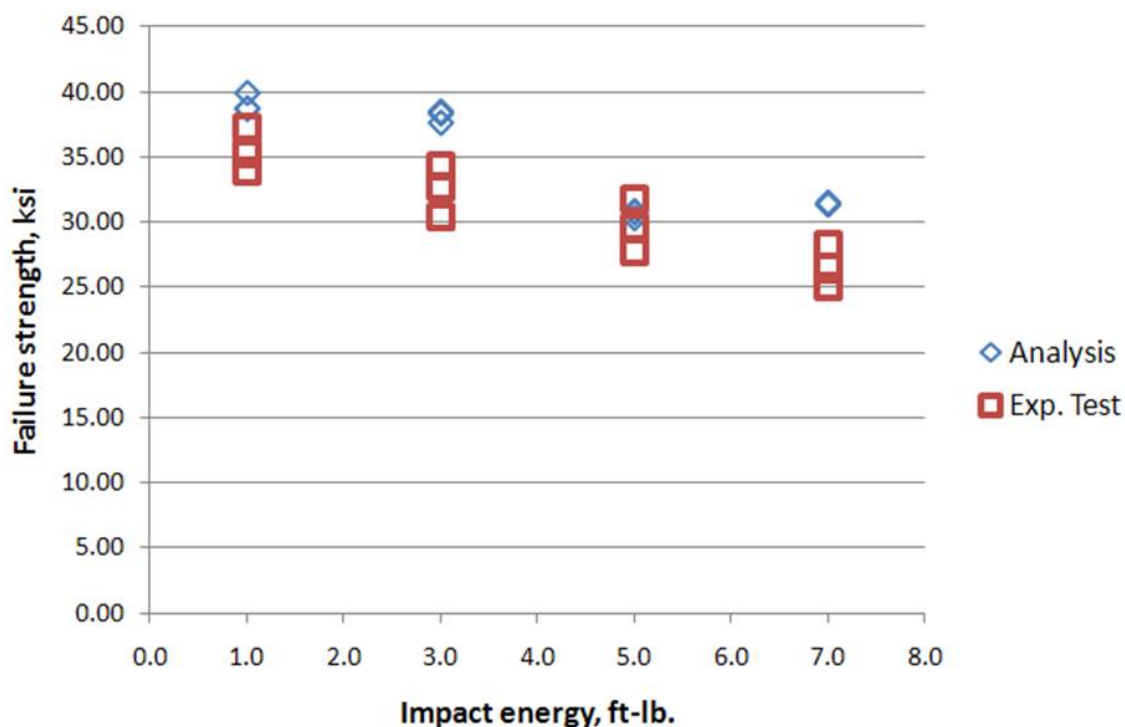


Figure 6.14: 6PCF-XX analysis results: comparison of 6PCF-XX test coupon analysis failure strength to experimental test results.

specific analysis result and the damage level of the test coupon. It is interesting to note that in the analysis predictions, there is very little spread in the CAI failure results for a given impact damage level, though the impact damage inputs do vary. This is contrast to the large amount of variation in the experimental CAI test results found at a certain impact energy level. It was shown in the sensitivity studies in Chapter 5 (specifically in Table 5.3), that the model sensitivity to damage definition inputs was small for the 6PCF-XX series analyses. Since, only the dent depth and diameter varied with each analysis and the remaining inputs were kept constant (since they came from the 6PCF-XX impact survey specimen and not the actual CAI test specimen), one can expect little variation in the analysis prediction results.

A comparison was again made between analysis predictions for indentation growth and experimental test measurements of select 6PCF-XX series test coupons using the DIC system. Analysis prediction results for dent size in the coupon width and load directions, and the maximum dent depth can be seen in Fig. 6.15, 6.16 and 6.17, respectively. Comparisons

were made with respect to the DIC experimental test results which were shown previously in Fig. 3.35, 3.36 and 3.37, respectively.

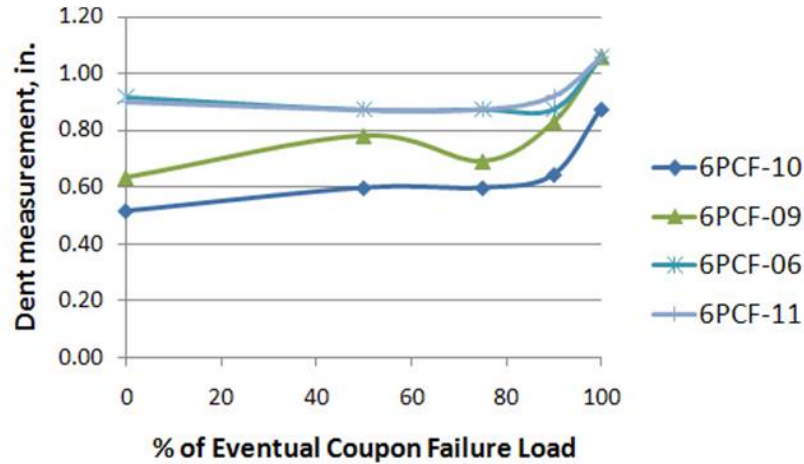


Figure 6.15: 6PCF-XX analysis results: dent growth in the coupon width direction (x-direction) predicted from FEA of 6PCF-XX test coupons.

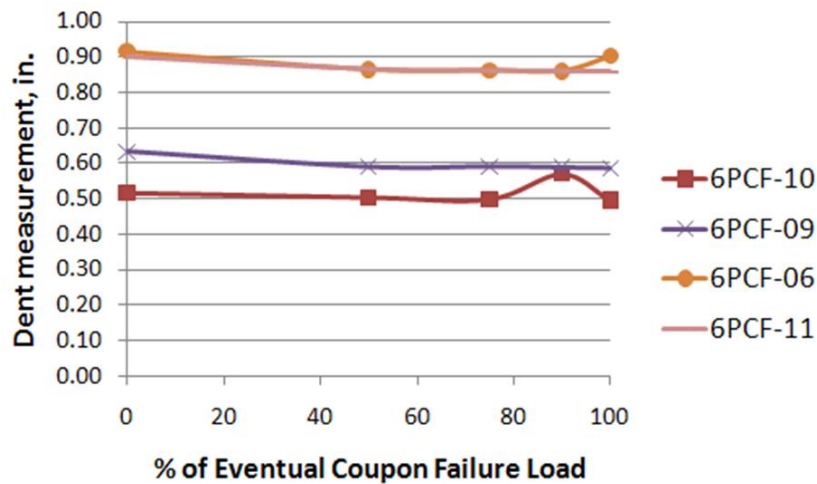


Figure 6.16: 6PCF-XX analysis results: dent growth in the coupon load direction (y-direction) predicted from FEA of 6PCF-XX test coupons.

There was little to no predicted growth of the residual dent during the FEA of 6PCF-XX series test coupons. This was expected from the experimental test results. Some growth appears at the very last stage of the coupon response in the coupon width direction, shown in Fig. 6.15. These results compare well to the experimental test results shown in Chapter

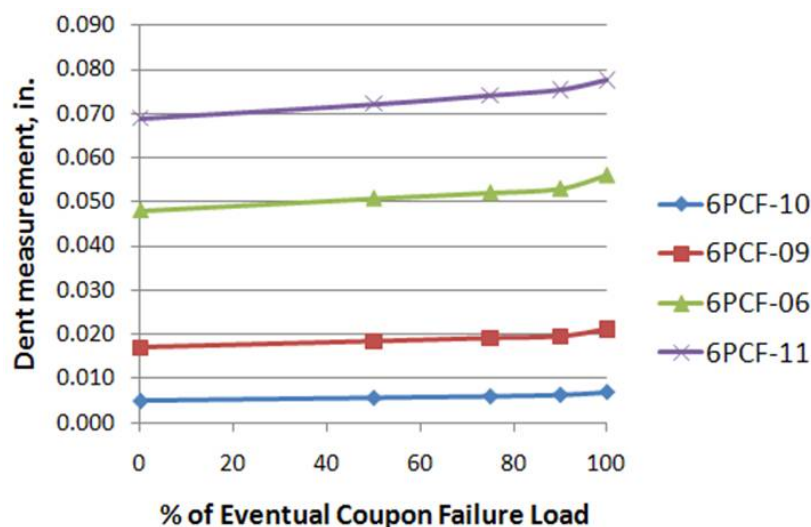


Figure 6.17: 6PCF-XX analysis results: maximum dent depth growth predicted from FEA of 6PCF-XX test coupons.

3 The correlation between the experimental test results and the FEA predictions is stronger for the 6PCF-XX series materials, than it was for the PXX or the 3PCF-XX series materials.

6.4 Parametric Study of CAI Response with Various Core Densities

One of the major conclusions of the present research is that there is a large dependence of the CAI failure mode in the sandwich panels studied on the density of the honeycomb core material included in their construction. In the present study, the traditional sandwich panel CAI failure mode, indentation propagation, is found for panels with the lower density 3 lb/ft³. honeycomb core. The higher density, 6 lb/ft³., core clearly produced a different failure mode, crack propagation, and higher failure strengths. As a result, a parametric study has been completed to determine the critical density of the honeycomb core at which the failure mode transitions from indentation propagation to crack propagation failure mode. In addition, one of the purposes of this study was to determine the increase in failure strength possible by increasing the core density, without changing any of the other parameters. The strength

increase was studied with respect to the mass penalty caused by increasing the honeycomb core density. The material properties which define the crush response of the various density Nomex honeycomb cores will be discussed in the following section. Following that, the results of the parametric study analyses will be presented.

6.4.1 Discussion of Core Crush Property Variance with Core Density

A single CAI model was chosen to determine the effect of the core density on the CAI response. For the parametric study, the geometry modeled corresponds to the 3PCF-XX and 6PCF-XX test coupons, so that a single 2.75 in. by 2.75 in. quadrant of a test coupon is modeled with 0.02 in. thick facesheets and a 0.75 in. thick core. Damage in each model used with the parametric study was modeled using the inputs for the 3PCF-13 test coupon, which were given previously in Table 6.8. The stiffness reductions for the damaged core, IFF damaged facesheet, and fiber fracture damaged facesheet regions' stiffness reductions are as follows, (and used in all other analyses discussed withing the present chapter:

1. "Damaged" core elements was reduced to 60% of their original stiffness.
2. The matrix constituent stiffness reduction was 90% in the IFF regions of the facesheet model.
3. The fiber constituent reduction was 99% and the matrix constituent stiffness reduction was 90% when fiber fracture is predicted in the PFA.

It was noted in the experimental test results discussed in Chapter 3, that the core density will have a small, but noticeable effect on damage formation in the sandwich panel. However, the damage was kept constant for the parametric study so that the honeycomb core properties are the only variable which can change the analysis results. The results of this study can be thought of as conservative, since impact damage formation was shown to decrease in size with increased core density.

The honeycomb core considered throughout the present research, in each of the three material systems considered, is a hexagonal cell Nomex honeycomb with 0.125 in. cell size. Commercially available Hexcel material property data lists core crush and plate shear data for this type of honeycomb at a variety of nominal densities, including the 3 and 6 lb/ft³. densities, which were primarily studied in the present research. The values for the core crush strength and modulus, for each density Nomex honeycomb core listed in the available data [86], is shown in Figs. 6.18 and 6.19, respectively.

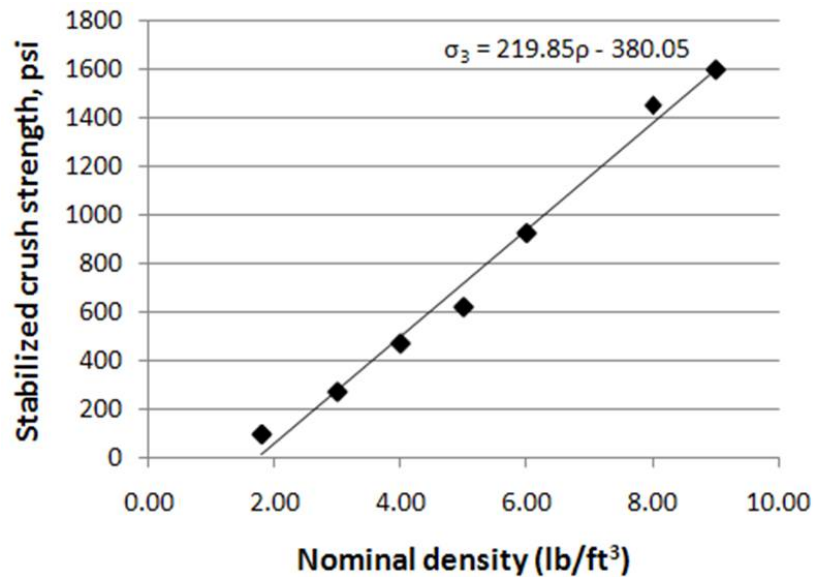


Figure 6.18: Core crush strength of Nomex honeycomb shown varying with nominal core density, and the data fit calculated for use with the parametric study analyses.

A linear relationship was found based on a regression fit of this data, which could then be implemented in the MATLAB function for ABAQUS input file creation. The linear relationships calculated in the present research for the core crush strength and linear elastic modulus are given in Figs. 6.18 and 6.19, respectively. The in-plane shear properties necessary for the FEM were also found, similarly. Other properties necessary, including the in-plane extensional moduli, were calculated using the relationships given in Gibson and Ashby [55]. The parametric study was completed with continuum core models representative of honeycomb core densities ranging from 3 to 6 lb/ft³., with a step size of 0.5 lb/ft³. The bounds on the honeycomb core density were chosen so that both indentation propagation

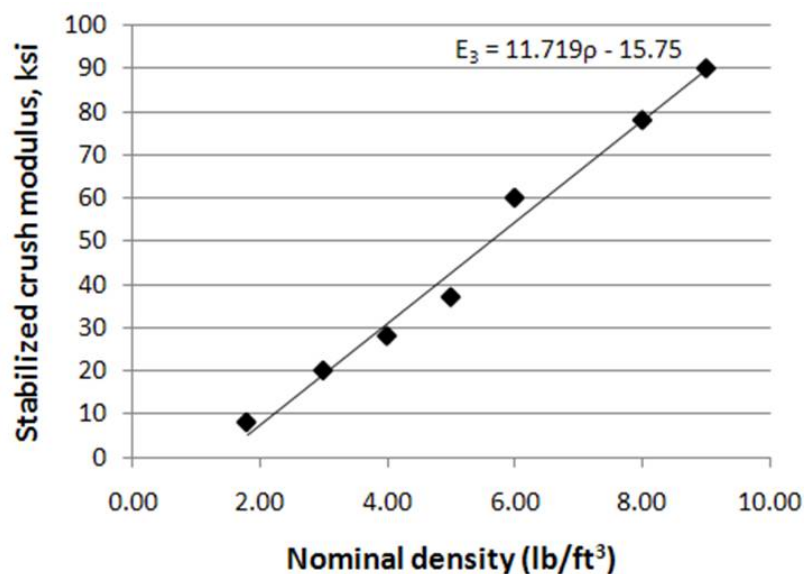


Figure 6.19: Core crush modulus of Nomex honeycomb shown varying with nominal core density, and the data fit calculated for use with the parametric study analyses.

and crack propagation failure modes would be represented in the parametric study results.

6.4.2 Results of the Parametric Study

The results of the parametric study clearly show the usefulness of a CAI model which can handle multiple failure modes. After each of the seven analyses was completed, both failure modes were represented in the parametric study. The failure strength was predicted for each honeycomb core density used in the analyses completed. The predicted failure strength vs. core density is shown in Fig. 6.20. The type of failure mode is indicated by the symbol and the color used for a particular data point.

From the results in Fig. 6.20, the following two conclusions can be made. First, the failure strength of the sandwich panel test coupon increases with honeycomb core density. Second, at a given honeycomb core density, the failure mode will transition from indentation propagation to crack propagation. This is clearly seen to occur near the 4 lb/ft³. core density level. It can also be seen that the failure strength has reached a maximum once the failure mode changes to crack propagation. This clearly suggests that a trivial mass penalty could

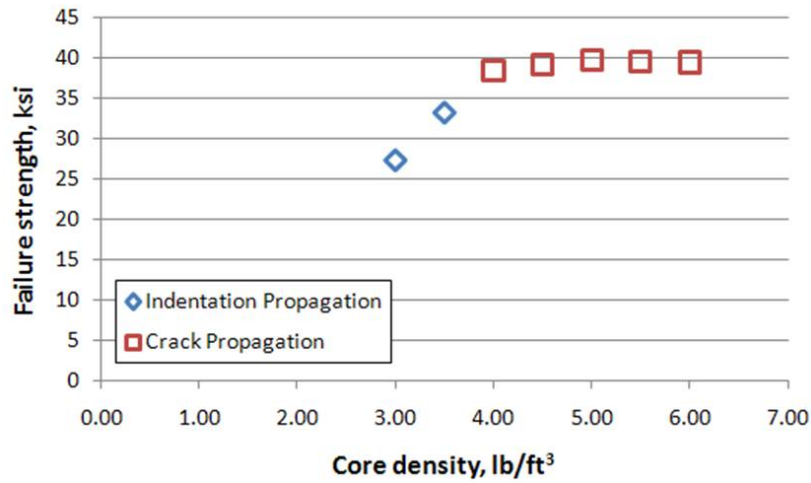


Figure 6.20: Parametric study results: failure strength vs. nominal core density associated with continuum core properties.

be added to the sandwich panel to obtain a significant strength increase. The predicted strength increase vs. the calculated mass penalty is considered in Fig. 6.21.

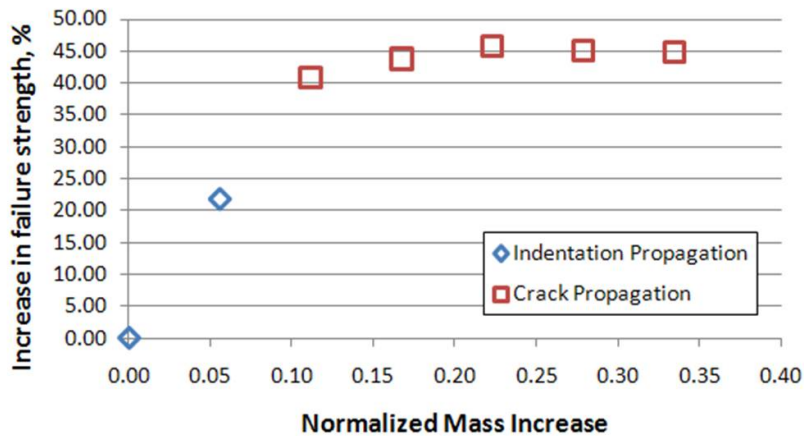


Figure 6.21: Parametric study results: percentage strength increase vs. normalized mass increase.

The increase in failure strength in Fig. 6.21 is calculated as a percentage of the three lb/ft³. failure strength. The mass of the test coupon model is normalized with respect to the complete sandwich panel structure, which includes both the facesheets and the core. The increase in mass is due only to the increase in core density, but is shown as a percentage of the complete panel mass. The strength increase is a maximum once the failure mode has

transitioned from indentation propagation to crack propagation. With respect to the data point representing the 4 lb/ft³. case, a strength increase of just over 40% was achieved for only a 10% weight penalty. Since the CAI strength of a composite material is typically one of the most conservative strength estimates, this predicted strength increase is very significant!

6.5 Conclusions from the Results of Using the New FEM for CAI Analysis

In the current chapter, results were presented for FEA completed using the new CAI analysis model for three sandwich panel material systems. The material systems, damage formation for these systems, and their CAI response had been rigorously described, in Chapters 2 and 3. The model successfully performed high fidelity representation of both the indentation propagation, and the crack propagation failure modes for the appropriate material systems. These representations included both large-scale out-of-plane deformation controlled by a classic core crush model, and fiber reinforced composites failure, as depicted by the commercial software, Heliuss:MCT. An analysis was completed which corresponded to each of the 32 experimental test coupons, and analysis results were then compared with experimental test results. In addition, the dependence of the CAI failure mode on honeycomb core density was examined using a parametric study.

Good correlation with experimental test results was demonstrated for many of the CAI analysis results. Some of the analyses resulted in larger error levels ($\sim 20\%$), which is similar to other CAI analysis models. Many of the new CAI analysis predictions had a much smaller error. Some of the analyses obtained with the new CAI model demonstrated less than a 1% error between analysis predictions and experimental test results. These results were obtained despite some uncertainty in the model inputs. Many of the details included in the present model were not previously available in CAI models, so the current study will have increased our understanding of CAI analysis. It is especially unique, that the current model is validated based on a large amount of experimental data, rather than just a

single data point. In addition, the usefulness of the model's ability to predict multiple CAI failure modes, through competing core and facesheet failure models, was demonstrated in a parametric study. The results showed that significant improvements in CAI failure strength can be obtained by small increases in core density for thin facesheet honeycomb core sandwich panels.

Chapter 6 completed the results of the current research. In Chapter 7, the conclusions of the current research will be discussed, and some suggestions with regards to future work in this research area are introduced.

Chapter 7

Conclusions and Future Work

Composite structures are increasingly being considered as lightweight alternatives in the design of tomorrow's aerospace vehicles, from small private propeller driven planes, to the newest commercial jetliners, and the next generation of heavy lift vehicles for future space exploration. They are already used extensively in modern commercial satellites. Currently, the major design challenges in composites pertain to damage repair, and ultimately, the understanding of damage formation and response of a composite structure with damage present. One aspect of the latter challenge is the understanding of composite sandwich structure response to compression after low velocity impact. This has been the subject of the present research, which has included both experimental testing and finite element analysis (FEA).

The current state of compression after impact (CAI) research was described in Chapter 1, with respect to both experimental testing and analysis. In the area of experimental testing, results are available in the literature for damage formation in composite laminate plates, as well as sandwich constructions with cellular, hexagonal honeycomb cores. CAI testing has been completed by various authors, and unique failure characteristics were demonstrated for sandwich constructions. The formation of damage can be evaluated using destructive techniques, as well as newer non-destructive evaluation (NDE). Many of these methods were used in the experimental testing portion of the present research. Chapter 1 continued with

an introduction to the current CAI analysis methods, and identified important areas of improvement which are needed for FEA. One of the tools identified was a progressive failure analysis (PFA) for damage propagation in the facesheets. Also, although both experimental testing and analysis work has been completed, the models available in the literature have received very little validation through comparison to experimental test results. One of the reasons for this is the lack of complete experimental detail available for any one specific material system in the literature, which is necessary for CAI modeling.

The current research contained a detailed experimental study, which produced new interesting results. In addition, it would later be used to aid and direct model development. In Chapter 2, the experimental testing techniques were introduced and the testing results were summarized for a single Nomex honeycomb core sandwich panel with thin woven fiber-glass reinforced facesheets. Damage formation was studied, as well as the CAI response. In addition, novel instrumentation and observation techniques were used to gain a detailed understanding of these tests, which has not been previously available. The experimental test portion of the current work continued in Chapter 3, with two additional material systems. Although these materials varied slightly from the original set discussed previously, they were identical to each except for one important difference. The density of the honeycomb core, 3 lb/ft³. in one material, and 6 lb/ft³. in the other, was used to assess the core density's effect on damage formation and CAI response. Two CAI failure modes were seen in test results, highlighting the need for new analysis model development.

The current state of FEA for the CAI response of thin facesheet honeycomb core sandwich panels was considered in Chapter 4. The subject of relevant theory, with respect to composite laminates, ABAQUS finite elements, and honeycomb core modeling, was discussed. Two finite element models (FEM) were used to obtain results for a small selection of the tested sandwich materials. First, a spring element core model, which was developed by Ratcliffe and Jackson [46], was used. Second, a solid element core model was discussed, which would provide the foundation for a new model to be developed in Chapter 5. In this chapter, a type of continuum damage model for PFA in composite laminates was discussed. This

failure model, which uses multicontinuum theory (MCT), is implemented in the commercially available software, Helius:MCT, by Firehole Composites. A custom version of this software was provided by Firehole for the present research, to allow its use with the FEM. The custom version allowed for software compatibility with the custom ABAQUS user subroutine, UMAT, used for out-of-plane compressive failure of the core with the present research. This software provided the ability to consider damage propagation in the facesheets, which was needed as previously discussed by this and other authors. The development of the new model continued in Chapter 5 with a detailed discussion of impact damage inclusion. Since a large amount of data was available from the experimental test results, a large amount of detail could be included. A mesh convergence study and a sensitivity study were completed using the new model and the results were presented.

Finally, in Chapter 6, results were presented for the FEA of each of the 32 CAI test coupons using unique models developed from experimental test data. These results were compared to experimental test results. Also, a parametric study was completed using the new FEM to obtain additional results for the CAI response of thin facesheet sandwich constructions with varying honeycomb core density. This completed the development and results of the present research. The present chapter will be used to highlight the important conclusions of this work, first for the experimental test results, and then for the analysis results and comparison to experiment. Finally, anticipated and suggested future work in the area of CAI response of thin-facesheet honeycomb core sandwich panels will be discussed.

7.1 Conclusions

Results for an experimental study and finite element analysis of thin facesheet honeycomb core sandwich panels in response to compression after impact (CAI) loading have been described. The experimental work consisted of tests to describe the damage resistance and damage tolerance of the sandwich panels in question. This work has been completed in an ideal setting for determining the response of these materials both to impact, as well as CAI

loading, at NASA Langley Research Center, in Hampton, VA. Using various instrumentations, a large amount of data has been presented. Some was then used for validation of the FEA. A new and interesting conclusion is made with regards to failure mode dependency on core density. This is supported by detailed instrumentation. The present analysis of sandwich panel test coupons focused primarily on the development and utilization of a FEM for prediction of the CAI response and failure. Elements of previous modeling attempts are used and combined with new techniques in the proposed model. The major analysis conclusions will focus on the new use of PFA in the facesheets and high fidelity impact damage representation. Results were produced for models developed from experimental test data, and compared to the experimental results. The conclusions made from research results are discussed in the following sections, first for experiments, and then analysis.

7.1.1 Experimental Testing Conclusions

A series of experiments was completed on three material systems consisting of honeycomb core sandwich panels with woven fiberglass fabric facesheets. The purpose of these tests was to understand damage formation in response to a low velocity impact, and then the failure response to CAI loading. The PXX series material coupons consisted of 1 in. thick, 3 lb/ft³. Nomex honeycomb core, and 0.02 in. thick woven E-glass facesheets. 3PCF-XX series materials consisted of 0.75 in. thick, 3 lb/ft³. Nomex honeycomb core and 0.02 in. thick woven S2-glass facesheets. The 6PCF-XX series panels were identical in construction to the 3PCF-XX series panels except that the Nomex honeycomb core had a nominal density of 6 lb/ft³.

Static indentation tests and low velocity impact tests were used to assess damage formation, as well as to select the impact energies of interest for CAI testing. Static indentation resulted in similar damage to drop impact, although the results were found to be conservative since lower energy was required in static indentation to produce the damage response typical of higher energy impacts. Force and displacement data was collected for static indentation. The area under the force vs. displacement curve was determined by numerical integration to

estimate the energy absorbed by the material during indentation. Typical damage included a residual dent in the facesheet, which was described by maximum dent depth and diameter. Another type of damage observed during static indentation was discoloration of the facesheets, which indicated areas of facesheet material fracture. Various levels of crushed core were found in the impacted region of the sandwich panel using destructive evaluation techniques. For each material system an energy level was determined at which complete facesheet fracture occurred. This energy level was determined to be constant for a particular material system.

Low velocity impact testing using a drop tower completed the study of damage formation in each the materials. Impact force vs. time data was collected for each impact recorded. Force was found to increase with impact energy until facesheet fracture occurred. The maximum force recorded for higher energy impacts did not increase, although the length of the impact did increase. Typically, for both static indentation and drop impact, the 3PCF-XX and 6PCF-XX series panels absorbed more energy and a higher impact force could be obtained before facesheet fracture, than PXX series panels. This was expected since the strength and stiffness of the woven S2-glass facesheet used in the 3PCF-XX and 6PCF-XX series coupons was higher than the E-glass materials used in the PXX series specimens. The types of damage found for drop impact was similar to static indentation. The depth and diameter of the impact damage dent was found to increase to a maximum before leveling with increasing impact energy. On the other hand, the amount of matrix and fiber cracks did continue to increase with impact energy. Typically, higher levels of impact damage were found in PXX series panels than in the other two material systems for a given energy level. From this result, the energy levels of interest for CAI testing included higher energy levels for 3PCF-XX and 6PCF-XX series panels, than for PXX specimens.

CAI tests were completed on PXX series coupons with damage from impacts of energies up to 2 ft-lbs. and on 3PCF-XX and 6PCF-XX series coupons with damage from impacts of energies up to 7 ft-lbs using a 0.5 in. hemispherically shaped impact tip. Coupons were nominally sized at 6 in. by 6 in. and the load application ends were potted to prevent

erroneous failure of the coupons ends clamped in the test fixture. Various types of instrumentation and recording equipment were used. Instrumentation recorded force, displacement, and strain information for each material coupon. Recording equipment, including high definition cameras, high speed photography, and digital image correlation (DIC) was used to ascertain the resulting failure mode.

Failure in the front, damaged facesheet of each material coupon was found to be the principal factor in global panel failure due to compressive loading. Panel failure was found to be indicated by a sudden, instantaneous drop in the force vs. displacement curve for each coupon. Failure strength for CAI specimen was compared to the compressive strength of an undamaged specimen. The reduction in residual strength of a material coupon was found to be most severe for lightly damaged coupons. Increasing levels of damage resulted in further reduction in residual strength, but the reduction between adjacent data points decreased in magnitude. New insight was gained into the CAI response and ultimate failure of test coupons using novel instrumentation techniques. High speed video photography captured images of failure. These images were not previously available in the literature. In addition, the DIC system was used to make full-field surface maps, and deformation measurements of the front, damaged facesheet of each of the experimental test specimens. The results shown in the current work quantified the stable growth of the impact damage dent at various times in the linear elastic portion of the CAI test response. These results confirmed the growth observed in test video, and provided clarity to coupon response, which had previously been observed only using large systems of strain gages.

Two CAI failure modes were found during the experimental investigation. In material systems with 3 lb/ft³. density honeycomb cores, an indentation propagation failure mode resulted which is essentially a local buckling of the facesheet due to the collapse of the honeycomb core beneath. A crack is present in the facesheet, but the propagation of the residual indentation transversely across the facesheet precedes the crack. In testing of the higher density, 6 lb/ft³. core materials, a second failure mode was found, which was termed crack propagation. A transverse fiber crack propagates across the facesheet, without any

local facesheet buckling or core crush. Since the 3PCF-XX and 6PCF-XX series panels are identical except for their honeycomb density, the failure mode was found to be dependent on this material property alone. Full field measurements using the DIC system and VIC-3D software also demonstrated the difference in these two material modes, prior to failure. It was concluded that the higher density core also resulted in very little dent growth, prior to failure. The effect of core density on damage formation and CAI response in honeycomb core sandwich panels highlighted the need for new analysis techniques.

7.1.2 Analysis Conclusions

A FEM with new analysis techniques implemented has been developed for the prediction of the CAI response of honeycomb core sandwich panels using the commercial finite element code, ABAQUS/Standard. A literature review was presented which outlined past work in this area and defined the state of the art in this area. The new FEM uses some techniques currently available, which worked well in previous models. The facesheets and the core of the new FEM were modeled separately using the following techniques. The non-linear core model consists of an idealization of the stabilized crush response found by experiment for a Nomex honeycomb core. This response can be defined by an initial linear elastic modulus, the core crush strength, and a stress reduction at failure. A spring element core model was studied which introduces this concept, since with spring elements this is the only core response that can be modeled. The force vs. displacement result of this model near failure was found to significantly differ from experimental observations, except in select cases. The reduction in reaction force at failure was shown to be “rounded,” instead of the instantaneous reduction seen in experimental tests. A solid, orthotropic continuum representation of the linear elastic response of the honeycomb core was included, in addition to the non-linear crush response. The core, modeled using solid brick elements was defined by a user subroutine. A solid element core model was presented in order to show the benefits of these modeling techniques. The solid element continuum representation of the honeycomb core was implemented using an ABAQUS user subroutine, UMAT. This subroutine, written in the FORTRAN programming

language, provides for both the linear elastic response of the core, as well as the non-linear through the thickness crushing response.

One of the major focuses of the current research was implementation of progressive failure analysis of the facesheets of honeycomb core sandwich panels for use in CAI analysis. The commercial software, Heliuss:MCT, was used for this. This software uses multicontinuum theory (MCT) failure theory for a continuum damage representation failure analysis of the facesheets during the analysis. The primary purpose of MCT is for higher accuracy in laminate failure prediction, by defining constituent level failure based on constituent level average stress states. The constituent level average stress states are found by decomposition from laminate average stress states using MCT. A successful implementation of PFA is absent from previous CAI models, so CAI analysis with this capability is concluded to be the first of its kind. The new FEM model has the ability to successfully model and predict multiple failure modes, including the two modes found in the experimental work presented in the present study: indentation propagation and crack propagation. The new model's results demonstrated high-fidelity physics based representations of both failure modes.

A mesh convergence study was completed to determine the new model's mesh dependency. The study showed that mesh dependence varied somewhat based on the failure mode exhibited by the sandwich panel structure. While the through the thickness mesh density was more important for the indentation propagation failure mode, the in-plane mesh density was shown to affect the crack propagation mode. The latter result confirms that the continuum damage propagation methods used by the Heliuss:MCT software is mesh dependent.

In addition, several other interesting developments in CAI analysis resulted from the present work. A highly detailed FEM representation of the impact damage in the CAI analysis model was used. The "damaged" regions of elements in both the core and facesheet were defined using measurements taken from the experimental work, and material property stiffness reductions. Since the implementation of the inputs used to define these components of the model (through a custom MATLAB language program which writes an ABAQUS input file) was quite intensive, a sensitivity study was used to assess the effect of the damage

properties on the model. They were also used to assess overall confidence in the model based on specific inputs.

Some inputs, such as dent diameter, and maximum dent depth, were evaluated as having an “excellent” level of confidence. This rating was given for inputs with low measurement uncertainty, which might also result in only small changes to model results if excessive errors were present. A “good” confidence rating was given to the diameter of the facesheet region associated with inter-fiber fracture. The reason for this was that a higher level of uncertainty exists for this measurement; however, it was demonstrated that the uncertainty would only result in a small net change in model results. Finally, the confidence in some model definitions was evaluated as “reduced.” First, the mesh density used was not the best for an accurate depiction of the depth of the damaged core. This issue could have been resolved with a change in the mesh pattern used. Still, it was shown that the depth of the core damage in the model was largely inconsequential, so long as at least some damage was present.

Finally, the “reduced” confidence label was also given to the stiffness reduction values. First, the core stiffness reduction uncertainty could have been improved by conducting a flatwise core compression test on the honeycomb core materials of interest. The matrix constituent stiffness reduction and the fiber constituent stiffness reduction are the two final areas of reduced confidence. These two properties are used in both the definition of initially damaged element material properties, as well as the progressive failure analysis completed by Helius:MCT. It was concluded that with the current continuum damage method, these values need to be improved using experimental testing of the woven fiberglass reinforced facesheets. Also, a more gradual stiffness reduction would be more appropriate to some of the material properties, namely, in-plane shear stiffness.

The new CAI model was used to analyze the CAI response of each of the 32 coupons tested to failure during experimental work. Results were given for failure load, failure stress, and failure strain. Specific consideration was given to analysis results for coupon failure strength for comparison to experimental test results, but any of the global failure measure-

ments could have been used. The new model showed similar error to other currently available CAI models for some of the analyses when compared to experiments. However, for many of the results, the resulting error was lower, and for some results, the error was significantly low. It was shown that each of the damage definition inputs have a small, but significant effect on the overall model results. Thus it is important to have a low uncertainty associated with the experimental test measurements used in the analysis model inputs. Acceptable analysis results were obtained for the current research, but improvements in the accuracy of the CAI model predictions could be made by improving the experimental test observations used.

The final result discussed in the present work was a parametric study on the effect of core density on sandwich panel CAI response. This result clearly showed that increasing the specimen's core density will change the failure mode from indentation propagation to crack propagation. In addition, CAI failure strength was increased with the core density increase, until the failure mode changed to crack propagation. The parametric study results showed that a substantially large CAI strength increase could be obtained for only a small increase in mass. This result demonstrates the new abilities of the new model for CAI analysis, as well as its benefit to engineering design.

7.2 Future Work

During the course of this research, several areas of future work were identified. First, some suggestions for future experimental testing will be discussed, then for future analysis work. There exists a great deal of results in the literature for CAI test results on coupon, but not enough work has been done on CAI testing at the component or full scale structural levels. With the advancements that have been made recently in development of digital image correlation measurements, there exists the possibility for an understanding not previously achieved for structural level CAI response.

Additionally, another area of future importance in CAI testing is materials that have been repaired. Frequently, in the commercial sector of the aerospace industry, damaged

composite components are replaced when they are inspected and found to contain damage. However, the repair of composite damage is an emerging research area. In the future, it is possible that the development and use of repair methods on composite structures will be seen in the operational use of aerospace structures, and perhaps other structures which contain composites as well (e.g. boat hulls). More work will need to be done in the area of compression testing of these damaged, then repaired, composite structures for evaluating various repair methods to be used in a commercial setting.

Future tasks were also identified in the area of analysis. More work will need to be done to improve the accuracy and reliability of existing models before they can be used outside of the academic research setting. There simply isn't enough confidence in the existing models. Also, in many cases the commercial alternative is to just replace, or in very few cases, repair damage. There is not enough emphasis on the possibility of damage that may be undetected. This research, as well as previous work, has shown the drastic strength reductions that can occur due to even light damage. CAI models can predict strength reductions due to light, undetectable damage, as well as larger mounts of damage, so future work should continue to improve these models.

One of the main tasks of the current research was the implementation of a composite laminate progressive failure analysis in the CAI model. This implementation was done through the use of special version of the commercial software, Helius:MCT. The changes that were implemented for this research are apparently planned for future, validated releases of the software, so it will be more widely available. This software has excellent value in composite laminate failure analysis, but improvements can be made. Key parameters used to calculate the post-failure stiffness of "damaged" elements still have large amounts of uncertainty associated with them. With more work and experience, more confidence in these failure criteria can be found. It was mentioned previously, that a more gradual reduction in material stiffness, especially where matrix plasticity and failure is concerned, would be highly beneficial and more indicative of the physical reality. This is already implemented in Helius:MCT for unidirectional composites, and possibly, Firehole is already developing this

for woven composites like the ones used in this research.

Continuum damage models for composites, such as Heliuss:MCT, are not the only emerging technology in composite failure theory. In fact, it can be argued that while they are the most developed, they are easy to understand and use, and they are a great resource, they are no longer on the cutting edge in terms of composite failure analysis. Other methods exist, some of which were discussed in Chapter 1. A great deal of emphasis in future work will need to be placed on the importance of matrix deformation and failure, particularly on the size, orientation, and placement of matrix cracks. Some of the models being developed currently are accounting for this. It will be interesting to see their implementation for low velocity impact damage formation in composites, as well as CAI.

References

- [1] Camarda, C., “Failure is not an option..its a requirement,” *50th AIAA/ASME/ASCE/AHS/ASC Structures, Structural Dynamics, and Materials Conference*, AIAA 2009-2255, Palm Springs, CA, 4-7 May 2009.
- [2] Tomblin, J., Lacy, T., Smith, B., Hooper, S., Vizzini, A., and Lee, S., “Review of damage tolerance for composite sandwich airframe structures,” FAA Technical Report DOT/FAA/AR-99/49, U.S. Department of Transportation Federal Aviation Administration Office of Aviation Research, Washington, D.C., August 1999.
- [3] “Composite Aircraft Structure,” FAA Advisory Circular AC 20-107B, CHG 1, August 2010.
- [4] Cantwell, W. and Morton, J., “The significance of damage and defects and their detection in composite materials: a review,” *The Journal of Strain Analysis for Engineering Design*, Vol. 27, No. 1, 1992, pp. 29 – 42.
- [5] Hosur, M., Karim, M., and Jeelani, S., “Experimental investigations on the response of stitched/unstitched woven S2-glass/SC15 epoxy composites under single and repeated low velocity impact loading,” *Composite Structures*, Vol. 61, 2003, pp. 89 – 102.
- [6] Hosur, M., Adbullah, M., and Jeelani, S., “Studies on the low-velocity impact response of woven hybrid composites,” *Composite Structures*, Vol. 67, 2005, pp. 253 – 262.
- [7] Baucom, J., Zikry, M., and Rajendran, A., “Low-velocity impact damage accumulation

REFERENCES

- in woven S2-glass composite systems,” *Composites and Science Technology*, Vol. 66, 2006, pp. 1229 – 1238.
- [8] Ambur, D., Starnes, J., Stoumbos, T., and Kapania, R., “Influence of large-deflection effects on the impact response of flat and curved composite panels,” *36th AIAA/ASME/ASCE/AHS/ASC Structures, Structural Dynamics and Materials Conference*, AIAA A95-30788, New Orleans, LA, April 1995.
- [9] Tomblin, J., Raju, K., and Arosteguy, G., “Damage resistance and tolerance of composite sandwich panels scaling effects,” FAA Technical Report DOT/FAA/AR-03/75, US Department of Transportation Federal Aviation Administration Office of Aviation Research, Washington, D.C., February 2004.
- [10] Raju, K., Smith, B., Tomblin, J., Liew, K., and Guarddon, J., “Impact damage resistance and tolerance of honeycomb core sandwich panels,” *Journal of Composite Materials*, Vol. 42, No. 4, 2008, pp. 385 – 412.
- [11] Tomblin, J., Raju, K., Acosta, J., Smith, N., and Romine, N., “Impact damage characterization and damage tolerance of composite sandwich airframe structures Phase II,” FAA Technical Report DOT/FAA/AR-02/80, US Department of Transportation Federal Aviation Administration Office of Aviation Research, Washington, D.C., October 2002.
- [12] Shyprykevich, P., Tomblin, J., Llciewicz, L., Vizzini, A., Lacy, T., and Hwang, Y., “Guidelines for analysis, testing, and nondestructive inspection of impact-damaged composite sandwich structures,” FAA Technical Report DOT/FAA/AR-02/121, US Department of Transportation Federal Aviation Administration Office of Aviation Research, Washington, D.C., March 2003.
- [13] Moody, C., Harris, J., and Vizzini, A., “Curvature effects on the damage tolerance of impact damaged composite sandwich panels,” *12th International Conference on Composite Materials*, Paris, France, July 1999.

REFERENCES

- [14] Ambur, D. and Cruz, J., “Low speed impact response characteristics of composite sandwich panels,” *AIAA/ASME/ASCE/AHS Structures, Structural Dynamics and Materials Conference Collected Technical Papers 4*, AIAA, 1995, pp. 2681 – 2689.
- [15] Foo, C., Chai, G., and Seah, L., “A model to predict low-velocity impact response and damage in sandwich composites,” *Composites Science and Technology*, Vol. 68, 2008, pp. 1348 – 1356.
- [16] Singh, A., Davidson, B., Eisenberg, D., Czabaj, M., and Zehnder, A., “Barely visible impact damage evaluation of composite sandwich structures,” *51st AIAA/ASME/ASCE/AHS/ASC Structures, Structural Dynamics, and Materials Conference*, Orlando, FL, April 2010.
- [17] Tomblin, J., Raju, K., Liew, J., and Smith, B., “Impact damage characterization and damage tolerance of composite sandwich airframe structures,” FAA Technical Report DOT/FAA/AR-00/44, US Department of Transportation Federal Aviation Administration Office of Aviation Research, Washington, D.C., January 2001.
- [18] Cantwell, W. and Morton, J., “The influence of varying projectile mass on the impact response of CFRP,” *Composite Structures*, Vol. 13, 1989, pp. 101 – 114.
- [19] Cantwell, W., “The influence of target geometry on the high velocity impact response of CFRP,” *Composite Structures*, Vol. 10, 1988, pp. 247 – 265.
- [20] Cantwell, W. and Morton, J., “Geometrical effects in the low velocity impact response of CFRP,” *Composite Structures*, Vol. 12, 1989, pp. 39 – 59.
- [21] Cantwell, W. and Morton, J., “Detection of impact damage in CFRP laminates,” *Composite Structures*, Vol. 3, 1985, pp. 241 – 257.
- [22] Yang, Z., Zhang, W., Tian, G., Song, Y., and Li, R., “Debond detection of shell/insulation in SRM by thermal wave NDT,” *48th AIAA Aerospace Sciences Meeting*, AIAA 2010-934, Orlando, FL, January 2010.

REFERENCES

- [23] Tomblin, J., Raju, K., Walker, T., and Acosta, J., "Damage tolerance of composite sandwich airframe structures - additional results," FAA Technical Report DOT/FAA/AR-05/33, US Department of Transportation Federal Aviation Administration Office of Aviation Research, Washington, D.C., October 2005.
- [24] "ICI Fiberite HYE 5377-SA Hercules IM7 12K Fiber, Fiberite 977-2 Toughened Epoxy Resin," Qualification Material Statistical Analysis Report NCP-RP-2008-016, National Center for Advanced Materials Performance, National Institute for Aviation Research, Wichita State University, January 2009.
- [25] Nettles, A. and Jackson, J., "Developing a material strength design value based on compression after impact damage for the Ares I composite interstage," NASA Technical Report NASA/TP-2009-215634, NASA, MSFC, Alabama, January 2009.
- [26] Rhodes, M., Williams, J., and Starnes Jr., J., "Low velocity impact damage in graphite-fiber reinforced epoxy laminates," *34th Conf. of the Reinforced Plastics/Composites Institute*, January 29 - February 2 1979.
- [27] Starnes, J., J.H., Rhodes, M., and Williams, J., "Effect of impact damage and holes on the compressive strength of a graphite/epoxy laminate," ASTM Special Technical Publication 696, ASTM, 1979.
- [28] Williams, J., Anderson, M., Rhodes, M., Starnes Jr., J., and Stroud, W., "Recent developments in the design, testing and impact-damage tolerance of stiffened composite panels," NASA Technical Memorandum 80077, NASA, April 1979.
- [29] Demuts, E., Whitehead, R., and Deo, R., "Assessment of damage tolerance in composites," *International Conference on Structural Impact and Crashworthiness*, Imperial College, London, U.K., July 1984.
- [30] Williams, J. and Rhodes, M., "Effect of resin on damage tolerance of graphite/epoxy laminates," ASTM Special Technical Publication 787, ASTM, 1983.

REFERENCES

- [31] Yan, H., Oskay, C., Krishnan, A., and Xu, L., “Compression-after-impact response of woven fiber reinforced composites,” *Composites Science and Technology*, Vol. 70, 2010, pp. 2128 – 2136.
- [32] Rhodes, M., “Low velocity impact on composite sandwich structures,” *2nd Air Force Conference on Fibrous Composites in Flight Vehicle Design*, May 1974.
- [33] Rhodes, M., “Impact fracture of composite sandwich structures,” *AIAA/ASME/SAE 16th Structures, Structural Dynamics and Materials Conference*, 1975.
- [34] McGowan, D. and Ambur, D., “Damage characteristics and residual strength of composite sandwich panels impacted with and without compression loading,” *39th AIAA/ASME/ASCE/AHS/ASC structures, structural dynamics, and materials conference*, 1998, pp. 713 – 723.
- [35] Tsang, P. and Lagace, P., “Failure mechanisms of impact-damaged sandwich panels under compression,” *35th AIAA/ASME/ASCE/AHS/ASC Structures, Structural Dynamics and Materials Conference*, 1994.
- [36] Moody, R., Harris, J. S., and Vizzini, A. J., “Width Effects on the Compression Strength of Composite Sandwich Structures after Barely Visible Impact Damage,” *AIAA/ASME/ASCE/AHS/ASC 40th Structures, Structural Dynamics and Materials Conference*, 1999.
- [37] Edgren, F., Asp, L., and Bull, P., “Compressive failure of impacted NCF composite sandwich panels - characterization of the failure process,” *Journal of Composite Materials*, Vol. 38, No. 6, 2004, pp. 495 – 514.
- [38] Moody, C. and Vizzini, A., “Damage tolerance of composite sandwich structures,” FAA Technical Report DOT/FAA/AR-99/91, US Department of Transportation Federal Aviation Administration Office of Aviation Research, Washington, D.C., January 2000.

REFERENCES

- [39] Kassapoglou, C. and Abbot, R., “A correlation parameter for predicting the compressive strength of composite sandwich panels after low speed impact,” *29th AIAA/ASME/ASCE/AHS/ASC Structures, Structural Dynamics, and Materials Conference*, April 1988.
- [40] Lie, S., *Damage resistance and damage tolerance of thin composite facesheet honeycomb panels*, Ms thesis, Massachusetts Institute of Technology, Cambridge, MA, March 1989.
- [41] Minguet, P., “A model for predicting the behavior of impact-damaged minimum gage sandwich panels under compression,” *AIAA/ASME/ASCE/AHS/ASC 32nd Structures, Structural Dynamics and Materials Conference*, 1991.
- [42] Tsang, P., *Impact resistance and damage tolerance of composite sandwich panels*, Phd dissertation, Massachusetts Institute of Technology, Cambridge, MA, 1994.
- [43] Xie, Z. and Vizzini, A., “A modified analytical model for damage propagation of a low-velocity impacted sandwich panel,” *ASC 17th Technical Conference on Composite Materials*, West Lafayette, IN, October 2002.
- [44] Xie, Z. and Vizzini, A., “Damage propagation in a composite sandwich panel subjected to increasing uniaxial compression after low-velocity impact,” *Journal of Sandwich Structures and Materials*, Vol. 7, 2005, pp. 269 – 288.
- [45] Staal, R., Mallinson, G., Jayaraman, K., and Horrigan, D., “Predicting failure loads of impact damaged honeycomb sandwich panels,” *Journal of Sandwich Structures and Materials*, Vol. 11, 2009, pp. 213 – 244.
- [46] Ratcliffe, J. and Jackson, W., “A finite element analysis for predicting the residual compressive strength of impact-damaged sandwich panels,” NASA Technical Report NASA/TM-2008-215341, NASA, NASA Langley Research Center, Hampton, VA, 2008.
- [47] Castani, B., Aminanda, Y., Bouvet, C., and Barrau, J.-J., “Core crush criterion to

REFERENCES

- determine the strength of sandwich composite structures subjected to compression after impact,” *Composite Structures*, Vol. 86, 2008, pp. 243 – 250.
- [48] McQuigg, T., Kapania, R., Scotti, S., and Walker, S., “Compression after impact testing of thin-facesheet honeycomb core sandwich panels,” *18th International Conference on Composites and Nano Engineering*, Anchorage, AK, July 2010.
- [49] Hwang, Y. and Lacy, T., “Numerical estimates of the compressive strength of impact-damaged sandwich composites,” *Journal of Composite Materials*, Vol. 41, No. 3, 2007, pp. 367 – 388.
- [50] Lacy, T. and Hwang, Y., “Numerical modeling of impact-damaged sandwich composites subjected to compression-after-impact loading,” *Composite Structures*, Vol. 61, 2003, pp. 115 – 128.
- [51] Czabaj, M., Zehnder, A., Davidson, B., Singh, A., and Eisenberg, D., “Compression after impact of sandwich composite structures: experiments and modeling,” *51st AIAA/ASME/ASCE/AHS/ASC Structures, Structural Dynamics, and Materials Conference*, 2010.
- [52] Xie, Z. and Vizzini, A., “On residual compressive strength prediction of composite sandwich panels after low-velocity impact damage,” *Sandwich Structures*, Vol. 7, 2005, pp. 363 – 372.
- [53] Xie, Z. and Vizzini, A., “The presence of a delamination in damage growth of an impacted sandwich panel,” *ASC 16th Technical Conference on Composite Materials*, Blacksburg, VA, September 2001.
- [54] Schubel, P., Rome, J., Goyal, V., and Tuck-Lee, J., “Predicting failure of damaged composite sandwich structures using compression-after-impact strength data,” *50th AIAA/ASME/ASCE/AHS/ASC Structures, Structural Dynamics, and Materials Conference*, 2009.

REFERENCES

- [55] Gibson, L. and Ashby, M., *Cellular solids: structure and properties*, Cambridge University Press, 2nd ed., 1997.
- [56] Hohe, J. and Becker, W., “Effective elastic properties of triangular grid structures,” *Composite Structures*, Vol. 45, 1999, pp. 131 – 145.
- [57] Hohe, J., Beschorner, C., and Becker, W., “Effective elastic properties of hexagonal and quadrilateral grid structures,” *Composite Structures*, Vol. 46, 1999, pp. 73 – 89.
- [58] Hohe, J. and Becker, W., “An energetic homogenization procedure for the elastic properties of general cellular sandwich cores,” *Composites: Part B*, Vol. 32, 2001, pp. 185 – 197.
- [59] Chen, D. and Ozaki, S., “Analysis of in-plane elastic modulus for a hexagonal honeycomb core: effect of core height and proposed analytical method,” *Composite Structures*, Vol. 88, 2009, pp. 17 – 25.
- [60] Hu, L. and Yu, T., “Dynamic crushing strength of hexagonal honeycombs,” *International Journal of Impact Engineering*, Vol. 37, 2010, pp. 467 – 474.
- [61] Foo, C., Chai, G., and Seah, L., “Mechanical properties of Nomex material and Nomex honeycomb structure,” *Composite Structures*, Vol. 80, 2007, pp. 588 – 594.
- [62] Aktay, L., Johnson, A., and Kröplin, B.-H., “Numerical modeling of honeycomb core crush behavior,” *Engineering Fracture Mechanics*, Vol. 75, 2008, pp. 2616 – 2630.
- [63] Gornet, L., Marguet, S., and Marckmann, G., “Modeling of Nomex honeycomb cores, linear and nonlinear behaviors,” *Mechanics of Advanced Materials and Structures*, Vol. 14, 2007, pp. 589 – 601.
- [64] Heimbs, S., “Virtual testing of sandwich core structures using dynamic finite element simulations,” *Computational Materials Science*, Vol. 45, 2009, pp. 205 – 216.

REFERENCES

- [65] Kaman, M., Solmaz, M., and Turan, K., “Experimental and numerical analysis of critical buckling load of honeycomb sandwich panels,” *Journal of Composite Materials*, 2010, pp. 1 – 13.
- [66] Feraboli, P., Deleo, F., Wade, B., Rassaian, M., Higgins, M., Byar, A., Reggiani, M., Bonfatti, A., DeOto, L., and Masini, A., “Predictive modeling of an energy-absorbing sandwich structural concept using the building block approach,” *Composites: Part A*, Vol. 41, 2010, pp. 774 – 786.
- [67] Abd El-Sayed, F., Jones, R., and Burgess, I., “A theoretical approach to the deformation of honeycomb based composite materials,” *Composites*, Vol. 10, No. 4, October 1979, pp. 209 – 214.
- [68] Dávila, C., Rose, C., and Iarve, E., “Modeling fracture and complex crack networks in laminated composites,” *Mathematical Methods and Models in Composites, Computational and Experimental Methods in Structures, V*, Mantič Ed. Imperial College Press, London, UK, accepted for publication, 2011.
- [69] Puck, A. and Schürmann, H., “Failure analysis of FRP laminates by means of physically based phenomenological models,” *Composites Science and Technology*, Vol. 58, 1998, pp. 1045 – 1067.
- [70] Puck, A. and Schürmann, H., “Failure analysis of FRP laminates by means of physically based phenomenological models,” *Composites Science and Technology*, Vol. 62, 2002, pp. 1633 – 1662.
- [71] Hashin, Z., “Failure criteria for unidirectional fiber composites,” *Journal of Applied Mechanics*, Vol. 47, 1980, pp. 329 – 334.
- [72] Lapczyk, I. and Hurtado, J., “Progressive damage modeling in fiber-reinforced materials,” *Composites: Part A*, Vol. 38, 2007, pp. 2333 – 2341.
- [73] Abaqus/Standard, Version 6.9-1, Dessault Systems, 2009.

REFERENCES

- [74] Garnich, M. and Hansen, A., “A multicontinuum theory for thermal-elastic finite element analysis of composite materials,” *Journal of Composite Materials*, Vol. 31, No. 1, 1997, pp. 71 – 86.
- [75] Mayes, J. and Hansen, A., “Composite laminate failure analysis using multicontinuum theory,” *Composites Science and Technology*, Vol. 64, 2004, pp. 379 – 394.
- [76] Schumacher, S. and Key, C., “CTH reference manual: Composite capability and technologies,” Sandia Report SAND2009-0403, Sandia National Laboratories, Albuquerque, NM, February 2009.
- [77] Knops, M. and Bögle, C., “Gradual failure in fibre/polymer laminates,” *Composites Science and Technology*, Vol. 66, 2006, pp. 616 – 625.
- [78] Mechanical Property Data, AAR Engineering Department, AAR Composites, 2009.
- [79] “Standard test method for compressive residual strength properties of damaged polymer matrix composite plates,” ASTM Test Standard, D 7137/D 7137M 07, December 2007.
- [80] “Standard test method for edgewise compressive strength of sandwich constructions,” ASTM Test Standard, C 364/C 364M 07, April 2007.
- [81] Phantom High Speed Cameras, Vision Research, Inc., www.visionresearch.com.
- [82] Vic-3D 2010, Correlated Solutions, Inc., www.correlatedsolutions.com.
- [83] Sutton, M., Orteu, J., and Schreier, H., *Image correlation for shape, motion, and deformation measurements: basic concepts, theory and applications*, Springer, 2006.
- [84] MATLAB R2009B, Ver. 7.9.0.529, The Math Works, August 12, 2009.
- [85] “ACG MTM45-1 6781 S-2 glass 35% RC,” Qualification Material Statistical Analysis Report, CAM-RP-2009-001, National Center for Advanced Materials Performance, NASA, National Institute for Aviation Research, Wichita State University, KS, February 2010.

REFERENCES

- [86] “HexWeb honeycomb attributes and properties,” HexCel Composites, Inc.
- [87] Hyer, M., *Stress analysis of fiber-reinforced composite materials*, WCB/McGraw-Hill, 1998.
- [88] Kapania, R., Soliman, H., Vasudeva, S., Hughes, O., and Makhecha, D., “Static analysis of sandwich panels with square honeycomb core,” *AIAA Journal*, Vol. 46, No. 3, 2008, pp. 627 – 634.
- [89] Dessault Systems, *Abaqus Analysis Users Manual. Version 6.9*, 2009.
- [90] Dessault Systems, *Abaqus Theory Manual. Version 6.9*, 2009.
- [91] Sanders Jr., J., “An improved first-approximation theory for thin shells,” NASA Technical Report R-24, NASA, 1959.
- [92] Helius:MCT Version 3.1, Firehole Technologies, Inc., 2009.
- [93] *Helius:MCT Theory Manual. Firehole Technologies, Inc.*, 2009.
- [94] Whitcomb, J. and Tang, X., “Effective moduli of woven composites,” *Journal of Composite Materials*, Vol. 35, No. 23, 2001, pp. 2127 – 2144.
- [95] Searles, K., Odegard, G., and Kumosa, M., “Micro- and mesomechanics of 8-harness satin woven fabric composites: I - evaluation of elastic behavior,” *Composites: Part A*, Vol. 32, 2001, pp. 1627 – 1655.
- [96] Gao, X.-L., Li, K., and Mall, S., “A mechanics-of-materials model for predicting Young’s modulus of damaged woven fabric composites involving three damage modes,” *International Journal of Solids and Structures*, Vol. 40, 2003, pp. 981 – 999.
- [97] Angioni, S., Meo, M., and Foreman, A., “A comparison of homogenization methods for 2-D woven composites,” *Composites: Part B*, Vol. 42, 2011, pp. 181 – 189.

REFERENCES

- [98] “B-basis design allowables for epoxy-based prepreg: 3M E-glass fabric 7781 / SP381,” Advanced General Aviation Transport Experiments, available on the NIAR AGATE website <http://www.niar.twsu.edu/agate/Documents/default.htm>, Last accessed June 9, 2011, September 2001.

Appendix A

Additional Results of CAI Experiments

Table A.1: Additional results of impact survey of PXX series materials: panel 1 damage metrics.

Panel	1	1	1	1	1
Location	1	2	3	4	5
Tip Size (in.)	0.5	0.5	0.5	0.5	0.5
Impact Energy (ft-lb.)	0.5	1.0	1.5	2.0	0.5
Drop Height (in.)	2.1875	4.375	6.6875	8.6875	2.1875
Max Force (lb.)	N/R	176.6	221.6	245.6	113.9
Impact Length (sec.)	N/R	0.00614	0.00606	0.00803	0.00665
Dent Depth (in.)	0.005	0.015	0.018	0.06	0.006
Dent Diameter (in.)	0.67	0.97	0.93	1.13	0.72

Table A.2: Additional results of impact survey of PXX series materials: panel 2 damage metrics.

Panel	2	2	2	2	2
Location	1	2	3	4	5
Tip Size (in.)	1.0	1.0	1.0	1.0	1.0
Impact Energy (ft-lb.)	1.0	2.0	3.0	4.0	4.0
Drop Height (in.)	4.375	8.6875	13.0625	17.4375	17.4375
Max Force (lb.)	182.3	282.0	361.0	N/R	408.8
Impact Length (sec.)	0.00615	0.00591	0.00596	N/R	0.00576
Dent Depth (in.)	0.009	0.015	0.023	0.032	0.03
Dent Diameter (in.)	0.92	1.18	1.35	1.43	1.48

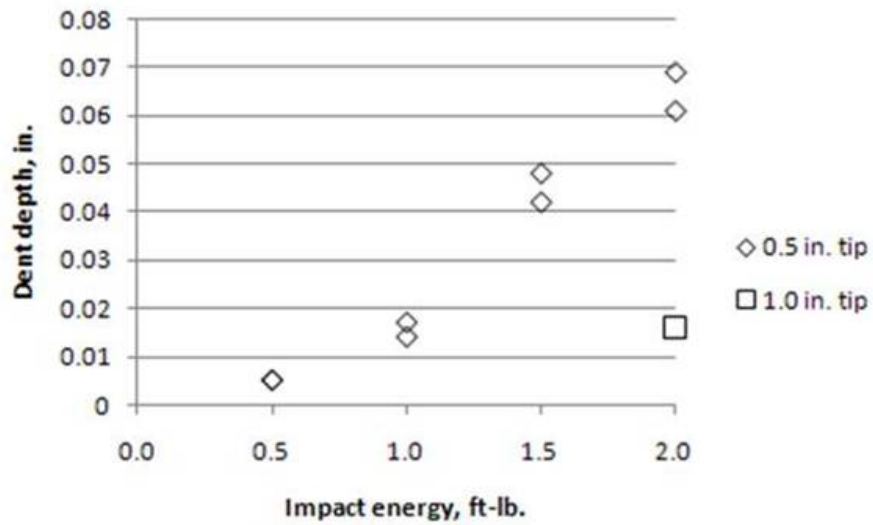


Figure A.1: Additional results of CAI testing of PXX series materials: residual dent depth vs. impact energy.

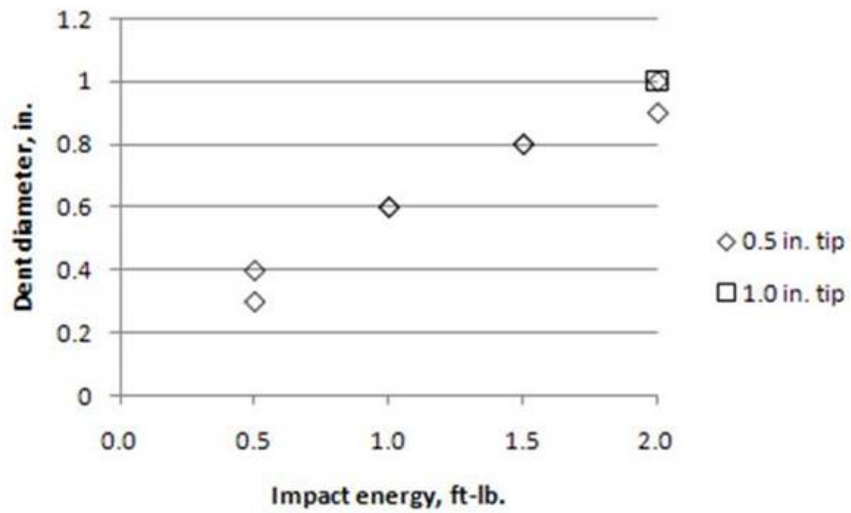


Figure A.2: Additional results of CAI testing of PXX series materials: residual dent diameter vs. impact energy.

Table A.3: Additional results of impact survey of PXX series materials: panel 3 damage metrics.

Panel	3	3	3	3	3	3	3	3	3	3	3	3
Location	1	2	3	4	5	6	7	8	9			
Tip Size (in.)	1.0	NONE	1.0	NONE	0.5	0.5	NONE	0.5	0.5			
Impact Energy (ft-lb.)	5.0	NONE	6.0	NONE	2.5	2.0	NONE	1.5	1.0			
Drop Height (in.)	21.75	NONE	26.125	NONE	10.875	8.6875	NONE	6.6875	4.375			
Max Force (lb.)	481.5	NONE	519.1	NONE	226.3	244.4	NONE	219.7	176.8			
Impact Length (sec.)	0.00541	NONE	0.00588	NONE	0.00963	0.00806	NONE	0.00656	0.00619			
Dent Depth (in.)	0.027	NONE	0.052	NONE	0.074	0.061	NONE	0.023	0.011			
Dent Diameter (in.)	1.53	NONE	1.48	NONE	1.05	1.15	NONE	1.07	0.88			

Table A.4: Additional results of CAI testing of PXX series materials: impact damage metrics.

Panel	Date Impacted	Damage Energy (ft-lb.)	Indentor Tip Size (in.)	Residual Dent Depth (in.)	Residual Dent Diameter (in.)
P01-000-F00	Undamaged	-	-	-	-
P02-000-F00	Undamaged	-	-	-	-
P03-000-F00	Undamaged	-	-	-	-
P04-005-F10	7/30/2009	1.0	0.5	0.014	0.6
P05-005-F10	7/30/2009	1.0	0.5	0.017	0.6
P06-005-F15	7/30/2009	1.5	0.5	0.042	0.8
P07-005-F15	7/30/2009	1.5	0.5	0.048	0.8
P08-005-F20	8/27/2009	2.0	0.5	0.061	0.9
P09-005-F20	8/27/2009	2.0	0.5	0.069	1.0
P10-010-F20	8/17/2009	2.0	1.0	0.016	1.0
P11-005-F05	8/27/2009	0.5	0.5	0.005	0.4
P12-005-F05	8/27/2009	0.5	0.5	0.005	0.3

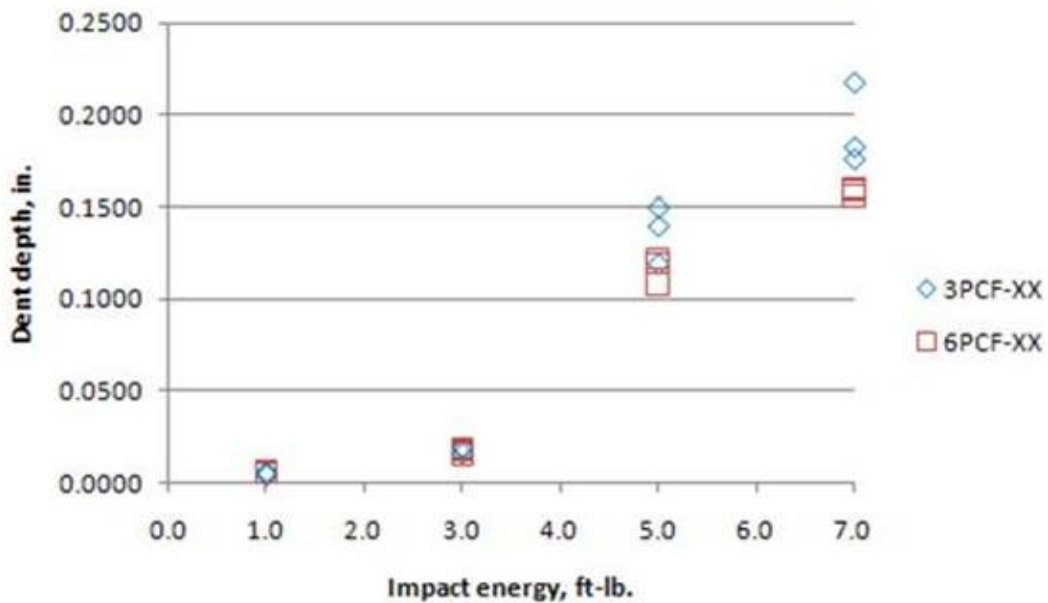


Figure A.3: Additional results of CAI testing of 3PCF-XX and 6PCF-XX series materials: residual dent depth for impacts on coupons used for CAI testing of 3PCF-XX and 6PCF-XX series materials.

Table A.5: Additional results of CAI testing of PXX series materials: CAI failure metrics.

Panel	Date and Time of Day Tested	Ambient Temperature (°F)	Ambient Humidity (%)	Damage Energy (ft-lb.)	Failure Stress (ksi)	Failure Load (lb.)	Failure Strain (μ -in/in)	Panel Compressive Modulus (Msi)
P01-000-F00	8/6/2009, 3:05pm	74.0	59.0	-	35.1	8290	10000	3.45
P02-000-F00	9/2/2009, 1:00pm	74.0	52.0	-	31.6	7520	8925	3.51
P03-000-F00	Untested	-	-	-	-	-	-	-
P04-005-F10	8/7/2009, 9:30am	73.8	63.0	1.0	26.8	6330	7700	3.45
P05-005-F10	9/2/2009, 3:00pm	74.0	52.0	1.0	25.7	6116	7283	3.48
P06-005-F15	8/25/2009, 9:45am	73.3	57.0	1.5	23.8	5619	6760	3.52
P07-005-F15	9/24/2009, 9:00am	73.8	61.0	1.5	24.2	5769	6900	3.44
P08-005-F20	9/2/2009, 9:45am	73.8	50.0	2.0	22.2	5289	6643	3.47
P09-005-F20	9/24/2009, 9:45am	73.8	64.0	2.0	22.5	5363	6332	3.50
P10-010-F20	8/25/2009, 10:30am	73.4	54.0	2.0	24.9	5881	7030	3.54
P11-005-F05	9/2/2009, 10:25am	74.3	51.0	0.5	30.6	7276	8674	3.48
P12-005-F05	9/24/2009, 10:45am	74.0	62.0	0.5	30.7	7301	8885	3.40

Table A.6: Additional results of CAI testing of 3PCF-XX and 6PCF-XX series materials: 3PCF-XX static indentation results.

Location	1	2	3	4	5
Indenter Size (in)	0.5	0.5	0.5	0.5	0.5
Max. Force (lb)	171.2	55.5	101.2	151.1	170.8
Indentation at Max. Force (in)	0.133	0.0514	0.0816	0.118	0.140
Energy to Max. Force (ft-lb)	0.963	0.116	0.346	0.709	1.001
Facesheet Fracture at Max. Force	YES	NO	NO	NO	YES

Table A.7: Additional results of CAI testing of 3PCF-XX and 6PCF-XX series materials: 6PCF-XX static indentation results.

Location	1	2	3	4	5	6
Indenter Size (in)	0.5	0.5	0.5	0.5	0.5	0.5
Max. Force (lb)	205.1	50.9	104.4	183.6	200.2	160.1
Indentation at Max. Force (in)	0.101	0.0280	0.0555	0.093	0.109	0.081
Energy to Max. Force (ft-lb)	0.891	0.0573	0.250	0.703	0.862	0.504
Facesheet Fracture at Max. Force	YES	NO	NO	NO	YES	NO

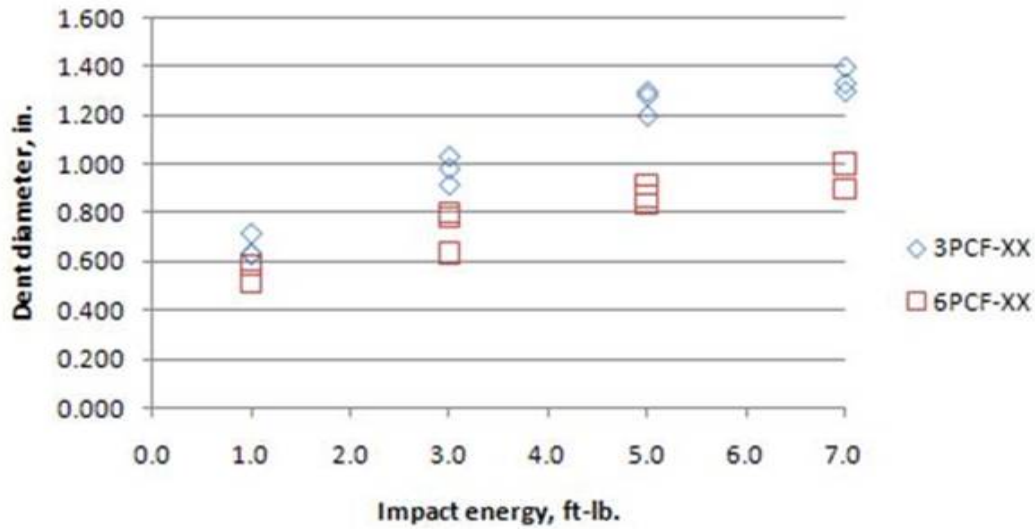


Figure A.4: Additional results of CAI testing of 3PCF-XX and 6PCF-XX series materials: residual dent diameter for impacts on coupons used for CAI testing of 3PCF-XX and 6PCF-XX series materials.

Table A.8: Additional results of CAI testing of 3PCF-XX and 6PCF-XX series materials: impact survey results describing the residual damage for 3PCF-XX materials.

Panel - Location	Damage Energy (ft lb.)	Size Tip (in.)	Dent Depth (in.)	Dent Dia (in.)	Crushed Core Max. Depth (in.)	Total Damage Depth (in.)	Core Damage Width (in.)	Notes on Core Damage
3PCF-6 - L1	1.0	0.5	0.0050	0.55	0.150	0.1550	0.867	much wavier core cell buckling, buckled core seems to extend at constant depth from damage center
3PCF-6 - L2	2.0	0.5	0.0080	0.867	0.217	0.2250	0.867	
3PCF-6 - L3	3.0	0.5	0.0105	0.917	0.167	0.1775	1.083	
3PCF-6 - L9	3.5	0.5	0.0210	1.167	0.200	0.2210	1.083	
3PCF-6 - L4	4.0	0.5	0.0920	1.183	0.150	0.2420	1.250	partial facesheet fracture observed
3PCF-6 - L5	5.0	0.5	0.1415	1.267	0.167	0.3085	1.417	
3PCF-6 - L6	6.0	0.5	0.1570	1.283	0.183	0.3400	1.167	complete facesheet fracture observed, voids in damaged region of core (no spring back), large differences between region directly underneath indentation and out region of core damage
3PCF-6 - L7	7.0	0.5	0.1810	1.333	0.200	0.3810	1.300	
3PCF-6 - L8	8.0	0.5	0.2440	1.383	0.217	0.4610	1.670	

Table A.9: Additional results of CAI testing of 3PCF-XX and 6PCF-XX series materials: impact survey results describing the force and length of impact for 3PCF-XX materials.

Panel - Location	Damage Energy (ft-lb.)	Size Tip (in.)	Maximum Impact Force (lb.)	Impact Length (sec.)
3PCF-6 - L1	1.0	0.5	178.1	0.00601
3PCF-6 - L2	2.0	0.5	264.1	0.00572
3PCF-6 - L3	3.0	0.5	312.5	0.00576
3PCF-6 - L9	3.5	0.5	321.9	0.00569
3PCF-6 - L4	4.0	0.5	334.4	0.00756
3PCF-6 - L5	5.0	0.5	332.8	0.00838
3PCF-6 - L6	6.0	0.5	353.1	0.00855
3PCF-6 - L7	7.0	0.5	389.0	0.0136
3PCF-6 - L8	8.0	0.5	375.0	0.00921

Table A.10: Additional results of CAI testing of 3PCF-XX and 6PCF-XX series materials: impact survey results describing the residual damage for 6PCF-XX materials.

Panel - Location	Damage Energy (ft. lb.)	Size Tip (in.)	Dent Depth (in.)	Dent Dia (in.)	Crushed Core Max. Depth (in.)	Total Damage Depth (in.)	Core Damage Width (in.)	Notes on Core Damage
6PCF-5 - L1	1.0	0.5	0.0045	0.533	0.100	0.1045	0.550	Small displacements, single cell wall fractures, width difficult to tell, seems to depend on cell alignment
6PCF-5 - L2	2.0	0.5	0.0095	0.717	0.100	0.1095	0.750	Same depth as 1.0 ft-lb but larger wall displacements
6PCF-5 - L3	3.0	0.5	0.0155	0.9	0.133	0.1485	0.733	Cut not quite in center of damage
6PCF-5 - L4	4.0	0.5	0.0760	0.933	0.083	0.1590	0.857	Severe crushing seen, cut not centered,
6PCF-5 - L5	5.0	0.5	0.1220	0.9	0.100	0.2220	0.783	Larger areas of core crinkle at edges of facesheet indentation. Severe delamination observed, Lower ply completely fractured
6PCF-5 - L6	6.0	0.5	0.1330	0.883	0.100	0.2330	0.817	
6PCF-5 - L7	7.0	0.5	0.1500	0.933	0.067	0.2170	0.833	cut not centered, facesheet completely fractured with open holes
6PCF-5 - L8	8.0	0.5	0.1660	0.933	0.133	0.2990	0.817	complete damage character change at edge of facesheet indentation, large amounts of damage directly under damage (0.533 dia for instance), trace damage in area surrounding
6PCF-5 - L9	9.0	0.5	0.1905	0.95	0.133	0.3235	0.833	void in core depth region, completely vacated by crushing with no rebound of core

Table A.11: Additional results of CAI testing of 3PCF-XX and 6PCF-XX series materials: impact survey results describing the force and length of impact for 6PCF-XX materials.

Panel - Location	Damage Energy (ft-lb.)	Size Tip (in.)	Maximum Impact Force (lb.)	Impact Length (sec.)
6PCF-5 - L1	1.0	0.5	214.1	0.00458
6PCF-5 - L2	2.0	0.5	295.3	0.00444
6PCF-5 - L3	3.0	0.5	373.4	0.00453
6PCF-5 - L4	4.0	0.5	407.8	0.00589
6PCF-5 - L5	5.0	0.5	417.2	0.00630
6PCF-5 - L6	6.0	0.5	400.0	0.00656
6PCF-5 - L7	7.0	0.5	425.0	0.00777
6PCF-5 - L8	8.0	0.5	429.7	0.00974
6PCF-5 - L9	9.0	0.5	471.9	0.0104

Table A.12: Additional results of CAI testing of 3PCF-XX and 6PCF-XX series materials: results for impacts on 3PCF-XX coupons used for CAI testing.

Panel	Date Impacted	Damage Energy (ft-lb.)	Indentor Tip Size (in.)	Residual Dent Depth (in.)	Residual Dent Diameter (in.)
3PCF-01	5/21/2010	3.0	0.5	0.0165	0.917
3PCF-02	5/21/2010	1.0	0.5	0.0050	0.633
3PCF-03	5/21/2010	3.0	0.5	0.0195	1.033
3PCF-04	UNDAMAGED	-	-	-	-
3PCF-05	5/21/2010	1.0	0.5	0.0060	0.717
3PCF-06	IMPACT SURVEY	-	-	-	-
3PCF-07	5/21/2010	7.0	0.5	0.2170	1.300
3PCF-08	5/21/2010	5.0	0.5	0.1500	1.200
3PCF-09	5/21/2010	7.0	0.5	0.1755	1.400
3PCF-10	5/21/2010	5.0	0.5	0.1195	1.300
3PCF-11	STATIC INDENT.	-	-	-	-
3PCF-12	5/21/2010	5.0	0.5	0.1400	1.283
3PCF-13	5/21/2010	3.0	0.5	0.0190	0.983
3PCF-14	UNDAMAGED	-	-	-	-
3PCF-15	5/21/2010	1.0	0.5	0.0045	0.633
3PCF-16	5/21/2010	7.0	0.5	0.1820	1.333

Table A.13: Additional results of CAI testing of 3PCF-XX and 6PCF-XX series materials: results for impacts on 6PCF-XX coupons used for CAI testing.

Panel	Date Impacted	Damage Energy (ft-lb.)	Indentor Tip Size (in.)	Residual Dent Depth (in.)	Residual Dent Diameter (in.)
6PCF-01	5/21/2010	7.0	0.5	0.1605	1.000
6PCF-02	5/21/2010	3.0	0.5	0.0155	0.783
6PCF-03	5/21/2010	5.0	0.5	0.1220	0.833
6PCF-04	UNDAMAGED	-	-	-	-
6PCF-05	IMPACT SURVEY	-	-	-	-
6PCF-06	5/21/2010	5.0	0.5	0.1190	0.917
6PCF-07	5/21/2010	1.0	0.5	0.0060	0.583
6PCF-08	UNDAMAGED	-	-	-	-
6PCF-09	5/21/2010	3.0	0.5	0.0170	0.633
6PCF-10	5/21/2010	1.0	0.5	0.0055	0.517
6PCF-11	5/21/2010	7.0	0.5	0.1560	0.900
6PCF-12	5/21/2010	5.0	0.5	0.1080	0.867
6PCF-13	STATIC INDENT.	-	-	-	-
6PCF-14	5/21/2010	7.0	0.5	0.1590	1.000
6PCF-15	5/21/2010	3.0	0.5	0.0185	0.800
6PCF-16	5/21/2010	1.0	0.5	0.0060	0.583

Table A.14: Additional results of CAI testing of 3PCF-XX and 6PCF-XX series materials: results for failure of 3PCF-XX series panels during CAI testing.

Panel	Date and Time of Day Tested	Ambient Temperature (°F)	Ambient Humidity (%)	Damage Energy (ft-lb.)	Failure Stress (ksi)	Failure Load (lb.)	Failure Strain (μ -in/in)	Panel Compressive Modulus (Msi)	Auxiliary Instrumentation
3PCF-01	8/5/2010, 11:30am	79.9	50.0	3.0	29.3	6450	8005	3.66	HSC
3PCF-02	8/9/2010, 11:30am	77.4	51.0	1.0	31.6	6953	8323	3.80	HSC/VIDEO
3PCF-03	9/2/2010, 3:00pm	76.9	52.0	3.0	29.9	6583	8150	3.67	DIC
3PCF-04	NOT TESTED	-	-	-	-	-	-	-	-
3PCF-05	9/8/2010, 3:30pm	77.0	50.0	1.0	33.9	7459	8865	3.82	DIC
3PCF-06	IMPACT SURVEY	-	-	-	-	-	-	-	-
3PCF-07	8/9/2010, 3:15pm	77.6	50.0	7.0	24.0	5283	6701	3.58	HSC/VIDEO
3PCF-08	8/10/2010, 1:30pm	79.0	51.0	5.0	26.3	5786	7094	3.71	HSC/VIDEO
3PCF-09	8/21/2010, 2:00pm	76.1	51.0	7.0	23.2	5103	6549	3.54	DIC
3PCF-10	8/19/2010, 4:30pm	78.1	58.0	5.0	23.7	5206	6670	3.55	DIC
3PCF-11	STATIC INDENT.	-	-	-	-	-	-	-	-
3PCF-12	8/25/2010, 11:00am	77.6	51.0	5.0	23.2	5097	6732	3.44	HSC
3PCF-13	8/25/2010, 3:00pm	77.9	52.0	3.0	29.1	6406	8033	3.62	HSC
3PCF-14	8/18/2010, 1:30pm	78.5	49.0	0.0	43.5	9580	12165	3.58	NONE
3PCF-15	8/26/2010, 10:30am	77.9	52.0	1.0	33.2	7307	9117	3.64	HSC
3PCF-16	8/24/2010, 2:00pm	78.8	51.0	7.0	22.0	4837	6597	3.33	HSC

Table A.15: Additional results of CAI testing of 3PCF-XX and 6PCF-XX series materials: results for failure of 6PCF-XX series panels during CAI testing.

Panel	Date and Time of Day Tested	Ambient Temperature (°F)	Ambient Humidity (%)	Damage Energy (ft-lb.)	Failure Stress (ksi)	Failure Load (lb.)	Failure Strain (μ -in/in)	Panel Compressive Modulus (Msi)	Auxiliary Instrumentation
6PCF-01	8/9/2010, 2:00pm	78.5	51.0	7.0	26.5	5826	7572	3.50	NONE
6PCF-02	8/5/2010, 4:00pm	79.9	50.0	3.0	30.5	6702	8789	3.47	HSC
6PCF-03	8/9/2010, 3:15pm	78.1	50.0	5.0	27.8	6107	7776	3.57	HSC/VIDEO
6PCF-04	NOT TESTED	-	-	-	-	-	-	-	-
6PCF-05	IMPACT SURVEY	-	-	-	-	-	-	-	-
6PCF-06	8/19/2010, 2:15pm	77.6	60.0	5.0	29.6	6510	8687	3.41	DIC
6PCF-07	8/10/2010, 10:00am	78.1	52.0	1.0	33.9	7462	9537	3.56	HSC/VIDEO
6PCF-08	8/17/2010, 11:00am	78.5	48.0	0.0	40.8	8967	11726	3.48	NONE
6PCF-09	9/8/2010, 10:30am	76.9	58.0	3.0	34.4	7557	10124	3.39	DIC
6PCF-10	9/8/2010, 2:00pm	76.3	53.0	1.0	37.2	8201	10916	3.41	DIC
6PCF-11	9/2/2010, 4:00pm	76.7	52.0	7.0	25.1	5512	7605	3.29	DIC
6PCF-12	8/26/2010, 3:00pm	77.9	53.0	5.0	31.8	6992	9489	3.35	HSC
6PCF-13	STATIC INDENT.	-	-	-	-	-	-	-	-
6PCF-14	8/24/2010, 2:00pm	78.8	51.0	7.0	28.3	6220	8012	3.53	HSC
6PCF-15	8/27/2010, 8:30am	77.8	51.0	3.0	32.7	7203	9926	3.30	HSC
6PCF-16	8/27/2010, 10:15am	78.5	51.0	1.0	35	7755	10256	3.44	HSC

REPORT DOCUMENTATION PAGE

*Form Approved
OMB No. 0704-0188*

The public reporting burden for this collection of information is estimated to average 1 hour per response, including the time for reviewing instructions, searching existing data sources, gathering and maintaining the data needed, and completing and reviewing the collection of information. Send comments regarding this burden estimate or any other aspect of this collection of information, including suggestions for reducing this burden, to Department of Defense, Washington Headquarters Services, Directorate for Information Operations and Reports (0704-0188), 1215 Jefferson Davis Highway, Suite 1204, Arlington, VA 22202-4302. Respondents should be aware that notwithstanding any other provision of law, no person shall be subject to any penalty for failing to comply with a collection of information if it does not display a currently valid OMB control number.
PLEASE DO NOT RETURN YOUR FORM TO THE ABOVE ADDRESS.

1. REPORT DATE (DD-MM-YYYY) 01-06-2011			2. REPORT TYPE Contractor Report		3. DATES COVERED (From - To)	
4. TITLE AND SUBTITLE Compression After Impact Experiments and Analysis on Honeycomb Core Sandwich Panels with Thin Facesheets					5a. CONTRACT NUMBER NNL09AA00A	
					5b. GRANT NUMBER	
					5c. PROGRAM ELEMENT NUMBER	
6. AUTHOR(S) McQuigg, Thomas D.					5d. PROJECT NUMBER	
					5e. TASK NUMBER	
					5f. WORK UNIT NUMBER 727950.04.03.23	
7. PERFORMING ORGANIZATION NAME(S) AND ADDRESS(ES) NASA Langley Research Center Hampton, VA 23681-2199					8. PERFORMING ORGANIZATION REPORT NUMBER	
9. SPONSORING/MONITORING AGENCY NAME(S) AND ADDRESS(ES) National Aeronautics and Space Administration Washington, DC 20546-0001					10. SPONSOR/MONITOR'S ACRONYM(S) NASA	
					11. SPONSOR/MONITOR'S REPORT NUMBER(S) NASA/CR-2011-217157	
12. DISTRIBUTION/AVAILABILITY STATEMENT Unclassified - Unlimited Subject Category 24 Availability: NASA CASI (443) 757-5802						
13. SUPPLEMENTARY NOTES Dissertation submitted to the Faculty of the Virginia Polytechnic Institute and State University in partial fulfillment of the requirements for the degree of Doctor of Philosophy in Aerospace Engineering, May 27, 2011 Langley Technical Monitor: Stephen J. Scotti						
14. ABSTRACT A better understanding of the effect of impact damage on composite structures is necessary to give the engineer an ability to design safe, efficient structures. Current composite structures suffer severe strength reduction under compressive loading conditions, due to even light damage, such as from low velocity impact. A review is undertaken to access the current state-of-development in the areas of experimental testing, and analysis methods. A set of experiments on honeycomb core sandwich panels, with thin woven fiberglass cloth facesheets, is described, which includes detailed instrumentation and unique observation techniques.						
15. SUBJECT TERMS Composite structures; Damage tolerance; Impact damage; Honeycomb cores; Sandwich panels; Finite element analysis; Multicontinuum Failure Theory						
16. SECURITY CLASSIFICATION OF:			17. LIMITATION OF ABSTRACT	18. NUMBER OF PAGES	19a. NAME OF RESPONSIBLE PERSON	
a. REPORT	b. ABSTRACT	c. THIS PAGE			19b. TELEPHONE NUMBER (Include area code)	
U	U	U	UU	286	STI Help Desk (email: help@sti.nasa.gov) (443) 757-5802	